

https://dspace.org/

Studies on the chemistry and biochemistry of gold(III) carboxamide pincer chelates

Razuwika, Rufaro

2024-06
University of the Witwatersrand, Johannesburg
https://hdl.handle.net/10539/45689
Razuwika, Rufaro. (2024). Studies on the chemistry and biochemistry of gold(III) carboxamide pincer chelates. [PhD thesis, University of the Witwatersrand, Johannesburg]. WIReDSpace. https://hdl.handle.net/10539/45689

Downloaded from a DSpace repository. https://dspace.org/

Studies on the chemistry and biochemistry of gold(III) carboxamide pincer chelates



WITS
UNIVERSITY

100
1922
2022

By: Rufaro Razuwika

A thesis submitted to the Faculty of Science, University of the Witwatersrand, Johannesburg, in fulfilment of the requirements for the degree of **Doctor of Philosophy.**

[June 2024]

Declaration

I, Rufaro Razuwika, solemnly declare that this thesis is entirely my original work and is being submitted for the Degree of Doctor of Philosophy at the University of the Witwatersrand, Johannesburg. I affirm that it has not been previously submitted for any degree or examination at any other University.

The synthesis and characterisation of the resulting compounds, along with all bioinorganic experiments, were conducted personally by me in the laboratory of Prof O. Q. Munro at the University of the Witwatersrand. The collection and refinement of single-crystal X-ray diffraction data were jointly undertaken by Prof O.Q. Munro and me at the University.

I executed computational studies using the local computer infrastructure, and Prof O. Q. Munro utilised his local computer at the University of the Witwatersrand and the Centre of High-Performance Computing (CHPC).

All *in vitro* procedures were meticulously conducted by Ruth Aronson under the guidance of Prof M. Kaur in collaboration with the University of the Witwatersrand.

I extend sincere gratitude to the National Research Foundation (NRF) for their financial support in the form of a bursary. I wish to emphasise that any opinions expressed, and conclusions drawn within this thesis are solely those of the author and do not necessarily reflect the views of the NRF.

RRuzuwika

(Signature of candidate)

3rd day of June 2024 at the University of the Witwatersrand

Abstract

Cancer, a group of diseases characterised by the uncontrollable growth of abnormal or mutated cells within an organ, is a global concern. Metallodrugs have emerged as promising solutions to this pandemic, leading to intense research on different metal complexes.

In this study, gold(III) carboxamide pincer complexes were evaluated as potential chemotherapeutic agents. The novel NNN-type carboxamide pincer molecules (ligands) effectively stabilising the gold(III) metal centre. The strong σ-donor properties of both the anionic and pyridine N groups further enhanced this stability. Ligands **1a-1f** exhibited atropisomerism, a common feature in drug discovery, and containing special heterocycles such as quinolones, indazole, benzophenone, and phenanthroline, which are particularly relevant in drug development. Atropisomerism, however, was lost upon metalation of the ligands.

Three complexes, **2d**, **2e**, and **2f**, were successfully synthesised and isolated. Complex **2d** was subjected to biochemical property testing and *in vitro* analysis due to its superior stability and solubility compared to **2e** (poor stability) and **2f** (poor solubility in the buffer solution used in the study). Speciation studies, combined with computational studies, suggested that **2d** exists as a neutral complex under physiological conditions. This inert complex demonstrated stability against the reducing agent glutathione, indicating resilience to reduction under physiological conditions.

DNA spectroscopic titration studies revealed that **2d** exhibited intensive interaction with ct-DNA, with binding constants K_{a1} = 1.48 x10^{9} M^{-1} and K_{a2} = 6.59 x10^{5} M^{-1}. This interaction resulted in a notable increase in the DNA melting point by 4 °C and an enhancement in viscosity in a dose-responsive manner. The DNA titrations, melting point, and viscosity studies suggested a dual binding mode of **2d** to ct-DNA, involving base binding with a nearly equal preference for A, T, G, and C bases, and groove binding.

Complex **2d** exhibited a high affinity towards the transport protein HSA (K_a values were 1.57 x10^{4} M^{-1}), suggesting that it can be transported in the body by means of the HSA-mediated pathway, enhancing its efficacy and stability. In comparison to its affinity towards DNA, there is a significant difference allowing for the successful transfer of **2d** from HSA to DNA. The poor solubility of complex **2d** in aqueous environments may have hindered its cellular uptake, but binding to HSA could mitigate this, ensuring minimal interference with its cytotoxicity towards different cancer cell lines. MTT studies demonstrated that **2d** has comparable cytotoxicity towards the breast cancer cell line MCF-7 with an IC_{50} of 9 μM. The IC_{50} for HT-29 was, however, too high to measure accurately (>100 μM).

In conclusion, complex **2d** exhibits promising anticancer properties based on its DNA binding studies and cytotoxicity evaluations. This suggests that this class of compounds can be applied in cancer treatments, with potential modifications to compounds **2e** and **2f** to improve their solubility and stability.

Acknowledgements

I extend my sincere gratitude to several individuals who have played pivotal roles in my academic journey:

I am profoundly grateful to Prof Orde Q. Munro, my esteemed mentor at Leeds University. Your influence was instrumental in my decision to pursue Chemistry for my honors. Despite our paths diverging during my PhD, I am immensely thankful for the invaluable mentorship and support you provided over the past six years. Your guidance enriched my learning experience beyond the typical PhD trajectory.

To my dedicated lab mates—Mark, Sheldon, Mathew, and Kebuile—thank you for being pillars of support on this challenging journey. Your emotional and intellectual backing made the path smoother, and your unwavering assistance during tribulations will forever be appreciated. Working alongside you was a privilege.

I extend my thanks to Dr Monika Nowakowska and Dr Sadhna Mathura, whose guidance was instrumental in helping me reach the finish line. Special gratitude to Prof Manuel Fernandez for valuable insights during the thesis write-up.

A heartfelt thank you to the support staff of the School of Chemistry at the University of the Witwatersrand. Your dedication ensured the smooth operation of the department, and the assistance from personnel in the NMR, MS, and X-ray departments was invaluable.

To my family, who stood by me with unwavering encouragement and support, I owe my deepest gratitude. My parents, for their enduring patience and belief in my abilities. My sister, for her hospitality, nourishment, and unyielding cheerleading.

Finally, I express gratitude to God for granting me the perseverance and tenacity needed to navigate this challenging academic journey.

This journey has been made richer by the collective contributions of each person mentioned, and for that, I am truly thankful.

Table of Contents

Declaration i

Abstract ii

Acknowledgements iii

Table of Contents iv

List of Figures vii

List of Schemes xi

List of Equations xii

1 Introduction 1

1.1 Cancer treatment options 1

1.1.1 Chemotherapy 3

1.1.2 The cell cycle and its relevance in cancer treatment 4

1.1.3 Classification of cell cycle chemotherapeutic drugs 7

1.1.4 Mode of action of cell cycle-specific chemotherapeutic drugs 9

1.2 Metallodrugs in cancer treatment 12

1.2.1 Properties of metallodrugs desirable in cancer treatment 12

1.2.2 Gold in cancer treatment 13

1.2.3 Pincer molecules 16

1.2.4 Nitrogen-containing heterocycles 20

1.3 Rationale and aims for the research 24

1.3.1 Hypothesis 24

1.3.2 General aims 24

1.3.3 Objectives 24

1.4 References 26

2. Experimental 40

2.1. General Methods 40

2.1.1. Instrumentation 40

2.2. Ligands Synthesis 42

2.2.1. N^2,N^6-Bis(isoquinolin-4-yl)pyridine-2,6-dicarboxamide (1a) 42

2.2.2. N^2,N^6-Bis(quinolin-3-yl)pyridine-2,6-dicarboxamide (1b) 43

2.2.3. N^2,N^6-Bis(quinolin-8-yl)pyridine-2,6-dicarboxamide (1c) 44

2.2.4. N^2,N^6-Bis(1-methyl-1H-indazol-3-yl)pyridine-2,6-dicarboxamide (1d) 45
2.2.5. N^2,N^6-Bis(2-benzoylphenyl)pyridine-2,6-dicarboxamide (1e) 46
2.2.6. N^2,N^6-Bis(1,10-phenanthrolin-5-yl)pyridine-2,6-dicarboxamide (1f) 47
2.3. Synthesis of gold(III) metal chelates 47
2.3.1. N^2,N^6-Bis(1-methyl-1H-indazol-3-yl)pyridine-2,6-dicarboxamide gold(III) chloride (2d) 48
2.3.2. N^2,N^6-Bis(2-benzoylphenyl)pyridine-2,6-dicarboxamide gold(III) chloride (2e) 49
2.3.3. N^2,N^6-Bis(1,10-phenanthrolin-5-yl)pyridine-2,6-dicarboxamide gold(III) chloride (2f) ... 50
2.4. Other attempts 50
2.4.1. N^2,N^6-Bis(1-methyl-1H-indazol-3-yl),(2H-silver(I)fluoride)pyridine-2,6-dicarboxamide gold(III) chloride (2di) 51
2.4.2. N^2,N^6-Bis(1-methyl-1H-indazol-3-yl),(2H-gold(I)chloride)pyridine-2,6-dicarboxamide gold(III) chloride (2dii) 52
2.5. Conclusion 52
2.6. References 52
3. Ligand Synthesis and Characterisation 54
3.1 Ligand chemistry and synthesis 55
3.2 Ligand characterisation 57
3.2.1 IR spectroscopy 57
3.2.2 Nuclear Magnetic Resonance (NMR) spectroscopy 59
3.2.3 Melting temperatures 61
3.2.4 UV-Vis Spectroscopy 62
3.2.5 Xray crystallography 66
3.3 Conformational analysis 76
3.3.1 X-ray crystallography and PM6 simulations 76
3.3.2 Circular Dichroism (CD) Spectroscopy 78
3.3.3 NMR 81
3.4 Summary and conclusion 85
3.5 References 85
4. Gold(III) Complexes Synthesis and Characterisation 89
4.1 Gold(III) complexes chemistry 89
4.2 Gold(III) complexes synthesis 90
4.3 Complex Characterisation 91

4.3.1 IR Spectroscopy 91
4.3.2 NMR Spectroscopy 93
4.3.3 UV-vis Spectroscopy 95
4.3.4 Unexpected metal complexes 97
4.3.5 X-ray Crystallography 101
4.4 Conclusion 108
4.5 References 108
5. Biochemistry and Cellular Biology 110
5.1 Instrumentation and Methods 110
5.2 *p*K_a determination 113
5.3 GSH binding studies (stability studies) 117
5.4 DNA binding studies 119
5.4.1 EMSA 119
5.4.2 UV-vis titration experiments (ct-DNA, nucleobases, nucleosides and nucleotides titrations) 121
5.4.3 Viscometry and melts 125
5.5 HSA binding studies 126
5.5.1 Thermodynamics of 2d binding to HSA 127
5.5.2 Site displacement assays 129
5.6 Cellular Biology 132
5.6.1 MTT assays 132
5.6.2 APOPercentage assay 133
5.7 Conclusion 134
5.8 References 135
6. Summary and conclusion 138
6.1. Summary of the study 138
6.2. Study evaluation 138
6.3. Future work 139

List of Figures

Figure 1.1. An illustration of some of the main techniques used for the treatment of cancer around the world.[20,21,23] (The figure was constructed using BioRender scientific illustration software https://www.biorender.com/) 2
Figure 1.2. An illustration of the different cell cycle phases: The cell cycle outlines the life of a cell from the time it is generated from a dividing parent cell until it splits into two daughter cells. The cycle consists of four successive phases: G_1, S, G_2, and M.[98,99] 4
Figure 1.11. Chemical structures of the carboxamide pincer ligands to be discussed in this thesis, with isoquinoline, quinolone, indazole, benzophenone and phenanthroline moieties. 25
Figure 1.12. Chemical structures of the proposed novel conventional gold(III) pincer chelates with isoquinoline, quinolone, indazole, benzophenone and phenanthroline moieties, to enhance potential interactions with DNA bases. 25
Figure 3.1. IR spectra of the synthesised carboxamide pincer ligands 1a-1f (left) in comparsion to the calculated data (right). 58
Figure 3.2. A comparison of the IR spectra of 1d from the experimental work (blue), and the calculated data (pink) 58
Figure 3.3. Illustration of the proton (a) and carbon (b) NMR spectra for 1a (maroon lines, main spectra). The inset figures, in each case, display the variation in the chemical shift of the amide NH protons and the C=O carbons for the pincer compounds 1b–1f. 60
Figure 3.4. (a) Experimental and (b) DFT-calculated electronic absorption spectra of 1d in DMSO. The absorption maxima are indicated for the experimental spectrum at 199, 222 and 285 nm. The absorption envelope for the DFT-calculated spectrum is plotted with a band width of 2200 cm^{-1} (full width at half maximum intensity, FWHM). (c) Absorption spectra at a concentration range between 3 and 38 μM, to calculate the extinction coefficients at the λ_{max} in (d) (Beer-Lambert's Law). 64
Figure 3.5. a) Experimental and b) DFT-calculated electronic absorption spectra of 1d in DMSO. The absorption maxima (λ_{max}) are indicated for the experimental spectrum at 199, 223 and 285 nm, The absorption envelope for the DFT-calculated spectrum is plotted with full width at half maximum intensity (FWHM) of 3000 cm^{-1} adjusted by -80 nm; c) Molecular orbital involved in the three most intense bands in the DFT-calculated electronic spectrum of 1d DMSO. The percentage contribution of the electronic transitions to each band is indicated. 65
Figure 3.6. Experimental electronic absorption spectra of 1a-1f in different solvents. 65
Figure 3.7. Selectively labelled views of the X-ray crystal structures of 1a–1e refined with non-spherical atom form factors (NoSpherA2 within Olex2). Thermal ellipsoids are rendered at the 50% probability level (C, N, O). Hydrogen atom thermal ellipsoids are scaled to have the same equivalent isotropic displacement parameter, $U_{(eq)}$, as the attached heavy atom. H-bond distances and angles for 1b: N5···H1S, 1.813(8) Å; H1···O2S, 2.086(6) Å; H3···O2S, 2.141(6) Å; H2S···O1S, 1.744(9) Å; N5···H1S–O1S, 168.3(7)°; N1–H1···O2S, 133.5(5)°; N3–H3···O2S, 158.8(5)°; O2S–H2S···O1S, 174.4(7)°. H-bond distances and angles for 1e: H1···O3, 1.96(1) Å; H3···O4, 1.86(1) Å; H22···O2, 2.18(1) Å; N1–H1···O3, 126(1)°; N3–H3···O4, 137(1)°; C22–H22···O2, 120.6(7)°. Space groups: $P2_1/c$, 1a; $P1$, 1b; $P2_12_12_1$, 1c; $P2/c$, 1d; $P2_1/n$, 1e. Significant nonbonded crystal packing and hydrogen bonding interactions break the intrinsic C_2 symmetry of 1a, 1b, and 1e, preventing their crystallisation in Sohncke space groups. Only 1d has exact C_2 symmetry in the crystalline solid state; however, crystallisation as a C_i symmetry dimer restricts it to a regular space group. Compound 1c has C_1 point group symmetry due to asymmetric packing interactions which break its C_2 symmetry. Since higher-symmetry oligomer formation is absent, 1c is the only compound of the series that crystallises in a chiral space group. 69
Figure 3.8. a) (a) View of the *C*i symmetry hydrogen-bonded dimers formed by monomers of 1a (top; symmetry codes *x*,*y*,*z* and 1-*x*,1-*y*,1-*z*) and 1d (bottom, exact C_2 point group symmetry; symmetry codes *x*,*y*,*z* and 1-*x*,*y*,1/2-

z). The linear chain of dimers (1a) or evenly spaced monomers (1d), where assembly is about centres of inversion in the lattice, favours crystallisation in non-Sohncke space groups. Non-polar hydrogen atoms are omitted for clarity; atoms involved in hydrogen bonding are rendered as spheres (arbitrary radii). (b) Illustration highlighting the nonplanarity of pincer 1c and the dihedral angle (Δ_2, 24.4°) between the planes passing through the central pyridine ring and the canted quinoline ring appended to the amide group containing carbonyl oxygen O2. Torsion angles defining the orientation of the second quinoline ring substituent ($\phi1'$–$\phi3'$) are defined; the equivalent torsion angles for the first quinoline ring (right side) are $\phi1$–$\phi3$ (i.e., unprimed). 71
Figure 3.9. View of a pair of neighboring molecules in the crystal lattice of 1b. The non-classical hydrogen bond C22–H22···N4 (2.491(7) Å) tips the quinoline ring out of the mean plane encompassing the central pyridine ring of the pincer, with the dihedral angle C19–N1–C2–C1 measuring 162.87(5)°. The dihedral angle for the second quinoline group (C25–N3–C11–C10, 176.31(5)°) is almost coplanar with the amide group and central pyridine ring. 73
Figure 3.10. Space filling views of the hydrogen-bonded C_i symmetry dimer of structure 1a. The diagram at the left is a view from above the dimer perpendicular to the plane of the pincer's central pyridine ring, while the diagram at the right is the same view rotated counterclockwise through 90° to highlight the out-of-plane arrangement of the two isoquinoline rings. The conformation of each monomer in the crystalline solid state is markedly different from the lowest-energy conformer in the gas phase (DFT simulation), which highlights the impact of crystal packing and dimer formation on the observed conformation. 74
Figure 3.11. View depicting the short nonbonded interactions (blue stippled bonds) between the lower quinoline ring of 1c and neighboring molecule heteroaromatic rings (contact distances are given in Å). The highlighted contacts constitute C–H···π type hydrogen bonding interactions which planarise the amide group (N1) and quinoline substituent by neatly sandwiching the substituent group. The quinoline ring appended to the second amide nitrogen atom (N5) lacks short contacts involving its aryl ring carbon atoms and thus has a more canted dihedral angle relative to the plane of the central pyridine ring of the pincer. 74
Figure 3.12. Histograms displaying the distribution of the torsion angles ϕ_1–ϕ_3 from an analysis of all available X-ray structures with the same functional group components as 1c in the CSD. For ϕ_2 and ϕ_3 there are < 6 structures in each case with the torsion angle < 90° in contrast to ϕ_1 which, though still rare (0.37% of 3815 structures), has slightly more conformers with inwardly flipped amide C=O groups. 75
Figure 3.13. a) Potential energy surface (3D) for 1c calculated by rotations of ϕ_1 and ϕ_1' (see Figure 3.7 and Figure 3.12) in the gas phase using the semi-empirical method PM6. The surface has 2-fold symmetry. b) The lowest energy barrier to rotation of ϕ_1 (23.11 kJ/mol) occurs at ϕ_1; $\phi_1' = 0°$; ±180° (contour map). The pathway involves the flipping of one amide C=O group while the other substituent maintains coplanarity with the central pyridine ring. The location of the X-ray structure of 1c is indicated and the global minimum occurs at ϕ_1; $\phi_1' = 160°$; 160° (mirrored at −160°; −160°). 76
Figure 3.14. Illustration of the different helicity found at two 2-fold screw axes for crystalline 1e. The central (intramolecular or "*endo*") axis reflects a P-helical conformation (right-handed helicity). Left-handed helicity, i.e., an M-helical conformation, involves the 2-fold screw axis located "*exo"* to the pincer cavity. 78
Figure 3.15. CD spectroscopy spectra for (a) compounds 1a-1f in powder form (crystals of 1e were crushed into a powder, and the spectra was the same with the powder) (b) in solution, (1a-1b and 1f dissolved in 2-methoxyethanol, 1c dissolved in Chloroform, 1e dissolved in THF). Resultant spectra were cleaned up using the Savitzky–Golay filter in Origin 2019b by 250 pts in (a) and 50 pts in (b). 79
Figure 3.16. a) Experimental and DFT-calculated (insert) CD spectra of C_2 symmetry 1c in chloroform. (b)The CD for the DFT-calculated spectrum is plotted with full width at half maximum intensity (FWHM) of 3000 cm^{-1}. 80

Figure 3.17. a) Illustration of the temperature-dependent changes in the ^{1}H NMR spectrum for 1d between 303 K and 363 K in deuterated DMF. The inset figure showcases the changes in signal multiplicity (d = doublet, t = triplet and q = quartet) seen for the aromatic protons of compound 1d. (b) Plot of the amide proton chemical shift as a function of temperature. 82
Figure 3.18. (a) Selected NMR scans of the amide proton for 1d as a function of total concentration in DMSO at 25°C. (b)) Simple polynomial fit of the concentration dependence of the amide proton chemical shift. From the nonlinearity of the graph, 1d likely undergoes weak dimerization in DMSO in accord with the equilibrium depicted in Equation 3.2. 84
Figure 4.1. An illustration of change in the IR spectra of 1d upon metalation with gold(III) (left), and the comparison between the experimental and calculated IR spectra of 2d (right). 92
Figure 4.2. An illustration of the changes in the ^{1}H (a) and ^{13}C (b) NMR spectra in DMSO upon chelation of 1d with gold(III) to yield 2d. 93
Figure 4.3. (a) Comparison between 1d (left) and 2d (right), illustrating the shift in the indazol bands, below 350 nm and the introduction of the bands at 439 nm, which is d-d transitions, (b) Experimental (left) and DFT-calculated (right) electronic absorption spectra of 2d in DMSO. The absorption maxima are indicated for the experimental spectrum at 267, 296 and 439 nm. The absorption envelope for the DFT-calculated spectrum is plotted with a bandwidth of 2200 cm^{-1} (full width at half maximum intensity, FWHM). (c) Absorption spectra at a concentration range between 172 and 357 μM, to calculate the extinction coefficients at the λ_{max} using the Beer-Lambert's Law. 96
Figure 4.4. Molecular orbitals involved in the three most intense bands in the DFT-calculated electronic spectrum of 1d in DMSO. The percentage contribution of the electronic transitions to each band are indicated. 97
Figure 4.5. 2D Structures of the unexpectedly synthesised pincer complexes according to X-ray crystallography (2di, 2dii and 3diii) and the proposed structure of 2diii. 98
Figure 4.5. 2D Structures of the unexpectedly synthesised pincer complexes according to X-ray crystallography (2di, 2dii and 3diii) and the proposed structure of 2diii. 98
Figure 4.6. Selectively labelled views of the X-ray crystal structures of 2d, 2di, 2dii, 2dT, 2e, 3d. Thermal ellipsoids are rendered at the 50% probability level and H atoms are drawn as spheres of an arbitrary radius. Space groups: P1, 2d, 2di, 2dii, 2dT; $P2_1/n$, 2e, 3d. Complexes 2d, 2di, 2dii, 2dT, 2e have C_i symmetry, but 3d maintains the C_2 symmetry, and none of them crystallise in a Sohncke space group. The indicated bonds and molecules in 2d, 2di, 2dii and 2dT were used as references when discussing the change in the molecules. 102
Figure 4.7. Illustration of change in plane angles between (a) the two arms of the pincer complexes with the Cl (2d) displaced with the Thymine (2dT), due to their difference in size. (b) the Cl^- ions and the plane of the pincer molecule in 3d. 106
Figure 4.8. X-ray crystallography structures of 1e show casing (a) the cation π interactions in the molecule. The molecule is in three planes, which are 14.20° (pink) and 23.02° (blue) relative to the main plane (green), and 23.19° of each other. (b) The distance between the sandwiched gold(III) metal ion centre and the two sandwiching C_6 rings 3.596 Å and 3.530 Å, at an angle of 166.83° of each other. 107
Figure 5.1. UV-Visible spectra for a) 2d (1.52×10^{-4} M) at pH range of 1–13, T = 37 ◦C, and b), c), d) plots of absorbance vs. pH at 292 460 and 330 nm respectively. 115
Figure 5.2. Illustration of a) Limiting spectra for reproduction and species assignment by TD-DFT Simulations and the insert is the spectrum calculated for all the species at different pHs. b) is the proposed speciation mechanism of 2d with the increase in pH as per calculated data. 116
Figure 5.3. Time dependence of the binding of GSH to 2d with ratios of [2d]:[GSH] between 10 and 160. a) shows first-order exponential fits of the kinetics at 15 °C as plots of absorbance against time, b) plots of k_{obs} against [2d], c) is the Arrhenius plot and d) is the Erying plot for the reaction of 2d with GSH. 118

Figure 5.3. Time dependence of the binding of GSH to 2d with ratios of [2d]:[GSH] between 10 and 160. a) shows first-order exponential fits of the kinetics at 15 °C as plots of absorbance against time, b) plots of k_{obs} against [2d], c) is the Arrhenius plot and d) is the Erying plot for the reaction of 2d with GSH. 118
Figure 5.4. EMSA agarose gel for 2d with calf thymus DNA (2.5 ng/well, 1x TAE buffer, 5% v/v DMSO). The DNA peaks formed are for supercoiled (SC), nicked-open circular (NOC), and linear (Lin). Lane 1 is the control lanes containing ct-DNA only. Lanes 2-14 has increasing concentrations of ethidium bromide (EB, 2–4), 2d (5–11), and Hoechst 33258 (HS, 12–14), and they compare the behaviour of a DNA intercalator, EB, the gold(III) complex, and a DNA minor groove binder, HS respectively. Experiments were done in triplicates and a representative assay is shown. 120
Figure 5.5. A representative of the triplicates for the UV-vis absorption spectra of 117 μM 2d in 0.10 M TRIS-HCl buffer 10% DMSO (red spectrum) after sequential additions of ct-DNA 0.1 μM (purple spectrum) and final concentration (37 μM ct-DNA) before precipitation (blue spectrum). The insert shows the isobestic points at low concentrations of DNA. The graph on the right is an illustration of the Uv-vis titration spectra at 342 nm with a change in concentration of the ratio of 2d:ct-DNA. 121
Figure 5.6. A representative of the triplicates for the UV-vis absorption spectra of 117 μM 2d in 0.10 M TRIS-HCl buffer 10% DMSO after sequential additions of DNA components and final concentration before precipitation. The graphs on the right are an illustration of the Uv-vis titration spectra at specified wavelengths with a change in ratio of 2d to the DNA components. 123
Figure 5.7. a) is an illustration of the structures of DNA components, purine bases guanine (G) and adenine (A) and the pyrimidines, cytosine (C) and thymine (T), examples of a nucleosides, thymidine and the nucleotide thymidine triphosphate. The bases binds to the ribose molecule through N1 for pyrimidines and N9 for the purines. b) is the crystal structure of a thymine molecule covalently bound to 2d through N3 by displacing the Cl^- ion. .. 124
Figure 5.8. a) A plot of the change in relative viscosity of ct-DNA solution with the increase in the ratio of 2d to ct-DNA at 37°C in 1x TAE buffer, 5% v/v DMSO at pH 7.4. b) The melt curves for ct-DNA with different concentrations of 2d to calculate T_m from the Boltzmann sigmoidal fit. The insert is the change in T_m with the change in [2d], fitted on a hill sigmoidal function, and ΔT_m is +2.7 °C. 126
Figure 5.9. a) A representation of the triplicates for the UV-vis absorption spectra of 150 μM 2d in 0.10 M TRIS-HCl buffer 10% DMSO after sequential additions of HSA from (0 μM to 50.4 μM) before precipitation at 37 °C b) An illustration of the Uv-vis titration spectra at 336 nm with a change in concentration of the ratio of 2d:HSA at 37 °C and c) the Van't-Hoff plot to determine the thermodynamic parameters for the binding of 2d to HSA. 128
Figure 5.10. The emission spectra of a) HSA-warfarin and b) HSA-dansyl glycine as a function of concentration, c) Normalised fluorescence emission spectrum of HSA-warfarin, HSA-warfarin-2d and warfarin and d) Normalised fluorescence emission spectrum of HSA-dansyl glycine, HSA-dansyl glycine-2d and dansyl glycine e)The % displacement of warfarin and dansyl glycine with an increace in [2d]. f) A double log plot of the fluorescence quenching to measure the reaction stoichiometry n, according to the Equation 19. The sample solutions were excited at 320 and 420 nm respectively for warfarin (5 μM) and dansyl glycine (5 μM) to determine the binding site of 2d on HSA (5 μM HSA in 50 mM potassium phosphate buffer at pH 7.4 at 37 °C). 131
Figure 5.11. An illustration of the conversion of MTT to formazan in the cells by mitochondrial reductases. 132
Figure 5.12. Growth inhibition of the HT-29 and MCF-7 cell lines with different doses of 2d (0, 0.2, 0.5, 1, 5, 10, 20, 50, and 100 μM) after 48 h. IC_{50} values for the HT-29 and MCF-7 cell lines were calculated to be, >100 and 9 μM respectively. 133
Figure 5.13. An illustration of apoptosis seen in HT-29 cells treated with test compounds after 48 and 72 hours. 134

List of Schemes

Scheme 1.1. An illustration of resonance in the amide bond when the π electrons are delocalised across the C–O or the C–N bonds, resulting in a hybrid structure with resonance.[253] 19
Scheme 1.2. An illustration of tautomerism in indazole. 21
Scheme 3.1. Illustration of the activation of a carboxylic acid with triphenyl phosphite and pyridine and subsequently its reaction with an amine. TPP is an oxo- and N-acceptor such that it deprotonates the acid, and accepts the oxalate together with the pyridine nitrogen, forming an unstable intermediate, which then facilitate the reaction of the amine with the carboxylate. [45,50] 55
Scheme 3.2. General synthetic scheme of the ligands 1a-f and their structures 56
Scheme 3.3. An outline depicting the scenarios, which allow molecules to crystallize in the 65 Sohncke space groups, i.e., those containing only symmetry operations of the first kind (rotations, roto translations, translations).[56] 66
Scheme 4.1. General synthetic scheme of the complexes 2d-f and their structures..... 91
Scheme 4.2. An illustration of the resonance in the pyridine molecule before and after metallation.[20] 94
Scheme 4.3. The illustration of the proposed mechanism for the formation of the a) AgF from $AgPF_6$ and the decomposition of the PF_6[24,25] and b) AuCl from $AuCl_4$ from the reduction of Au(III) to Au(I) in the presence of $NaBH_4$, at high temperatures, and c) the reaction of AgF and AuCl with the 2d resulting in 2di and 2dii respectively. 100
Scheme 4.4. Illustration of the synthesis of 2diii (MS = $KAuCl_4$; (I) = ACN at 40 °C, 15 h; n=+1) and 3diii (Metal salt = $PdCl_2$, (I) = THF at room temperature °C, 10 h; n=0) 101

List of Equations

$A = \log I0I = \varepsilon lc$ Equation 3.1 62

2 A ⇌ A_2 Equation 3.2 83

$[2dH_2]^{2+} \rightleftharpoons [2dH]^{+} \rightleftharpoons [2d] \rightleftharpoons [2dH_2O]^{+} \rightleftharpoons [2dOH]$, Equation 5.1 114

$A_T = A \times A_A + B \times A_B + C \times A_C + D \times A_D + E \times A_E$ Equation 5.2 114

$A_T = (A_A \times 10^{-4pH} + K_1A_B \times 10^{-3pH} + K_1K_2\ A_C \times 10^{-2pH} + K_1K_2K_3\ A_D \times 10^{-pH} + K_1K_2K_3K_4A_E)/(\ 10^{-4pH} + K_1 \times 10^{-3pH} + K_1K_2 \times 10^{-2pH} + K_1K_2K_3 \times 10^{-pH} + K_1K_2K_3K_4)$ ..... Equation 5.3 114

2d + GSH ⇌ 2d-GSH + Cl^- Equation 5.4 117

$At = Ao + Ao\text{-}A \propto e(\text{-}kobs \cdot t)$ Equation 5.5[17] 117

$kobs = k2\ [2d]$ Equation 5.6[17] 117

$k2 = Ae\text{-}EaRT$ Equation 5.7[17,18] 117

$\ln k2 = \ln A + (\text{-}EaRT) \cdot 1T$ **Equation 5.8**[18] 117

$k2 = kbTh \cdot e\text{-}\Delta G\ /\ RT = kbTh \cdot e\text{-}(\Delta H\text{-}T\Delta S)\ /\ RT$ Equation 5.9 117

$\ln k2 = \ln kbh + \ln T\text{-}\Delta G \ddagger RT = \ln kbh + \ln T\text{-}\Delta H \ddagger RT + \Delta S \ddagger R$ Equation 5.10[18] 118

$\ln k2T = 23.76 + \Delta S \ddagger R\text{-}\Delta H \ddagger R \cdot 1T$ **Equation 5.11**[18] 118

$2d + HSA \rightleftharpoons 2d\text{–}HSA$ Equation 5.12 127

$kon2dHSA = koff[2d\text{-}HSA]$ Equation 5.13 127

$konk0ff = 2d\text{-}HSA2dHSA = Ka = 1Kd$ **Equation 5.14**[60] 127

$\Delta G0 = \Delta H\text{-}T\Delta S = \text{-}RT\ln Ka$ Equation 5.15[60] 128

$\ln Ka = \Delta HR \cdot 1T\text{-}\Delta SR$ Equation 5.16[60] 128

$slope = \Delta HR$ Equation 5.17[60] 128

$y\text{–}intercept = \Delta SR$ Equation 5.18[60] 128

$\log I0\text{-}II = \log Ka + n\log[2d]$ **Equation 5.19** 130

Abbreviations

ALL - acute lymphoblastic leukaemia

AML - acute myeloid leukaemia

ATR - ataxia telangiectasia and Rad3-related protein

ATRi - ataxia telangiectasia and Rad3-related protein inhibitor

CDK - cyclin-dependent kinase

CDK7i - cyclin-dependent kinase 7 inhibitor

CHK1i - CHK1 inhibitor

CRPC - castration-resistant prostate cancer CDK4/6i - cyclin-dependent kinase 4/6 inhibitor

DFT – Density Functional Theory

DNA – Deoxyribose Nucleic Acid

ER - oestrogen receptor

FT-IR - Fourier-transform infrared spectroscopy

HGSOC - high-grade serous ovarian cancer

HL - Hodgkin lymphoma

HRMS – High Resolution Mass Spectrometry

HRR - homologous recombination repair

NMR – Nuclear Magnetic Resonance

NSCLC - non-small-cell lung cancer

UV-Vis – Ultraviolet Visible Spectroscopy

MPS1i, MPS1 inhibitor

p21i, p21 inhibitor

RSC – replication stress checkpoint

SAC – spindle assembly checkpoint

SCLC - small-cell lung cancer

TNBC - triple-negative breast cancer

WEE1i - WEE1 inhibitor

1 Introduction

In 2018, cancer stood as the second leading cause of global human fatalities, contributing to an estimated 9.6 million deaths and accounting for one in every six recorded deaths.[1,2] Cancer is a complex group of diseases characterised by the uncontrolled growth of abnormal or mutated cells within an organ, with the potential to metastasise to adjacent parts of the body.[2–4] Common cancer types in men encompass prostate, lung and bronchus, colorectal, urinary bladder, and skin cancers. In contrast, prevalent cancers among women include breast, lung and bronchus, colorectal, cervical, and skin cancers.[5–10]

Cancer imposes a substantial burden on individuals, families, communities, and healthcare systems.[2,11] Early detection, quality treatment, and survivorship care in nations with robust healthcare systems have improved survival rates for various cancer types.[2,12–14] Unfortunately, many cancer patients in low to middle-income countries lack access to timely, high-quality diagnosis and treatment due to the inadequate capacity of healthcare systems to handle the disease burden.[11–13,15] Consequently, cancer patients in most African countries experience the worst outcomes and the shortest survival rates globally. This underscores the urgent need for more equitable and accessible cancer diagnosis and treatment options on the continent.[16–19]

1.1 Cancer treatment options

Despite significant progress in cancer treatment, it still lags behind the progression of the disease.[1] The primary goal of cancer treatment is to eradicate cancer cells, preventing their proliferation and metastasis.[20–22] Various treatment options are available (**Figure 1.1**). including radiation therapy, hormone therapy, immunotherapy, stem cell or bone marrow transplant, targeted therapy, surgery, cryoablation, and chemotherapy.[20,21,23] These options are briefly outlined below.

- **Radiation therapy**: This utilises high-energy beams, primarily X-rays, to destroy cancer cells or shrink tumours by targeting cancerous cells while protecting healthy tissue. It is mainly used for localised tumours and cannot be applied to malignant tumours.
- **Hormone therapy:** This method uses medication to remove, block, or add specific hormones to decelerate the growth of cancers requiring these hormones.[24–29] Its application is limited to breast and prostate cancers.
- **Immunotherapy:** This method stimulates the body's immune system to attack cancer cells while mitigating the side effects of other treatments.[30–35] Patient response and therapy viability are unpredictable, necessitating additional biomarkers, increasing treatment costs.[36]
- **Stem cell or bone marrow transplant:** This involves replacing lost bone marrow cells resulting from chemotherapy and radiation therapy. Commonly used in blood cancers and lymph node cancers[37–44] This is one of the most expensive cancer treatment options and is not easily accessible to everyone.

- **Targeted therapy**: This method uses small-molecule drugs and monoclonal antibodies to target specific molecular targets involved in cancer growth. Its efficiency increases if the correct target is identified, but identifying these targets is challenging.[45–47]
- **Surgery:** This involves excising cancerous tissue to remove or debunk tumours. It involves local treatment for solid tumours in one area, therefore, it is not suitable for leukaemia or metastasised cancers.[21,48,49] Another downside is that it requires expertise and infrastructure.
- **Cryoablation:** This uses extremely cold gas to freeze and eradicate cancerous tissue.[50–53] It requires specialised machinery for imaging tumours, which are not easily accessible in most middle-income countries.[51]
- **Chemotherapy:** This is the focus of this study. It utilises drugs to treat cancer cells. It is difficult to cure cancer completely with chemotherapy alone, thus it is often used in conjunction with surgery and radiotherapy to achieve this result. Chemotherapy however, can shrink tumours and alleviate symptoms.[3,54–57]

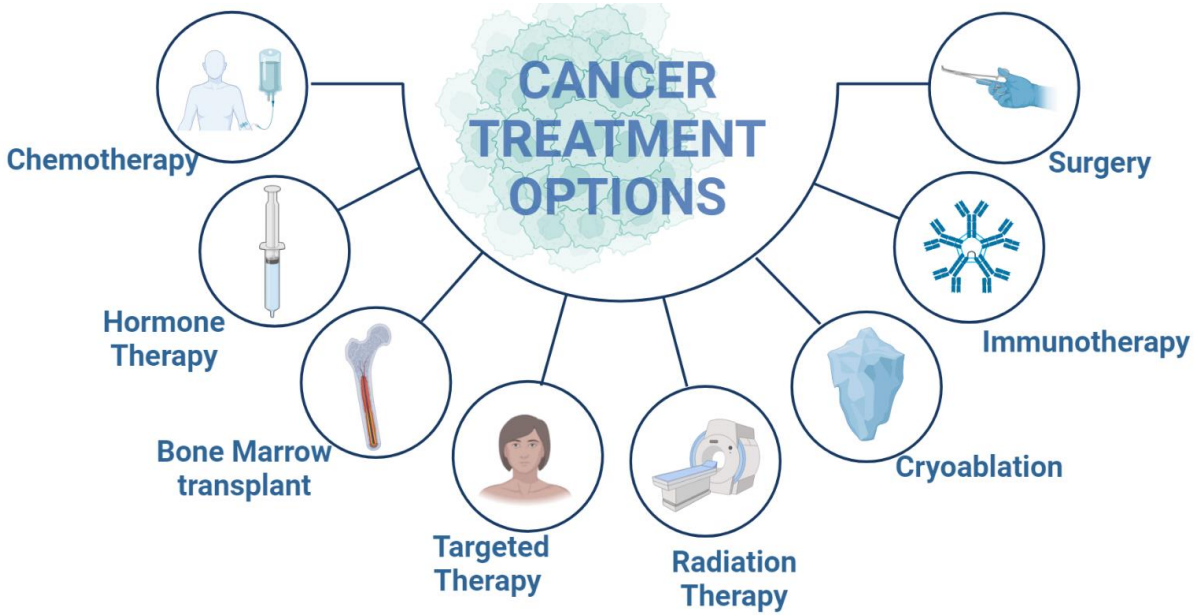


Figure 1.1**.** An illustration of some of the main techniques used for the treatment of cancer around the world.[20,21,23] **(**The figure was constructed using BioRender scientific illustration software https://www.biorender.com/)

Surgery, radiation therapy, and chemotherapy are the most frequently employed among these treatment options and are often used in combination.[46,58–62] Unfortunately, low-income countries lack the oncology resources and expertise required for advanced treatment methods such as surgery.[16,63,64] Consequently, cancer fatality rates in these countries are disproportionately high.[16,65]

Chemotherapy, on the other hand, is an easily accessible and less invasive alternative to many treatment options, making it a preferable choice for cancer treatment in these countries.[59,60] Despite its side effects—such as nausea, weight changes, and hair loss due to damage to healthy cells, as well as the development of drug resistance—chemotherapy remains the most efficient method for treating cancer. [66] As a result, extensive research is being conducted to identify chemotherapeutic drugs that are efficient, affordable, and cause minimal damage to healthy cells.[54]

1.1.1 Chemotherapy

As defined earlier, chemotherapy involves the use of one or more anticancer drugs within a standardized chemotherapy regimen to prevent the proliferation of cancer cells and the spreading of tumours. [3,54–56] Ideal chemotherapeutic drugs must be capable of halting cell proliferation or inducing cell apoptosis. Crucially, they should exhibit a higher affinity for cancerous cells while minimizing effects on healthy cells, thereby reducing adverse side effects.[55,67] Considerable effort has been invested in understanding the biochemistry of chemotherapeutic drugs.

Chemotherapeutic agents promote cell death (apoptosis) by disrupting cellular macromolecular production or function.[54,68–70] The faster cancer cells divide, the more susceptible they are to these agents, leading to tumour shrinkage.[70,71] Chemotherapy drugs are administered in cycles, with schedules determined by cell type, division rate, and the effective period of a specific medicine.[67,69,72] Ultimately, a chemotherapeutic drug's ability to destroy cancer cells depends on its capacity to halt cell division at specific stages of the cell cycle and/or induce cell apoptosis.[58,68,73–75]

Chemotherapy medicines typically influence the production and function of macromolecular molecules in neoplastic cells. While it was previously believed that chemotherapy drugs achieved this only through direct interaction with cellular DNA at specific points in the cell cycle (cell cycle-specific chemotherapeutics),[76–78] recent studies have shown that certain metal complexes can interact with, and inhibit enzymes and proteins essential for cell survival and react with cellular components, producing harmful species that lead to cell death (cell cycle non-specific chemotherapeutics).[76,79,80] For instance, gold(I) complexes can inhibit thioredoxin reductase and glutathione reductase, which are essential proteins for cell survival.[81] These are two of the many proteins necessary for the survival of cells, and so inhibition of these enzymes leads to cell death.

Certain chemotherapeutic drugs, particularly metal complexes, can generate reactive oxygen species (ROS) and reactive nitrogen species (RNS), which are toxic to cells.[82] These radicals alter DNA and protein structures, leading to changes in DNA bases and loss of protein function, ultimately causing cell apoptosis.[83–89]

Unlike cell non-specific chemotherapeutics, cell cycle-specific chemotherapeutics interfere with DNA, RNA, or protein synthesis involved in the cell cycle, disrupting the appropriate functioning of the preformed molecule or interfering with cell division.[54]

Studies have demonstrated that cancer, and consequently chemotherapeutic design, is significantly influenced by the cell cycle, which controls cell multiplication and proliferation.[72,90–92] For example, cell cycle non-specific chemotherapeutic drugs kill cancer cells during G_0, (resting phase), involving the production of toxins and inhibition of cellular functions essential for cell survival.[87,88,93] Conversely, cell cycle-specific chemotherapeutic medicines kill cancer cells exclusively when they divide during the G_1 (first gap), G_2 (second gap), S (synthesis) and M (mitotic) phases (**Figure 1.2**).[94,95] Understanding the cell cycle is crucial for comprehending cancer and developing effective chemotherapeutic strategies.[67,72,90]

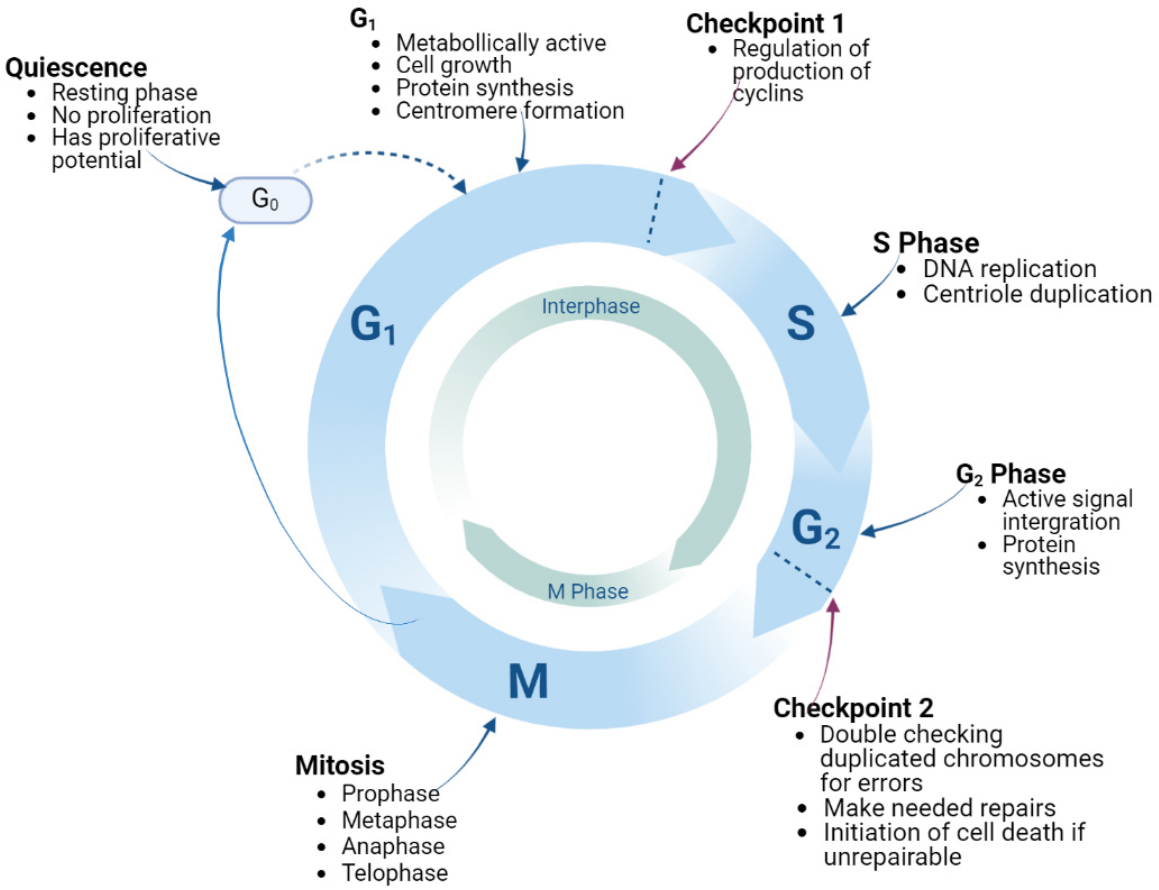


Figure 1.2. An illustration of the different cell cycle phases: The cell cycle outlines the life of a cell from the time it is generated from a dividing parent cell until it splits into two daughter cells. The cycle consists of four successive phases: G_1, S, G_2, and M. [98,99]

1.1.2 The cell cycle and its relevance in cancer treatment

The cell cycle in eukaryotes is governed by two critical events: genomic DNA replication and subsequent segregation between daughter cells.[67,90,96] While uncontrolled cell progression (replication) and defective cell cycle checkpoints (illustrated in **Figure 1.2**) were initially thought to be the main reasons for cells becoming cancerous, recent studies have revealed that disrupting only certain aspects of cell control can lead to continued cell division in cancer cells.[72,90,97,98] Cancer cells excel at evading cell death, often failing to exit the cell cycle and continuing to proliferate.[72]

Cell division in eukaryotes, both unicellular and multicellular, is regulated by a complex network of systems, checks, and balances to prevent errors before permitting a cell to enter and advance through the cell cycle.[72,92] This network ensures sequential duplication of cellular material during interphase and subsequent division into two genetically identical daughter cells during mitosis. The cell cycle is intricately regulated by a network of components with a singular objective: the timely and precise duplication and segregation of genomic DNA.[91]

During the cell cycle, DNA replication occurs in the S phase of interphase, where DNA replication is initiated but is not completed. Gap phases, known as G_1 and G_2, separate the S phase from the M

phase and play a crucial role in regulating the cell cycle.[67,72,90,91] G_1 is a metabolically active phase where RNA synthesis and protein expression occur, and the cell grows and increases DNA volume. Cells in G_1 can enter a non-proliferative state known as quiescence or G_0, which is common in most cells in an adult body.[66,97,99] Cells in G_1 decide to proceed to the S phase based on a complex network of regulatory signals, or they remain in, initiate DNA replication, and enter the cell cycle.[96,100] In G_1, the decision to proceed to the S phase depends on a complex network of regulatory signals otherwise, the cell will remain in G_1.[101,102] The timely and precise regulation of the cell cycle ensures the accurate duplication and segregation of genomic DNA.[67,94,95]

After the S phase, further cell growth and the synthesis of proteins and necessary organelles occur in the G_2 phase. An additional decision-making window is found in this phase. In this window, duplicated genetic material is checked for errors, and cell death is triggered upon failing to fix the errors. Cells entering the M phase begin chromatin condensation and central alignment of chromosomes. The M phase is the mitotic phase, which consists of four primary stages and is accompanied by cytokinesis (**Figure 1.2)**.[72,92]

During the cell cycle, checkpoints are essential in ensuring proper regulation and control of cell proliferation. These checkpoints respond to various signals, such as DNA damage, to halt, slow down, or proceed with cell division. Of these checkpoints, the G_1 checkpoint is particularly significant, as it is during this phase that cells enter the cell cycle or recede into G_0. During G_1, cells respond to extracellular signals, and progression to division becomes autonomous.[103] This is also a DNA replication stress checkpoint, which controls the replication of DNA damage due to external factors like UV radiation, physical or chemical damage. On the other hand, the DNA damage checkpoint in G_2 is where accumulation and propagation of DNA damage due to mistakes in DNA replication is controlled.[96,104,105]

To avoid chromosome nondisjunction, cancer cells also depend on a working mitotic checkpoint, thus it is believed that this checkpoint is rarely compromised.[98] This discovery regarding the function of checkpoints in cancer led to a better knowledge of cell cycle control in cancer and indicated its dependence on checkpoint functions, opening new therapeutic possibilities. If the DNA damage checkpoint is compromised, continuous cell division is allowed despite the accumulation of genetic errors.[72,106,107]

It has been observed that cancer cells can bypass the G_1 restriction point without requiring extracellular signals, which enables them to proceed to division while remaining in the cell cycle.[103] This results in the bypassing of the second checkpoint, which could have led to cell death due to damaged DNA. Eventually, the cancerous cells can successfully undergo cytokinesis, producing defective daughter cells that can re-enter the cycle and begin the replication process again. This uncontrolled cell replication and proliferation ultimately lead to the development of cancer.[90,99,108]

Conclusively the ability to bypass these checkpoints results in uncontrolled and accelerated cell division and proliferation, which is a hallmark of cancer development.[72] Since cancer cells are highly dependent on the cell cycle, it is a very good target to stop cancer cell proliferation. With this knowledge, many

drugs targeting different stages of the cell cycle have been researched and approved for the treatment of cancer in recent years, some of which are outlined in **Table 1.1.**[72]

Table 1.1. Examples of chemotherapy drugs targeting different stages of the cell cycle. [72]

Drugs	Clinical use	Reference
	Induced cell cycle exit (G_1 to S transition)	
Palbociclib	Approved for HER2 and ER^+ for metastatic breast cancer; clinical trials for various solid tumours	113–115
Ribociclib	Approved for HER2 and ER^+ for metastatic breast cancer; clinical trials for various solid tumours	34,113,116,117
Abemaciclib	Approved for HER2 and ER^+ metastatic breast cancer; clinical trials for various solid tumours	113,118–120
Samuraciclib (ICEC0942)	Phase I/II, AML, ER^+ breast cancer	113
	Induced cell cycle progression (G_2 to M transition)	
Adavosertib (AZD1775)	Phase II, relapsed small-cell lung cancer, acute myeloid leukaemia, ovarian cancer, non-small-cell lung cancer, gastric adenocarcinoma and multiple advanced solid tumours	104,121
	Replication stress tolerance impairment (S phase)	
Berzosertib (VX-970)	Phase II, recurrent ovarian, metastatic urothelial carcinoma and primary peritoneal or fallopian tube cancer	104
PrexasertibL (Y2606368)	Phase II, BRCA1/BRCA2-mutated breast, SCLC, or ovarian cancer, HGSOC, TNBC, metastatic CRPC and advanced solid tumours with HRR defects or genetic alterations symptomatic to replication stress.	104
MK-8776	Phase II, relapsed AML (with or without cytarabine); Phase I, acute leukaemia, lymphoma advanced solid tumours	104
	Induction of catastrophic genome instability (S-phase)	
Taxanes	Approved for a wide range of cancers, including ovarian cancer, lung cancer, breast cancer, oesophageal cancer, prostate cancer, bladder cancer and melanoma	122–124
Vinca alkaloids	Approved for a range of cancers, including AML, ALL, NSCLC, HL and neuroblastoma	122,125
MPS inhibitors	Phase I clinical trials in neuroblastoma, medulloblastoma and breast cancer (together with taxanes). Recently entered	101,126–129
Aurora B inhibitors	Phase II in multiple myeloma, AML, prostate cancer and SCLC; Phase I in multiple solid tumours	130
	Induced DNA damage (G_0)	
Cisplatin	Approved for treatment of sarcomas, lymphomas, leukaemia, breast, ovarian, testicular, head and neck and cervical cancers	60,80

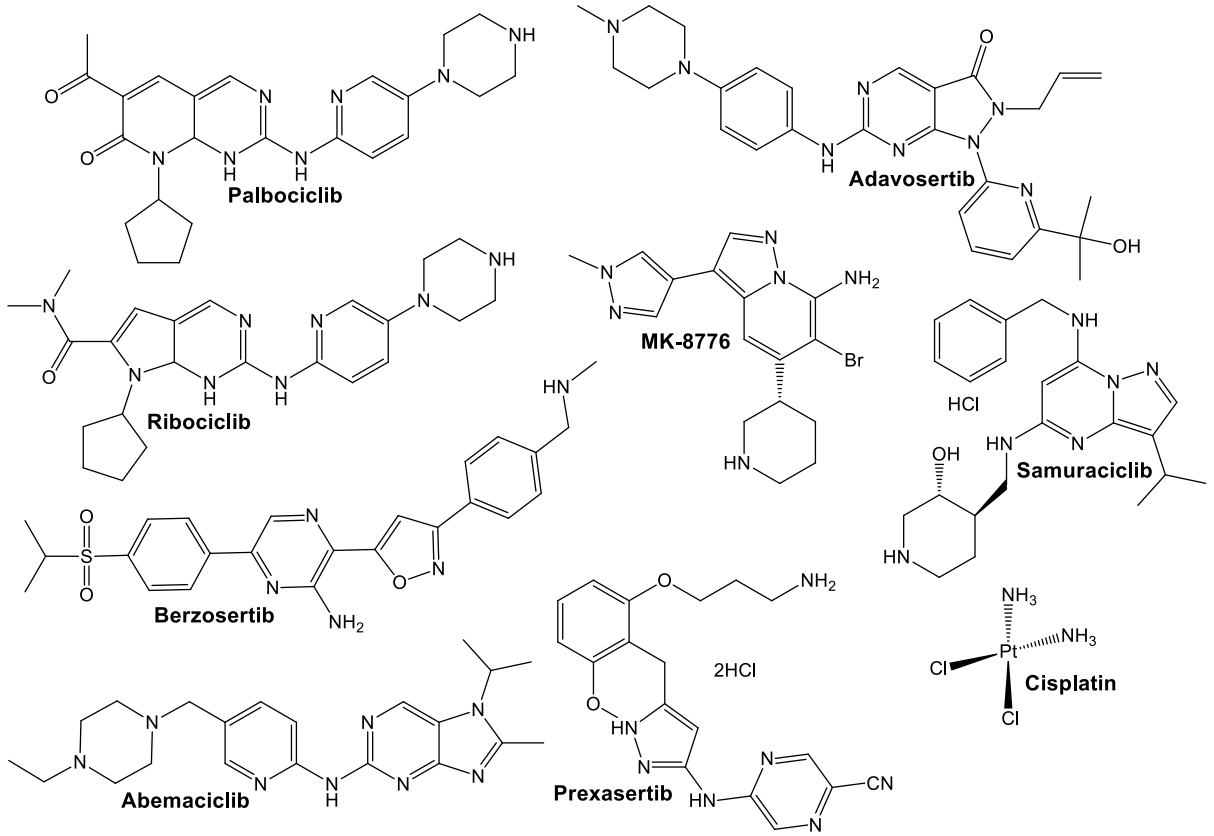


Figure 1.3. The molecular structures of the compounds discussed in **Table 1.1**.

1.1.3 Classification of cell cycle chemotherapeutic drugs

Apart from being cell-cycle-specific and cell cycle non-specific, chemotherapeutic drugs are generally classified according to how they interact with different components of the cells in cancer treatment (mainly DNA), to quench cell proliferation. As such, they are classified into alkylating agents, antimetabolites, antimicrotubular agents, and antibiotics, as outlined in **Table 1.2**[54]

Table 1.2. Different classes of chemotherapeutic drugs

Drug class	Pharmacodynamics	Examples	References
Antibiotics[131,132]			
	Inhibit RNA and DNA synthesis by binding to and producing breaks in single and double-stranded DNA, thus damaging the DNA and leading to cell death	actinomycin D daunomycin bleomycin	97,133,134 135,136 137,138
Antimicrotubular agents			
Topoisomerase I inhibitors	Block the release of topoisomerase I from the cleavable complex or prevent the re-ligation of DNA and the subsequent steps to complete the cell cycle.	epipodophyllotoxin, irinotecan, topotecan	139,140
Topoisomerase II inhibitors	Inhibit DNA and RNA synthesis by binding to the enzyme and inducing DNA breakage, eventually leading to cell death.	Mitoxantrone	140
Taxanes	Disrupt the balance of microtubule polymerisation and depolymerisation, resulting in abnormal cellular function and replication disruption, and inhibiting microtubule assembly.	paclitaxel, docetaxel, cabazitaxel	126
Vinca alkaloids	They inhibit microtubule formation by binding to tubulin, thereby arresting the cells in the M-phase and ultimately stopping cell division	vinblastine, vincristine, vinorelbine	92,141–143
Antimetabolites			
Cytidine analogues	Directly inhibit the enzymes, DNA methyltransferase or DNA polymerase	azacitidine, cytarabine, gemcitabine, decitabine	144–146
Folate antagonists	Depletes folate, which is an essential vitamin in the synthesis of purine nucleotides and thymidylate	Methotrexate, pemetrexed	147–151
Purine analogues	act as false metabolites as they are analogues of guanine	cladribine, clofarabine, nelarabine	152–154
Pyrimidine analogues	Inhibits thymidine synthetase and interferes with DNA synthesis and repair	fluorouracil (5-FU) and capecitabine (prodrug of 5-FU)	59,155
Alkylating agents			
nitrosoureas Triazenes nitrogen mustard-bendamustine alkyl sulfonate ethyleneimine Platinum analogues	Inhibit DNA replication by forming an unstable alkyl group upon reaction with nucleophilic centres on nucleic acids and proteins	carmustine, lomustine dacarbazine, procarbazine, temozolomide cyclophosphamide, ifosfamide busulfan thiotepa Cisplatin, carboplatin, oxaliplatin	59,156–161

Other drugs not mentioned in any of the classes above include hydroxyurea, tretinoin, arsenic trioxide, and proteasome inhibitors. Most of these drugs are cell-cycle-specific. Hydroxyurea inhibits the activity of the enzyme ribonucleoside diphosphate reductase. On the other hand, tretinoin (a vitamin A derivative) and arsenic trioxide promote and induce cell differentiation of cancerous cells and not proliferation.[109–113] Proteases also participate in tumour growth and progression at both the primary and

metastatic sites. Protease inhibitors interfere with the ability of these enzymes to help metastasise the cancerous cells.[114,115]

1.1.4 Mode of action of cell cycle-specific chemotherapeutic drugs

As mentioned earlier, DNA is the main target molecule for cell-cycle-specific chemotherapeutic drugs in cancer treatment. This is validated by its explicit participation in cell replication and division, transferring of genetic material, and control of cellular functions. [96,100,116,117] As such, the binding of chemotherapeutical drugs on DNA disrupts all the mentioned processes as this frequently causes DNA damage or influences protein interactions with DNA.[116,118,119] To understand how drugs bind to DNA, we need to briefly unpack the structure of DNA.

DNA is found in the body in the form of a double helix,[120] with each strand composed of four nucleobases: adenine (A), thymidine (T), guanosine (G), and cytosine (C).[117,121] These nucleobases are connected through phosphodiester linkages, involving covalent bonds between deoxyribose sugars and phosphate groups.[117,122,123] The orientation of the phosphodiester bond, which binds carbon-3 of one nucleotide's sugar to carbon-5 of the next nucleotide's sugar, determines the direction of the DNA strand. Two strands of DNA are held together primarily by hydrogen bonds between A and T (two hydrogen bonds) and between C and G (three hydrogen bonds), resulting in the double-helical structure of DNA.[120,121] These DNA strands are oriented antiparallel to each other, with one strand running in the 5'-3' direction and the other in the 3'-5' direction.[124,125] The helical structure of DNA and the nucleobases are illustrated in **Figure 1.4**.

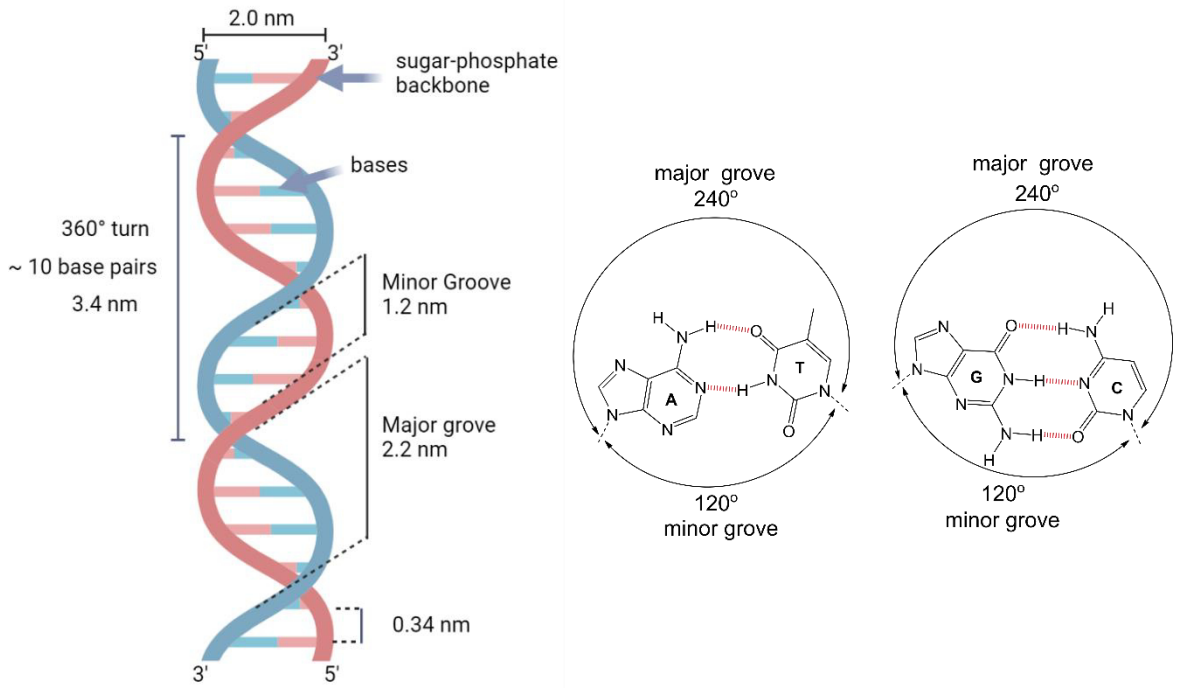


Figure 1.4. The double-helical structure of β-form DNA, the most prevalent conformer of DNA, with distinct major and minor grooves. The structural data linked with β-DNA are displayed (helical pitch of ~34 nm, approximately 10 residues per turn, 34.3° twist angle between residues, and a diameter of 2.0 nm). The chemical structure of the residues and their complimentary interactions are depicted in the inset. The strands direction is also specified.[167,171,177,178]

The base pairs, which are non-polar, are facing the helix's centre inside, while the sugar-phosphate backbone, which is polar, forms the helix's exterior. This is why DNA is a polar molecule and is soluble in water.[126,127] Regions of the DNA double helix where the two strands are in proximity are known as the minor groove, while regions, where the strands are farther apart, are known as the major groove. These grooves expose diverse functional groups as possible binding sites for proteins, chemicals and medicines.[117,128–131] The major difference between the major and minor grooves is that the major groove has the N and O atoms of the base pairs pointing inward towards the helical axis, whereas the minor groove has the N and O atoms pointing outwards. Due to this, interactions of ligands to DNA in the major groove are usually hydrophobic, while the interactions include electrostatic and hydrogen bonding in the minor groove.[130,132–135]

Cell cycle-specific chemotherapeutic drugs typically interact with DNA through intercalation, groove binding and base binding, and this is explained in detail below.[136]

Intercalating compounds insert between two adjacent bases and interact with them through π-stacking.[137,138] This is possible due to the planar configuration and aromaticity of the nucleobases. Chemotherapeutic drugs, with planar geometry, can intercalate with DNA by inserting themselves between the planar bases of DNA.[29] This will alter the helical configuration of the DNA by unwinding DNA with concomitant inhibition of replication, transcription and the winding and packing of the DNA by topoisomerase enzymes.[139,140] Significant π-π electron interactions occur due to the aromaticity in the metal complexes and the DNA bases. This provides a suitable medium for intermolecular electron transfer between the DNA bases and the metal complexes in proximity.[89,141,142] Certain DNA metallo-intercalators result in the oxidation of the DNA and its damage.[142]

Groove-binding compounds bind to DNA in the exposed major and minor grooves. The interaction is through hydrogen bonding with the DNA bases, Van der Waals forces generalised electrostatic forces with the walls of the DNA groove,[133–135,143] and covalent bonding with the nucleobases which are nucleophilic.[144–148] This binding results in the inhibition of topoisomerases and other enzymes which need to bind to DNA to facilitate DNA replication. The compounds are usually pseudo-crescent-shaped, which enables them to insert themselves into the grooves of the DNA double helix.[29]

Groove binding is different from intercalation, which usually occurs between base pairs in the DNA strand. Unlike intercalators which elongate the DNA, minor groove binding agents inhibit topoisomerase I by stabilizing the topoisomerase I - DNA cleavable complex.[149] The DNA will not be repaired after it has been cleaved if the cleavable complex is stable. An example of an organic minor groove binding agent is Distamycin A, and it has been modified by coordinating iron and copper to the ligand.[150,151]

Another example is Et-743 (ecteinascidin-743 or trabectedin), a naturally occurring anticancer drug, that covalently attaches to the minor groove, exposing the major groove pocket for protein binding.[152] As a result, a wide range of proteins and other essential components in transcription-coupled nucleotide excision repair (NER) are inhibited. Due to the sequence specificity of Et-743 and mitomycin C, another minor groove binder, they have much higher DNA binding selectivity than normal DNA alkylators.[152,153]

Base-binding (covalent DNA adducts) compounds interact through coordination interactions with one or more DNA bases. Binding of the compounds to two or more bases results in intra-strand cross-linking if the bases are on the same strand and inter-strand cross-linking when on different DNA strands.[76] Such binding typically distorts the configuration of the DNA helix, leading to the inhibition of replication and transcription.[154]

These crosslinks bend DNA significantly towards the major groove,[155] exposing a minor groove binding pocket to which several proteins, which include high-motility group box proteins (HMGB), transcription factor repair proteins, and other damage recognition proteins, can bind and act on the DNA.[156] A very common example of such drugs is cisplatin, which is a platinum complex.

Figure 1.5 illustrates how different cell cycle-specific chemotherapeutic drugs interact with DNA and their examples. Cisplatin creates intra-strand cross-links, bending the DNA towards the major groove and opening the minor groove for potential protein attachment. Some drugs build inter-strand cross linkages like nitrogen mustard. Antibiotic mitomycin C groove binds and bends the DNA helix to expose the main groove-binding pocket. Finally, doxorubicin, a DNA intercalator splits DNA strands that are bound by Topoisomerase II. More examples of such drugs are illustrated in **Table 1.3.**

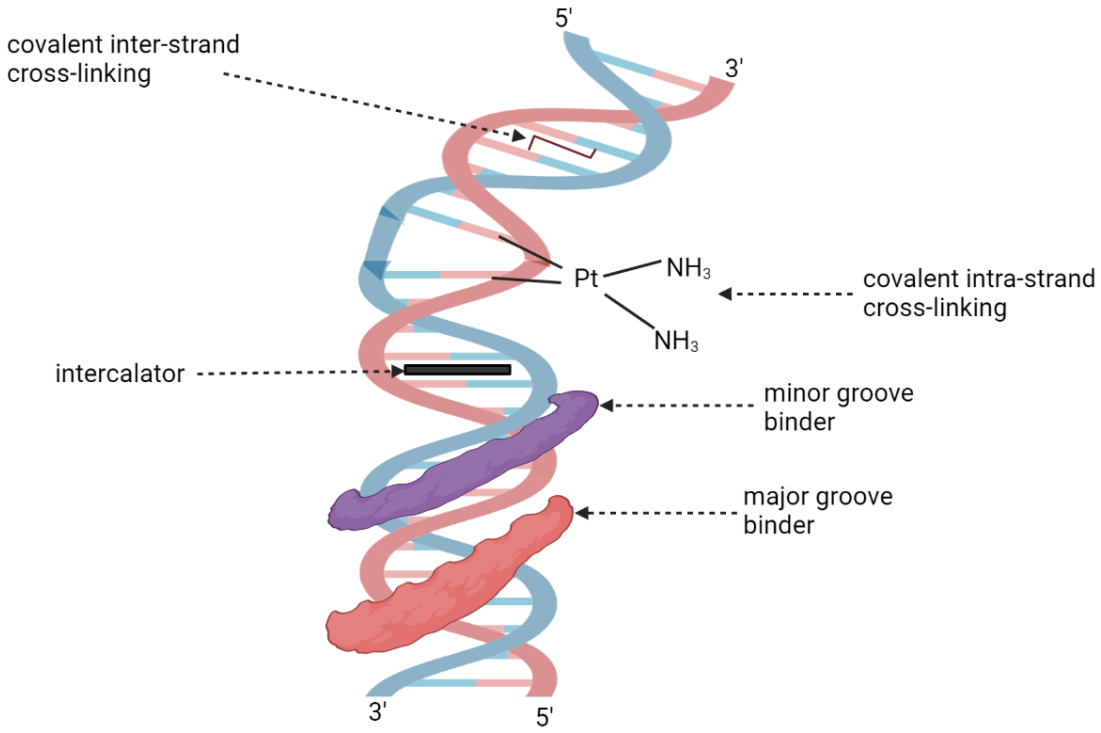


Figure 1.5. An illustration of how clinically relevant anti-cancer medicines interact with DNA in a variety of ways.[80,136,146,153,160]

Table 1.3. Examples of DNA interacting agents, groove binding agents and covalent binding agents to DNA that are currently being used in the pharmaceutical industry. [161]

Non-covalent binding agents		Covalent DNA adducts and direct DNA damage
Groove binding agents	**DNA intercalator**	
Berenil	Aminoacridines	Busulfan
Bisbenzimadoles	Arylaminoalcohols	Camptothecin
Bleomycin	Coumarins	Chlorambucil
Chloroquine	Cystodytin J	Clomesone
Chromomycin A3	Diplamine	Cyclodisone
Diamidine-2-phenylindole	Daunomycin	Ionizing radiation
Distamycin A Et-743 (ecteinascidin-743)	Quinolines and quinoxalines	Nitrogen mustard
Guanyl isfuramidine	Ethidium bromide	Nitrosoureas
Mithramycin	Proflavine	Oxidative-stress agents
Natamycin	Echinomycin	UV radiation
Netropsin	Chlorpheniramine	Busulfan
Pentamidine	Methapyrilene	Camptothecin
Pilcamycin	Tamoxifen	Cisplatin
SN6999	Bis-naphthalimide	
SN7167	Doxorubicin	
Hoechst 33258	Indoles	

Since one of the properties of a good chemotherapeutic drug is having a multifaceted approach to successful induction of cell death, DNA is the ideal target because of its structural diversity.[157] This diversity provides for different binding sites for various chemotherapeutic drugs. Although some interactions are more toxic to healthy cells than others, drugs targeting DNA are some of the most effective anticancer drugs and have proven to be clinically appropriate.[158]

Research on new chemotherapeutic drugs is imperative due to the increased drug resistance and cytotoxicity of current drugs, which is mainly caused by low selectivity towards cancerous cells.[55,80] As such, research on different types of drugs which target DNA and other proteins is underway, and these include natural products, organic molecules and metallodrugs.[159–161]

1.2 Metallodrugs in cancer treatment

Metallodrugs have a history of being applied in the treatment of various diseases which includes syphilis (treated with salvarsan, an arsenic(III) antimicrobial compound),[162] tuberculosis (treated with $K[Au(CN)_2]$, a gold(I) complex), and rheumatoid arthritis (treated with auranofin, a gold(I) complex).[163,164] This then prompted the research on metallodrugs as potential anticancer drugs.[165,166]

Metal complexes are of special interest due to several factors which include their variety in charge variation, manipulatable structure and binding, metal-ligand interaction, Lewis acid properties, availability of partially filled d-shells and their redox activity.[167,168]

1.2.1 Properties of metallodrugs desirable in cancer treatment

Metal complexes can be manipulated to be positive, negative or neutral, to allow for binding of these compounds to specific cellular components. An example is positively charged complexes that can easily bind to DNA.

Metal complexes can also aggregate to a broad variety of coordination geometries that give them distinct forms, in contrast to organic molecules. The metal and its oxidation state affect the bond length, bond angle, and coordination site. Additionally, different molecular species that confer a wide range of coordination numbers and geometries as well as kinetic features that cannot be achieved by other methods can be created by structurally altering metal-based complexes.[169–171]

The metal-ligand interaction in metal complexes result mostly in complexes that are distinct from those of the individual metals or ligands. Ligand exchange reactions are influenced by the thermodynamic and kinetic characteristics of metal-ligand interactions and metals that can go through this process have an advantage when it comes to interacting and working with biological molecules.[167,171]

Metal ions have a strong affinity for electrons, thus they can quickly polarize the groups that are coordinated to them, which speeds up the hydrolysis process in biological setups. A key factor to consider in the design of the coordination complex is the oxidation state of the metal ions as a large number of metal ions in metallodrugs are prone to oxidation and reduction processes. Metal ions frequently function as coordinated substrate activators and as participants in redox-active locations for charge accumulation in biological redox catalysis.[168,171]

Due to these properties, metal complexes can successfully exploit different DNA binding sites due to their high tolerance for structural and electronic modification.[127] Furthermore, metal complexes have the potential to interact with a wide range of molecular targets, not just DNA, allowing for the creation of a drug with a multi-faceted approach.[172]

Following these findings, researchers began looking into the anticancer potential of metal complexes extensively.[137,173,174] Cisplatin, a platinum(II) complex, was the first metallodrug to pass clinical trials for the treatment of cancer in 1978.[175] Platinum(II) complexes, cisplatin, oxaliplatin and carboplatin have since been amongst the most successful metallodrugs for chemotherapy, being particularly effective clinically.[76,77,175]

The drawback in the use of platinum(II) based drugs is their lack of true specificity as they also target highly proliferating healthy cells, which leads to toxic side effects. This has resulted in limited dosage of the drugs, which ultimately leads to drug resistance. [176,177] Research on anticancer metallodrugs has since branched off to other metals including rhodium, iridium, copper, ruthenium, palladium, nickel and more recently, gold complexes.[165,173,178-179]

1.2.2 Gold in cancer treatment

Gold complexes were researched as potential anticancer drugs based on three main rationales. (i) Gold has previously been applied in pharmaceutics as gold(I) for the treatment of tuberculosis.[180] This implied that gold has pharmaceutical properties. (ii) Gold(III) is isostructural and isoelectric to platinum(II) (Pt^{2+} and Au^{3+} are both d^8 ions),[178,181] which is the metal ion in cisplatin, the above-mentioned successful anticancer drug. (iii) Gold(I) and gold(III) can form stable complexes with known anti-tumour agents, enhancing their activity on tumour cells.[181].

The unique properties of gold outlined in this section distinguish it from other metals. Gold is inert in nature, which gives it resistance to chemical and physical attacks.[182] Its high electronegativity value of 2.54 on the Pauling scale, which is similar to that of carbon (2.55), makes the Au-C bond highly covalent and resistant to hydrolysis.[182] This property makes it resistant to ligand exchange, which reduces the probability of side reactions in biological media.

Some heavy transition metals, such as platinum, mercury, and gold, are heavily influenced by relativistic effects (an increase in the distance between an atom's nucleus and 5d orbitals, while its distance with 6s orbitals decreases), with gold being the most affected due to the expansion of its 5d orbitals and contraction of its 6s and 6p shells.[182–184] Additionally, these effects, along with the lanthanide contraction, decrease the covalent radius of gold(I) and its bonds with carbon are thus stronger and highly covalent as compared to gold(III) are almost equal to that of silver(III).[185,186] In general, the bond length for gold(III) bonded to alkyl and aryl ligands is between 1.27 – 1.30 Å, while it is reduced to 0.85 Å with ionic ligands. This enables accommodation of the metal centre in the plane of porphyrins, which are essential biological molecules.[187]

Relativistic effects ultimately affect metal-ligand bonding (bond length and stability) thus dictating the reactivity of metal complexes.[183] The reactivity sequence of gold is usually characterised as Au-H > Au-O > Au-C or Au-H > Au-C > Au-O, is the reverse of other metal centres, such as platinum (Pt-O > Pt-H > Pt-C). This allows for a chance to explore different ligands which might not have been compatible with platinum.[183]

One aspect to note is that gold(I) has filled up 5d orbitals (d^{10}), which causes it to behave like a main group element and form linear, two-coordinate complexes. This results in a reluctance to interact with donor ligands perpendicular to the molecular axis. On the other hand, gold(III) has a partially filled 5d orbital (d^8), giving it properties similar to those of transition metals, particularly heavy metals, and adopting a square-planar coordination geometry.[184,188] This is a property essential for the intercalation of metal complexes to DNA.

Despite following a similar trend, the bond energies between Au(I) and ligands (Au(I)-L) are higher compared to the bond energies between Au(III) and ligands (Au(III)-L). This is the reason the Au(III) in the Au(III)-L is not stable and is easily reduced to Au(I). This property is essential in medical chemistry where there is a need for this reaction with the release of ligands as mentioned earlier.[157,167] The reduction of gold(III) to gold(I) is associated with the production of reactive oxygen species, including peroxides and free radicals, under appropriate biological conditions.[189] Gold complexes are of significant interest in cell cycle non-specific cancer treatment, where the goal is to destroy cancerous cells because they could produce these reactive oxygen species, which causes damage to cellular DNA, leading to apoptosis.

Studies have been underway to mitigate gold(III)'s instability under physiological conditions, mainly due to its high reduction potential. To date, this has primarily been the drawback for the application of gold(III) in pharmaceuticals.[179] These studies have shown that since gold(III) is a hard Lewis acid, its metal complexes can be stabilised against reduction and demetalation by coordinating the metal ion with hard donor atoms such as nitrogen, oxygen, and fluorine.[178,182,190,191]

Increasing the denticity of the gold(III) metal centre was discovered to stabilise the gold(III) complexes from ligand exchange and reduction. Earlier studies on gold(III) complexes as potential chemotherapeutic drugs (**Figure 1.6**) were conducted with a monodentate ligand ([$AuCl_3$(Hpm)] (**1**) and a bidentate ligand ([$AuCl_2$(pm)]) (**2**), where pm is 2-pyridyl methanol.[165] Despite exhibiting promising *in vitro* cytotoxicity, especially on cisplatin-resistant cancer cell lines, the complexes were not stable in aqueous conditions (ligand exchange).[165,191,192]

Although ligand exchange reactions in the complexes were still prevalent at low pH,[179,193] the complexes were found to distort calf thymus DNA and some polynucleotides.[165] This reinforced the idea that gold(III) metal complexes could be applied in cancer treatment.

Keeping in mind that coordinating gold(III) ions to polydentate ligands with strong σ-donor atoms or monoanionic atoms improved their stability, metal complexes with higher denticity than two were investigated.[193] Stable complexes have been described with tridentate or pincer ligands (**3**),[190,194,195] (the main focus in this study), tetradentate ligands, porphyrins (**4**) (highly effective against selected types of cancer, but also highly toxic),[196] corroles (**5**) (high cytotoxicity)[197,198] and cyclams (**6**).[199,200].

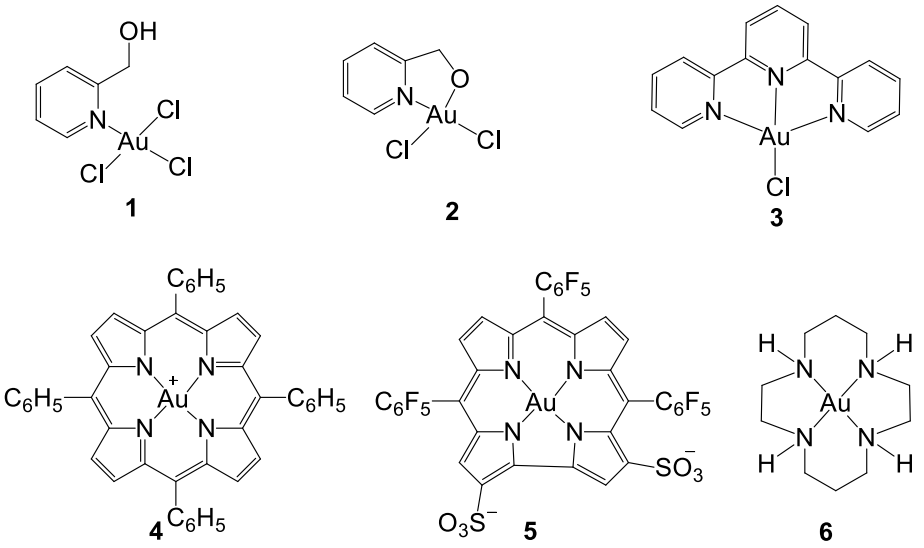


Figure 1.6. Examples of different classes of gold(III) complexes reported to be stable and to show cytotoxicity against cancer cells: monodentate **1,** $AuCl_3$(Hpm), bidentate (cyclometalated) **2** $AuCl_2$(pm), tridentate (pincers) **3** [Au(terpy)Cl], tetradentate **4** [Au(porphyrin)], **5** [Au(corroles)] and **6** [Au(cyclam)]$(ClO_4)_2$Cl.

Due to the properties of gold(III) complexes outlined in this section, gold(III) complexes are desirable candidates in cancer treatment.[201] Some of these gold (III) inhibit DNA by intercalation, groove binding etc.[202] Because of these advantages, gold(III) complexes are of particular interest in the medical field.[191]

Despite some gold(III) complexes showing better cytotoxicity and immunomodulatory effects than successful platinum complexes, no gold metallodrugs have yet passed clinical trials due to their negative side effects.[81] Consequently the main goal in the research of gold(III) complexes is to mitigate these side effects and improve their cytotoxicity. Extensive research on gold(III) metal complexes is therefore underway to come up with a gold(III) complex with high efficacy that can overcome drug resistance and have close to no side effects.

Another way to achieve this feat is by incorporating moieties with some known biological properties or anticancer properties into the gold(III) complex. Since the nature of the ligands plays a very important role in stabilising the gold(III) complex, these moieties of interest are incorporated into the ligand. As a result, special care has to be taken in the design of these ligands.

In the design of gold(III) complexes, ligands made up of chemical groups with S, O and N as donor atoms and with known pharmacological properties, such as the amide group, indazole, quinolone. benzophenone and phenanthroline groups are preferred. These pharmacological properties are most likely conferred onto the complex molecule.[203–205]

Numerous chemical groups of interest in nature, have been thoroughly investigated thus far, with several of these groups and their characteristics being discussed in this study due to their specific biological activities.[165,173,196,197,206–209]

1.2.3 Pincer molecules

Pincer molecules are tridentate chelating compounds which coordinate with the central metal by occupying its coplanar sites in a meridional configuration.[210–213] Pincer molecules generally have a central anchoring site (backbone), two equivalent “arms” which can form an achiral or chiral pocket (depending on their structure), and the metal binding site, which is usually the tridentate chelating motif forming a functional cavity at the centre of the molecule (**Figure 1.7**).[210]

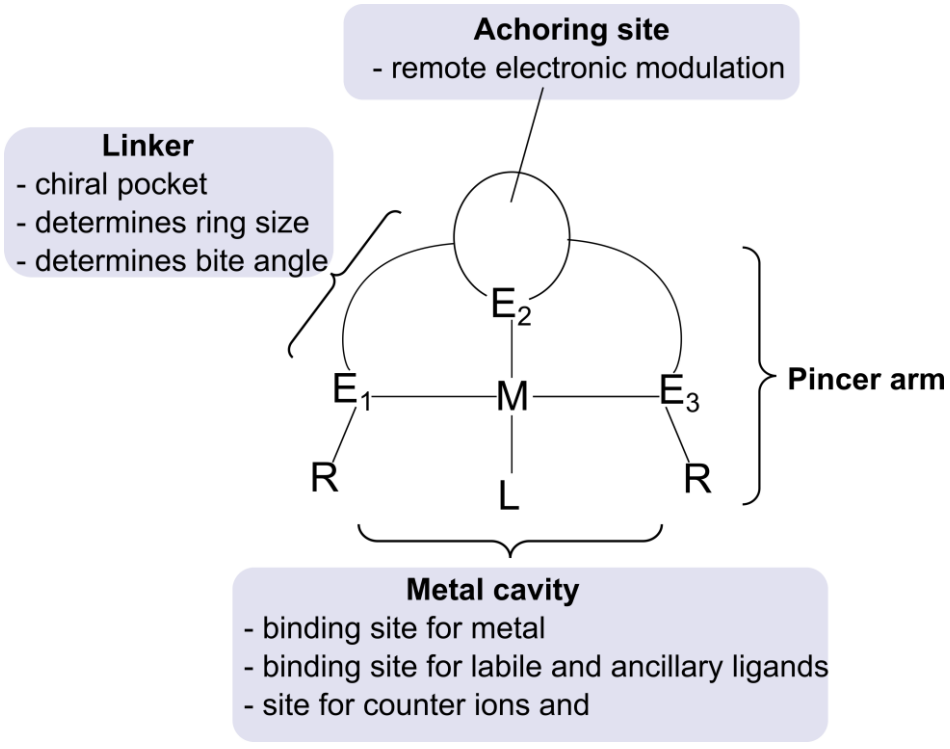


Figure 1.7. An illustration of the general structure of pincer molecules, showing the anchoring site, pincer arms and metal cavity, the donor atoms E_1, E_2 and E_3, the metal M and the labile ligand L.

Pincers are stereo and electronically versatile due to their modularity to achieve certain reactivity. The anchor in the molecule controls the electron density on the central donor atom, E_2, which controls the electron density of the metal atom on the *trans* position (*trans*-influence).[214,215] The linker, which is part

of the arms, is sometimes referred to as the chiral pocket as chirality can be introduced to the molecule on this site. This is in addition to its ability to control electron density on the donor atoms E_1 and E_3, affecting their reactivity to the metal centre M.[215] The size of the linker affects the chelate and bite angle of the molecule which greatly influences the stability of the pincer complex.[211,216]

The donor atoms E_1 and E_3 are also part of the pincer arms, and they provide electronic control on the metal centre by measure of their Lewis hardness and softness. As a result, together with E_2, they affect the reactivity of M on its free coordination site L.[217] R provides steric modulations to the molecule, influences the accessibility of the cavity for metal binding and provides a cavity for counter ions. Chirality can also be introduced on this site. [211,215,217]

Pincer molecules and their complexes usually have very labile chloro- and hydroxy groups, making these compounds very susceptible to nucleophilic substitution.[210,218] The denticity of pincer molecules increases the stability of the complex, as chelation through two or more bonds increases the stability of the metal complex and reduces ligand dissociation.[219] The ability of pincer ligands to form adjacent five- and six-membered rings coordinated to a metal ion by manipulating the linker also contributes to the stability of the metal complexes.[193] Five-membered rings are more abundant than six-membered metallacyclic pincers. [220–223]

Although the anchor of a pincer molecule is generally planar and tends to form planar metal complexes, the size, and orientation of the groups constituting the pincer arms will dictate the global conformation as well as the physical and chemical properties of the molecule. Consequently, pincer compounds may be designed to function in a wide range of applications. These include separation and detection technologies, [224,225] complexing anions,[226,227] as catalysts,[228,229] as anion receptors,[230] as potential ion channels in membranes[225,231], and they have recently been of interest in drug discovery.

Since pincer ligands often contain aromatic backbones, these pincer ligands and their complexes are usually planar and rigid. The planarity allows for intercalation in DNA molecules, which makes pincer molecules good ligands for gold(III) complexes.[201] The rigidity of these ligands allows the ligands to exert a high degree of steric control on the remaining coordination site's environment, thus controlling its reactivity.[232] In the pharmaceutical industry, steric control in a metal complex plays an important role in reducing its toxicity as side reactions are controlled.[206,232] The high thermal and chemical stability of pincer molecules makes them popular across the natural sciences,[233,234] as these properties induce their ability to autonomously control the reactivity of the metal centres.[210,211]

Pincers are often hemiliable and this makes for easier displacement of certain functional groups. This is a useful phenomenon in catalysis and pharmacology as it offers variations in binding modes.[211,235,236] This also allows the pincer molecules to adapt to steric and electronic demands, as they can interchange between tridentate, bidentate and monodentate, thus changing conformations accordingly.[235,236]

The extensive modularity and tunability of pincers give pincer molecules a wide variety of applications in chiral synthesis, catalysis and the pharmaceutical industry. It also enables the introduction of other

properties like chirality, to the pincer ligand or complex by adding specific moieties with the desirable properties as substituents in the vicinity of the coordination sphere.[210,237,238]

Even though many pincer molecules do not have any stereogenic centres, flexibility and steric effects involving the pincer arms may induce axial chirality (helicity) in the nominally planar molecule, producing atropisomers. [228,229]

Pincer molecules are often classified into different classes depending on their donor atoms to the metal centre, for example NCN, PCP, CNC and NNN.[210] The group consisting of NCN, PCP, CNC, SNS, PNP and SeNSe pincers are the most popular and most studied among all pincers.[210] This is mainly due to their relative ease of synthesis compared to the other pincers. These pincers typically induce chirality in the constituents around the coordination sphere. The NCN and CNC pincers have been of more interest due to their enhanced ability to reduce ligand leaching. The NCN pincers are fluxional and sometimes change the oxidation state of the metal centre, which is an interesting phenomenon in catalysis and potentially in biomolecules.[239–241] Homoatomic donor group pincer systems are relatively rare, but research on these pincers has recently gained traction, e.g., NNN type pincers..[210]

NNN pincers are well known for their ability to stabilise the high and low oxidation states of transition metals.[182,190,193] The nitrogens in the NNN pincer can be neutral or anionic, and this helps control the reactivity of the labile group, which controls its reactivity with biomolecules in the biological application.[210] They also have a high balance between reactivity and stability.[242] These pincer ligands are generally stable to reduction, air and moisture, making them easy to transport and store. [242,243] This makes them very favourable in medicinal chemistry, where metal complexes are exposed to all the mentioned conditions in biological systems.

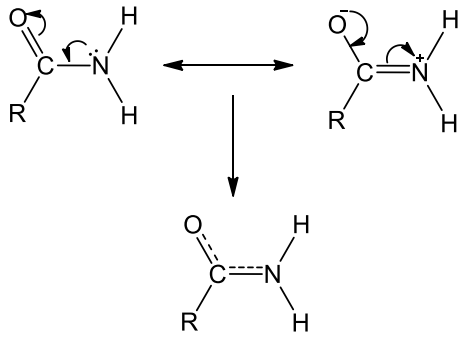
NNN pincer systems have three nitrogens as the donor atoms, and they are generally synthesised from bis(imino)pyridine, bis(2-pyridyl imino)isoindole, 2,6-bis(5-tert-butyl-1H-pyrazole-3-yl)pyridine and 2,6-bis amido pyridines.[244] Bis(carboxamide) pincer complexes, which are the focus of this study, are an example of the 2,6-bis amido pyridine-based NNN-type pincer systems.

Bis(carboxamide) pincer molecules contain an amide bond, which is one of the most important and abundant bonds in biological systems. It is the most prevalent in biomolecules including peptides, proteins, DNA and RNA.[245] Amide bonds are very stable due to their ability to form resonance structures, enabling biomolecules to adopt stable 3D structures. Compounds with the amide bond tend to be hydrogen bond donors and or acceptors, which is an important aspect in pharmacology, as this allows for interaction with DNA and other cellular components in desired ways.[132,246–248]

The amide bond has enhanced stability because of the resonance across the bond.[249] The carbonyl carbon is electron deficient as the shared π-electron pair is drawn towards the inordinately electronegative oxygen. In turn, the lone pair of electrons on the amide nitrogen is delocalised across the C–N bond (**Scheme 1.1**).[250,251]

Because of the instability of both species, they do not exist in both forms, but as a resonance instead. This is also the reason why the nitrogen is sp^2 hybridised and not sp^3 hybridised, and the bond is rigid

(cannot rotate). This angle is therefore planar and the bonds around the nitrogen and carbon are ~120°.[252,253] This resonance also enhances the strength of this bond and the stability of the molecules. Given that the nitrogen lone pair is delocalised onto the π-bond, it loses its basicity, and cannot react with Lewis acids. The oxygen however has an abundance of electrons, hence it acts as a Lewis base, so it reacts easily with Lewis acids (forms strong H-bonding). Contrastingly, the electrophilicity on the amide carbon is reduced by the resonance and is less susceptible to nucleophilic attacks.[249] As such, amide-based compounds have successfully been applied for cancer treatment (**Figure 1.8** and **Table 1.4**). These compounds target different areas in the cell cycle of cancerous cells. For example, Dasatinib, Acridine carboxamide, Dacarbazine and Opaganib.



Scheme 1.1. An illustration of resonance in the amide bond when the π electrons are delocalised across the C–O or the C–N bonds, resulting in a hybrid structure with resonance.[253]

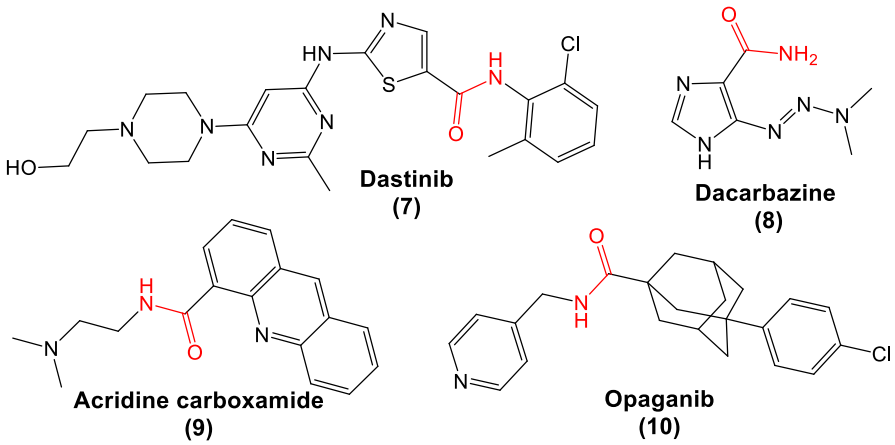


Figure 1.8. Examples of pharmaceutical drugs currently in use containing the amide bond, highlighted in red.

Table 1.4. Examples of amide-based chemotherapeutic drugs, their clinical use and pharmacology

Drugs	Clinical use	Pharmacology	References
Amide-based			
Dasatinib **(7)**	Approved for the treatment of lymphoblastic or chronic myeloid leukaemia with resistance to prior therapy	A tyrosine kinase inhibitor which inhibits the kinases of the SRC family (SRC, LCK, YES, FYN), EPHA2, BCR-ABL, c-KIT, and PDGFRβ	254–259
Acridine carboxamide **(8)**	Underwent clinical trials for the treatment of brain and central nervous system tumours and lung cancer	Exhibits topoisomerase inhibition and antineoplastic activities. It disrupts DNA repair and replication and inhibits RNA and protein synthesis, which causes cell death by intercalating into DNA and inhibiting both topoisomerases I and II.	260,261 262,263
Dacarbazine **(9)**	Approved for the treatment of malignant melanoma and Hodgkin's disease	Acts as an alkylating agent. It is a purine analogue and interacts with the thiol groups	264–267
Opaganib **(10)**	Approved for the treatment of prostate cancer	Blocks the synthesis of sphingosine 1-phosphate (S1P) and its activities by selectively inhibiting sphingosine kinase-2 (SK2)	268–274

As mentioned earlier, R components in **Figure 1.7** are one of the groups modified in pincer to introduce new characteristics to the complex. The efficacy of designed pincer molecules can be improved by adding chemical moieties with desirable qualities. One group of interest especially in this study is nitrogen-containing heterocycles (NCHs).

1.2.4 Nitrogen-containing heterocycles

Heterocycles are some of the crucial building blocks for several synthetic and semi-synthetic drugs. Specifically, NCHs are amongst the world's highest selling drugs due to their flexibility toward various biological scaffolds and pharmaceutical products. Different nitrogen-containing heterocycles include indoles, quinazolines, carbazoles, quinoxalines, norharmane[275] oxadiazole, thiazole, purines, pyrimidines, antipyrines, quinolines, indazoles, phenones and phenanthrolines. [254,276,277] Despite the large pool of NCHs, this study mainly focused on the latter four.

Quinoline is an aromatic heterocyclic organic compound with the chemical formula C_9H_7N, produced by a benzene ring fusion with pyridine at two neighbouring carbon atoms, resulting in a bicyclic structure.[278] The quinoline ring is considered an electron-deficient system, due to the electronegativity difference between nitrogen (3.04) and carbon (2.55). It demonstrates both nucleophilic (it has a delocalised π-electron system, which makes it electron-deficient and thus capable of acting as an electrophile by accepting a pair of electrons from a nucleophile) and electrophilic (nitrogen has a lone pair of electrons, making it susceptible to electrophilic attacks), which are properties similar to pyridine.[279] The clinical observation demonstrates that even when a person inhales a 0.001 ppm level of quinoline for 8 hours, it is completely nontoxic; in contrast, even a lower concentration of benzene causes various biological disorders such as cancer.[278] This makes it a more favourable compound for pharmacological uses.

Quinoline derivatives are commonly used as “parental” compounds in the synthesis of molecules with medicinal benefits, particularly those with anti-malarial and anti-microbial properties. Several quinolines and their compounds have been shown to have antimicrobial, antifungal, hypotensive, anti-HIV, analgesic, anti-inflammatory and antitumour properties. Quinoline and its analogues have lately been investigated for their modes of action in inhibiting tyrosine kinases, proteasome, tubulin polymerisation, topoisomerase, and DNA repair.[280] The substitution of a group in a suitable position of a bioactive molecule has been found to have a significant pharmacological impact.[281] The quinoline nucleus has spontaneously elicited many alkaloids with antitumour activity, such as camptothecin.[282] Examples of such compounds including camptothecin (**11**) and neratinib (**12**) are illustrated in **Figure 1.9** and **Table 1.4**.

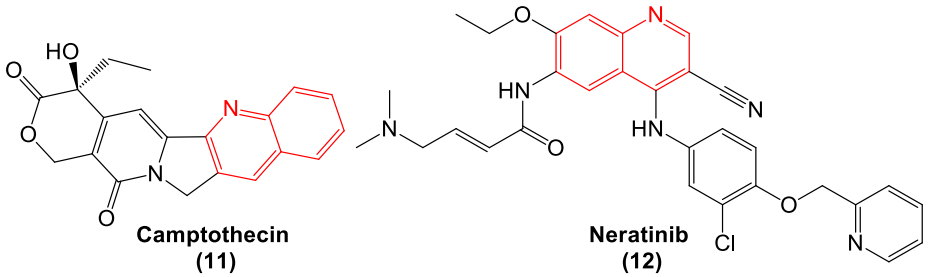
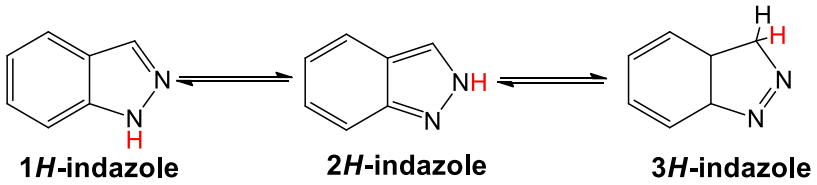


Figure 1.9. Examples of pharmaceutical drugs currently in use containing different isomers of the quinoline ring, highlighted in red.

Indazole is a heterocyclic product of the ring condensation of pyrazole with the benzene ring. It has two nitrogen atoms and can exhibit annular tautomerism, where one proton can occupy two or more positions in heterocyclic molecules, and consequently exists as three tautomers 1*H*-indazole and 2*H*-indazole and 3*H*-indazole (**Scheme 1.2**).[283] The 1*H*-indazole tautomer is thermodynamically stable as compared to the 2*H*- and 3*H*-indazole, thus making it the predominant tautomer.[284,285] Indazole is a 10-π electron aromatic heterocyclic system, which resembles both pyridine and pyrrole, thus exhibiting properties of both.



Scheme 1.2. An illustration of tautomerism in indazole.

The indazole scaffold has just recently gained traction as a building block in pharmaceutical and medicinal chemistry. This has resulted in extensive studies being done on the indazole group, together with its bioisosteres.[286] The indazole group is a huge phenomenon in cellular biology as it is an analogue of purine bases.[287,288] Despite its scarcity in nature, numerous synthetic indazole derivatives have exhibited pharmacological and biological properties such as anti-inflammatory, analgesic and antiarrhythmic,[289] antibacterial,[290] anti-fungal[291] anti-HIV,[292–298] and anti-tumour properties.[299–301] This

has resulted in the synthesis of novel indazole motifs to be employed as building blocks for the next generation of medications and has immense potential.[288]

Some examples of indazole-based drugs currently being used in cancer treatment are illustrated in **Figure 1.10** and **Table 1.5**. These include granisetron (1-methyl-N-((1S,5R)-9-methyl-9-azabicyclo[3.3.1]nonan-2-yl)-1H-indazole-3-carboxamide),[302–304] axitinib (N-methyl-2-[[3-[(E)-2-pyridin-2-ylethenyl]-1H-indazol-6-yl]sulfanyl]benzamide),[305] pazopanib (5-({4-[(2,3-Dimethyl-2H-indazol-6-yl)methylamino]pyrimidin-2-yl}amino)-2-methylbenzenesulfonamide),[306–309] niraparib ((S)-2-(4-(piperidin-3-yl)phenyl)-2H-indazole-7-carboxamide)[310–312] and lonidamine (LND) (1-(2,4-dichloro-benzyl)-indazole-3-carboxylic acid).[313,314]

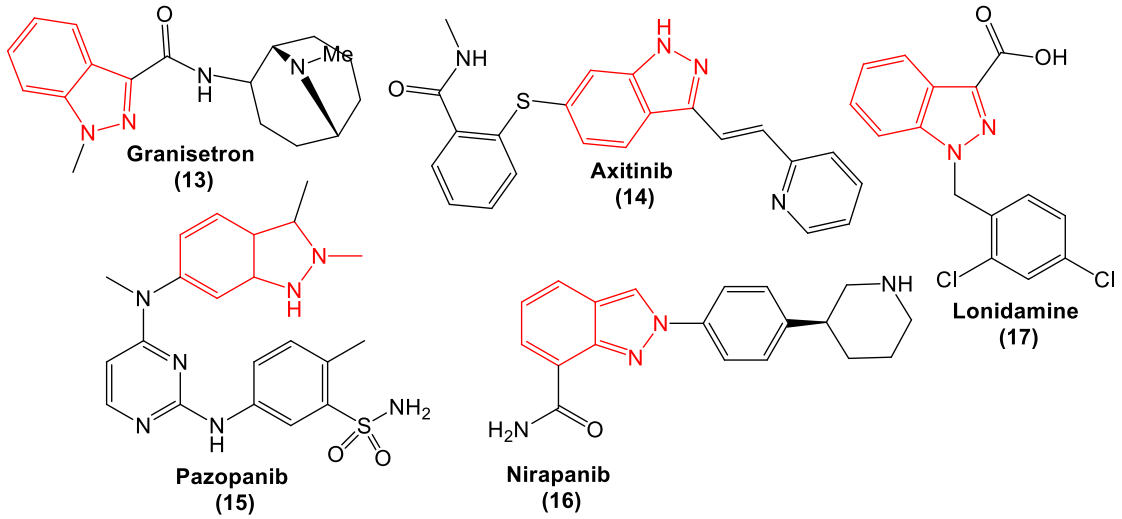


Figure 1.10. Examples of pharmaceutical drugs currently in use containing the indazole ring, highlighted in red.

Benzophenones and phenanthrolines are not very common in the pharmaceutical industry, but they have gained traction in recent years due to their biological activities.[315–318] Despite their promising result in different treatment plans, none of these drugs have been approved for medicinal use yet, according to the drug bank.[319] Examples of drugs under investigation are outlined in **Table 1.5**.

Table 1.5. Examples of different NCHs based chemotherapeutic drugs, their clinical use and pharmacology.

Drugs	Clinical use	Pharmacology	References
Quinolines			
Neratinib (**12**)	Approved for HER2, HER4, EGFR and ER^+ for breast cancer, clinical trials for various solid tumours	Inhibits the auto phosphorylation of tyrosine receptors by tyrosine kinase.	[320,321]
Camptothecin (**11**)	Experimented on various cancer cell lines	Inhibits topoisomerase I by blocking DNA relegation, resulting in DNA damage	[322]
Benzophenone			
Benzophenone derivatives	Experiments on human breast cancer cell line (MCF-7)	Tubulin polymerization inhibition.	[279]
Benzophenone sulfonamide derivatives	Experiment on the CCRF-CEM Vcr1000 cancer cell line	Inhibits P-glycoprotein (P-gp) and could serve as anticancer agents	[316]
Phenanthroline			
APTO-253	Phase I clinical trial for acute myeloid leukaemia (AML)	Induces cyclin-dependent kinase inhibitor CDKN1A (p21) production, promoting G_0-G_1 cell-cycle arrest, and triggers apoptosis.	[323]
1,10-Phenanthroline	Experiments on the lymphoblast cell cycle	Inhibits the progression of the cell cycle from G1 to S phases by chelating the necessary metals.	[318]
Indazoles			
Granisetron (**13**)	Approved for relieving nausea and vomiting during cancer treatment and after surgery.	A serotonin receptor (5HT-3 specific) antagonist that has been utilised in cancer chemotherapy patients as an antiemetic and antinauseant.	[302–304]
Axitinib (**14**)	Approved for advanced renal cell carcinoma and kidney cell cancer, clinical trials for the treatment of pancreatic and thyroid cancer.	A tyrosine kinase inhibitor that inhibits vascular endothelial growth factor receptors (VEGFR-1, VEGFR-2, VEGFR-3)	[305]
Pazopanib (**15**)	Approved for advanced renal cell carcinoma and advanced soft tissue sarcoma in individuals who have already received chemotherapy.	Inhibits tyrosine kinase by targeting vascular endothelial growth factor receptors (EGFR) 1, 2, and 3, platelet-derived growth factor receptor-alpha and -beta, and c-kit.	[306–309]
Niraparib (**16**)	Approved for treatment of recurrent epithelial ovarian, fallopian tube, or primary peritoneal cancer previously treated with platinum-based chemotherapy	Inhibits poly (ADP-ribose) polymerases (PARP) 1 and 2, which are involved in DNA repair, causing cellular cytotoxicity.	[310–312]
Lonidamine (**17**)	Investigated various cancer cell lines and tumours.	inhibit aerobic glycolysis in cancer cells, thereby decreasing cellular ATP	[313,314,324]

1.3 Rationale and aims for the research

Gold(III) pincer complexes are still relatively rare compared to other metal pincer complexes despite being widely used in the catalysis and pharmaceutical fields.[14, 21-23] Literature shows that these metal complexes interact with DNA through groove binding,[173] intercalations,[173,201,208] and alkylation,[209,325] thus having the potential to target cancerous cells, resulting in apoptosis and reducing the proliferation of these cells. Despite all these speculations, none of the gold pincers to date has been approved for cancer treatment, hence the continuous study on these complexes.

It has been discussed in this chapter how gold complexes have shown some potential cancer treatment. In the design of this research, there were key factors which were taken into consideration. To begin with, gold(III) complexes have been proven to have excellent anticancer properties.[178,179,197,201] The square planar configuration of the gold(III) complexes enables them to easily intercalate into the DNA without much hindrance. The crescent shape and helicity of gold(III) complexes synthesised might enable them to bind into the minor groove of DNA and inhibit topoisomerase I. Gold(III) pincer compounds have labile Cl^-/OH^- , which enables their nucleophilic substitution with the DNA bases and amino acids on proteins. This also gives the complexes to directly inhibit or change the functions of proteins. Since the proposed complexes have characteristics suitable for cancer cell cytotoxicity, it is apparent to gain a better understanding of the compounds.

One of the main goals of this research is to synthesise stable gold(III) complexes at physiological conditions. To achieve this, the NNN pincer framework plays a huge role. Nitrogens are strong δ-donors with the ability to stabilise the Au^{3+} ions at physiological pH, temperature and pressure. The multidentate nature and the rigidity of pincers also help to improve the stability of these complexes.

The indazole, benzophenone, phenanthroline, quinoline and isoquinoline moieties will be incorporated into the arms of the pincer structure so that they can impart their properties on the resultant metal complexes and improve their efficacy in cancer treatment. It is also envisioned that these moieties could also improve the solubility of these neutral metal complexes in aqueous media due to their polarity.

1.3.1 Hypothesis

The central hypothesis of this thesis is that:

i) The designed pincer ligands will stabilise the gold(III) ion in the metal complex and the complex will be sufficiently hydrophilic for use in aqueous solutions.
ii) The design of the target compounds may aid in their interaction with the DNA, promote the damage of cellular DNA and reduce cell proliferation.

1.3.2 General aims

The main aims of this study are to:

i) Synthesise gold(III) carboxamide pincer chelates to add to the library of gold(III) metal complexes.
ii) Investigate their stability and biochemical and biological properties.

1.3.3 Objectives

i) Synthesis of carboxamide pincer ligands (**Figure 1.11**)

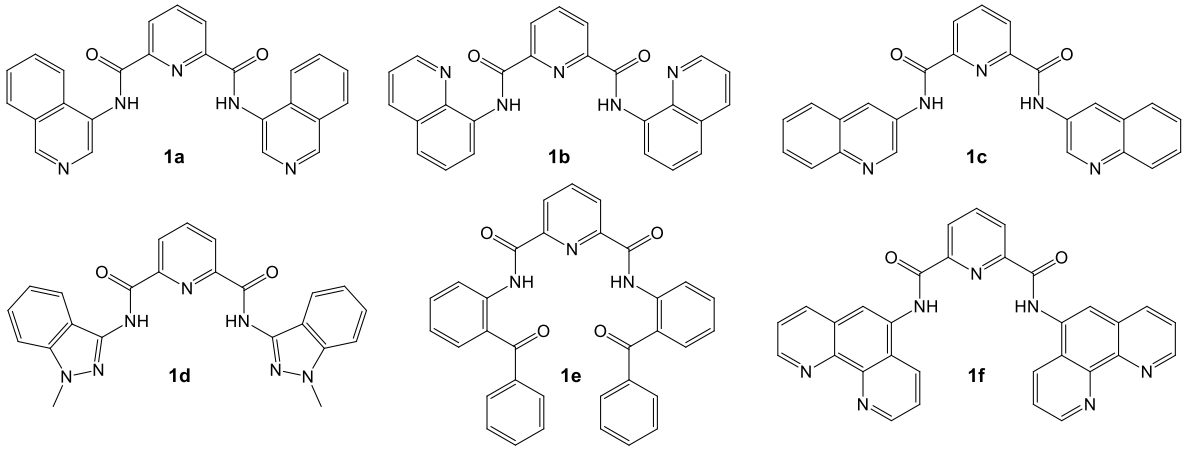


Figure 1.3. Chemical structures of the carboxamide pincer ligands to be discussed in this thesis, with isoquinoline, quinolone, indazole, benzophenone and phenanthroline moieties.

ii) Synthesis of gold(III) carboxamide pincer ligand complexes (**Figure 1.12**)

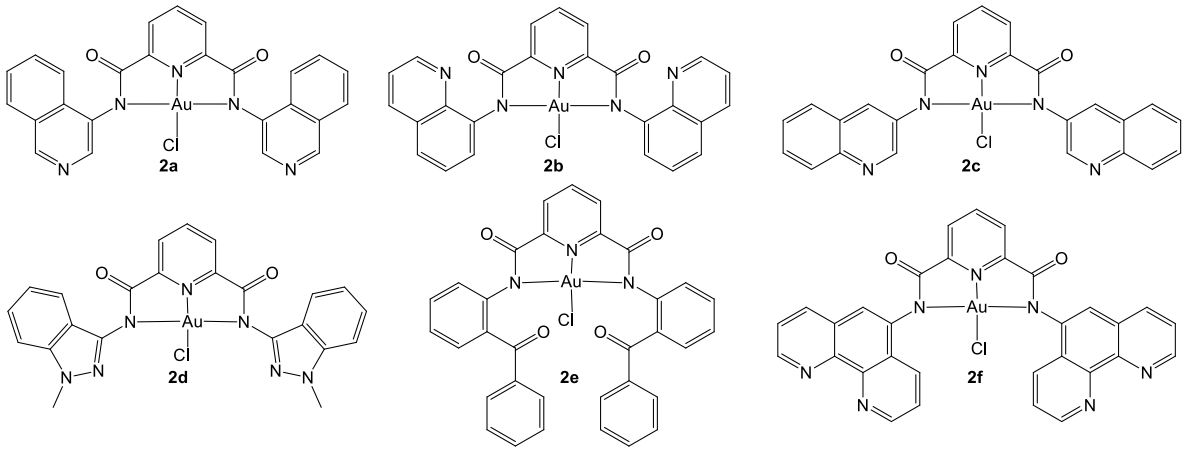


Figure 1.4. Chemical structures of the proposed novel conventional gold(III) pincer chelates with isoquinoline, quinolone, indazole, benzophenone and phenanthroline moieties, to enhance potential interactions with DNA bases.

iii) Characterisation of the synthesised ligands and complexes by spectroscopy:
The synthesised compounds will be analysed by, Fourier-Transform Infrared spectroscopy (FT-IR), Nuclear Magnetic Resonance spectroscopy (NMR), High-Resolution Mass Spectrometry (HRMS) and Circular dichroism (CD) spectroscopy. This is to understand the structure and the conformation of the synthesised compounds.

iv) Characterisation of the synthesised ligands and complexes by X-ray crystallography: The synthesised compounds will be analysed by X-ray crystallography to understand the molecular structure and the conformation of the synthesised compounds.

v) Biochemistry of one of the synthesised complexes:
PH speciation studies will be done to determine the compound in solution at the pH at which the DNA binding studies are conducted. To determine the resistance of the compounds to

reduction, binding studies with a known biological reducing agent, glutathione (GSH) will be conducted.

The binding constants of the complexes, their modes of binding, and their effects on DNA will be studied using electrophoretic mobility assays, spectroscopic titrations, viscometry and DNA melts. These tests will help in screening for complexes that can bind to DNA and these will be tested for cytotoxicity of different cell lines.

The binding constants of the complexes to DNA will be compared to that of the transport protein Human Serum Albumin (HSA) using spectroscopic titrations to determine their efficacy.

vi) Biological activity experiments:

National Cancer Institute (NCI) cytotoxicity screening methods are used to determine the GI_{50} (concentration at which the cancer cells proliferation is inhibited by 50%), IC_{50} (when growth inhibition of the cells is inhibited by 50%), and LC_{50} (Lethal Dose - the concentration at which 50% cell death is induced). These values will be calculated from growth inhibition as a function of compound dose. This test is to determine the activity of the novel complexes on cancerous cells and determine their efficacy. The calculated values will be compared to some clinically approved drugs and some promising pre-existing anticancer agents.

vii) Computational analysis:

The experimental data will be compared to and corroborated with calculated data from DFT calculations to help explain the electronic structures as well as steric and conformational parameters relevant to delineating the interaction of the complexes with macromolecular targets such as DNA.

1.4 References

1. Cancer statistics, 2023 - Siegel - 2023 - CA: A Cancer Journal for Clinicians - Wiley Online Library. Accessed March 9, 2023. https://acsjournals.onlinelibrary.wiley.com/doi/10.3322/caac.21763
2. Cancer. Accessed March 9, 2023. https://www.who.int/health-topics/cancer
3. Nygren P. What is cancer chemotherapy? *Acta Oncol*. 2001;40(2-3):166-174. doi:10.1080/02841860151116204
4. Weinberg RA. How Cancer Arises. *Sci Am*. 1996;275(3):62-70. Accessed July 19, 2023. https://www.jstor.org/stable/24993349
5. Siegel RL, Miller KD, Jemal A. Cancer statistics, 2018. *CA Cancer J Clin*. 2018;68(1):7-30. doi:10.3322/caac.21442
6. Siegel RL, Miller KD, Wagle NS, Jemal A. Cancer statistics, 2023. *CA Cancer J Clin*. 2023;73(1):17-48. doi:10.3322/caac.21763
7. Siegel RL, Miller KD, Jemal A. Cancer statistics, 2020. *CA Cancer J Clin*. 2020;70(1):7-30. doi:10.3322/caac.21590
8. Weir HK, Thun MJ, Hankey BF, et al. Annual report to the nation on the status of cancer, 1975-2000, featuring the uses of surveillance data for cancer prevention and control. *J Natl Cancer Inst*. 2003;95(17):1276-1299. doi:10.1093/jnci/djg040
9. Cronin KA, Scott S, Firth AU, et al. Annual report to the nation on the status of cancer, part 1: National cancer statistics. *Cancer*. 2022;128(24):4251-4284. doi:10.1002/cncr.34479
10. Henley SJ, Ward EM, Scott S, et al. Annual report to the nation on the status of cancer, part I: National cancer statistics. *Cancer*. 2020;126(10):2225-2249. doi:10.1002/cncr.32802
11. Ferlay J, Colombet M, Soerjomataram I, Siegel R, Torre L, Jemal A. Global and regional estimates of the incidence and mortality for 38 cancers: GLOBOCAN 2018. *World Health Organ Int Agency Res Cancer Lyon Fr*. 2018;14.
12. Allemani C, Matsuda T, Carlo VD, et al. Global surveillance of trends in cancer survival: analysis of individual records for 37,513,025 patients diagnosed with one of 18 cancers during 2000–2014 from 322 population-

based registries in 71 countries (CONCORD-3). *Lancet Lond Engl*. 2018;391(10125):1023. doi:10.1016/S0140-6736(17)33326-3
13. Pramesh CS, Badwe RA, Bhoo-Pathy N, et al. Priorities for cancer research in low- and middle-income countries: a global perspective. *Nat Med*. 2022;28(4):649-657. doi:10.1038/s41591-022-01738-x
14. Miller KD, Nogueira L, Devasia T, et al. Cancer treatment and survivorship statistics, 2022. *CA Cancer J Clin*. 2022;72(5):409-436. doi:10.3322/caac.21731
15. Gersten O, Wilmoth JR. The Cancer Transition in Japan since 1951. *Demogr Res*. 2002;7(5):271-306. doi:10.4054/DemRes.2002.7.5
16. Bahnassy AA, Abdellateif MS, Zekri ARN. Cancer in Africa: Is It a Genetic or Environmental Health Problem? *Front Oncol*. 2020;10. Accessed March 9, 2023. https://www.frontiersin.org/articles/10.3389/fonc.2020.604214
17. World Health Organization. Health systems in Africa: Community perceptions and perspectives: the report of a multi-country study. Published online 2012.
18. Moeti M, Kunowu F. AfricaRenewal. 2016;30(3):1-39. https://www.un.org/africarenewal/magazine/issue/december-2016-march-2017
19. Azevedo MJ. The State of Health System(s) in Africa: Challenges and Opportunities. *Hist Perspect State Health Health Syst Afr Vol II*. Published online February 3, 2017:1-73. doi:10.1007/978-3-319-32564-4_1
20. Cancer Treatment: Types, Diagnosis & Cost, Treatment in India. Published August 1, 2022. Accessed July 13, 2023. https://www.healthyatra.com/cancer-treatment-types-diagnosis-cost-treatment-in-india
21. Husain LS, Collins K, Reed M, Wyld L. Choices in cancer treatment: a qualitative study of the older women's (>70 years) perspective. *Psychooncology*. 2008;17(4):410-416. doi:10.1002/pon.1242
22. Engel J, Eckel R, Kerr J, et al. The process of metastasisation for breast cancer. *Eur J Cancer Oxf Engl 1990*. 2003;39(12):1794-1806. doi:10.1016/s0959-8049(03)00422-2
23. Miglietta F, Bottosso M, Griguolo G, Dieci MV, Guarneri V. Major advancements in metastatic breast cancer treatment: when expanding options means prolonging survival. *ESMO Open*. 2022;7(2):100409. doi:10.1016/j.esmoop.2022.100409
24. Brennan A, Hickey M. The use of menopausal hormone therapy after cancer. *Best Pract Res Clin Obstet Gynaecol*. 2022;81:22-30. doi:10.1016/j.bpobgyn.2021.11.005
25. Drăgănescu M, Carmocan C. Hormone Therapy in Breast Cancer. *Chirurgia (Bucur)*. 2017;112(4):413. doi:10.21614/chirurgia.112.4.413
26. Kuhle CL, Kapoor E, Sood R, Thielen JM, Jatoi A, Faubion SS. Menopausal hormone therapy in cancer survivors: A narrative review of the literature. *Maturitas*. 2016;92:86-96. doi:10.1016/j.maturitas.2016.07.018
27. Ravnikar VA. Compliance with hormone therapy. *Am J Obstet Gynecol*. 1987;156(5):1332-1334. doi:10.1016/0002-9378(87)90173-6
28. Cognitive effects of hormone therapy in men with prostate cancer - Nelson - 2008 - Cancer - Wiley Online Library. Accessed July 13, 2023. https://acsjournals.onlinelibrary.wiley.com/doi/full/10.1002/cncr.23658
29. Tripathy D, Im SA, Colleoni M, et al. Ribociclib plus endocrine therapy for premenopausal women with hormone-receptor-positive, advanced breast cancer (MONALEESA-7): a randomised phase 3 trial. *Lancet Oncol*. 2018;19(7):904-915. doi:10.1016/S1470-2045(18)30292-4
30. Borghaei H, Smith MR, Campbell KS. Immunotherapy of cancer. *Eur J Pharmacol*. 2009;625(1):41-54. doi:10.1016/j.ejphar.2009.09.067
31. Borgers JSW, Heimovaara JH, Cardonick E, et al. Immunotherapy for cancer treatment during pregnancy. *Lancet Oncol*. 2021;22(12):e550-e561. doi:10.1016/S1470-2045(21)00525-8
32. Trapani JA, Darcy PK. Immunotherapy of cancer. *Aust Fam Physician*. 2020;46(4):194-198. doi:10.3316/informit.741814295491394
33. Zaidi N, Jaffee EM. Immunotherapy transforms cancer treatment. *J Clin Invest*. 2019;129(1):46-47. doi:10.1172/JCI126046
34. Rescigno M, Avogadri F, Curigliano G. Challenges and prospects of immunotherapy as cancer treatment. *Biochim Biophys Acta BBA - Rev Cancer*. 2007;1776(1):108-123. doi:10.1016/j.bbcan.2007.07.003
35. Li Y, Ayala-Orozco C, Ranjan Rauta P, Krishnan S. The application of nanotechnology in enhancing immunotherapy for cancer treatment: current effects and perspective. *Nanoscale*. 2019;11(37):17157-17178. doi:10.1039/C9NR05371A
36. Gupta S, Shukla S. Limitations of Immunotherapy in Cancer. *Cureus*. 14(10):e30856. doi:10.7759/cureus.30856
37. Bagó JR, Sheets KT, Hingtgen SD. Neural stem cell therapy for cancer. *Methods*. 2016;99:37-43. doi:10.1016/j.ymeth.2015.08.013
38. Chu DT, Nguyen TT, Tien NLB, et al. Recent Progress of Stem Cell Therapy in Cancer Treatment: Molecular Mechanisms and Potential Applications. *Cells*. 2020;9(3):563. doi:10.3390/cells9030563

39. Han L, Shi S, Gong T, Zhang Z, Sun X. Cancer stem cells: therapeutic implications and perspectives in cancer therapy. *Acta Pharm Sin B*. 2013;3(2):65-75. doi:10.1016/j.apsb.2013.02.006
40. Kim SU, de Vellis J. Stem cell-based cell therapy in neurological diseases: A review. *J Neurosci Res*. 2009;87(10):2183-2200. doi:10.1002/jnr.22054
41. Maroufi NF, Vahedian V, Hemati S, et al. Targeting cancer stem cells by melatonin: Effective therapy for cancer treatment. *Pathol - Res Pract*. 2020;216(5):152919. doi:10.1016/j.prp.2020.152919
42. Phi LTH, Sari IN, Yang YG, et al. Cancer Stem Cells (CSCs) in Drug Resistance and their Therapeutic Implications in Cancer Treatment. *Stem Cells Int*. 2018;2018:e5416923. doi:10.1155/2018/5416923
43. Sagar J, Chaib B, Sales K, Winslet M, Seifalian A. Role of stem cells in cancer therapy and cancer stem cells: a review. *Cancer Cell Int*. 2007;7(1):9. doi:10.1186/1475-2867-7-9
44. Stuckey DW, Shah K. Stem cell-based therapies for cancer treatment: separating hope from hype. *Nat Rev Cancer*. 2014;14(10):683-691. doi:10.1038/nrc3798
45. Tsimberidou AM. Targeted therapy in cancer. *Cancer Chemother Pharmacol*. 2015;76(6):1113-1132. doi:10.1007/s00280-015-2861-1
46. Pucci C, Martinelli C, Ciofani G. Innovative approaches for cancer treatment: current perspectives and new challenges. *ecancermedicalscience*. 2019;13:961. doi:10.3332/ecancer.2019.961
47. Bazak R, Houri M, Achy SE, Kamel S, Refaat T. Cancer active targeting by nanoparticles: a comprehensive review of literature. *J Cancer Res Clin Oncol*. 2015;141(5):769-784. doi:10.1007/s00432-014-1767-3
48. Wyld L, Audisio RA, Poston GJ. The evolution of cancer surgery and future perspectives. *Nat Rev Clin Oncol*. 2015;12(2):115-124. doi:10.1038/nrclinonc.2014.191
49. Surgery for Cancer - NCI. Published April 29, 2015. Accessed July 13, 2023. https://www.cancer.gov/about-cancer/treatment/types/surgery
50. Erinjeri JP, Clark TWI. Cryoablation: Mechanism of Action and Devices. *J Vasc Interv Radiol JVIR*. 2010;21(8 Suppl):S187-S191. doi:10.1016/j.jvir.2009.12.403
51. Kwak K, Yu B, Lewandowski RJ, Kim DH. Recent progress in cryoablation cancer therapy and nanoparticles mediated cryoablation. *Theranostics*. 2022;12(5):2175-2204. doi:10.7150/thno.67530
52. Cryoablation: Cryotherapy, Cryosurgery. Cleveland Clinic. Accessed August 15, 2023. https://my.clevelandclinic.org/health/treatments/16903-cryoablation
53. Parvinian A, Kurup AN, Atwell TD, Schmit GD, Schmitz JJ, Morris JM. Percutaneous Cryoablation of Large Tumors: Safety, Feasibility, and Technical Considerations. *Cardiovasc Intervent Radiol*. 2022;45(1):69-79. doi:10.1007/s00270-021-03025-7
54. Amjad MT, Chidharla A, Kasi A. Cancer Chemotherapy. In: *StatPearls*. StatPearls Publishing; 2023. Accessed March 28, 2023. http://www.ncbi.nlm.nih.gov/books/NBK564367/
55. Brown A, Kumar S, Tchounwou PB. Cisplatin-Based Chemotherapy of Human Cancers. *J Cancer Sci Ther*. 2019;11(4):97. Accessed March 27, 2023. https://www.ncbi.nlm.nih.gov/pmc/articles/PMC7059781/
56. Chabner BA, Roberts TG. Chemotherapy and the war on cancer. *Nat Rev Cancer*. 2005;5(1):65-72. doi:10.1038/nrc1529
57. Rich JN, Bao S. Chemotherapy and Cancer Stem Cells. *Cell Stem Cell*. 2007;1(4):353-355. doi:10.1016/j.stem.2007.09.011
58. Shahzad H. *Neoplasm*. BoD – Books on Demand; 2018.
59. Boyle P, Ngoma T, Sullivan R, Brawley O. Cancer in Africa: the way forward. *ecancermedicalscience*. 2019;13:953. doi:10.3332/ecancer.2019.953
60. Treatments | Cancercare | South Africa. Cancercare. Accessed August 15, 2023. https://cancercare.co.za/treatments/
61. Cancer treatments: MedlinePlus Medical Encyclopedia. Accessed August 15, 2023. https://medlineplus.gov/ency/patientinstructions/000901.htm
62. Thomas GM. Improved Treatment for Cervical Cancer — Concurrent Chemotherapy and Radiotherapy. *N Engl J Med*. 1999;340(15):1198-1200. doi:10.1056/NEJM199904153401509
63. Barton MB, Frommer M, Shafiq J. Role of radiotherapy in cancer control in low-income and middle-income countries. *Lancet Oncol*. 2006;7(7):584-595. doi:10.1016/S1470-2045(06)70759-8
64. Horton S, Gauvreau CL. Cancer in Low- and Middle-Income Countries: An Economic Overview. In: Gelband H, Jha P, Sankaranarayanan R, Horton S, eds. *Cancer: Disease Control Priorities, Third Edition (Volume 3)*. The International Bank for Reconstruction and Development / The World Bank; 2015. Accessed July 13, 2023. http://www.ncbi.nlm.nih.gov/books/NBK343620/
65. Anderson BO, Yip CH, Smith RA, et al. Guideline implementation for breast healthcare in low-income and middle-income countries. *Cancer*. 2008;113(S8):2221-2243. doi:10.1002/cncr.23844
66. Mukherjee S. *The Emperor of All Maladies: A Biography of Cancer*. Reprint edition. Scribner; 2011.

67. Kohn KW, Jackman J, O'Connor PM. Cell cycle control and cancer chemotherapy. *J Cell Biochem*. 1994;54(4):440-452. doi:10.1002/jcb.240540411
68. Pérez-Herrero E, Fernández-Medarde A. Advanced targeted therapies in cancer: Drug nanocarriers, the future of chemotherapy. *Eur J Pharm Biopharm*. 2015;93:52-79. doi:10.1016/j.ejpb.2015.03.018
69. Sun Y, Liu Y, Ma X, Hu H. The Influence of Cell Cycle Regulation on Chemotherapy. *Int J Mol Sci*. 2021;22(13):6923. doi:10.3390/ijms22136923
70. Cancer Cells and Chemotherapy - What is Chemotherapy? - Chemocare. Accessed July 18, 2023. https://chemocare.com/chemotherapy/what-is-chemotherapy/cancer-cells-chemotherapy.aspx
71. Mitchison TJ. The proliferation rate paradox in antimitotic chemotherapy. *Mol Biol Cell*. 2012;23(1):1-6. doi:10.1091/mbc.E10-04-0335
72. Matthews HK, Bertoli C, de Bruin RAM. Cell cycle control in cancer. *Nat Rev Mol Cell Biol*. 2022;23(1):74-88. doi:10.1038/s41580-021-00404-3
73. Zugazagoitia J, Guedes C, Ponce S, Ferrer I, Molina-Pinelo S, Paz-Ares L. Current Challenges in Cancer Treatment. *Clin Ther*. 2016;38(7):1551-1566. doi:10.1016/j.clinthera.2016.03.026
74. Sudhakar A. History of Cancer, Ancient and Modern Treatment Methods. *J Cancer Sci Ther*. 2009;01(02):i-iv. doi:10.4172/1948-5956.100000e2
75. Pearl LH, Schierz AC, Ward SE, Al-Lazikani B, Pearl FMG. Therapeutic opportunities within the DNA damage response. *Nat Rev Cancer*. 2015;15(3):166-180. doi:10.1038/nrc3891
76. Dasari S, Tchounwou PB. Cisplatin in cancer therapy: molecular mechanisms of action. *Eur J Pharmacol*. 2014;740:364-378. doi:10.1016/j.ejphar.2014.07.025
77. Ghosh S. Cisplatin: The first metal based anticancer drug. *Bioorganic Chem*. 2019;88:102925. doi:10.1016/j.bioorg.2019.102925
78. Babak MV, Meier SM, Huber KVM, et al. Target profiling of an antimetastatic RAPTA agent by chemical proteomics: relevance to the mode of action †Electronic supplementary information (ESI) available: Experimental, crystallographic, biological and mass spectrometric data, full list of proteins detected by chemical proteomics. CCDC 972667 and 972668. For ESI and crystallographic data in CIF or other electronic format see DOI: 10.1039/c4sc03905j Click here for additional data file. Click here for additional data file. *Chem Sci*. 2015;6(4):2449-2456. doi:10.1039/c4sc03905j
79. Arnesano F, Losacco M, Natile G. An Updated View of Cisplatin Transport. *Eur J Inorg Chem*. 2013;2013(15):2701-2711. doi:10.1002/ejic.201300001
80. Hospers GAP, Mulder NH, De Vries EGE. Mechanisms of cellular resistance to cisplatin. *Med Oncol Tumor Pharmacother*. 1988;5(3):145-151. doi:10.1007/BF02986437
81. Zou T, Lum CT, Lok CN, Zhang JJ, Che CM. Chemical biology of anticancer gold(III) and gold(I) complexes. *Chem Soc Rev*. 2015;44(24):8786-8801. doi:10.1039/C5CS00132C
82. Cadet J, Wagner JR. DNA Base Damage by Reactive Oxygen Species, Oxidizing Agents, and UV Radiation. *Cold Spring Harb Perspect Biol*. 2013;5(2):a012559. doi:10.1101/cshperspect.a012559
83. Bayr H. Reactive oxygen species. *Crit Care Med*. 2005;33(12):S498. doi:10.1097/01.CCM.0000186787.64500.12
84. Jena NR. DNA damage by reactive species: Mechanisms, mutation and repair. *J Biosci*. 2012;37(3):503-517. doi:10.1007/s12038-012-9218-2
85. Kohen R, Nyska A. Oxidation of Biological Systems: Oxidative Stress Phenomena, Antioxidants, Redox Reactions, and Methods for Their Quantification. *TOXICOLOGIC PATHOLOGY*. 2002;30(6):620-650. doi:10.1080/0192623029016672 4
86. Martemucci G, Costagliola C, Mariano M, D'andrea L, Napolitano P, D'Alessandro AG. Free Radical Properties, Source and Targets, Antioxidant Consumption and Health. *Oxygen*. 2022;2(2):48-78. doi:10.3390/oxygen2020006
87. Lobo V, Patil A, Phatak A, Chandra N. Free radicals, antioxidants and functional foods: Impact on human health. *Pharmacogn Rev*. 2010;4(8):118-126. doi:10.4103/0973-7847.70902
88. Halliwell B. Reactive Species and Antioxidants. Redox Biology Is a Fundamental Theme of Aerobic Life. *Plant Physiol*. 2006;141(2):312-322. doi:10.1104/pp.106.077073
89. Hall DB, Holmlin RE, Barton JK. Oxidative DNA damage through long-range electron transfer. *Nature*. 1996;382:731. http://dx.doi.org/10.1038/382731a0
90. Hartwell LH, Kastan MB. Cell Cycle Control and Cancer. *Science*. 1994;266(5192):1821-1828. Accessed March 23, 2023. https://www.jstor.org/stable/2885030
91. Collins K, Jacks T, Pavletich NP. The cell cycle and cancer. *Proc Natl Acad Sci U S A*. 1997;94(7):2776-2778. doi:10.1073/pnas.94.7.2776
92. Molnar C, Gair J. 6.2 The Cell Cycle. Published online May 14, 2015. Accessed March 23, 2023. https://opentextbc.ca/biology/chapter/6-2-the-cell-cycle/

93. Avendaño C, Menéndez JC. Chapter 4 - Anticancer Drugs Acting via Radical Species, Photosensitizers and Photodynamic Therapy of Cancer. In: Avendaño C, Menéndez JC, eds. *Medicinal Chemistry of Anticancer Drugs*. Elsevier; 2008:93-138. doi:10.1016/B978-0-444-52824-7.00004-4
94. Cooper GM, Hausman RE. *The Cell: A Molecular Approach*. 4th ed. ASM Press ; Sinauer Associates; 2007.
95. Weng J. Brain as an Emergent Finite Automaton: A Theory and Three Theorems. *Int J Intell Sci*. 2015;5(2):112-131. doi:10.4236/ijis.2015.52011
96. Gaillard H, García-Muse T, Aguilera A. Replication stress and cancer. *Nat Rev Cancer*. 2015;15(5):276-289. doi:10.1038/nrc3916
97. Cohen-Sharir Y, McFarland JM, Abdusamad M, et al. Aneuploidy renders cancer cells vulnerable to mitotic checkpoint inhibition. *Nature*. 2021;590(7846):486-491. doi:10.1038/s41586-020-03114-6
98. Aneuploidy renders cancer cells vulnerable to mitotic checkpoint inhibition - PMC. Accessed March 27, 2023. https://www.ncbi.nlm.nih.gov/pmc/articles/PMC8262644/
99. Pardee AB. G1 events and regulation of cell proliferation. *Science*. 1989;246(4930):603-608. doi:10.1126/science.2683075
100. Forment JV, O'Connor MJ. Targeting the replication stress response in cancer. *Pharmacol Ther*. 2018;188:155-167. doi:10.1016/j.pharmthera.2018.03.005
101. Murray AW. Recycling the Cell Cycle: Cyclins Revisited. *Cell*. 2004;116(2):221-234. doi:10.1016/S0092-8674(03)01080-8
102. Malumbres M, Barbacid M. Mammalian cyclin-dependent kinases. *Trends Biochem Sci*. 2005;30(11):630-641. doi:10.1016/j.tibs.2005.09.005
103. Sherr CJ. Cancer cell cycles. *Science*. 1996;274(5293):1672-1677. doi:10.1126/science.274.5293.1672
104. Sale JE. Translesion DNA synthesis and mutagenesis in eukaryotes. *Cold Spring Harb Perspect Biol*. 2013;5(3):a012708. doi:10.1101/cshperspect.a012708
105. Friedberg, E.C., Walker, G.C., Siede, W., Wood, R.D., Schultz, R.A. and Ellenberger, T. (2006) DNA Repair and Mutagenesis. 2nd Edition, ASM Press, Washington DC. - References - Scientific Research Publishing. Accessed March 27, 2023. https://www.scirp.org/(S(i43dyn45teexjx455qlt3d2q))/reference/ReferencesPapers.aspx?ReferenceID=1451215
106. Yao Y, Dai W. Genomic Instability and Cancer. *J Carcinog Mutagen*. 2014;5:1000165. doi:10.4172/2157-2518.1000165
107. Bonora M, Missiroli S, Perrone M, Fiorica F, Pinton P, Giorgi C. Mitochondrial Control of Genomic Instability in Cancer. *Cancers*. 2021;13(8):1914. doi:10.3390/cancers13081914
108. Vander Heiden MG, Cantley LC, Thompson CB. Understanding the Warburg Effect: The Metabolic Requirements of Cell Proliferation. *Science*. 2009;324(5930):1029-1033. doi:10.1126/science.1160809
109. Katz KA. Topical Tretinoin, Lung Cancer, and Lung-Related Mortality. *Arch Dermatol*. 2008;144(7):945-946. doi:10.1001/archderm.144.7.945
110. Sangolli PM. Does Topical Tretinoin Used for Chemoprevention Cause Increased Mortality? *J Cutan Aesthetic Surg*. 2009;2(2):101-102. doi:10.4103/0974-2077.58526
111. Singh Dhakad R, Kumar Tekade R, Kumar Jain N. Cancer Targeting Potential of Folate Targeted Nanocarrier under Comparative Influence of Tretinoin and Dexamethasone. *Curr Drug Deliv*. 2013;10(4):477-491.
112. Miller WH Jr, Schipper HM, Lee JS, Singer J, Waxman S. Mechanisms of Action of Arsenic Trioxide1. *Cancer Res*. 2002;62(14):3893-3903.
113. Introduction: The History of Arsenic Trioxide in Cancer Therapy | The Oncologist | Oxford Academic. Accessed July 17, 2023. https://academic.oup.com/oncolo/article/6/S2/1/6387658
114. Eatemadi A, Aiyelabegan HT, Negahdari B, et al. Role of protease and protease inhibitors in cancer pathogenesis and treatment. *Biomed Pharmacother*. 2017;86:221-231. doi:10.1016/j.biopha.2016.12.021
115. Yang Y, Hong H, Zhang Y, Cai W. Molecular Imaging of Proteases in Cancer. *Cancer Growth Metastasis*. 2009;2:13-27. Accessed March 31, 2023. https://www.ncbi.nlm.nih.gov/pmc/articles/PMC2838618/
116. Baranovskiy AG, Babayeva ND, Suwa Y, Gu J, Pavlov YI, Tahirov TH. Structural basis for inhibition of DNA replication by aphidicolin. *Nucleic Acids Res*. 2014;42(22):14013-14021. doi:10.1093/nar/gku1209
117. Travers A, Muskhelishvili G. DNA structure and function. *FEBS J*. 2015;282(12):2279-2295. doi:10.1111/febs.13307
118. Pingoud A, Jeltsch A, Maxwell A, Sherratt D. Enzymes that keep DNA under control. *EMBO Rep*. 2001;2(4):271-276. doi:10.1093/embo-reports/kve073
119. Drlica K, Kreiswirth B. 4-Quinolones and the Physiology of DNA Gyrase. In: Liu LF, ed. *Advances in Pharmacology*. Vol 29. DNA Topoisomerases: Biochemistry and Molecular Biology. Academic Press; 1994:263-283. doi:10.1016/S1054-3589(08)60549-9

120. Chargaff Erwin, Lipshitz Rakoma, Green Charlotte, Hodes ME. THE COMPOSITION OF THE DESOXYRIBONUCLEIC ACID OF SALMON SPERM. *J Biol Chem*. 1951;192(1):223-230. doi:10.1016/S0021-9258(18)55924-X
121. Sinden RR. *DNA Structure and Function*. Gulf Professional Publishing; 1994.
122. de Chadarevian S, Kamminga H. *Representations of the Double Helix*. Whipple Museum of the History of Science; 2002.
123. Avery OT, MacLeod CM, McCarty M. STUDIES ON THE CHEMICAL NATURE OF THE SUBSTANCE INDUCING TRANSFORMATION OF PNEUMOCOCCAL TYPES : INDUCTION OF TRANSFORMATION BY A DESOXYRIBONUCLEIC ACID FRACTION ISOLATED FROM PNEUMOCOCCUS TYPE III. *J Exp Med*. 1944;79(2):137-158. doi:10.1084/jem.79.2.137
124. Nakamura T, Zhao Y, Yamagata Y, Hua Y jin, Yang W. Watching DNA polymerase η make a phosphodiester bond. *Nature*. 2012;487(7406):196-201. doi:10.1038/nature11181
125. Dickson KS, Burns CM, Richardson JP. Determination of the Free-Energy Change for Repair of a DNA Phosphodiester Bond *. *J Biol Chem*. 2000;275(21):15828-15831. doi:10.1074/jbc.M910044199
126. Subirana JA, Soler-López M. Cations as Hydrogen Bond Donors: A View of Electrostatic Interactions in DNA. *Annu Rev Biophys Biomol Struct*. 2003;32(1):27-45. doi:10.1146/annurev.biophys.32.110601.141726
127. Turel I, Kljun J. Interactions of metal ions with DNA, its constituents and derivatives, which may be relevant for anticancer research. *Curr Top Med Chem*. 2011;11(21):2661-2687. doi:10.2174/156802611798040787
128. Harteis S, Schneider S. Making the Bend: DNA Tertiary Structure and Protein-DNA Interactions. *Int J Mol Sci*. 2014;15(7):12335-12363. doi:10.3390/ijms150712335
129. Alberts B, Johnson A, Lewis J, Raff M, Roberts K, Walter P. DNA-Binding Motifs in Gene Regulatory Proteins. In: *Molecular Biology of the Cell. 4th Edition*. Garland Science; 2002. Accessed July 24, 2023. https://www.ncbi.nlm.nih.gov/books/NBK26806/
130. Chiu TP, Rao S, Mann RS, Honig B, Rohs R. Genome-wide prediction of minor-groove electrostatic potential enables biophysical modeling of protein–DNA binding. *Nucleic Acids Res*. 2017;45(21):12565-12576. doi:10.1093/nar/gkx915
131. Ma N, van der Vaart A. Anisotropy of B-DNA Groove Bending. *J Am Chem Soc*. 2016;138(31):9951-9958. doi:10.1021/jacs.6b05136
132. Todd AK, Adams A, Thorpe JH, Denny WA, Wakelin LP, Cardin CJ. Major groove binding and “DNA-induced” fit in the intercalation of a derivative of the mixed topoisomerase I/II poison N-(2-(dimethylamino)ethyl)acridine-4-carboxamide (DACA) into DNA: X-ray structure complexed to d(CG(5-BrU)ACG)2 at 1.3-A resolution. *J Med Chem*. 1999;42(4):536-540. doi:10.1021/jm980479u
133. Morávek Z, Neidle S, Schneider B. Protein and drug interactions in the minor groove of DNA. *Nucleic Acids Res*. 2002;30(5):1182-1191. Accessed July 20, 2023. https://www.ncbi.nlm.nih.gov/pmc/articles/PMC101234/
134. Wemmer DE, Dervan PB. Targeting the minor groove of DNA. *Curr Opin Struct Biol*. 1997;7(3):355-361. doi:10.1016/S0959-440X(97)80051-6
135. Tabernero L, Bella J, Alemán C. Hydrogen bond geometry in DNA-minor groove binding drug complexes. *Nucleic Acids Res*. 1996;24(17):3458-3466. doi:10.1093/nar/24.17.3458
136. Řeha D, Kabeláč M, Ryjáček F, et al. Intercalators. 1. Nature of Stacking Interactions between Intercalators (Ethidium, Daunomycin, Ellipticine, and 4‘,6-Diaminide-2-phenylindole) and DNA Base Pairs. Ab Initio Quantum Chemical, Density Functional Theory, and Empirical Potential Study. *J Am Chem Soc*. 2002;124(13):3366-3376. doi:10.1021/ja011490d
137. Kellett A, Molphy Z, Slator C, McKee V, Farrell NP. Molecular methods for assessment of non-covalent metallodrug–DNA interactions. *Chem Soc Rev*. 2019;48(4):971-988. doi:10.1039/C8CS00157J
138. Li S, Cooper VR, Thonhauser T, Lundqvist BI, Langreth DC. Stacking Interactions and DNA Intercalation. *J Phys Chem B*. 2009;113(32):11166-11172. doi:10.1021/jp905765c
139. Neto BAD, Lapis AAM. Recent Developments in the Chemistry of Deoxyribonucleic Acid (DNA) Intercalators: Principles, Design, Synthesis, Applications and Trends. *Molecules*. 2009;14(5):1725-1746. doi:10.3390/molecules14051725
140. Casini A, Kelter G, Gabbiani C, et al. Chemistry, antiproliferative properties, tumor selectivity, and molecular mechanisms of novel gold(III) compounds for cancer treatment: a systematic study. *JBIC J Biol Inorg Chem*. 2009;14(7):1139-1149. doi:10.1007/s00775-009-0558-9
141. Murphy CJ, Arkin MR, Jenkins Y, et al. Long-Range Photoinduced Electron Transfer Through a DNA Helix. *Science*. 1993;262(5136):1025-1029. doi:10.1126/science.7802858
142. Sugiura Y, Shiraki T, Konishi M, Oki T. DNA intercalation and cleavage of an antitumor antibiotic dynemicin that contains anthracycline and enediyne cores. *Proc Natl Acad Sci*. 1990;87(10):3831-3835. doi:10.1073/pnas.87.10.3831

143. Neidle S. Crystallographic insights into DNA minor groove recognition by drugs. *Biopolymers*. 1997;44(1):105-121. doi:10.1002/(SICI)1097-0282(1997)44:1<105::AID-BIP7>3.0.CO;2-Z
144. Shim EJ, Przybylski JL, Wetmore SD. Effects of Nucleophile, Oxidative Damage, and Nucleobase Orientation on the Glycosidic Bond Cleavage in Deoxyguanosine. *J Phys Chem B*. 2010;114(6):2319-2326. doi:10.1021/jp9113656
145. Breugst M, Corral Bautista F, Mayr H. Nucleophilic Reactivities of the Anions of Nucleobases and Their Subunits. *Chem – Eur J*. 2012;18(1):127-137. doi:10.1002/chem.201102411
146. Stone MP, Huang H, Brown KL, Shanmugam G. Chemistry and Structural Biology of DNA Damage and Biological Consequences. *Chem Biodivers*. 2011;8(9):1571-1615. doi:10.1002/cbdv.201100033
147. Enoch SJ, Cronin MTD. A review of the electrophilic reaction chemistry involved in covalent DNA binding. *Crit Rev Toxicol*. 2010;40(8):728-748. doi:10.3109/10408444.2010.494175
148. Stachowicz-Kuśnierz A, Korchowiec J. Nucleophilic properties of purine bases: inherent reactivity versus reaction conditions. *Struct Chem*. 2016;27(2):543-555. doi:10.1007/s11224-015-0583-y
149. Chen AY, Yu C, Gatto B, Liu LF. DNA minor groove-binding ligands: a different class of mammalian DNA topoisomerase I inhibitors. *Proc Natl Acad Sci U S A*. 1993;90(17):8131-8135. Accessed July 18, 2023. https://www.ncbi.nlm.nih.gov/pmc/articles/PMC47302/
150. Shultz PG, Taylor JS, Dervan PB. Design synthesis of a sequence-specific DNA cleaving molecule. (Distamycin-EDTA)iron(II). *J Am Chem Soc*. 1982;104(24):6861-6863. doi:10.1021/ja00388a101
151. Bailly C, Chaires JB. Sequence-Specific DNA Minor Groove Binders. Design and Synthesis of Netropsin and Distamycin Analogues. *Bioconjug Chem*. 1998;9(5):513-538. doi:10.1021/bc980008m
152. Bonfanti M, La Valle E, Fernandez Sousa Faro J, et al. Effect of ecteinascidin-743 on the interaction between DNA binding proteins and DNA. *Anticancer Drug Des*. 1999;14(3):179-186.
153. Jin S, Gorfajn B, Faircloth G, Scotto KW. Ecteinascidin 743, a transcription-targeted chemotherapeutic that inhibits MDR1 activation. *Proc Natl Acad Sci U S A*. 2000;97(12):6775-6779. Accessed July 18, 2023. https://www.ncbi.nlm.nih.gov/pmc/articles/PMC18735/
154. Fridman AS, Brabec V, Haroutiunian SG, Wartell RM, Lando DY. Melting of Cross-Linked DNA V. Cross-Linking Effect Caused by Local Stabilization of the Double Helix. *J Biomol Struct Dyn*. 2003;20(4):533-545. doi:10.1080/07391102.2003.10506870
155. Zhu Y, Wang Y, Chen G. Differences in conformational dynamics of [Pt3(HPTAB)]6+–DNA adducts with various cross-linking modes. *Nucleic Acids Res*. 2009;37(17):5930-5942. doi:10.1093/nar/gkp618
156. Stehlikova K, Kostrhunova H, Kasparkova J, Brabec V. DNA bending and unwinding due to the major 1,2-GG intrastrand cross-link formed by antitumor cis-diamminedichloroplatinum(II) are flanking-base independent. *Nucleic Acids Res*. 2002;30(13):2894-2898. Accessed July 24, 2023. https://www.ncbi.nlm.nih.gov/pmc/articles/PMC117060/
157. Westhuizen D van der, Bezuidenhout DI, Munro OQ. Cancer molecular biology and strategies for the design of cytotoxic gold(I) and gold(III) complexes: a tutorial review. *Dalton Trans*. 2021;50(47):17413-17437. doi:10.1039/D1DT02783B
158. Siddik ZH. Mechanisms of Action of Cancer Chemotherapeutic Agents: DNA-Interactive Alkylating Agents and Antitumour Platinum-Based Drugs. In: Alison MR, ed. *The Cancer Handbook*. John Wiley & Sons, Ltd; 2005:chap84b. doi:10.1002/0470025077.chap84b
159. Ahmad MA, Aung Y yu, Widati AA, et al. A Perspective on Using Organic Molecules Composing Carbon Dots for Cancer Treatment. *Nanotheranostics*. 2023;7(2):187-201. doi:10.7150/ntno.80076
160. Demain AL, Vaishnav P. Natural products for cancer chemotherapy. *Microb Biotechnol*. 2011;4(6):687-699. doi:10.1111/j.1751-7915.2010.00221.x
161. González-Ballesteros MM, Mejía C, Ruiz-Azuara L. Metallodrugs: an approach against invasion and metastasis in cancer treatment. *FEBS Open Bio*. 2022;12(5):880-899. doi:10.1002/2211-5463.13381
162. Mjos KD, Orvig C. Metallodrugs in Medicinal Inorganic Chemistry. *Chem Rev*. 2014;114(8):4540-4563. doi:10.1021/cr400460s
163. Abdou HE, Mohamed AA, Fackler JP, et al. Structures and properties of gold(I) complexes of interest in biochemical applications. *Coord Chem Rev*. 2009;253(11):1661-1669. doi:10.1016/j.ccr.2009.02.010
164. Kean WF, Hart L, Buchanan WW. Auranofin. *Rheumatology*. 1997;36(5):560-572. doi:10.1093/rheumatology/36.5.560
165. Calamai P, Carotti S, Guerri A, et al. Cytotoxic effects of gold(III) complexes on established human tumor cell lines sensitive and resistant to cisplatin. *Anticancer Drug Des*. 1998;13(1):67-80.
166. Gelasco A, Lippard SJ. Anticancer Activity of Cisplatin and Related Complexes. In: Clarke MJ, Sadler PJ, eds. *Metallopharmaceuticals I: DNA Interactions*. Topics in Biological Inorganic Chemistry. Springer; 1999:1-43. doi:10.1007/978-3-662-03815-4_1

167. Haas KL, Franz KJ. Application of metal coordination chemistry to explore and manipulate cell biology. *Chem Rev*. 2009;109(10):4921-4960. doi:10.1021/cr900134a
168. Frezza M, Hindo S, Chen D, et al. Novel metals and metal complexes as platforms for cancer therapy. *Curr Pharm Des*. 2010;16(16):1813-1825. doi:10.2174/138161210791209009
169. Yan YK, Melchart M, Habtemariam A, Sadler PJ. Organometallic chemistry, biology and medicine: ruthenium arene anticancer complexes. *Chem Commun Camb Engl*. 2005;(38):4764-4776. doi:10.1039/b508531b
170. Salga MS, Ali HM, Abdulla MA, Abdelwahab SI. Acute oral toxicity evaluations of some zinc(II) complexes derived from 1-(2-salicylaldiminoethyl)piperazine Schiff bases in rats. *Int J Mol Sci*. 2012;13(2):1393-1404. doi:10.3390/ijms13021393
171. Ndagi U, Mhlongo N, Soliman ME. Metal complexes in cancer therapy – an update from drug design perspective. *Drug Des Devel Ther*. 2017;11:599-616. doi:10.2147/DDDT.S119488
172. Messori L, Merlino A. Cisplatin binding to proteins: A structural perspective. *Coord Chem Rev*. 2016;315:67-89. doi:10.1016/j.ccr.2016.01.010
173. van der Westhuizen D, Slabber CA, Fernandes MA, et al. A Cytotoxic Bis(1,2,3-triazol-5-ylidene)carbazolide Gold(III) Complex Targets DNA by Partial Intercalation. *Chem – Eur J*. 2021;27(32):8295-8307. doi:10.1002/chem.202100598
174. Alderden RA, Hall MD, Hambley TW. The Discovery and Development of Cisplatin. *J Chem Educ*. 2006;83(5):728. doi:10.1021/ed083p728
175. Prestayko AW, D'Aoust JC, Issell BF, Crooke ST. Cisplatin (cis-diamminedichloroplatinum II). *Cancer Treat Rev*. 1979;6(1):17-39. doi:10.1016/S0305-7372(79)80057-2
176. Alcindor T, Beauger N. Oxaliplatin: a review in the era of molecularly targeted therapy. *Curr Oncol*. 2011;18(1):18-25. Accessed July 25, 2023. https://www.ncbi.nlm.nih.gov/pmc/articles/PMC3031353/
177. Wagstaff AJ, Ward A, Benfield P, Heel RC. Carboplatin. *Drugs*. 1989;37(2):162-190. doi:10.2165/00003495-198937020-00005
178. Messori L, Marcon G. Gold complexes as antitumor agents. *Met Ions Biol Syst*. 2004;42:385-424.
179. Bertrand B, Williams MRM, Bochmann M. Gold(III) Complexes for Antitumor Applications: An Overview. *Chem – Eur J*. 2018;24(46):11840-11851. doi:10.1002/chem.201800981
180. Koch E, Fischer W. Normalizers of space groups: A useful tool in crystal-structure description, comparison and determination. *Z Für Krist - Cryst Mater*. 2006;221(1):1-14. doi:10.1524/zkri.2006.221.1.1
181. Shaw RJ, Kosmatka M, Bardeesy N, et al. The tumor suppressor LKB1 kinase directly activates AMP-activated kinase and regulates apoptosis in response to energy stress. *Proc Natl Acad Sci*. 2004;101(10):3329-3335. doi:10.1073/pnas.0308061100
182. Rocchigiani L, Bochmann M. Recent Advances in Gold(III) Chemistry: Structure, Bonding, Reactivity, and Role in Homogeneous Catalysis. *Chem Rev*. 2021;121(14):8364-8451. doi:10.1021/acs.chemrev.0c00552
183. Roşca DA, Wright JA, Bochmann M. An element through the looking glass: exploring the Au–C, Au–H and Au–O energy landscape. *Dalton Trans*. 2015;44(48):20785-20807. doi:10.1039/C5DT03930D
184. Leyva-Pérez A, Corma A. Similarities and Differences between the "Relativistic" Triad Gold, Platinum, and Mercury in Catalysis. *Angew Chem Int Ed*. 2012;51(3):614-635. doi:10.1002/anie.201101726
185. Schwerdtfeger P, Boyd PDW, Brienne S, Burrell AK. Relativistic effects in gold chemistry. 4. Gold(III) and gold(V) compounds. *Inorg Chem*. 1992;31(16):3411-3422. doi:10.1021/ic00042a016
186. Pérez-Bitrián A, Baya M, Casas JM, Martín A, Menjón B, Orduna J. An Organogold(III) Difluoride with a trans Arrangement. *Angew Chem Int Ed*. 2018;57(22):6517-6521. doi:10.1002/anie.201802379
187. Harrach G, Valicsek Z, Horváth O. Water-soluble silver(II) and gold(III) porphyrins: The effect of structural distortion on the photophysical and photochemical behavior. *Inorg Chem Commun*. 2011;14(11):1756-1761. doi:10.1016/j.inoche.2011.08.003
188. Fürstner A, Davies PW. Catalytic Carbophilic Activation: Catalysis by Platinum and Gold π Acids. *Angew Chem Int Ed*. 2007;46(19):3410-3449. doi:10.1002/anie.200604335
189. Gaudet J, Bondo KK, Song Z, et al. Effect of gold oxidation state on the epoxidation and hydrogenation of propylene on Au/TS-1. *J Catal*. 2011;280(1):40-49. doi:10.1016/j.jcat.2011.03.001
190. Johnson MW, DiPasquale AG, Bergman RG, Toste FD. Synthesis of Stable Gold(III) Pincer Complexes with Anionic Heteroatom Donors. *Organometallics*. 2014;33(16):4169-4172. doi:10.1021/om500663m
191. Messori L, Marcon G, Orioli P. Gold(III) compounds as new family of anticancer drugs. *Bioinorg Chem Appl*. 2003;1(2):177-187. doi:10.1155/S1565363303000141
192. Serra J, Font P, Sosa Carrizo ED, et al. Cyclometalated gold(iii) complexes: noticeable differences between (N,C) and (P,C) ligands in migratory insertion †Electronic supplementary information (ESI) available: Detailed experimental conditions and procedures, analytical data, theoretical details (PDF), crystallographic data for compounds 5A-H2O and 5A-Cl, and DFT optimized structures (XYZ). CCDC 1574199 and 1574200. For ESI

and crystallographic data in CIF or other electronic format see DOI: 10.1039/c7sc04899h. *Chem Sci*. 2018;9(16):3932-3940. doi:10.1039/c7sc04899h
193. Roth T, Wadepohl H, Gade LH. Cationic BPI-Gold(III) Complexes: Controlling Ligating and Nonligating Anions. *Eur J Inorg Chem*. 2016;2016(8):1184-1191. doi:10.1002/ejic.201600024
194. Schmidbaur H. Metallo-Drugs: Development and Action of Anticancer Agents. *Z Für Naturforschung B*. 2018;73(5):355-357. doi:10.1515/znb-2018-0036
195. Bertrand B, Bochmann M, Fernandez-Cestau J, Rocchigiani L. Chapter 31 - Pincer Complexes of Gold: An Overview of Synthesis, Reactivity, Photoluminescence, and Biological Applications. In: Morales-Morales D, ed. *Pincer Compounds*. Elsevier; 2018:673-699. doi:10.1016/B978-0-12-812931-9.00031-1
196. Che CM, Sun RWY, Yu WY, Ko CB, Zhu N, Sun H. Gold (III) porphyrins as a new class of anticancer drugs: cytotoxicity, DNA binding and induction of apoptosis in human cervix epitheloid cancer cells. *Chem Commun*. 2003;(14):1718-1719.
197. Teo RD, Gray HB, Lim P, Termini J, Domeshek E, Gross Z. A cytotoxic and cytostatic gold(III) corrole. *Chem Commun*. 2014;50(89):13789-13792. doi:10.1039/C4CC06577H
198. Rabinovich E, Goldberg I, Gross Z. Gold(I) and Gold(III) Corroles. *Chem – Eur J*. 2011;17(44):12294-12301. doi:10.1002/chem.201102348
199. Kimura E, Kurogi Y, Koike T, Shionoya M, Iitaka Y. GOLD(III)-CYCLAM COMPLEXES. X-RAY CRYSTAL STRUCTURE AND A USEFUL MACROCYCLIC EFFECT ON THE REDUCTION OF GOLD(III). *J Coord Chem*. Published online September 23, 2006. doi:10.1080/00958979308035142
200. Messori L, Orioli P, Tempi C, Marcon G. Interactions of Selected Gold(III) Complexes with Calf Thymus DNA. *Biochem Biophys Res Commun*. 2001;281(2):352-360. doi:10.1006/bbrc.2001.4358
201. Kostova I, Publishers BS. Gold Coordination Complexes as Anticancer Agents. *Anticancer Agents Med Chem*. 6(1):19-32. Accessed July 25, 2023. https://www.eurekaselect.com/article/3
202. Wang JC. Cellular roles of DNA topoisomerases: a molecular perspective. *Nat Rev Mol Cell Biol*. 2002;3(6):430-440. doi:10.1038/nrm831
203. Yang Y, Guo Y, Xia S, Ma X, Wu X. Synthesis, Structure, and Properties of Complexes Based on 2,4-Bis-(triazol-1-yl)benzoic Acid as a Ligand. *ACS Omega*. 2022;7(22):18276-18291. doi:10.1021/acsomega.1c07351
204. Kuznetsova A, Matveevskaya V, Pavlov D, Yakunenkov A, Potapov A. Coordination Polymers Based on Highly Emissive Ligands: Synthesis and Functional Properties. *Materials*. 2020;13(12):2699. doi:10.3390/ma13122699
205. Henderson I. Tuning the Properties of Metal-Ligand Complexes to Modify the Properties of Supramolecular Materials. *Open Access Diss*. Published online May 1, 2012. doi:https://doi.org/10.7275/w9wa-k694
206. Oulmidi A, Radi S, Idir A, et al. Synthesis and cytotoxicity against tumor cells of pincer N-heterocyclic ligands and their transition metal complexes. *RSC Adv*. 11(55):34742-34753. doi:10.1039/d1ra05918a
207. Arsenijević N, Volarevic V, Milovanovic M, Bugarčić ŽD. Gold(III) Complexes, Cytotoxic Effects. In: Kretsinger RH, Uversky VN, Permyakov EA, eds. *Encyclopedia of Metalloproteins*. Springer; 2013:922-927. doi:10.1007/978-1-4614-1533-6_564
208. Radisavljević S, Bratsos I, Scheurer A, et al. New gold pincer-type complexes: synthesis, characterization, DNA binding studies and cytotoxicity. *Dalton Trans*. 2018;47(38):13696-13712. doi:10.1039/C8DT02903B
209. Radisavljević S, Petrović B. Gold(III) Complexes: An Overview on Their Kinetics, Interactions With DNA/BSA, Cytotoxic Activity, and Computational Calculations. *Front Chem*. 2020;8:379. doi:10.3389/fchem.2020.00379
210. Lawrence MA, Green KA, Nelson PN, Lorraine SC. Pincer ligands—Tunable, versatile and applicable. *Polyhedron*. 2018;143:11-27.
211. Peris E, Crabtree RH. Key factors in pincer ligand design. *Chem Soc Rev*. 2018;47(6):1959-1968.
212. Niedbała P, Jurczak J. A new class of “pincer” receptors – macrocyclic systems containing an incorporated amide group. *J Coord Chem*. 2021;74(1-3):424-432. doi:10.1080/00958972.2020.1867313
213. Kang SO, Johnson TS, Day VW, Bowman-James K. Pyridine-2,6-dicarboxamide pincer-based macrocycle: a versatile ligand for oxoanions, oxometallates, and transition metals. *Supramol Chem*. 2018;30(4):305-314. doi:10.1080/10610278.2017.1361534
214. Kasera A, Biswas JP, Ali Alshehri A, Ahmed Al-Thabaiti S, Mokhtar M, Maiti D. Transition metal pincer complexes: A series of potential catalysts in CH activation reactions. *Coord Chem Rev*. 2023;475:214915. doi:10.1016/j.ccr.2022.214915
215. Choi J, MacArthur AHR, Brookhart M, Goldman AS. Dehydrogenation and Related Reactions Catalyzed by Iridium Pincer Complexes. *Chem Rev*. 2011;111(3):1761-1779. doi:10.1021/cr1003503
216. Wolters LP, Koekkoek R, Bickelhaupt FM. Role of Steric Attraction and Bite-Angle Flexibility in Metal-Mediated C–H Bond Activation. *ACS Catal*. 2015;5(10):5766-5775. doi:10.1021/acscatal.5b01354

217. Esfandiari M, Havaei G, Zahiri S, Mohammadnezhad G. Pincer complex immobilization onto different supports: Strategies and applications. *Coord Chem Rev*. 2022;472:214778. doi:10.1016/j.ccr.2022.214778
218. Moriuchi T, Bandoh S, Miyaji Y, Hirao T. A novel heterobimetallic complex composed of the imide-bridged [3]ferrocenophane and the tridentate palladium(II) complex. *J Organomet Chem*. 2000;599(2):135-142. doi:10.1016/S0022-328X(99)00748-2
219. Sengupta A, Seitz A, Merz KMJr. Simulating the Chelate Effect. *J Am Chem Soc*. 2018;140(45):15166-15169. doi:10.1021/jacs.8b09371
220. Yang YF, Chen G, Hong X, Yu JQ, Houk KN. The Origins of Dramatic Differences in Five-Membered vs Six-Membered Chelation of Pd(II) on Efficiency of C(sp3)–H Bond Activation. *J Am Chem Soc*. 2017;139(25):8514-8521. doi:10.1021/jacs.7b01801
221. Omae I. Applications of Cyclometalation Five-Membered Ring Products and Intermediates as Catalytic Agents. *Mod Res Catal*. 2016;5(3):51-74. doi:10.4236/mrc.2016.53006
222. Seifert S, Schmidt D, Shoyama K, Würthner F. Base-Selective Five- versus Six-Membered Ring Annulation in Palladium-Catalyzed C–C Coupling Cascade Reactions: New Access to Electron-Poor Polycyclic Aromatic Dicarboximides. *Angew Chem Int Ed*. 2017;56(26):7595-7600. doi:10.1002/anie.201702889
223. Cattalini L, Cassol A, Marangoni G, Rizzardi G, Rotondo E. The relative stability of five and six-membered chelate rings in palladium(II) complexes containing bidentate thioethers. *Inorganica Chim Acta*. 1969;3:681-684. doi:10.1016/S0020-1693(00)92577-5
224. Hiratani K, Taguchi K. 2,6-Bis[N-(8-quinolyl)carbamoyl]pyridine as a Highly Selective Extractant for Cu(II). *Bull Chem Soc Jpn*. 1990;63(11):3331-3333. doi:10.1246/bcsj.63.3331
225. Babcock WC, Baker RW, Lachapelle ED, Smith KL. Coupled transport membranes II: The mechanism of uranium transport with a tertiary amine. *J Membr Sci*. 1980;7(1):71-87. doi:10.1016/S0376-7388(00)83186-5
226. Costero AM, José Bañuls M, José Aurell M, Ward MD, Argent S. Biphenyl macrolactams in anion complexation. Selective naked-eye fluoride recognition. *Tetrahedron*. 2004;60(42):9471-9478. doi:10.1016/j.tet.2004.07.088
227. Dorazco-González A, Höpfl H, Medrano F, Yatsimirsky AK. Recognition of anions and neutral guests by dicationic pyridine-2, 6-dicarboxamide receptors. *J Org Chem*. 2010;75(7):2259-2273.
228. Roy M, Berezhnaia V, Villa M, et al. Stereoselective Syntheses, Structures, and Properties of Extremely Distorted Chiral Nanographenes Embedding Hextuple Helicenes. *Angew Chem Int Ed*. 2020;59(8):3264-3271. doi:10.1002/anie.201913200
229. Jeletic MS, Lower CE, Ghiviriga I, Veige AS. Chemical Exchange Saturation Transfer (CEST) as a Tool to Measure Ligand Flexibility of Chelating Chiral Di-N-heterocyclic Carbene Complexes. *Organometallics*. 2011;30(21):6034-6043. doi:10.1021/om200913c
230. Choi K, Hamilton AD. Macrocyclic anion receptors based on directed hydrogen bonding interactions. *Coord Chem Rev*. 2003;240(1-2):101-110. doi:10.1016/S0010-8545(02)00305-3
231. Yamnitz CR, Negin S, Carasel IA, Winter RK, Gokel GW. Dianilides of dipicolinic acid function as synthetic chloride channels. *Chem Commun*. 2010;46(16):2838-2840.
232. Gu S, Nielsen RJ, Taylor KH, et al. Use of Ligand Steric Properties to Control the Thermodynamics and Kinetics of Oxidative Addition and Reductive Elimination with Pincer-Ligated Rh Complexes. *Organometallics*. 2020;39(10):1917-1933. doi:10.1021/acs.organomet.0c00122
233. Moulton CJ, Shaw BL. Transition metal–carbon bonds. Part XLII. Complexes of nickel, palladium, platinum, rhodium and iridium with the tridentate ligand 2, 6-bis [(di-t-butylphosphino) methyl] phenyl. *J Chem Soc Dalton Trans*. 1976;(11):1020-1024.
234. A. Danopoulos A, D. Tulloch AA, Winston S, Eastham G, B. Hursthouse M. Chelating and 'pincer' dicarbene complexes of palladium; synthesis and structural studies. *Dalton Trans*. 2003;0(5):1009-1015. doi:10.1039/B209739G
235. Jeffrey JC, Rauchfuss TB. Metal complexes of hemilabile ligands. Reactivity and structure of dichlorobis(o-(diphenylphosphino)anisole)ruthenium(II). *Inorg Chem*. 1979;18(10):2658-2666. doi:10.1021/ic50200a004
236. Miecznikowski JR, Gründemann S, Albrecht M, et al. Outer sphere anion participation can modify the mechanism for conformer interconversion in Pd pincer complexes. *Dalton Trans*. 2003;(5):831-838. doi:10.1039/B210784H
237. Roddick DM. Tuning of PCP Pincer Ligand Electronic and Steric Properties. In: van Koten G, Milstein D, eds. *Organometallic Pincer Chemistry*. Topics in Organometallic Chemistry. Springer; 2013:49-88. doi:10.1007/978-3-642-31081-2_3
238. Singh V, Singh R, Hazari AS, Adhikari D. Unexplored Facet of Pincer Ligands: Super-Reductant Behavior Applied to Transition-Metal-Free Catalysis. *JACS Au*. 2023;3(4):1213-1220. doi:10.1021/jacsau.3c00077

239. Hosokawa T, Asada T, Kamikawa K. Theoretical Examination of the Plausible Reaction Process for Stereoselective Synthesis of Hexapole Helicene via a Palladium-Catalyzed [2 + 2 + 2] Cyclotrimerization of [5]Helicenyl Aryne. *J Phys Chem A*. 2020;124(4):652-661. doi:10.1021/acs.jpca.9b09533
240. Olazábal CA, Gabbaï FP, Cowley AH, Carrano CJ, Mokry LM, Bond MR. Intramolecular Base Stabilization of Cobalt–Gallium and Cobalt–Indium Compounds. *Organometallics*. 1994;13(2):421-423. doi:10.1021/om00014a008
241. Mancano G, Page MJ, Bhadbhade M, Messerle BA. Hemilabile and bimetallic coordination in Rh and Ir complexes of NCN pincer ligands. *Inorg Chem*. 2014;53(19):10159-10170. doi:10.1021/ic501158x
242. Keskin E, Arslan H. Palladium complexes containing NNN pincer type ligands and their activities in Suzuki-Miyaura cross coupling reaction. *Heliyon*. 2023;9(7):e17608. doi:10.1016/j.heliyon.2023.e17608
243. Shinde VN, Bhuvanesh N, Kumar A, Joshi H. Design and Syntheses of Palladium Complexes of NNN/CNN Pincer Ligands: Catalyst for Cross Dehydrogenative Coupling Reaction of Heteroarenes. *Organometallics*. 2020;39(2):324-333. doi:10.1021/acs.organomet.9b00695
244. Wang B, Howard IG, Pope JW, Conte ED, Deng Y. Bis(imino)pyridine iron complexes for catalytic carbene transfer reactions. *Chem Sci*. 2019;10(34):7958-7963. doi:10.1039/C9SC02189B
245. Mahesh S, Tang KC, Raj M. Amide Bond Activation of Biological Molecules. *Mol J Synth Chem Nat Prod Chem*. 2018;23(10):2615. doi:10.3390/molecules23102615
246. Li H, Goldstein BM. Carboxamide group conformation in the nicotinamide and thiazole-4-carboxamide rings: implications for enzyme binding. *J Med Chem*. 1992;35(19):3560-3567. doi:10.1021/jm00097a013
247. Lowe PR, Sansom CE, Schwalbe CH, Stevens MFG, Clark AS. Antitumor imidazotetrazines. 25. Crystal structure of 8-carbamoyl-3-methylimidazo[5,1-d]-1,2,3,5-tetrazin-4(3H)-one (temozolomide) and structural comparisons with the related drugs mitozolomide and DTIC. *J Med Chem*. 1992;35(18):3377-3382. doi:10.1021/jm00096a013
248. Peek ME, Lipscomb LA, Haseltine J, et al. Asymmetry and dynamics in bis-intercalated DNA. *Bioorg Med Chem*. 1995;3(6):693-699. doi:10.1016/0968-0896(95)00064-N
249. Clayden J, Greeves N, Warren S. *Organic Chemistry*. OUP Oxford; 2012.
250. Ouellette RJ, Rawn JD. 22 - Carboxylic Acid Derivatives. In: Ouellette RJ, Rawn JD, eds. *Organic Chemistry (Second Edition)*. Academic Press; 2018:665-710. doi:10.1016/B978-0-12-812838-1.50022-0
251. Lanigan RM, Sheppard TD. Recent Developments in Amide Synthesis: Direct Amidation of Carboxylic Acids and Transamidation Reactions. *Eur J Org Chem*. 2013;2013(33):7453-7465. doi:10.1002/ejoc.201300573
252. Pauling L, Corey RB, Branson HR. The Structure of Proteins. *Proc Natl Acad Sci U S A*. 1951;37(4):205-211. Accessed July 22, 2022. https://www.ncbi.nlm.nih.gov/pmc/articles/PMC1063337/
253. Edison AS. Linus Pauling and the planar peptide bond. *Nat Struct Biol*. 2001;8(3):201-202. doi:10.1038/84921
254. Das J, Chen P, Norris D, et al. 2-Aminothiazole as a Novel Kinase Inhibitor Template. Structure−Activity Relationship Studies toward the Discovery of N-(2-Chloro-6-methylphenyl)-2-[[6-[4-(2-hydroxyethyl)-1-piperazinyl)]-2-methyl-4-pyrimidinyl]amino)]-1,3-thiazole-5-carboxamide (Dasatinib, BMS-354825) as a Potent pan-Src Kinase Inhibitor. *J Med Chem*. 2006;49(23):6819-6832. doi:10.1021/jm060727j
255. Steinberg M. Dasatinib: A tyrosine kinase inhibitor for the treatment of chronic myelogenous leukemia and philadelphia chromosome—positive acute lymphoblastic leukemia. *Clin Ther*. 2007;29(11):2289-2308. doi:10.1016/j.clinthera.2007.11.005
256. Talpaz M, Shah NP, Kantarjian H, et al. Dasatinib in Imatinib-Resistant Philadelphia Chromosome–Positive Leukemias. *N Engl J Med*. 2006;354(24):2531-2541. doi:10.1056/NEJMoa055229
257. Parsons SJ, Parsons JT. Src family kinases, key regulators of signal transduction. *Oncogene*. 2004;23(48):7906-7909. doi:10.1038/sj.onc.1208160
258. Ortiz MA, Mikhailova T, Li X, Porter BA, Bah A, Kotula L. Src family kinases, adaptor proteins and the actin cytoskeleton in epithelial-to-mesenchymal transition. *Cell Commun Signal*. 2021;19(1):67. doi:10.1186/s12964-021-00750-x
259. Roskoski R. Src protein-tyrosine kinase structure and regulation. *Biochem Biophys Res Commun*. 2004;324(4):1155-1164. doi:10.1016/j.bbrc.2004.09.171
260. European Organisation for Research and Treatment of Cancer - EORTC. *Open Label Phase II Study on XR5000 Administered as a 5 Day Infusion in Advanced Non Small Cell Lung Cancer*. clinicaltrials.gov; 2012. Accessed July 16, 2023. https://clinicaltrials.gov/study/NCT00004151
261. Murray V, Chen JK, Galea AM. The potential of acridine carboxamide Pt complexes as anticancer agents : a review. *Anticancer Agents Med Chem*. 2014;14(5):695-705. doi:10.2174/1871520613136660361
262. NCI Thesaurus. Accessed February 6, 2023. https://ncithesaurus.nci.nih.gov/ncitbrowser/ConceptReport.jsp?dictionary=NCI_Thesaurus&ns=ncit&code=C2203

263. PubChem. Acridine Carboxamide. Accessed February 6, 2023. https://pubchem.ncbi.nlm.nih.gov/substance/347828217
264. PubChem. CID 5351166. Accessed February 6, 2023. https://pubchem.ncbi.nlm.nih.gov/compound/5351166
265. Al-Badr AA, Alodhaib MM. Chapter Four - Dacarbazine. In: Brittain HG, ed. *Profiles of Drug Substances, Excipients and Related Methodology*. Vol 41. Academic Press; 2016:323-377. doi:10.1016/bs.podrm.2015.12.002
266. Ahmad I, Ahmad M. Dacarbazine as a minor groove binder of DNA: Spectroscopic, biophysical and molecular docking studies. *Int J Biol Macromol*. 2015;79:193-200. doi:10.1016/j.ijbiomac.2015.04.055
267. Martindale W, Reynolds JEF. *Martindale: The Extra Pharmacopoeia*. 31st ed. Royal Pharmaceutical Society; 1996.
268. Smith CD, Maines LW, Keller SN, et al. Recent Progress in the Development of Opaganib for the Treatment of Covid-19. *Drug Des Devel Ther*. 2022;16:2199-2211. doi:10.2147/DDDT.S367612
269. Opaganib. Accessed February 6, 2023. https://go.drugbank.com/drugs/DB12764
270. Schrecengost RS, Keller SN, Schiewer MJ, Knudsen KE, Smith CD. Downregulation of Critical Oncogenes by the Selective SK2 Inhibitor ABC294640 Hinders Prostate Cancer Progression. *Mol Cancer Res MCR*. 2015;13(12):1591-1601. doi:10.1158/1541-7786.MCR-14-0626
271. Ding X, Chaiteerakij R, Moser CD, et al. Antitumor effect of the novel sphingosine kinase 2 inhibitor ABC294640 is enhanced by inhibition of autophagy and by sorafenib in human cholangiocarcinoma cells. *Oncotarget*. 2016;7(15):20080-20092. doi:10.18632/oncotarget.7914
272. Venant H, Rahmaniyan M, Jones EE, et al. The Sphingosine Kinase 2 Inhibitor ABC294640 Reduces the Growth of Prostate Cancer Cells and Results in Accumulation of Dihydroceramides *In Vitro* and In Vivo. *Mol Cancer Ther*. 2015;14(12):2744-2752. doi:10.1158/1535-7163.MCT-15-0279
273. RedHill Biopharma - Opaganib - COVID-19. Accessed February 6, 2023. https://www.redhillbio.com/our-programs/pipeline/opaganib/covid-19/default.aspx
274. RedHill Biopharma - Our Programs - Pipeline - Opaganib. Accessed February 6, 2023. https://www.redhillbio.com/our-programs/pipeline/opaganib/default.aspx
275. Sahoo CR, Paidesetty SK, Padhy RN. Norharmane as a potential chemical entity for development of anticancer drugs. *Eur J Med Chem*. 2019;162:752-764. doi:10.1016/j.ejmech.2018.11.024
276. Petrou A, Fesatidou M, Geronikaki A. Thiazole Ring—A Biologically Active Scaffold. *Molecules*. 2021;26(11):3166. doi:10.3390/molecules26113166
277. Sahoo J, Sahoo CR, Nandini Sarangi PK, Prusty SK, Padhy RN, Paidesetty SK. Molecules with versatile biological activities bearing antipyrinyl nucleus as pharmacophore. *Eur J Med Chem*. 2020;186:111911. doi:10.1016/j.ejmech.2019.111911
278. Jain S, Chandra V, Kumar Jain P, Pathak K, Pathak D, Vaidya A. Comprehensive review on current developments of quinoline-based anticancer agents. *Arab J Chem*. 2019;12(8):4920-4946. doi:10.1016/j.arabjc.2016.10.009
279. Carta D, Balasso A, Caliceti P, Ferlin MG. Design, Synthesis, and Photophysical Properties of Pyrroloquinoline-Based Compounds Showing Strong Blue Fluorescence as Potential Dyes for Biomedical Applications. *ChemMedChem*. 2015;10(11):1846-1862. doi:10.1002/cmdc.201500366
280. Zhang J, Yang PL, Gray NS. Targeting cancer with small molecule kinase inhibitors. *Nat Rev Cancer*. 2009;9(1):28-39. doi:10.1038/nrc2559
281. Ilakiyalakshmi M, Arumugam Napoleon A. Review on recent development of quinoline for anticancer activities. *Arab J Chem*. 2022;15(11):104168. doi:10.1016/j.arabjc.2022.104168
282. Wall ME, Wani MC, Cook CE, Palmer KH, McPhail AT, Sim GA. Plant Antitumor Agents. I. The Isolation and Structure of Camptothecin, a Novel Alkaloidal Leukemia and Tumor Inhibitor from Camptotheca acuminata1,2. ACS Publications. doi:10.1021/ja00968a057
283. Dong J, Zhang Q, Wang Z, Huang G, Li S. Recent Advances in the Development of Indazole-based Anticancer Agents. *ChemMedChem*. 2018;13(15):1490-1507. doi:10.1002/cmdc.201800253
284. Fc T, H R, If A, Mj C, Mt D, I B. Synthesis and structural characterization of 1- and 2-substituted indazoles: ester and carboxylic acid derivatives. *Mol Basel Switz*. 2006;11(11). doi:10.3390/11110867
285. Dong J, Zhang Q, Wang Z, Huang G, Li S. Recent Advances in the Development of Indazole-based Anticancer Agents. *ChemMedChem*. 2018;13(15):1490-1507. doi:10.1002/cmdc.201800253
286. Ali NAS, Dar BA, Pradhan V, Farooqui M. Chemistry and biology of indoles and indazoles: a mini-review. *Mini Rev Med Chem*. 2013;13(12):1792-1800. doi:10.2174/1389557511313120009
287. Sági G, Szũcs K, Vereb G, Otvös L. Synthesis and enzymatic activity of some new purine ring system analogues of adenosine 3',5'-cyclic monophosphate. *J Med Chem*. 1992;35(24):4549-4556. doi:10.1021/jm00102a006

288. Mal S, Malik U, Mahapatra M, Mishra A, Pal D, Paidesetty SK. A review on synthetic strategy, molecular pharmacology of indazole derivatives, and their future perspective. *Drug Dev Res*. 2022;83(7):1469-1504. doi:10.1002/ddr.21979
289. Mosti L, Menozzi G, Fossa P, et al. Synthesis and preliminary biological evaluation of novel N-substituted 1-amino-3-[1-methyl(phenyl)-1H-indazol-4-yloxy]-propan-2-ols interesting as potential antiarrhythmic, local anaesthetic and analgesic agents. *Arzneimittelforschung*. 2000;50(11):963-972. doi:10.1055/s-0031-1300319
290. Tandon VK, Yadav DB, Chaturvedi AK, Shukla PK. Synthesis of (1,4)-naphthoquinono-[3,2-c]-1H-pyrazoles and their (1,4)-naphthohydroquinone derivatives as antifungal, antibacterial, and anticancer agents. *Bioorg Med Chem Lett*. 2005;15(13):3288-3291. doi:10.1016/j.bmcl.2005.04.066
291. Raffa D, Daidone G, Maggio B, Schillaci D, Plescia F. Synthesis and Antiproliferative Activity of Novel 3-(Indazol-3-yl)-quinazolin-4(3H)-one and 3-(Indazol-3-yl)-benzotriazin-4(3H)-one Derivatives. *Arch Pharm (Weinheim)*. 1999;332(9):317-320. doi:10.1002/(SICI)1521-4184(19999)332:9<317::AID-ARDP317>3.0.CO;2-R
292. Sun JH, Teleha CA, Yan JS, Rodgers JD, Nugiel DA. Efficient Synthesis of 5-(Bromomethyl)- and 5-(Aminomethyl)-1-THP-Indazole. *J Org Chem*. 1997;62(16):5627-5629. doi:10.1021/jo970375b
293. Patel M, Kaltenbach RF, Nugiel DA, et al. The synthesis of symmetrical and unsymmetrical P1/P1' cyclic ureas as HIV protease inhibitors. *Bioorg Med Chem Lett*. 1998;8(9):1077-1082. doi:10.1016/s0960-894x(98)00175-9
294. Han W, Pelletier JC, Hodge CN. Tricyclic ureas: A new class of HIV-1 protease inhibitors. *Bioorg Med Chem Lett*. 1998;8(24):3615-3620. doi:10.1016/S0960-894X(98)00659-3
295. Boulouard M, Schumann-Bard P, Butt-Gueulle S, et al. 4-Substituted indazoles as new inhibitors of neuronal nitric oxide synthase. *Bioorg Med Chem Lett*. 2007;17(11):3177-3180. doi:10.1016/j.bmcl.2007.03.024
296. Arán VJ, Ochoa C, Boiani L, et al. Synthesis and biological properties of new 5-nitroindazole derivatives. *Bioorg Med Chem*. 2005;13(9):3197-3207. doi:10.1016/j.bmc.2005.02.043
297. Rodgers JD, Johnson BL, Wang H, et al. Potent cyclic urea HIV protease inhibitors with benzofused heterocycles as P2/P2′ groups. *Bioorg Med Chem Lett*. 1996;6(24):2919-2924. doi:10.1016/S0960-894X(96)00531-8
298. Bräse S, Gil C, Knepper K. The recent impact of solid-phase synthesis on medicinally relevant benzoannelated nitrogen heterocycles. *Bioorg Med Chem*. 2002;10(8):2415-2437. doi:10.1016/S0968-0896(02)00025-1
299. Cerecetto H, Gerpe A, González M, Arán VJ, de Ocáriz CO. Pharmacological properties of indazole derivatives: recent developments. *Mini Rev Med Chem*. 2005;5(10):869-878. doi:10.2174/138955705774329564
300. Jakupec MA, Reisner E, Eichinger A, et al. Redox-Active Antineoplastic Ruthenium Complexes with Indazole: Correlation of *in Vitro* Potency and Reduction Potential. *J Med Chem*. 2005;48(8):2831-2837. doi:10.1021/jm0490742
301. Showalter HH, Angelo MM, Berman EM, et al. Benzothiopyranoindazoles, a new class of chromophore modified anthracenedione anticancer agents. Synthesis and activity against murine leukemias. *J Med Chem*. 1988;31(8):1527-1539.
302. Feyer P, Seegenschmiedt MH, Steingraeber M. Granisetron in the control of radiotherapy-induced nausea and vomiting: a comparison with other antiemetic therapies. *Support Care Cancer*. 2005;13(9):671-678. doi:10.1007/s00520-004-0766-3
303. Tan M. Granisetron: new insights into its use for the treatment of chemotherapy-induced nausea and vomiting. *Expert Opin Pharmacother*. 2003;4(9):1563-1571. doi:10.1517/14656566.4.9.1563
304. Gan TJ. Selective serotonin 5-HT3 receptor antagonists for postoperative nausea and vomiting: are they all the same? *CNS Drugs*. 2005;19(3):225-238. doi:10.2165/00023210-200519030-00004
305. Gross-Goupil M, François L, Quivy A, Ravaud A. Axitinib: A Review of its Safety and Efficacy in the Treatment of Adults with Advanced Renal Cell Carcinoma. *Clin Med Insights Oncol*. 2013;7:269-277. doi:10.4137/CMO.S10594
306. Deeks ED. Pazopanib. *Drugs*. 2012;72(16):2129-2140. doi:10.2165/11209950-000000000-00000
307. Deng Y, Sychterz C, Suttle AB, et al. Bioavailability, metabolism and disposition of oral pazopanib in patients with advanced cancer. *Xenobiotica*. 2013;43(5):443-453. doi:10.3109/00498254.2012.734642
308. Sonpavde G, Hutson TE, Sternberg CN. Pazopanib, a potent orally administered small-molecule multitargeted tyrosine kinase inhibitor for renal cell carcinoma. *Expert Opin Investig Drugs*. 2008;17(2):253-261. doi:10.1517/13543784.17.2.253
309. Verweij J, Sleijfer S. Pazopanib, a new therapy for metastatic soft tissue sarcoma. *Expert Opin Pharmacother*. 2013;14(7):929-935. doi:10.1517/14656566.2013.780030
310. Heo YA, Duggan ST. Niraparib: A Review in Ovarian Cancer. *Target Oncol*. 2018;13(4):533-539. doi:10.1007/s11523-018-0582-1

311. Ison G, Howie LJ, Amiri-Kordestani L, et al. FDA Approval Summary: Niraparib for the Maintenance Treatment of Patients with Recurrent Ovarian Cancer in Response to Platinum-Based Chemotherapy. *Clin Cancer Res Off J Am Assoc Cancer Res*. 2018;24(17):4066-4071. doi:10.1158/1078-0432.CCR-18-0042
312. Chen A. PARP inhibitors: its role in treatment of cancer. *Chin J Cancer*. 2011;30(7):463-471. doi:10.5732/cjc.011.10111
313. Brawer MK. Lonidamine: Basic Science and Rationale for Treatment of Prostatic Proliferative Disorders. *Rev Urol*. 2005;7(Suppl 7):S21-S26. Accessed April 12, 2023. https://www.ncbi.nlm.nih.gov/pmc/articles/PMC1477623/
314. Carapella CM, Paggi MG, Calvosa F, et al. Lonidamine in the combined treatment of malignant gliomas. A randomized study. *J Neurosurg Sci*. 1990;34(3-4):261-264.
315. Surana K, Chaudhary B, Diwaker M, Sharma S. Benzophenone: a ubiquitous scaffold in medicinal chemistry. *MedChemComm*. 2018;9(11):1803-1817. doi:10.1039/C8MD00300A
316. Farman S, Javed A, Arshia null, et al. Benzophenone Sulfonamide Derivatives as Interacting Partners and Inhibitors of Human P-glycoprotein. *Anticancer Agents Med Chem*. 2020;20(14):1739-1751. doi:10.2174/1871520620666200516144403
317. Wang G, Liu W, Tang J, et al. Design, synthesis, and anticancer evaluation of benzophenone derivatives bearing naphthalene moiety as novel tubulin polymerization inhibitors. *Bioorganic Chem*. 2020;104:104265. doi:10.1016/j.bioorg.2020.104265
318. Falchuk KH, Krishan A, Sullivan J. 1,10-Phenanthroline Inhibition of Lymphoblast Cell Cycle1. *Cancer Res*. 1977;37(7_Part_1):2050-2056.
319. Search Results | DrugBank Online. Accessed October 10, 2023. https://go.drugbank.com/unearth/q?searcher=drugs&query=phenanthroline
320. Segovia-Mendoza M, González-González ME, Barrera D, Díaz L, García-Becerra R. Efficacy and mechanism of action of the tyrosine kinase inhibitors gefitinib, lapatinib and neratinib in the treatment of HER2-positive breast cancer: preclinical and clinical evidence. *Am J Cancer Res*. 2015;5(9):2531-2561. Accessed March 30, 2023. https://www.ncbi.nlm.nih.gov/pmc/articles/PMC4633889/
321. Rabindran SK, Discafani CM, Rosfjord EC, et al. Antitumor activity of HKI-272, an orally active, irreversible inhibitor of the HER-2 tyrosine kinase. *Cancer Res*. 2004;64(11):3958-3965. doi:10.1158/0008-5472.CAN-03-2868
322. Ryckebusch A, Garcin D, Lansiaux A, et al. Synthesis, Cytotoxicity, DNA Interaction, and Topoisomerase II Inhibition Properties of Novel Indeno[2,1-c]quinolin-7-one and Indeno[1,2-c]isoquinolin-5,11-dione Derivatives. *J Med Chem*. 2008;51(12):3617-3629. doi:10.1021/jm800017u
323. Local A, Zhang H, Benbatoul KD, et al. APTO-253 Stabilizes G-quadruplex DNA, Inhibits MYC Expression, and Induces DNA Damage in Acute Myeloid Leukemia Cells. *Mol Cancer Ther*. 2018;17(6):1177-1186. doi:10.1158/1535-7163.MCT-17-1209
324. Avendaño C, Menéndez JC. Chapter 10 - Drugs That Inhibit Signaling Pathways for Tumor Cell Growth and Proliferation: Kinase Inhibitors. In: Avendaño C, Menéndez JC, eds. *Medicinal Chemistry of Anticancer Drugs (Second Edition)*. Elsevier; 2015:391-491. doi:10.1016/B978-0-444-62649-3.00010-7
325. Mishina Y, Duguid EM, He C. Direct Reversal of DNA Alkylation Damage. *Chem Rev*. 2006;106(2):215-232. doi:10.1021/cr0404702

2. Experimental

2.1. General Methods

All reactions reported in this study were carried out either under reflux or at room temperature. Reactions were carried out in air. Those reactions requiring inert conditions were carried out in argon using the Schlenk line and cannula techniques. Chemicals used in reactions were purchased from Sigma-Aldrich, abcr GmbH and Merck Group, and used without further purification. All solvents were purchased from Sigma-Aldrich, ACE Chemicals and MINEMA Chemicals (Pty) Ltd and were used as received. Acetonitrile was dried on 5 Å molecular sieves from Sigma-Aldrich. Aluminium sheets pre-coated with silica gel 60 F254 (from Merck) were used for thin-layer chromatography (TLC) to track the completion of the reactions. Deionised water was purified on a Direct-Q 3 UV Remote Type 1 ultrapure RO water purification Unit with a Millipore automatic sanitization module.

2.1.1. Instrumentation

All the characterisation was done using instruments at the School of Chemistry at the University of the Witwatersrand (Johannesburg, South Africa).

FTIR spectra were recorded using a Bruker Alpha FTIR spectrometer with an attenuated total reflectance platinum T Diamond 1 Refl reflection accessory. A single crystal of crystalline samples or a micro spatula tip full of powder samples, was placed on the platform of the FTIR instrument and crushed between the platform and the diamond head before recording the spectrum for each sample. The rubber band method was used for the baseline correction of the spectra. There were 64 baseline points, and 10 iterations were made to the spectrum. The spectral resolution of 1.0 cm^{-1} was acquired with 32 scans per sample. Although the main regions of interest were from 3400-1500 cm^{-1}, the instrument recorded data between 4000-400 cm^{-1}.

^{1}H and ^{13}C NMR spectra were recorded at 298 K with either a Bruker Avance III 500 spectrometer equipped with an Oxford magnet (11.744 T) or an Avance III 400 spectrometer equipped with a Bruker magnet (9.395 T). Either a 5 mm PABBO BB-1H/ D Z-GRD Z113652/ 0093 or a 5 mm PABBO BB/ 19F-1H/ D Z-GRD Z108618/ 0316 probe was used at the frequencies of 500.13 and 400.25 MHz respectively for ^{1}H NMR and 125.13 and 100.62 MHz for ^{13}C NMR. The compounds were dissolved in deuterated solvents (chloroform-d_1, dimethyl sulfoxide-d_6 (DMSO), acetonitrile-d_3 (MeCN), methanol-d_3, or N,N dimethylformamide-d_7 (DMF)). Standard Bruker pulse programs were used, and chemical shifts were reported in δ (ppm) relative to the deuterated solvent signal. ^{1}H chemical shifts were referenced at 7.26, 2.50, 2.11, 4.87 and 2.92 ppm for $CDCl_3$, $(CD_3)_2SO$, CD_3CN, CD_3OD, and $(CD_3)_2NOCD$, respectively; whereas δ ^{13}C shifts were referenced at 77.16, 39.52, 118.26, 49.00 and 163.15 ppm, respectively. The coupling constants were measured in Hertz (Hz) and these were calculated from peak separations of the same nucleus. All data were processed using MestReNova 12.0.0-20080 and ^{1}H, ^{13}C APT, COSY, NOSY, HSQC and HMBC were used to assign chemical shifts for all observed peaks.

UV-vis (electronic) spectra were recorded on a single-beam Agilent 8453 spectrophotometer or a Specord 210® Plus double-beam spectrometer (Analytik-Jena) using WinASPECT Plus version 4.2.0.0. Cell holders were thermostatted at 298 K using an external water circulator; 1.0 cm path length quartz cuvettes and spectroscopic grade DMSO or acetonitrile were used for all measurements. The spectra were recorded from 200-400 nm for the ligands (only peaks in the ultraviolet region of the electromagnetic spectrum, below 400 nm were observed), and from 200-700 nm for the metal chelate, (d metals are active in the visible light region of the spectrum). A 0.1 M solution for each sample was diluted until the absorbance was below 0.5 at the wavelength of interest. The absorbance at specific concentrations was used to calculate the molar attenuation coefficient (ε) at specific wavelengths for each sample.

High-Resolution Mass Spectroscopy (HRMS) were recorded with a Bruker compact Q-TOF high-resolution mass spectrometer by direct infusion at a flow rate of 5 µL/min for 1 min, with Bruker Daltronics HyStar 3.2 SR4 software. Chromatograms were analysed with Bruker Compass Data Analysis software (Version 4.3). Samples of pure compounds (typically *ca*. 10 µg/mL) were prepared in acetonitrile or ethanol for metal chelates and HPLC-grade methanol for ligands. Solutions were acidified using 0.1% (v/v) formic acid to obtain spectra in the positive electron spray (ESI+) mode.

Melting temperatures were determined visually on a hot-stage microscope instrument from JM-Inst. Melting points were only determined for the ligands **1a-f** because all metal gold(III) complexes decomposed above 473 K.

X-ray diffraction X-ray diffraction intensity data were recorded on a Bruker Apex II 3-circle X-ray diffractometer or a Bruker D8 Venture 4-circle X-ray diffractometer at 153(1) or 173(1) K (Oxford CryoStream) using Mo Kα radiation. Crystals were mounted in Paratone® oil using nylon micro-loops (Hampton) or polymer micro-grippers (MiTeGeN) for data collection. Using Olex2 1.5,[44] the structures were solved with the ShelXT[45] structure solution program (intrinsic phasing) and then refined using least squares minimisation to a good model (anisotropic atoms for all non-H atoms) with the ShelXL[46] refinement package. Each structure was further refined with Olex2 1.5 before implementing the final refinement cycles using non-spherical atom form factors (NSAFF) with NoSpherA[47] running in Olex2. The NSAFF were calculated from the electron density derived from a single determinant SCF wavefunction at the r^{2}SCAN[48]/cc-pVTZ[49] level of theory for a fragment of the crystal using Orca 5.0.4[50] for the density functional theory (DFT) calculations.

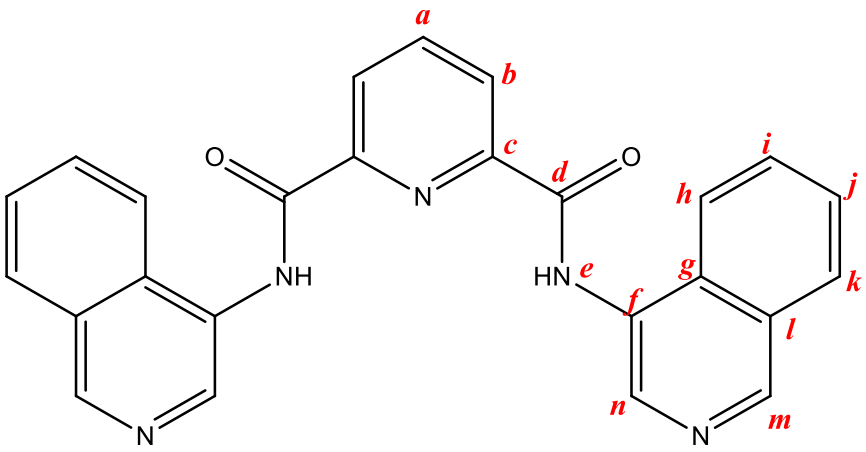
Circular dichroism (CD) spectra were recorded on a JASCO J-1500 MCD spectrometer in 1.0 cm path length quartz cuvettes using spectroscopic grade chloroform, methanol, or tetrahydrofuran (THF) as solvents. CD spectra of solid samples were recorded in diffuse reflectance mode using an integrating sphere and powdered compounds compressed into a 1.0-cm diameter sample holder. The CD will be discussed in more detail in **Chapter 5**.

2.2. Ligands Synthesis

A method by Barnes *et.al* was adapted and used for the synthesis of ligands **1a-1f** in this study.[4] All synthesised carboxamide pincer ligands are novel except for **1c**, which has been synthesised by Hiratani and Kaguchi.[5] Crystallographic structures obtained for ligands **1a-e** are all novel, and the data has been deposited into the Cambridge Structural Database (CSD).

Generally, 2,6-Pyridine dicarboxylic acid (1 eq) and the appropriate amine (2.1 eq) were heated under solvent reflux for several hours in the presence of triphenyl phosphite (2 eq) with pyridine as the solvent. The products were then precipitated from solution by adding ethanol or hexane to the cooled reaction mixtures. Specific details are given below.

2.2.1. N^2,N^6-Bis(isoquinolin-4-yl)pyridine-2,6-dicarboxamide (1a)



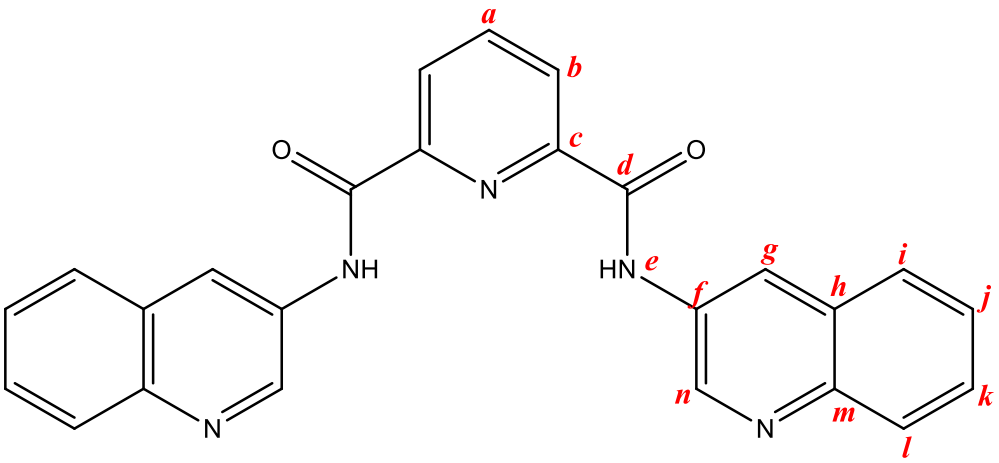
2,6-Pyridine dicarboxylic acid (1.494 mmol, 0.2507 g) and 4-amino isoquinoline (3.208 mmol, 0.4619 g) were stirred in 15 mL pyridine for 10 minutes at room temperature before adding triphenyl phosphite (3 mmol, 0.7862 mL) and heating the reaction mixture under reflux for 4 h. After cooling the solution, ethanol was added to the reaction mixture, which was then left to stand on ice until a precipitate formed. The white precipitate was filtered off (Hirsch funnel) and washed with cold ethanol before being allowed to air-dry. Yield: 0.6096 g, 97%. Single crystals were grown by slow diffusion of acetonitrile into a solution of the compound dissolved in DMSO.

Chemical formula $C_{25}H_{17}N_5O_2$. **^{1}H NMR** (400 MHz, DMSO-d_6) δ 11.43 (s, 2H, *e*), 9.32 (s, 2H, *n*), 8.71 (s, 2H, *m*), 8.48 (d, *J* = 7.7 Hz, 2H, *b*), 8.38 (dd, *J* = 8.4, 7.1 Hz, 1H, *a*), 8.23 (d, *J* = 8.2 Hz, 2H, *k*), 8.11 (d, *J* = 8.4 Hz, 2H, *h*), 7.89 (ddd, *J* = 8.3, 6.8, 1.3 Hz, 2H, *i*), 7.77 (t, *J* = 7.5 Hz, 2H, *j*). **^{13}C NMR** (101 MHz, DMSO-d_6) δ 163.14 *d*, 151.14 *n,* 148.56 *c*, 141.11 *m*, 140.39 *a*, 132.13 *f*, 130.99 *i*, 128.68 *g*, 128.33 *l*, 128.02 *k j*, 125.72 *b*, 122.76 *h*. **HRMS (ESI+)** *m/z* calculated for $C_{23}H_{18}N_5O_2$ $[M+H]^+$: 420.1455; found 420.1457. **UV-vis**: [DMSO λ_{max} nm (10^3 ε, M^{-1} cm^{-1})] 277 (10.9), 309 (9.2), 323 (10.5). **FTIR**: (powder, cm^{-1}): 1677.07 (C=O), 3283.13 (N–H), 3372.95 (N–H). **Melting temperature**: 400 – 410 °C.

Crystal data for 1a: $C_{25}H_{17}N_5O_2$ (*M* = 419.446 g mol^{-1}): monoclinic, space group $P2_1/c$ (no. 14), *a* = 8.7392(4) Å, *b* = 14.6766(8) Å, *c* = 15.2758(8) Å, β = 102.656(2)°, *V* = 1911.70(17) $Å^3$, *Z* = 4, *T* = 173.15 K, μ(Mo Kα) = 0.096 mm^{-1}, D_{calc} = 1.457 g cm^{-3}, 38141 reflections measured (6.14° ≤ 2Θ ≤ 66.46°),

7297 unique (R_{int} = 0.0277, R_{σ} = 0.0189) which were used in all calculations. The final R_1 was 0.0187 ($I \geq 2\sigma(I)$) and wR_2 was 0.0410 (all data).

2.2.2. N^2,N^6-Bis(quinolin-3-yl)pyridine-2,6-dicarboxamide (1b)

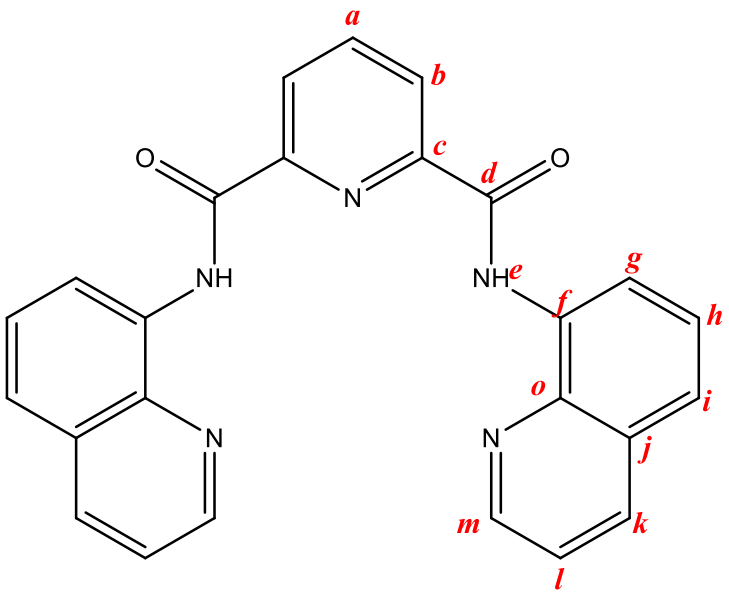


The same procedure described for **1a** was used with minor changes. 2,6-Pyridine dicarboxylic acid (1.496 mmol, 0.2510 g) was reacted with 3-aminoquinoline (3.208 mmol, 0.4625 g) in place of 4-amino-isoquinoline. A yellow crystalline powder was produced after filtering off the precipitate and air-drying. Yield: 0.5907 g, 94%. Single crystals were grown by slow evaporation from a solution of **1b** in methanol.

Chemical formula $C_{25}H_{17}N_5O_2$. **^{1}H NMR** (400 MHz, DMSO-d_6) δ 11.41 (s, 2H, *e*), 9.35 (d, *J* = 2.5 Hz, 2H, *n*), 8.95 (d, *J* = 2.5 Hz, 2H, *g*), 8.43 (d, *J* = 7.7 Hz, 2H, *b*), 8.33 (dd, *J* = 8.3, 7.1 Hz, 1H, *a*), 8.01 (dt, *J* = 8.3, 1.5 Hz, 4H, *i,l*), 7.69 (ddd, *J* = 8.5, 6.8, 1.4 Hz, 2H, *k*), 7.60 (ddd, *J* = 8.1, 6.8, 1.3 Hz, 2H, *j*).**^{13}C NMR** (101 MHz, DMSO-d_6) δ 162.34 *d*, 148.37 *c*, 145.88 *n*, 144.53 *f*, 140.30 *a*, 131.79 *m,* 128.52 *k*, 127.93 *i,l*, 127.70 *h*, 127.26 *j*, 125.66 *b*, 124.59 *g*. **HRMS (ESI+)** *m/z* calculated for $C_{25}H_{18}N_5O_2$ $[M+H]^+$: 420.1455; found 420.1455. **UV-vis** [DMSO; λ_{max}, nm (10^3 ε, M^{-1} cm^{-1})]: 275 (23.6), 312 (17.5), 324 (17.7), 338 (15.9). **FTIR**: (powder, cm^{-1}): 1682.70 (C=O), 3191.12 (N–H). **Melting temperature**: 370 – 377 °C.

Crystal Data for 1b. $C_{25}H_{17}N_5O_4 \cdot C_2H_6$ (*M* = 483.531 g mol^{-1}): triclinic, space group *P*-1 (no. 2), *a* = 7.2743(3) Å, *b* = 11.3528(5) Å, *c* = 14.9566(5) Å, α = 76.605(1)°, β = 78.871(1)°, γ = 78.901(2)°, *V* = 1164.76(8) $Å^3$, *Z* = 2, *T* = 153.00 K, μ(Mo Kα) = 0.095 mm^{-1}, D_{calc} = 1.379 g cm^{-3}, 85728 reflections measured (5.78° ≤ 2Θ ≤ 66.42°), 8894 unique (R_{int} = 0.0459, R_{σ} = 0.0265) which were used in all calculations. The final R_1 was 0.0290 ($I \geq 2\sigma(I)$) and wR_2 was 0.0453 (all data).

2.2.3. N^2,N^6-Bis(quinolin-8-yl)pyridine-2,6-dicarboxamide (1c)

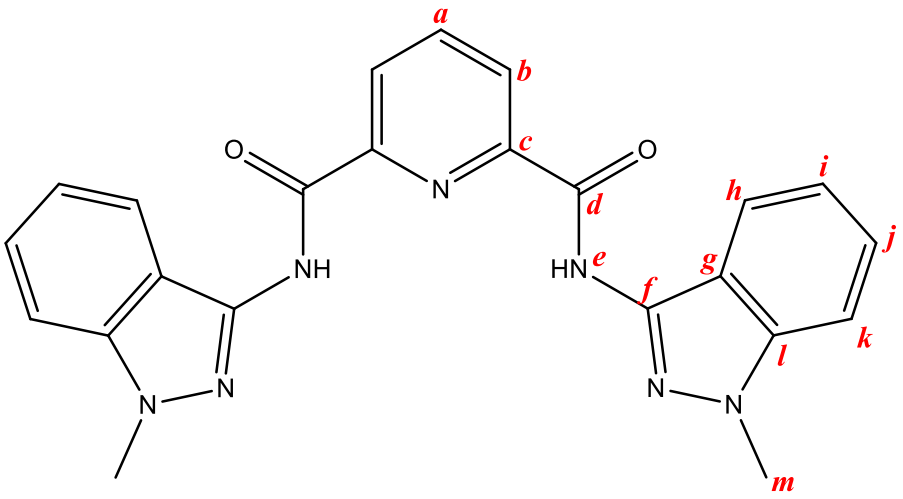


The same procedure described for **1a** was used with minor changes. 2,6-Pyridine dicarboxylic acid (1.497 mmol, 0.2512 g) was reacted with 8-aminoquinoline (3.198 mmol, 0.4610 g) in place of 4-amino-isoquinoline. A pale-yellow flaky powder was filtered off and dried. Yield: 0.6159 g, 98%. Single crystals were grown by slow evaporation from a solution of **1c** in chloroform.

Chemical formula $C_{25}H_{17}N_5O_2$. **^{1}H NMR** (500 MHz, Chloroform-*d*) δ 12.36 (s, 2H *e*), 9.03 (dd, *J* = 7.3, 1.5 Hz, 2H *m*), 8.59 (d, *J* = 7.7 Hz, 2H *b*), 8.27 (dd, *J* = 4.2, 1.6 Hz, 2H *g*), 8.20 (dd, *J* = 8.1, 2.0 Hz, 3H *a,i*), 7.70 – 7.61 (m, 4H *l,k*), 7.33 (dd, *J* = 8.2, 4.1 Hz, 2H *h*). **^{13}C NMR** (126 MHz, Chloroform-*d*) δ 162.02 *d*, 149.14 *c*, 148.79 *g*, 139.63 *f*, 139.33 *a*, 136.14 *i*, 134.45 *o*, 128.08 *j*, 127.38 *l*, 125.44 *b*, 122.35 *k*, 121.42 *h*, 117.31 *m*. **HRMS (ESI+)** *m/z* calculated for $C_{25}H_{18}N_5O_2$ $[M+H]^+$: 420.1455; found 420.1462. **UV-vis** [DMSO; λ_{max}, nm (10^3 ε, M^{-1} cm^{-1})]: 326 (86.0), **FTIR**: (powder, cm^{-1}): 1677.70 (C=O), 3320.57 (N–H), 3266.48 (N–H). **Melting temperature**: 308 – 319 °C.

Crystal Data for 1c. $C_{25}H_{17}N_5O_2$ (*M* = 419.446 g mol^{-1}): orthorhombic, space group $P2_12_12_1$ (no. 19), *a* = 4.4778(2) Å, *b* = 16.9420(7) Å, *c* = 25.8329(10) Å, *V* = 1959.76(14) $Å^3$, *Z* = 4, *T* = 173.15 K, μ(Mo Kα) = 0.094 mm^{-1}, D_{calc} = 1.422 g cm^{-3}, 30705 reflections measured (5.76° ≤ 2Θ ≤ 56.54°), 4830 unique (R_{int} = 0.0305, R_σ = 0.0205) which were used in all calculations. The final R_1 was 0.0172 ($I \geq 2\sigma(I)$) and wR_2 was 0.0292 (all data).

2.2.4. N^2,N^6-Bis(1-methyl-1H-indazol-3-yl)pyridine-2,6-dicarboxamide (1d)

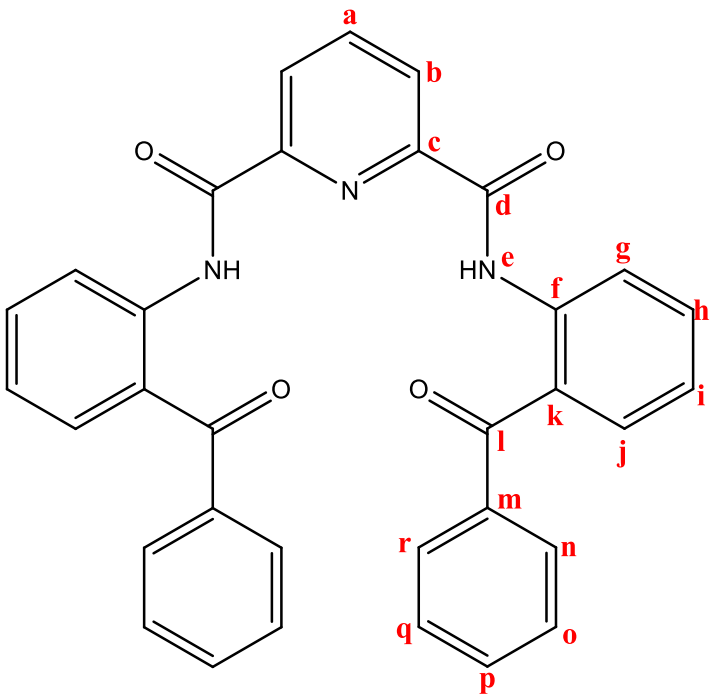


The same procedure described for **1a** was used with minor changes. 2,6-pyridine dicarboxylic acid (1.496 mmol, 0.2510 g) was reacted with 3-amino-1-methyl-1H-indazole (3.200 mmol, 0.4415 g) in place of 4-amino-isoquinoline. After cooling the reaction mixture, hexane was added to the solution, and the reaction flask was left to stand on ice until a precipitate formed. The cream-coloured precipitate was filtered, washed with cold ethanol, and air-dried. Yield 0. 5930 mg, 93%. Single crystals were grown by slow evaporation from a solution of **1d** of acetonitrile.

Chemical formula $C_{23}H_{19}N_7O_2$. **^{1}H NMR** (400 MHz, DMSO-d_6) δ 11.79 (d, J = 2.6 Hz, 2H *e*), 8.46 (d, J = 7.7 Hz, 2H *b*), 8.34 (dd, J = 8.3, 7.2 Hz, 1H *a*), 7.84 (dq, J = 8.2, 1.1 Hz, 2H *k*), 7.64 (d, J = 8.5 Hz, 2H *h*), 7.44 (ddd, J = 8.3, 6.9, 1.1 Hz, 2H *i*), 7.15 (ddd, J = 7.9, 6.8, 0.8 Hz, 2H *j*), 4.05 (s, 6H *m*). **^{13}C NMR** (101 MHz, DMSO-d_6) δ 162.31 *d*, 148.55 *c*, 140.86 *l*, 139.95 *a*, 138.24 *g*, 126.56 *i*, 125.49 *b*, 122.25 *k*, 119.89 *j*, 117.47 *f*, 109.77 *h*, 35.24 *m*. **HRMS (ESI+)** *m/z* calculated for $C_{23}H_{20}N_7O_2$ $[M+H]^+$: 426.1673; found 426.1674. **UV-vis** [CH_3CN; λ_{max}, nm (10^3 ε, M^{-1} cm^{-1})]: 199 (71.1), 222 (18.4), 285 (15.2). **FTIR**: (powder, cm^{-1}): 1690.18 (C=O), 3309.89 (N–H). **Melting temperature**: 298 – 305 °C.

Crystal Data for 1d. $C_{23}H_{19}N_7O_2$ (M = 425.453 g mol^{-1}): monoclinic, space group $P2/c$ (no. 13), a = 10.4220(2) Å, b = 11.8014(3) Å, c = 8.6298(2) Å, β = 112.076(1)°, V = 983.60(4) Å^3, Z = 2, T = 153.15 K, μ(Mo Kα) = 0.097 mm^{-1}, D_{calc} = 1.437 g cm^{-3}, 23461 reflections measured (4.22° ≤ 2Θ ≤ 63.28°), 3318 unique (R_{int} = 0.0294, R_σ = 0.0180) which were used in all calculations. The final R_1 was 0.0259 ($I \geq 2\sigma(I)$) and wR_2 was 0.0639 (all data).

2.2.5. N^2,N^6-Bis(2-benzoylphenyl)pyridine-2,6-dicarboxamide (1e)

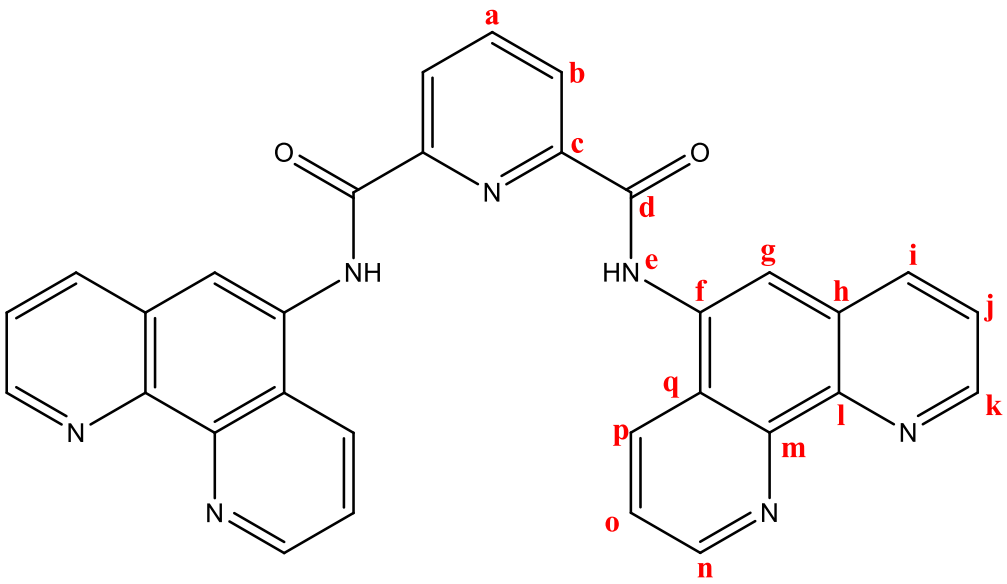


The same procedure described for **1a** was used with minor changes. 2,6-Pyridine dicarboxylic acid (1.495 mmol, 0.2509 g) was reacted with 2-amino benzophenone (3.203 mmol, 0.6318 g) in place of 4-amino-isoquinoline. After cooling the reaction mixture, ethanol was added to the solution and the reaction flask was left to stand on ice until a precipitate formed. The pale orange precipitate was filtered, washed with cold ethanol, and left to air-dry. Yield: 0.7490 mg, 95%. Single crystals were grown in a binary mixture of ethanol and water (50% v/v).

Chemical formula $C_{33}H_{23}N_3O_4$. **^{1}H NMR** (400 MHz, DMSO-d_6) δ 12.32 (s, 2H *e*), 8.54 (d, 2H *g*), 8.35 (d, *J* = 7.7 Hz, 2H *b*), 8.04 (t, *J* = 7.8 Hz, 1H *a*), 7.69 – 7.57 (m, 8H *h j n r*), 7.49 (t, 2H *i*), 7.31 (t, *J* = 7.7 Hz, 4H *o q*), 7.28 – 7.22 (m, 2H *p*). **^{13}C NMR** (101 MHz, DMSO-d_6) δ 197.65 *l*, 161.89 *d*, 148.56 *c*, 139.28 *a*, 138.30 *f k*, 133.26 *g*, 132.59 *h*, 132.26 *j*, 130.06 *n r*, 128.00 *o q*, 127.34 *m*, 125.12 *b*, 123.57 *i*, 122.85 *p*. **HRMS (ESI+)** *m/z* calculated for $C_{33}H_{24}N_3O_4$ $[M+H]^+$: 526.1761; found 526.1760. **UV-vis** [DMSO; λ_{max}, nm (10^3 ε, M^{-1} cm^{-1})]: 333 (18.5). **FTIR** (powder, cm^{-1}): 1619.35 (amide C=O), 1550.12 (benzophenone C=O), 3431.41 (N–H). **Melting temperature**: 207 – 212 °C.

Crystal Data for 1e. $C_{33}H_{23}N_3O_4$ (*M* = 525.568 g mol^{-1}): monoclinic, space group $P2_1/n$ (no. 14), *a* = 8.4952(2) Å, *b* = 18.3345(4) Å, *c* = 16.2123(3) Å, β = 90.689(1)°, *V* = 2524.97(9) $Å^3$, *Z* = 4, *T* = 153.15 K, μ(Mo Kα) = 0.092 mm^{-1}, D_{calc} = 1.383 g cm^{-3}, 38759 reflections measured (3.36° ≤ 2Θ ≤ 56.76°), 6322 unique (R_{int} = 0.0562, R_σ = 0.0479) which were used in all calculations. The final R_1 was 0.0330 ($I \geq 2\sigma(I)$) and wR_2 was 0.0550 (all data).

2.2.6. N^2,N^6-Bis(1,10-phenanthrolin-5-yl)pyridine-2,6-dicarboxamide (1f)



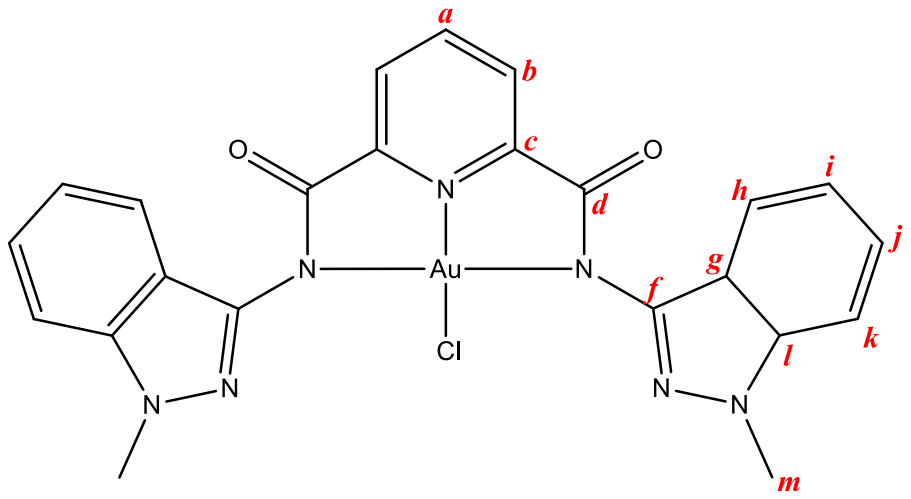
The same procedure described for **1a** was used with minor changes. 2,6-Pyridine dicarboxylic acid (1.496 mmol, 0.2510 g) was reacted with 1,10-phenanthrolin-5-amine (3.336 mmol, 0.6570 g) in place of 4-amino-isoquinoline. After cooling the reaction mixture, ethanol was added to the solution and the flask was left to stand on ice until a precipitate formed. The pale orange precipitate was isolated by gravity filtration, washed with cold ethanol, and left to air-dry. Yield: 0.7658 mg, 98%.

Chemical formula $C_{31}H_{19}N_7O_2$. **^{1}H NMR** (500 MHz, DMSO-d_6) δ 11.61 (s, 2H *e*), 9.19 (dd, *J* = 4.2, Hz 2H *k*), 9.12 (dd, *J* = 4.3, 1.7 Hz, 2H *n*), 8.69 (dd, *J* = 8.3, 1.8 Hz, 2H *i*), 8.59 (dd, *J* = 8.1, 1.7 , 1.6 Hz, 2H *p*), 8.53 (d, *J* = 7.7 Hz, 2H *b*), 8.45 – 8.41 (m, 1H *a*), 8.27 (s, 2H *g*), 7.91 (dd, *J* = 8.3, 4.3 Hz, 2H *j*), 7.82 (dd, *J* = 8.1, 4.3 Hz, 2H *o*). **^{13}C NMR** (126 MHz, DMSO-d_6) δ 163.53 *d*, 150.69 *k*, 150.45 *n*, 148.98 *c*, 146.27 *l*, 144.80 *m*, 140.82 *a*, 136.72 *p*, 133.14 *i*, 131.83 *f*, 128.37 *q*, 126.34 *h*, 126.13 *b*, 124.24 *o*, 124.06 *g*, 123.70 *j*. **HRMS (ESI+)** *m/z* calculated for $C_{31}H_{20}N_7O_2$ $[M+H]^+$: 522.5357; found. 522.1773. **UV-vis** [DMSO; λ_{max}, nm (10^3 ε, M^{-1} cm^{-1})]: 269 (75.0), 315 (15.6). **FTIR** (powder, cm^{-1}): 1658.67 (C=O), 3380.22 (N–H). Melting temperature: 270 – 279 °C.

2.3. Synthesis of gold(III) metal chelates

All synthesised metal complexes in this study are novel. Different methods were tried until the desirable gold(III) pincer complexes were synthesised without side reactions. Generally, $KAuCl_4$ and the ligand of interest were reacted in a one-pot reaction in different proportions and solvents. The products precipitated from the reaction solution upon cooling down. Specific details are given below.

2.3.1. N^2,N^6-Bis(1-methyl-1H-indazol-3-yl)pyridine-2,6-dicarboxamide gold(III) chloride (2d)

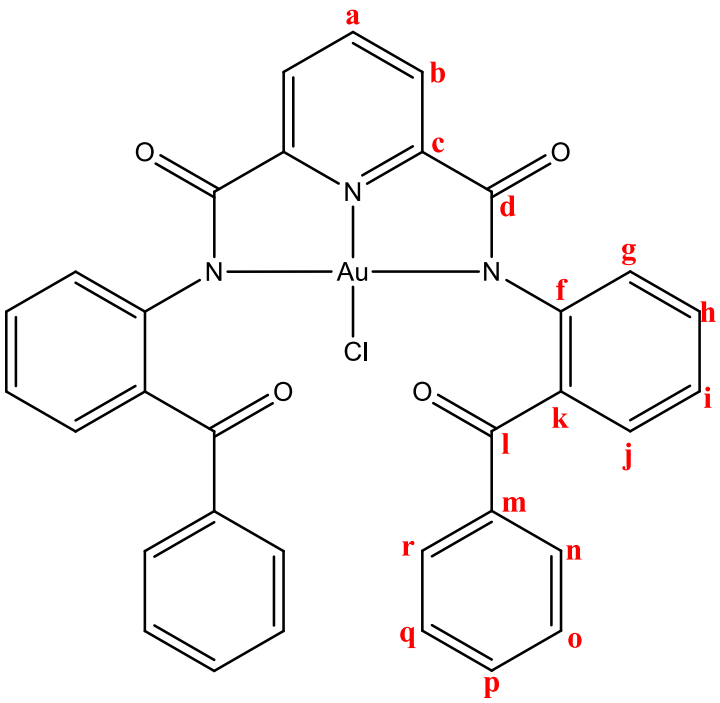


1d (0.3000 mmol, 0.1275 g) was dissolved in acetonitrile (4 mL) and $KAuCl_4$ (0.4500 mmol, 0.1700 g) was dissolved in distilled water (12 mL). The metal salt was slowly added to the ligand solution and refluxed for 15 h. A reddish precipitate was filtered off from the red solution and was washed several times with cold water and air-dried. Yield: 0.17658 mg, 89%. Single crystals were grown by slow diffusion of *tert*-butyl alcohol into a solution of the compound dissolved in DMSO.

Chemical formula $Au[C_{23}H_{17}N_7O_2]Cl$. **^{1}H NMR** (400 MHz, DMSO-d_6) δ 8.75 (t, J = 7.9 Hz, 1H *a*), 8.28 (d, J = 7.8 Hz, 2H *b*), 7.73 (dt, J = 8.1, 1.0 Hz, 2H *k*), 7.53 (d, J = 8.5 Hz, 2H *h*), 7.38 (ddd, J = 8.3, 6.9, 1.1 Hz, 2H *i*), 7.15 (t, J = 7.5 Hz, 2H *j*), 3.98 (s, 6H *m*). **^{13}C NMR** (101 MHz, DMSO-d_6) δ 170.36 *d*, 147.20 *a*, 144.93 *c*, 143.78 *f*, 140.94 *l*, 129.25 *b*, 126.37 *i*, 120.80 *k j*, 119.47 *g*, 109.95 *h*, 35.99 *m*. **HRMS (ESI+)** m/z calculated for $Au[C_{23}H_{18}N_7O_2]Cl$ $[M+H]^+$: 656.095; found: 656.086 **UV-vis** [DMSO; λ_{max}, nm (10^3 ε, M^{-1} cm^{-1})]: 267 (8.17), 296 (8.25),439 (3.67). **FTIR** (powder, cm^{-1}): 1683.12 (C=O).

Crystal Data for 2d. $C_{23}H_{17}AuClN_7O_2$ (M = 655.85 g mol^{-1}), monoclinic, space group P-1(no. 2), a = 8.8115(3) Å, b = 10.4987(3) Å, c = 12.0821(4) Å, α = 74.233(2)°, β = 90.6890(10)°, γ = 81.344(2)°, V = 1058.58(6) $Å^3$, Z = 2, T = 153.15 K, μ(MoKα) = 7.114 mm^{-1}, D_{calc} = 2.058 g cm^{-3}, 59569 reflections measured (3.518° ≤ 2Θ ≤ 66.494°), 8133 unique reflections (R_{int} = 0.0387, R_σ = 0.0240) which were used in all calculations. The final R_1 was 0.0194 (I > 2σ(I)) and wR_2 was 0.0437 (all data).

2.3.2. N^2,N^6-Bis(2-benzoylphenyl)pyridine-2,6-dicarboxamide gold(III) chloride (2e)

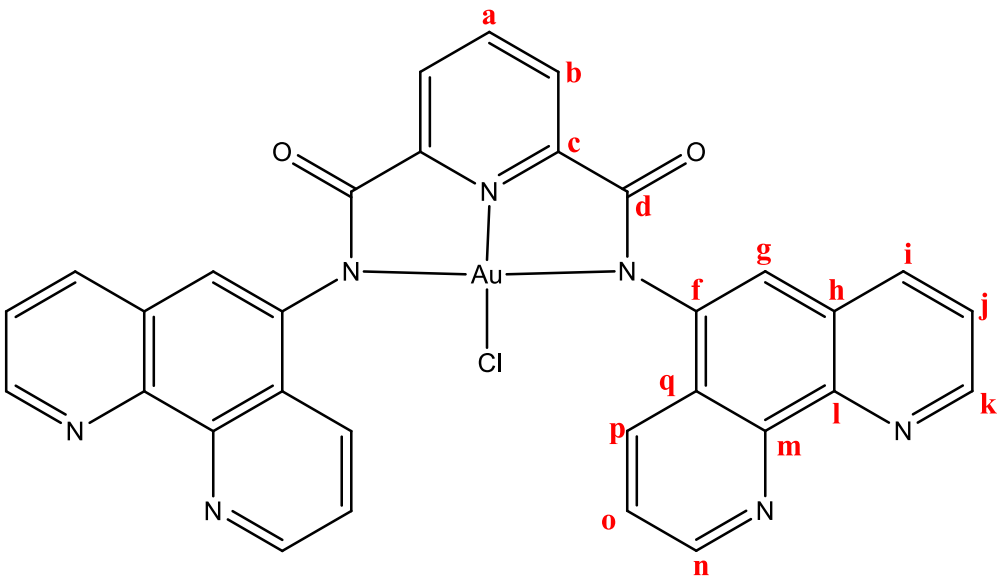


The same procedure as **2d** was applied with **1e** (0.3001 mmol. 0.1277 g) in place of **1d**. A reddish precipitate was filtered off from the red solution and was washed several times with cold water and air-dried. The precipitate was dissolved in hot methanol and allowed to recrystallise. It was then filtered off and washed with cold methanol and left to dry. Yield: 0.0182 g (8%). Single crystals were grown by slow evaporation from a solution of **2e** in methanol.

Chemical formula $Au[C_{33}H_{21}N_3O_4]Cl$ **^{1}H NMR** (400 MHz, DMSO-d_6) δ 8.62 (q, J = 8.1 Hz, 1H *a*), 8.09 (dd, J = 7.8, 5.7 Hz, 2H *b*), 7.70 – 7.63 (m, 2H *g*), 7.63 – 7.58 (m, 2H *j*), 7.58 – 7.53 (m, 4H *n r*), 7.53 – 7.43 (m, 4H *h i*), 7.43 – 7.29 (m, 6H *o p q*). **^{13}C NMR** (101 MHz, DMSO-d_6) δ 170.36 *d*, 147.20 *a*, 144.93 *c*, 143.78 *g*, 140.94 *l*, 129.25 *b*, 126.37 *i*, 120.49 *f*, 120.46 *k*, 119.47 *j*, 109.95 *h*, 35.68 *m*. **HRMS (ESI+)** m/z calculated for $Au[C_{33}H_{22}N_3O_4]Cl$ $[M+H]^+$: 756.088; found: 756.436. **UV-vis** [DMSO; λ_{max}, nm (10^3 ε, M^{-1} cm^{-1})]: 333 (18.5). **FTIR** (powder, cm^{-1}): 1660.38 (benzophenone C=O), 1683.07 (amide C=O).

Crystal Data for 2e. $C_{33}H_{21}AuClN_3O_4$ (M = 755.95 g mol^{-1}), monoclinic, space group $P2_1/n$(no. 14), a = 13.3998(5) Å, b = 12.9269(5) Å, c = 12.0821(4) Å, α = γ = 90°, β = 96.1180(10)°, V = 2728.85(18) Å^3, Z = 4, T = 193 K, μ(MoKα) = 3.021 mm^{-1}, D_{calc} = 1.821 g cm^{-3}, 329197 reflections measured (3.032° ≤ 2Θ ≤ 61.356°), 8133 unique reflections (R_{int} = 0.0583, R_σ = 0.0190) which were used in all calculations. The final R_1 was 0.0194 (I > 2σ(I)) and wR_2 was 0.0437 (all data).

2.3.3. N^2,N^6-Bis(1,10-phenanthrolin-5-yl)pyridine-2,6-dicarboxamide gold(III) chloride (2f)



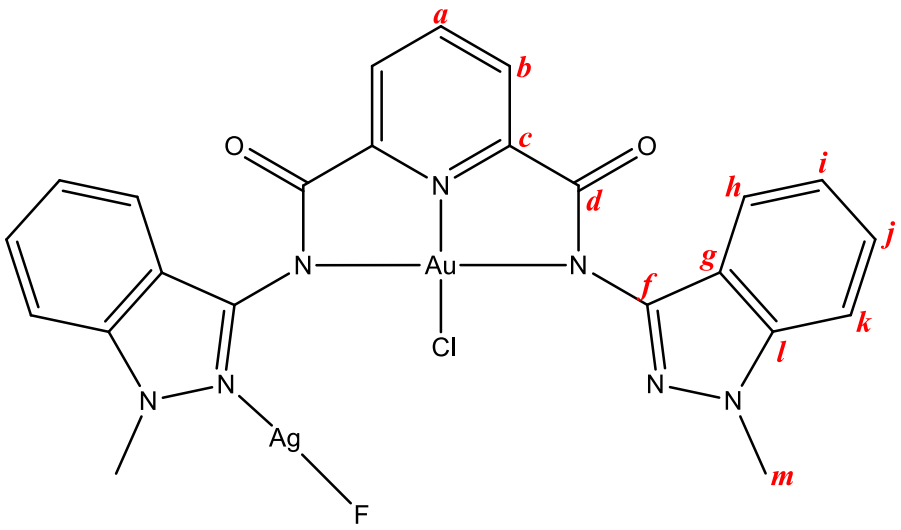
The same procedure as **2d** was applied with **1f** (0.3000 mmol. 0.1565 g) in place of **1d**. An orange precipitate formed upon cooling down the reaction, which was filtered, washed with cold ethanol and left to air-dry. Yield: 0.1573 mg, 70% yield**.**

Chemical formula $Au[C_{31}H_{17}N_7O_2]Cl$. **^{1}H NMR** (400 MHz, DMSO-d_6) δ 9.72 (d, *J* = 5.7 Hz, 2H *k*), 9.67 (dd, *J* = 5.6, 1.2 Hz, 2H *n*), 9.55 – 9.48 (m, 2H *p*), 9.37 (dd, *J* = 8.1, 2.9 Hz, 2H *i*), 8.93 (dt, *J* = 12.8, 7.9 Hz, 1H *a*), 8.52 (m, 6H *b g j*), 8.42 (dd, *J* = 8.4, 5.7 Hz, 2H *o*). **^{13}C NMR** (101 MHz, DMSO-d_6) δ 170.23 *d*, 149.52 *k*, 148.05 *n*, 147.77 *a*, 144.76 *c*, 143.46 *p*, 143.23 *i* 140.15 *f*, 138.92 *m*, 137.50 *g*, 137.42 *l*,, 130.25 *b*, 129.47 *q*,, 128.12 *h*, 126.30 *o*, 126.17 *j*. **HRMS (ESI+)** *m/z* calculated for $Au[C_{31}H_{18}N_7O_2]Cl$ $[M+H]^+$: 752.93; found 752.71. **UV-vis** [DMSO; λ_{max}, nm (10^3 ε, M^{-1} cm^{-1})]: 262 (10 253), 309 (16 347). **FTIR** (powder, cm^{-1}): 1658.67 (C=O).

2.4. Other attempts

The metal complexes in this section were synthesised using methods which were modified from the method by Casini *et al*.[6,7] Different methods were employed for the synthesis of the metal complexes, and listed in this section are some of the noteworthy products from these trials. These metal complexes were characterised using X-ray crystallography and it was concluded that they were minor products during crystallisation as they could not be detected by characterisation using any other method, (FTIR, HRMS and NMR). The characterisation data was the same as **2d**, and the products **2di** and **2d**ii could not be isolated to characterise individually. Details on the products in this section are explained in **Chapter 4**.

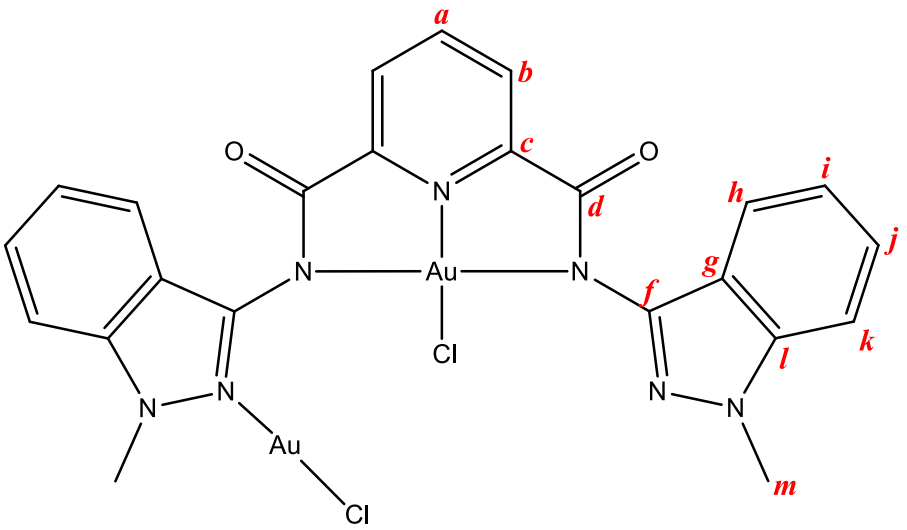
2.4.1. N^2,N^6-Bis(1-methyl-1H-indazol-3-yl),(2H-silver(I)fluoride)pyridine-2,6-dicarboxamide gold(III) chloride (2di)



1d (0.300 mmol, 0.1277 g) and $KAuCl_4$ (0.300 mmol, 0.1201 g) were dissolved separately in 9 mL acetonitrile. The metal salt was slowly added to the ligand mixture and stirred at room temperature for 5 minutes. $AgPF_6$ (0.6 mmol, 0.0700 g) in distilled water (3 mL) was added to the reaction solution and left to reflux for 15h. The ratio of water to acetonitrile in the reaction was 3:1. A reddish precipitate was filtered off from the resultant red solution, washed several times with cold ethanol-water and air-dried. Yield: 0.1746 g, 89%. Single crystals were grown by slow diffusion of ethanol into a solution of the compound dissolved in DMSO.

Crystal Data for 2di. $Au[C_{23}H_{17}N_5O_2(AgF)]Cl$ (M = 782.72 g mol^{-1}), monoclinic, space group P-1(no. 2), a = 8.670(3) Å, b = 11.448(4) Å, c = 13.101(5) Å, α = 105.91(19)°, β = 97.97(2)°, γ = 97.98(2)°, V = 1216.9(8) Å^3, Z = 2, T = 173.15 K, μ(MoKα) = 6.976 mm^{-1}, D_{calc} = 2.136 g cm^{-3}, 33227 reflections measured (3.290° ≤ 2Θ ≤ 56.890°), 6088 unique reflections (R_{int} = 0.0829, R_σ = 0.0654) which were used in all calculations. The final R_1 was 0.0532 (I > 2σ(I)) and wR_2 was 0.1381 (all data).

2.4.2. N^2,N^6-Bis(1-methyl-1H-indazol-3-yl),(2H-gold(I)chloride)pyridine-2,6-dicarboxamide gold(III) chloride (2dii)



1d (0.3 mmol, 0.1275 g) was dissolved in 9 mL acetonitrile, and $KAuCl_4$ (0.600 mmol, 0.2200 g) dissolved in 2 mL distilled water was added to the solution and stirred for 5 minutes. $NaBF_3$ (0.6 mmol, 0.0658 g) in 1mL distilled water was added to the reaction solution and left to reflux for 15h. The ratio of water to acetonitrile was 3:1. A reddish precipitate was filtered off from the red solution, washed several times with cold ethanol-water and air-dried. Yield: 0.1601 mg, 81%. Single crystals were grown by slow diffusion of *tert*-butyl alcohol into a solution of the compound dissolved in DMSO.

Crystal Data for 2dii. $Au^{III}[C_{23}H_{17}N_5O_2(Au^{I}Cl)]Cl$ (M = 737.99 g mol^{-1}), monoclinic, space group P-1 (no. 2), a = 8.5381(4) Å, b = 11.3000(5) Å, c = 13.1055(6) Å, α = 104.735(2)°, β = 97.970(3)°, γ = 98.032(3)°, V = 1190.65(10) Å^3, Z = 2, T = 153.15 K, μ(MoKα) = 8.542 mm^{-1}, D_{calc} = 2.059 g cm^{-3}, 32956 reflections measured (3.032° ≤ 2Θ ≤ 58.068°), 6312 unique reflections (R_{int} = 0.0476, R_σ = 0.0405) which were used in all calculations. The final R_1 was 0.0569 (I > 2σ(I)) and wR_2 was 0.1394 (all data).

2.5. Conclusion

All six proposed carboxamide pincer ligands, **1a-1f**, were successfully synthesised and fully characterised. The crystallographic structures were obtained for structures of **1a-1e**, which correlated with the proposed structures, and characterisation data from spectroscopy. Three of the proposed carboxamide pincers (**2d-2f**) were metallated with gold(III) to yield the desired complexes.

2.6. References

1 O. V. Dolomanov, L. J. Bourhis, R. J. Gildea, J. a. K. Howard and H. Puschmann, *J Appl Cryst*, 2009, **42**, 339–341.
2 G. M. Sheldrick, *Acta Cryst A*, 2015, **71**, 3–8.
3 G. M. Sheldrick, *Acta Cryst C*, 2015, **71**, 3–8.
4 D. J. Barnes, R. L. Chapman, R. S. Vagg and E. C. Watton, *Journal of Chemical & Engineering Data*, 1978, **23**, 349–350.
5 K. Hiratani and K. Taguchi, *BCSJ*, 1990, **63**, 3331–3333.

6 A. Casini, G. Kelter, C. Gabbiani, M. A. Cinellu, G. Minghetti, D. Fregona, H.-H. Fiebig and L. Messori, *J Biol Inorg Chem*, 2009, **14**, 1139–1149.
7 H.-Q. Liu, T.-C. Cheung, S.-M. Peng and C.-M. Che, *J. Chem. Soc., Chem. Commun.*, 1995, 1787–1788.

3. Ligand Synthesis and Characterisation

The work in this chapter has been reported in a manuscript that was published in the New Journal of Chemistry.[1]

Pincer molecules have been widely studied across the natural sciences due to their high thermal stability[2,3] and ability to sterically control the metal centres to which they are bound as tridentate ligands in metal chelates.[4,5] Some pincer molecules can selectively extract metal ions from the solution, which makes them important in separation and detection technologies.[6,7] Although pincers are mainly used as chelating agents, several of them display additional functionality by complexing anions.[8,9] Moreover, pincer-type receptors have been studied as potential ion channels in membranes due to their cation/anion-binding cores and their ability to form π-stacked arrays.[7,10]

Pincer compounds can be asymmetrical or symmetrical. The latter generally have two equivalent "arms" which can form an achiral or chiral pocket (depending on their structure). These structural attributes play an important role in metal complexes, especially in C_2-symmetric catalysts capable of chiral induction,[11,12] and these pincers are capable of functioning as anion receptors.[13] For the most part, the core of a pincer molecule is planar. However, the size and orientation of the groups constituting the arms will dictate the global conformation as well as the physical and chemical properties of the molecule. Consequently, pincer compounds may be designed to function in particular ways.

Even though many pincer molecules do not have stereogenic centres, flexibility and steric effects involving the pincer arms may introduce axial chirality (helicity) in the nominally planar molecule, producing atropisomers.[11,12] The helicity in pincer molecules arises from the presence of a 2-fold rotation axis in the molecule, favouring crystallisation in space groups containing 2-fold and 2-fold screw axes.[14] These compounds are therefore classified as P if they display right-handed helicity or exhibit a negative CD spectrum; the opposite is true for M isomers. Familiar examples of non-pincer atropisomers which possess C_2 symmetry and such chirality include the bidentate ligand BINAP (2,2′-bis(diphenylphosphino)-1,1′-binaphthyl)[15] and *ortho*-condensed polycyclic aromatic compounds (i.e., helicenes).[16,17]

Atropisomers arise due to the constrained rotation about a single bond due to steric strain; the influence of the steric strain on rotation allows for the isolation of various conformers.[15,18] Notably, atropisomerism is a significant phenomenon in medicinal chemistry and plays an important role in pharmaceutical design,[18–20] the behaviour of several natural products (e.g. Gossypol),[21] and the development of catalysts capable of asymmetric induction—specifically chirality-inducing ligands (e.g. BINOL and BINAP).[22]

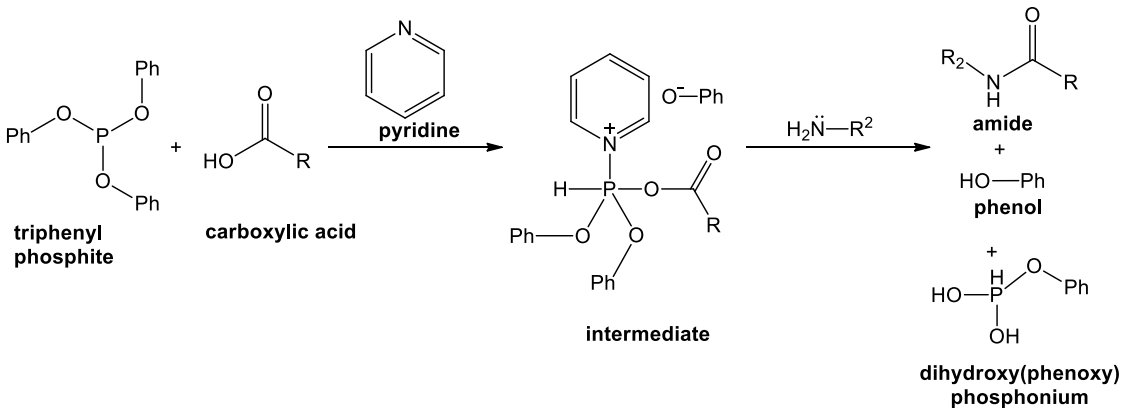
Bis(carboxamide) pincer molecules are a class of pincer molecules that have two amide groups connecting the substituent arms to the pincer core and typically display enhanced stability, which is attributable to the presence of the amide bond.[23–25] Delocalization of electrons involving the amide nitrogen lone pairs and adjacent aromatic rings further enhances the compounds' stability. Bis(carboxamide) pincers have been widely studied as their metal complexes but rarely as individual

molecules.[26] Their stability at elevated temperatures and under a range of physical and chemical conditions,[4,5,25,27] coupled with their potential chirality, suggests that metal-free bis(carboxamide) pincers might find applications in catalysis,[5,28–31] luminescent material,[32–35] molecular sensors,[36–38] drug-design,[39] ion transport,[40,41] and extraction metallurgy.[6,42,43]

In this chapter, we report on the synthesis, characterisation, and electronic and physical structures of several novel and broadly related bis(carboxamide) pincer compounds with intrinsic C_2 symmetry (gas and solution phase) as a foundation for exploring their future as C_2-symmetry ligands for biological catalysis (notably chiral induction) or other applications including pharmacology.

3.1 Ligand chemistry and synthesis

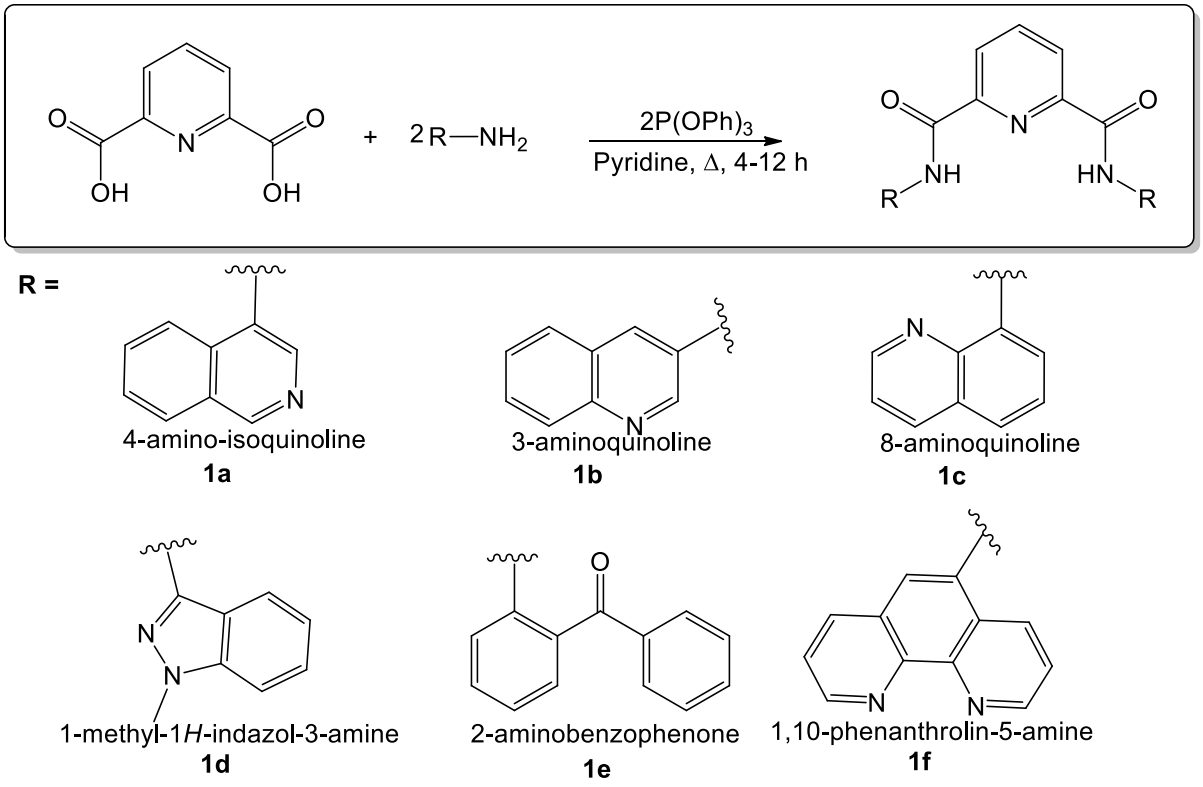
The synthesis of all carboxamide pincer ligands in this study (**1a-1f**) involved the formation of the amide bond between a pyridine-2,6-dicarboxylic acid and the selected amines. The amide bond formation follows a nucleophilic substitution reaction involving carbonyls, such as esters, acid chlorides, acid azides, and acid anhydrides, with an amine.[44–46] The direct formation of an amide from an acid and an amine typically requires strong heating or an activator.[46,47] One common activator is an acid, which protonates the oxygen, thereby enhancing the nucleophilicity of the carbonyl carbon and activating the reaction. Other activators, such as triphenyl phosphite (TPP), an oxo-acceptor, were utilised in this study. In the reaction, TPP behaves according to **Scheme 3.1**.[48–50]



Scheme 3.1. Illustration of the activation of a carboxylic acid with triphenyl phosphite and pyridine and subsequently its reaction with an amine. TPP is an oxo- and N-acceptor such that it deprotonates the acid, and accepts the oxalate together with the pyridine nitrogen, forming an unstable intermediate, which then facilitate the reaction of the amine with the carboxylate. [45,50]

The synthesis of ligands **1a-f** in this study followed a method previously employed by Barnes *et al.*, as outlined in (**Scheme 3.2**). All ligands were synthesised in a one-step route through a one-pot reaction, as depicted in **(Scheme 3.2)**.[51] Amines of interest were dissolved in pyridine along with pyridine-2,6-dicarboxylic acid for 40 minutes at 40 °C. Following this, the activator TTP, shown in **Scheme 3.1**, was added dropwise over 10 minutes and the reaction refluxed at 90 ˚C for 4h. The reaction involved the amine, carboxylic acid, and the activator TTP in a 2.1:1:2 ratio, respectively, where two amine molecules reacted with one molecule of the acid. Excess amine was used to ensure the reaction reached completion. Ethanol was introduced to the resulting solution, and the mixture was left to precipitate

overnight at room temperature. While all starting materials were soluble in ethanol, the product was not, allowing for a clean product without the need for additional purification. The exception was **1f**, which precipitated directly from the solution. White and cream precipitates were filtered under vacuum and washed with cold ethanol. Despite high yields ranging from 94-98%, the products exhibited poor solubility attributed to strong intermolecular interactions.



Scheme 3.2. General synthetic scheme of the ligands **1a-f** and their structures

Computational studies, specifically Density Functional Theory (DFT) calculations, were implemented to gain a deeper understanding and elucidate the characteristics of the compounds. These calculations were carried out using Gaussian W09, and input structures were created or modified using GaussView 6.0.16. Data interpretation was further facilitated using GaussSum 3.0. X-ray crystal structures were utilised as input data, while **1f**, lacking an X-ray crystal structure, did not undergo computational studies. Geometric optimisations and frequency calculations were conducted using the HSEH1PBE method in the SDD basis set, and the energy of the orbitals was computed with the TD-SCF/HSEH1PBE method in the SDD basis set unless specified otherwise. The results from these computational studies are discussed whenever pertinent to the topic at hand.

Only exemplary spectra are presented in this chapter, while the complete set of spectra can be found in the supplementary information provided in a separate document. Mass spectroscopic data is not discussed in this chapter; however, the data is available in **Chapter 2** and in the supplementary information (**Section 1.4, Figures S26-S35**).

3.2 Ligand characterisation

3.2.1 IR spectroscopy

The formation of the amide bond was a critical indicator of successful ligand formation, and consequently, changes in the NH and C=O bands were the primary characteristics in all spectra. The presence of a single N-H stretching peak on ligands **1a-f**, which shifted downfield compared to the primary amine on the synthons, served as confirmation of amide bond formation. Additionally, the appearance of the amide C-N band in the spectrum further confirmed the formation of amide bonds (although the C-N is challenging to define as it is in the fingerprint region). According to **Table 3.1**, all significant bands were observed within the expected ranges from the literature,[52,53] supporting the deduction that compounds **1a-f** were successfully synthesised. Importantly, the spectra from experimental data were consistent with the calculated data for all ligands, as illustrated in **Figure 3.1** and **Figure 3.1**

Table 3.1. Frequency of characteristic IR absorption bands for **1a-1f** from the experimental data in cm^{-1}.

	C=O	N-H stretch	N-H Bend (In-plane bend)	N-H Bend (Out of plane bend)	C-N stretch
1a	1677.07	3282.09	1540.63	745.68	1333.23
1b	1682.70	3192.12	1592.96	744.92	1368.86
1c	1677.70	3320.75, 3296.48	1531.13	746.77	1327.97
1d	1690.98	3309.89	1583.04	731.58	1247.72
1e	1695.07	3209.41	1510.09	740.69	1242.71
1f	1675.65	3298.28	1500.65	738.39	1421.55/1382.56

Since compounds **1a-1f** share the same general functional groups, their spectra exhibit considerable similarity (**Figure 3.1**). The values obtained from the calculated data () closely align with the experimental data (**Table 3.3**), with differences potentially arising from variations in the physical conditions of the experiments. Notably, the most significant difference was observed in the amide nitrogen, which could be attributed to (i) intra- and inter-molecular hydrogen bonding and (ii) delocalisation across the O-C-N bond. These factors were challenging to fully consider in the calculations. Despite their overall similarity, the pincers exhibit different types of hydrogen bonding, as deduced from their crystallographic data, which may contribute to deviations in the calculated data. Hydrogen bonding also influences the delocalisation of electrons across the O-C-N bond, leading to differences in the frequencies of the amide bonds.

Table 3.2. Calculated IR frequency for significant absorption bands of **1a-e** in cm^{-1}.

	C=O stretch/ N-H in-plane stretch wagging		N-H stretch		N-H out of plane wagging	
	symmetric	asymmetric	symmetric	asymmetric	symmetric	asymmetric
1a	1706.40	1699.42	3621.51	3613.07	803.84	747.04
1b	1706.71	1700.65	3599.02	3586.80	819.93	762.09
1c	1667.76	1654.26	3501.68	3499.79	906.90	896.07
1d	1717.39	1710.62	3618.89	3605.38	777.05	730.03
1e	1694.61	1687.54	3378.11	3371.27	805.06	793.38
1f	-	-	-	-	-	-

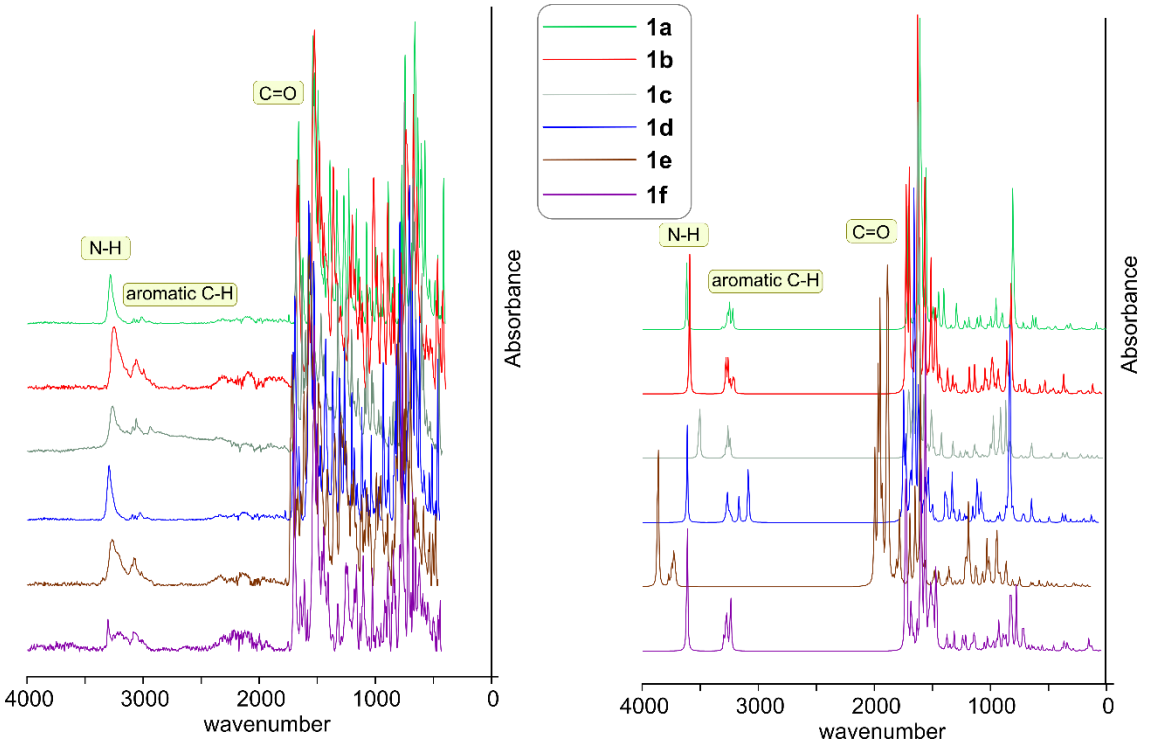


Figure 3.1. IR spectra of the synthesised carboxamide pincer ligands **1a-1f** (left) in comparsion to the calculated data (right).

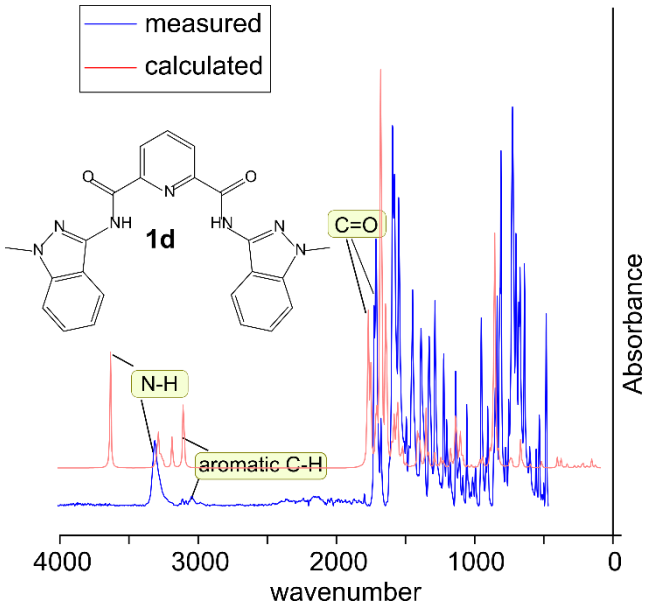


Figure 3.2. A comparison of the IR spectra of **1d** from the experimental work (blue), and the calculated data **(pink)**

Table 3.3. The percentage difference between calculated and experimental IR data for **1a**

	C=O stretch	N-H stretch	N-H out of plane wagging
Experimental	1677.07	3282.09	745.68
Calculated	1706.40	3621.51	747.04
% Difference	1.73	9.83	0.18

Overall, the introduction of the amide NH spectroscopy peaks confirmed the synthesis of new compounds with an amide bond.

3.2.2 Nuclear Magnetic Resonance (NMR) spectroscopy

Following the confirmation of all anticipated peaks, NMR was employed to elucidate the 2D structure of **1a-1f**. ^{1}H, ^{13}C and 2D NMR spectra were primarily used to characterise the pincers. The main characteristic of the pincers is the amide proton, which is signalised by a single peak downfield in the spectrum, between 9 and 13 ppm, **Table 3.4** and **Figure 3.3**. The chemical shifts of the amide proton are highly influenced by the arms of the pincer since they are the only variable in the molecules.

The pincer arms in **1a**–**1c** comprise different structural isomers of quinoline. There is enhanced deshielding of the amide protons due to the proximity of the quinoline nitrogen atoms to the amide proton 2–3 atoms away; hence the proton signals are found further downfield in the spectrum in comparison to the proton signals in **1e** and **1f**. Of the three quinolines, **1c** has the highest NH chemical shift, which is attributed to the proximity of the proton of interest to the adjacent molecule through space. The amide proton signal for **1d** falls within a similar range for the same reason, although the chemical shift is higher due to the presence of the indazole ring. The amide proton in **1d** has a higher chemical shift than the amide proton in **1e** because the benzophenone group on the arms of **1e** reduces the electron-donating capacity of the entire group when compared to the phenanthroline group in **1f**. The same principles apply to the chemical shifts of the amide carbons.

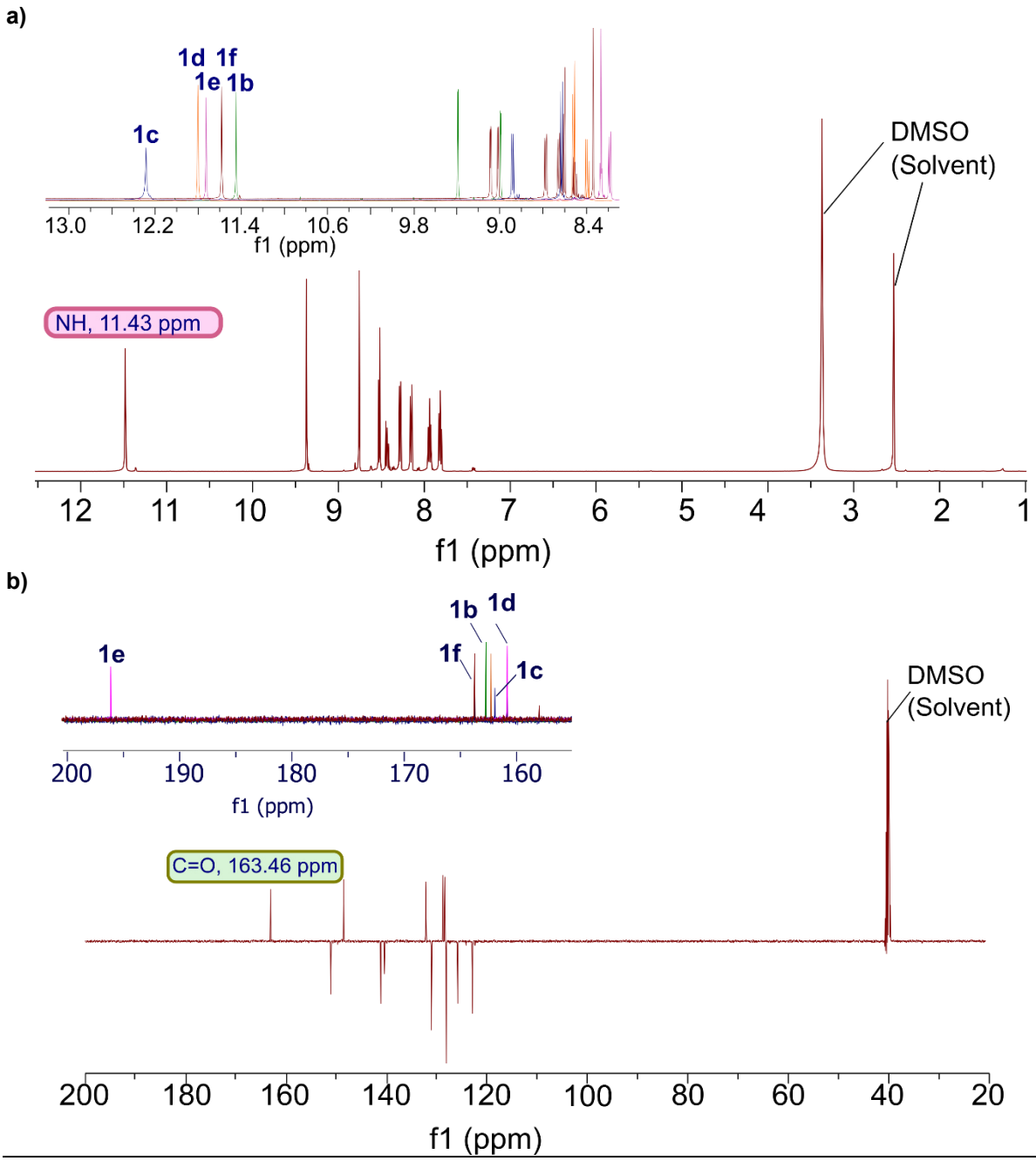


Figure 3.3. Illustration of the proton **(a)** and carbon **(b)** NMR spectra for **1a** (maroon lines, main spectra). The inset figures, in each case, display the variation in the chemical shift of the amide NH protons and the C=O carbons for the pincer compounds **1b–1f.**

Table 3.4. Chemical shifts for selected atoms in the synthesised carboxamide ligands in ppm

	Amide NH	Amide C	Pyridine H (a)	Pyridine H (b)	Pyridine C (a)	Pyridine C (b)	Pyridine C (c)
1a	11.43	163.46	8.38	8.48	140.39	125.72	148.56
1b	11.45	162.82	8.33	8.43	140.30	125.66	148.37
1c	12.36	164.27	8.27	8.59	139.63	125.44	148.70
1d	11.80	161.85	8.34	8.46	138.24	125.49	148.55
1e	12.24	161.89	8.04	8.35	139.28	125.12	148.56
1f	11.61	163.53	8.43	8.53	140.82	126.13	148.98

Given that ligands **1a-1f** share the same backbone motif, the signals for these atoms are expected to appear within a similar range on the spectrum, typically within ~2 ppm of each other. However, the chemical shifts of the protons and carbons of interest are significantly influenced by the type of intermolecular interactions present in the compound. Generally, **1a-c** should exhibit similar chemical shifts, with the main differences likely residing in the aromatic region corresponding to the quinoline groups due to differences in the arrangement of atoms.

In reference to the X-ray data in **Section 3.2.5**, **1c** exhibits intermolecular hydrogen bonding, resulting in the amide protons shifting to a chemical shift as compared to **1a** and **1b**, which do not exhibit intramolecular or intermolecular hydrogen bonding. The amine protons in **1c** are involved in hydrogen bonding, thus there is enhanced deshielding on those specific protons, thus the peaks are further downfield. The NH protons in **1e** exhibit the same phenomenon as **1b**, as the protons are also involved in hydrogen (intramolecular) bonding. For **1d**, the chemical shift for the NH protons is slightly higher as it is involved in intermolecular hydrogen bonding. Overall the peaks for protons not involved in any form of hydrogen bonding appear at lower chemical shifts.

In summary, NMR spectroscopy provided valuable insights into the structures of the synthesised carboxamide ligands, and confirmed the successful synthesis of the carboxamide pincer ligands **1a-1f**.

3.2.3 Melting temperatures

The vast difference in the melting temperature ranges of the isomeric pincers (**Table 3.5**) is attributed to the structural differences in the pincer arms. The presence of the amide bond in the molecules facilitated intermolecular and/or intramolecular hydrogen bonding.[26] This property influenced the solubility and melting temperatures of the compounds. Molecules with intermolecular hydrogen bonding, typically, exhibit stronger interactions between the molecules and hence have a higher melting point.[26,54,55] The synthesised compounds **1a-f** demonstrated high dissolution temperatures, particularly in solvents with moderate polarity. The polarity of the solvent played a crucial role in the solubility of these polar molecules.

The nitrogen-containing heterocycles on the pincer arms contributed to the polarity of the synthesised compounds. Different orientations of these arms in various compounds exposed different groups, affecting the overall polarity of the complex. Exposing polar groups in the compound increased their polarity, rendering them soluble in polar solvents. Such compounds favoured intermolecular hydrogen bonding, leading to interactions between molecules through electrostatic forces, ultimately elevating their melting points. While these compounds could dissolve in other polar solvents at elevated temperatures, they tended to precipitate out of the solution at temperatures below 10 °C, posing challenges for tests at very low temperatures, such as temperature-variable NMR.[26]

The reported melting temperatures of the pincers fall within the range of 207 °C to 410 °C (**Table 3.5**). These high melting temperatures demonstrate the enhanced stability of the compounds, which showed no decomposition at elevated temperatures (above 200 °C). This presumably reflects strong intermolecular interactions, like hydrogen bonding, which requires more energy for melting relative to compounds bound by hydrophobic interactions and π-stacking. The extensiveness of π-stacking in

compounds, however, significantly affects the strength of the intermolecular interactions; the aromatic nature of **1a**–**1f** likely enhances their stability further.

Figures 3.8, 3.9 and 3.10, illustrate the type of hydrogen bonding in each compound. Pincer **1a** has the highest melting point as it exhibits intermolecular hydrogen bonding, unlike the other pincers, which only exhibit intramolecular hydrogen bonding. The crystallographic data of **1b** did not provide enough information on the type of intermolecular interactions between the molecules, as methanol co-crystallised with the compounds. It is, however, assumed that the high melting temperature resulted from strong intermolecular interactions in the compound. Pincer **1c**, which exhibits intramolecular hydrogen bonding, has the lowest melting temperature among the quinoline-based pincers, as the main forces of intermolecular interactions in the compound are π-stacking and hydrophobic interactions. Pincer **1d** is an anomaly to this trend as it has a significantly lower melting temperature than **1c** despite exhibiting inter-molecular hydrogen bonding. Pincer **1e** has the lowest melting point of all the pincers. The pincer arms of **1e** are flexible and do not allow for close packing, as there is additional distortion, which results in the arms losing their planarity. All the other pincers, however, π-stack to different degrees. **1f** presumably exhibits the most π-stacking because of the three aromatic rings on each pincer arm, thus enhancing the interaction between its atoms.

Table 3.5. Melting temperature of **1a-f**, the type of interactions between molecules and their solubilities in different solvents. Information on this kind of bonding was extracted from the crystallographic data explained in **Section 3.2.5**

	1a	**1b**	**1c**	**1d**	**1e**	**1f**
Melting Temperature range (°C)	400-410	370-377	308-319	298-305	207-212	270-279
Hydrogen bonding type	Intermolecular	Intermolecular	Intramolecolar	Intermolecular	Intramolecular	Intramolecular
Intermolecular interactions	Dipole-dipole attraction	Dipole-dipole attraction	Hydrophobic	Dipole-dipole attraction	Hydrophobic	Hydrophobic
Solvent with the best solubility	DMSO	DMSO	Chloroform	DMSO/ Acetonitrile	Methanol	DMSO
Solubility conditions	Very high temperatures >200 °C	High temperature >150 °C	Room temperature	Slightly high temperature >50 °C	Slightly high temperature >50 °C	High temperature >200 °C

3.2.4 UV-Vis Spectroscopy

UV spectroscopy was used to calculate the molar attenuation coefficient of the ligands according to the Beer-Lambert law (**Equation 3.1**)

$$\mathbf{A = \log\left(\frac{I_0}{I}\right) = \varepsilon lc} \qquad \text{Equation 3.1}$$

Where

- A is absorbance,
- I_0 and I are initial light intensity and intensity of the light transmitted through respectively,
- ε is molar absorption coefficient,
- l is path length, and
- c is concentration of solution.

Changes in the concentration of the solution result in shifts of the bands of interest, either to the left or right, or up and down. Band shifts to longer wavelengths (red-shift) and shifts to shorter wavelengths (blue-shift) are termed bathochromic shifts and hypochromic shifts, respectively. Hyperchromism and hypochromism refer to changes in the absorption band's peak intensity, respectively.[56]

Aromaticity (conjugation) in compounds **1a-1f** reduces the energy between HOMO and LUMO, enabling the absorption of light measureable by spectrophotometers, which typically measure above 200 nm for organic molecules. This is attributed to the availability of π-electrons, allowing for π→π* transitions. These transitions occur below 400 nm with ε between 100 and10000 M^{-1} cm^{-1} (**Table 3.6**). An example of how this data was calculated is illustrated in **Figure 3.4**.

The data was corroborated with the calculated data as illustrated in **Figure 3.5a)** and **b).** The experimental data showed that the main transitions were π→π* transitions, consistent with expectations for these aromatic compounds (**Figure 3.5c)**).

Table 3.6. Extinction coefficients at λ_{max} for π→π* transitions in ligands **1a-1f.**

	solvent	**λ_{max} (nm)** **ε (M^{-1} cm^{-1})**	**λ_{max} (nm)** **ε (M^{-1} cm^{-1})**	**λ_{max} (nm)** **ε (M^{-1} cm^{-1})**	**λ_{max} (nm)** **ε (M^{-1} cm^{-1})**
1a	DMSO	277 1.0932×10^4	309 9.219×10^3	323 1.0513×10^4	
1b	DMSO	275 2.3626×10^4	312 1.7499×10^4	324 1.7699×10^4	338 1.5887×10^4
1c	DMSO	326 8.6031×10^4			
1d	MeCN	223 1.8459×10^4	285 1.5214×10^4		
1e	DMSO	330 7.388×10^3			
1f	DMSO	269 7.5016×10^4	315 1.5699×10^4		

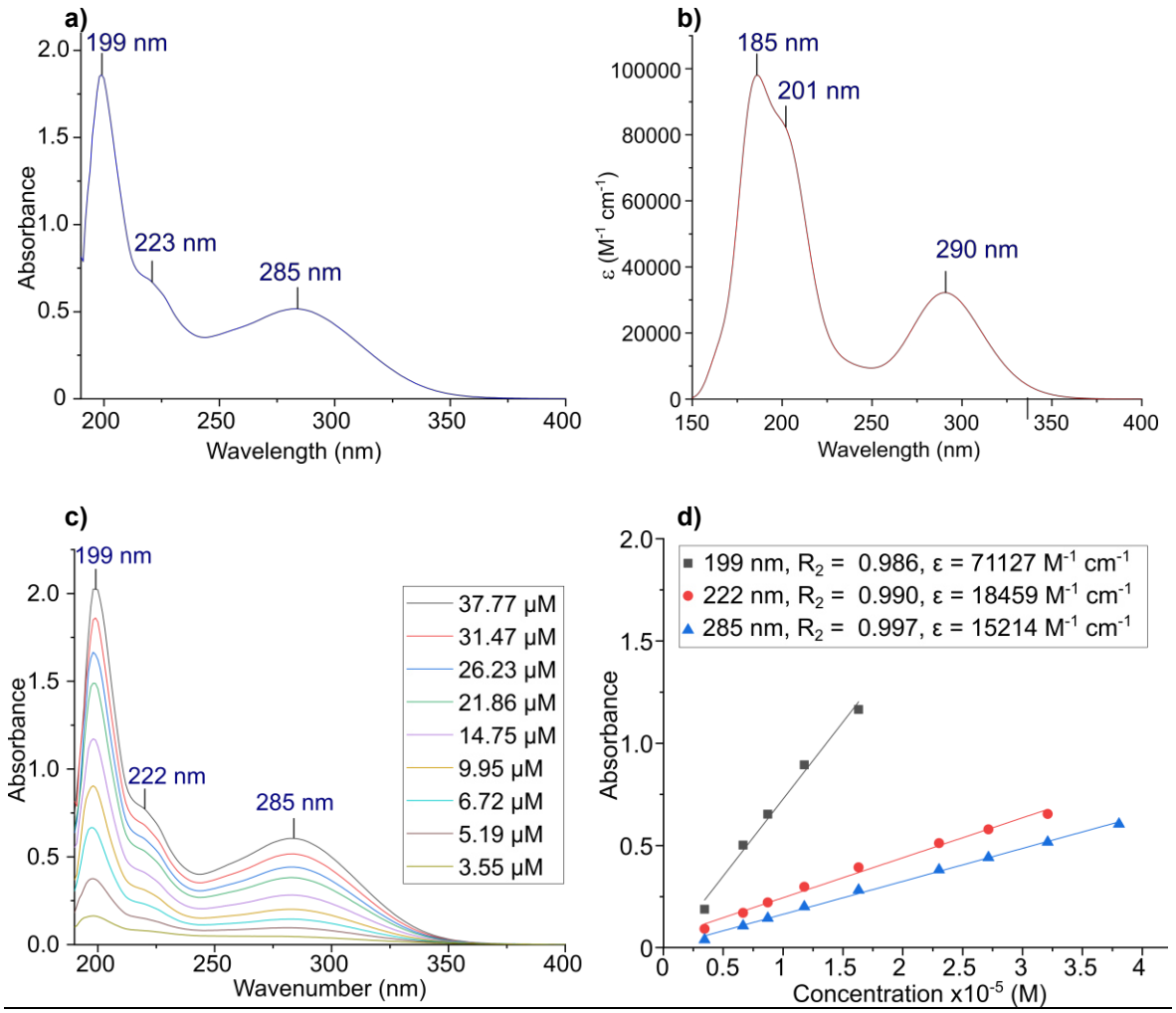


Figure 3.4. (a) Experimental and **(b)** DFT-calculated electronic absorption spectra of **1d** in DMSO. The absorption maxima are indicated for the experimental spectrum at 199, 222 and 285 nm. The absorption envelope for the DFT-calculated spectrum is plotted with a band width of 2200 cm^{-1} (full width at half maximum intensity, FWHM). **(c)** Absorption spectra at a concentration range between 3 and 38 μM, to calculate the extinction coefficients at the λ_{max} in **(d)** (Beer-Lambert's Law).

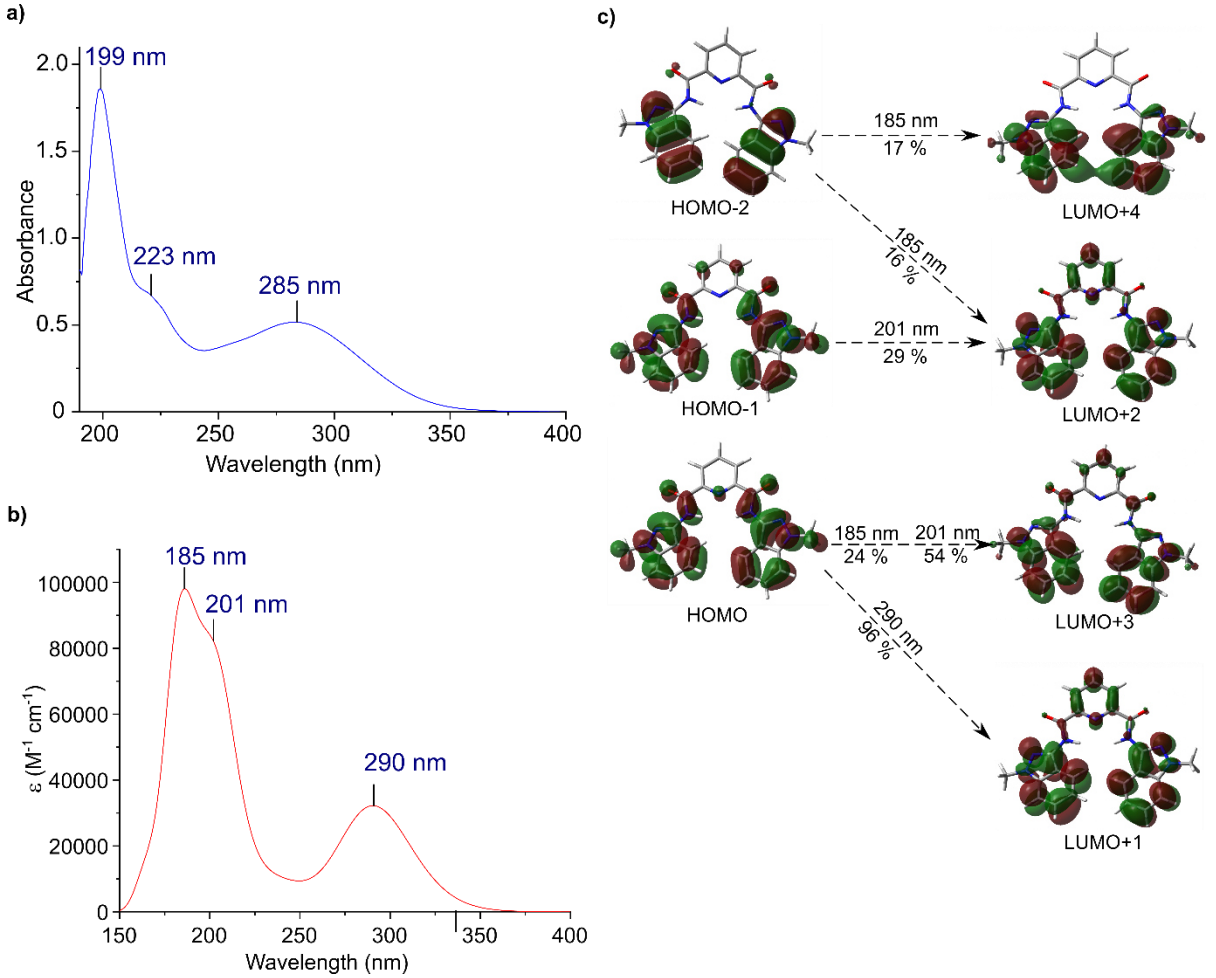


Figure 3.5. a) Experimental and **b)** DFT-calculated electronic absorption spectra of **1d** in DMSO. The absorption maxima (λ_{max}) are indicated for the experimental spectrum at 199, 223 and 285 nm, The absorption envelope for the DFT-calculated spectrum is plotted with full width at half maximum intensity (FWHM) of 3000 cm^{-1} adjusted by -80 nm; **c)** Molecular orbital involved in the three most intense bands in the DFT-calculated electronic spectrum of **1d** DMSO. The percentage contribution of the electronic transitions to each band is indicated.

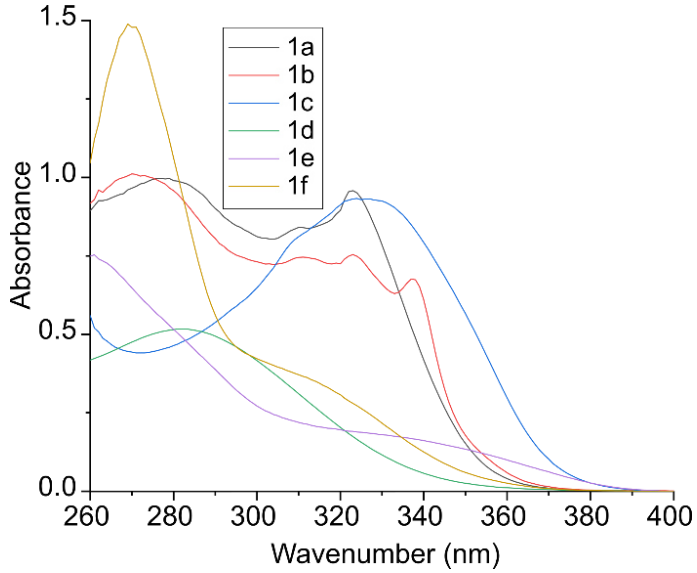


Figure 3.6. Experimental electronic absorption spectra of **1a-1f** in different solvents**.**

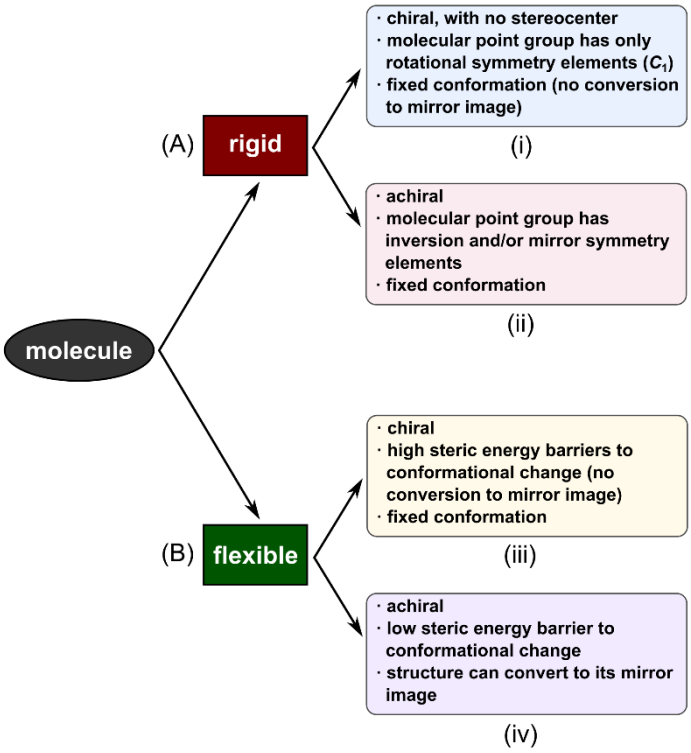
The spectra of **1a-c** are nearly identical, displaying numerous peaks in the range of 300-380 nm (**Figure 3.6**). While the peaks in **1a** and **1b** are more resolved, there is a hint of bands in a similar range in **1c** (with a shoulder at 310 nm).

Based on the characterisation data, it was concluded that the desired products were successfully synthesised and subsequently utilised for the synthesis of the metal complexes.

3.2.5 Xray crystallography

There are more than 600 carboxamide pincer molecules recorded in the CSD, and none of them is being reported in this study, so it is certain that they are novel. It was mentioned in **Chapter 2** that the 2D structure of **1b** has been reported, the absence of any records of the pincer in the CSD database implies that this X-ray crystal structure has not been studied before.

Although pincer molecules do not have any stereogenic centres, flexibility and steric effects involving the pincer arms may induce axial chirality (helicity) in the nominally planar molecule, producing atropisomers.[12,11] Helicity ensuing from the presence of a 2-fold rotation axis in the molecule, favors crystallisation in space groups containing 2-fold and 2-fold screw axes.[14] Familiar examples of non-pincer molecules which possess C_2 symmetry and such chirality include the didentate ligand BINAP (2,2′-bis(diphenylphosphino)-1,1′-binaphthyl)[15] and *ortho*-condensed poly-cyclic aromatic compounds (i.e., helicenes[16,17]).



Scheme 3.3. An outline depicting the scenarios, which allow molecules to crystallize in the 65 Sohncke space groups, i.e., those containing only symmetry operations of the first kind (rotations, roto translations, translations).[56]

Scheme 3.3 outlines how molecules with no stereocenters crystallise in Sohncke space groups. The molecules can be rigid, locking them in one conformer, or flexible, which allows them to interchange

between conformers. Pincer molecules are usually flexible as rotations are typically feasible about specific torsion angles (i.e., there are several internal degrees of freedom). Facile conversion to a mirror image conformer is typically allowed if the barrier to rotation of spatially separate groups (i.e., the pincer arms) in the molecule is low, as listed in scenario (iv) of **Scheme 3.3**. This normally requires that intramolecular nonbonded interactions remain above a distance threshold limit of *ca.* 1.5 Å for such rotations.[57] Scenario (iii) prevails when this threshold cannot be met, and the molecule becomes locked in one conformation. Scenario (iii) results in spontaneous resolution and the compound crystallizes in only one conformer; the crystal structure then falls under a chiral Sohncke space group, usually $P2_12_12_1$. This phenomenon is absent in scenario (iv), so the compound crystallizes as a racemate and its crystals will belong to an achiral Sohncke space group.[57]

3.2.5.1 Ligands crystallographic data

Crystals suitable for X-ray diffraction were grown for **1a**–**1e** either by slow solvent diffusion or by slow evaporation. The diffraction data were collected at low temperature (≤ 173.15 K) to $2\theta > 56°$, even for the weakest diffracting samples. The structures refined to impressively low *R*-factors (typically ~2% and ~5–9% better R_1 and wR_2 values, respectively) using non-spherical atom form factors (NoSpherA[58] implemented in Olex2[59]) from electron density distributions calculated at the r^{2}SCAN[60]/cc-pVTZ[61] level of theory (DFT).

The low-temperature X-ray structures of the five pincer compounds are shown in **Figure 3.7**, and their crystal and structure refinement data is tabulated in **Table 3.7**. All the compounds studied exhibit intrinsic C_2 symmetry (or C_{2v} symmetry in the case of **1d**) in the gas phase or in solution (DFT simulations, *vide infra*) which hinges on each arm within the pincer having identical dihedral angles spanning the amide linker groups. Exact C_2 symmetry is mainly feasible for relatively rigid, isolated structures. However, the mean conformation of a statistical ensemble of symmetrically substituted flexible pincers containing a 2-fold axis of rotation in solution may also display C_2 point group symmetry if the planar C_{2v} structure is a transition state between inverted C_2 symmetry conformers and thus only transiently populated. In the crystalline solid state, and to allow for close packing, significant non-bonded packing interactions, hydrogen-bonding, and dimer or oligomer formation are likely to induce local twisting of the lowest energy C_2 symmetry conformer or introduce an additional symmetry element such as a centre of inversion. Distortions will clearly destroy any intrinsic C_2 symmetry, while the formation of dimeric inversion pairs (C_i symmetry) through hydrogen bonding between C_2 symmetry monomers, would preserve the intrinsic C_2 symmetry of each interacting moiety but ensure crystallization in a non-Sohncke space group. Thus, the expectation is that flexible pincers with intrinsic C_2 symmetry will rarely crystallize with exact crystallographic C_2 symmetry in a Sohncke space group.

From the X-ray structures of **1a**–**1e** (**Figure 3.7**), only **1c** crystallises as a monomer in the chiral Sohncke space group $P2_12_12_1$; its conformation is, however, distorted by crystal packing interactions and thus lacks precise C_2 symmetry (despite this being possible in the gas phase). Although uncommon in the literature, pincers based on a pyridine core that crystallize in chiral space groups are known and typically exhibit C_1 point group symmetry due to deviations from ideal C_2 symmetry engendered by

crystal packing forces. Three pertinent examples highlighting this general trend are *N*,*N*'-bis(2-methoxyphenyl)pyridine-2,6-dicarboxamide (CSD code CABWUY, space group $P2_12_12_1$),[62] tetra-*n*-butylammonium *N*,*N*'-bis(2,3-dimethyl-1*H*-inden-7-yl)-2,6-pyridinedicarboxamide fluoride (EDIKOS, $P2_1$),[40] and 2,6-dicarbonyl-bis(2'-amino-2''-*L*-methylalaninebenzanilidyl)pyridine (GICKEY, *P*1).[41] The latter pincer compound contains enantiopure pincer arms and possesses helical symmetry, making it suitable as a tridentate ligand for chiral induction in catalysis. Of the 250 bis(arylcarboxamide)pyridine pincers currently present in the Cambridge Structural Database (CSD),[63] only 13 or 5% of the non-macrocyclic structures crystallize in chiral space groups (*P*1 and $P2_12_12_1$ being the most common). As might be expected, the structure of **1c** reported here at 173 K is broadly similar to that reported at 294 K (CSD code NIWNUD, $P2_12_12_1$);[64] the data quality is, however, superior.

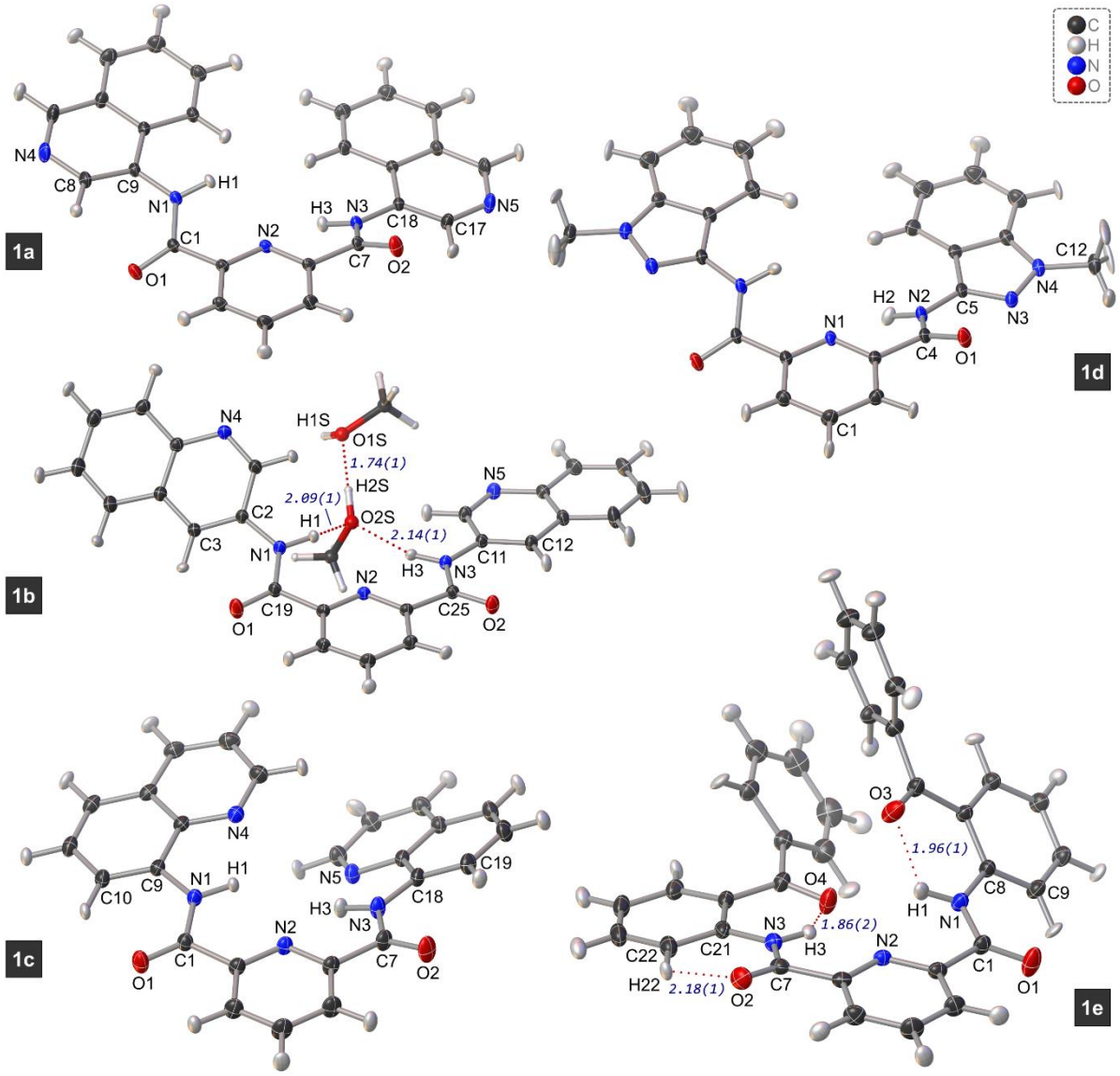


Figure 3.7. Selectively labelled views of the X-ray crystal structures of **1a–1e** refined with non-spherical atom form factors (NoSpherA2 within Olex2). Thermal ellipsoids are rendered at the 50% probability level (C, N, O). Hydrogen atom thermal ellipsoids are scaled to have the same equivalent isotropic displacement parameter, $U_{(eq)}$, as the attached heavy atom. H-bond distances and angles for **1b:** N5···H1S, 1.813(8) Å; H1···O2S, 2.086(6) Å; H3···O2S, 2.141(6) Å; H2S···O1S, 1.744(9) Å; N5···H1S–O1S, 168.3(7)°; N1–H1···O2S, 133.5(5)°; N3–H3···O2S, 158.8(5)°; O2S–H2S···O1S, 174.4(7)°. H-bond distances and angles for 1e: H1···O3, 1.96(1) Å; H3···O4, 1.86(1) Å; H22···O2, 2.18(1) Å; N1–H1···O3, 126(1)°; N3–H3···O4, 137(1)°; C22–H22···O2, 120.6(7)°. Space groups: $P2_1/c$, **1a;** $P\bar{1}$, **1b;** $P2_12_12_1$, **1c**; $P2/c$, **1d;** $P2_1/n$, **1e.** Significant nonbonded crystal packing and hydrogen bonding interactions break the intrinsic C_2 symmetry o**f 1a, 1b,** and **1e,** preventing their crystallisation in Sohncke space groups. Only **1d** has exact C_2 symmetry in the crystalline solid state; however, crystallisation as a C_i symmetry dimer restricts it to a regular space group. Compound **1c** has C_1 point group symmetry due to asymmetric packing interactions which break its C_2 symmetry. Since higher-symmetry oligomer formation is absent**, 1c** is the only compound of the series that crystallises in a chiral space group.

Table 3.7. Crystal data and structure refinement for **1a-1e.**

	1a	**1b**	**1c**	**1d**	**1e**
Empirical formula	$C_{25}H_{17}N_5O_2$	$C_{27}H_{25}N_5O_4$	$C_{25}H_{17}N_5O_2$	$C_{23}H_{19}N_7O_2$	$C_{33}H_{23}N_3O_4$
Formula weight	419.43	483.52	419.43	425.45	525.54
Temperature/K	173.15	153	173.15	153.15	153.15
Crystal system	monoclinic	triclinic	Orthorhombic	Monoclinic	Monoclinic
Space group	$P2_1/c$	P-1	$P2_12_12_1$	P2/c	$P2_1/n$
a/Å	8.7392(4)	7.2743(3)	4.4778(2	10.4220(2)	8.4952(2)
b/Å	14.6766(8)	11.3528(5)	16.9420(7)	11.8014(3)	18.3345(4)
c/Å	15.2758(8)	14.9566(5)	25.8329(10)	8.6298(2)	16.2123(3)
α/°	90	76.6050(10)	90	90	90
β/°	102.656(2)	78.8710(10)	90	112.0760(10)	90.6890(10)
γ/°	90	78.901(2)	90	90	90
Volume/Å^3	1911.70(17)	1164.76(8)	1959.76(14)	983.60(4)	2524.97(9)
Z	4	2	4	2	4
ρ_{calc}g/cm^3	1.457	1.379	1.422	1.437	1.382
μ/mm^{-1}	0.096	0.095	0.094	0.097	0.092
F(000)	872	508	872	444	1096.0
Crystal size/mm^3	0.40 × 0.20 × 0.20	0.37 × 0.24 × 0.10	0.50 × 0.06 × 0.02	0.50 × 0.30 × 0.13	0.22 x 0.16 0.14
Radiation	MoKα (λ = 0.71073)	MoKα (λ = 0.71073)	MoKα (λ = 0.71073)	MoKα (λ = 0.71073)	MoKα (λ 0.71073)
2Θ range for data collection/°	5.526 to 66.466	5.778 to 66.428	5.526 to 66.466	4.218 to 63.288	3.354 to 56.7
Index ranges	-13 ≤ h ≤ 13, -22 ≤ k ≤ 22, -23 ≤ l ≤ 23	-11 ≤ h ≤ 11, -17 ≤ k ≤ 17, -23 ≤ l ≤ 22	-5 ≤ h ≤ 5, -22 ≤ k ≤ 22, -34 ≤ l ≤ 34	-15 ≤ h ≤ 15, -17 ≤ k ≤ 17, -12 ≤ l ≤ 10	-11 ≤ h ≤ 11, ≤ k ≤ 24, -21 ≤ 20
Reflections collected	38057	85712	30791	23433	38759
Independent reflections	7299 [R_{int} = 0.0277, R_{sigma} = 0.0189]	8894 [R_{int} = 0.0459, R_{sigma} = 0.0265]	4830 [R_{int} = 0.0305, R_{sigma} = 0.0205]	3319 [R_{int} = 0.0293, R_s = 0.0173]	6322 [R 0.0562, R_{sign} 0.0479]
Data/restraints/parameters	7299/0/297	8894/0/343	4830/0/347	3319/0/151	6322/0/361
Goodness-of-fit on F^2	1.017	1.067	1.045	1.052	1.025
Final R indexes [I>=2σ (I)]	R1 = 0.0408, wR2 = 0.1152	R_1 = 0.0487, wR_2 = 0.1225	R1 = 0.0328, wR2 =	R_1 = 0.0429, wR_2 = 0.1150	R_1 = 0.04 wR_2 = 0.0944
Final R indexes [all data]	R1 = 0.0493,	R_1 = 0.0663,	R1 = , wR2 =	R_1 = 0.0517,	R_1 = 0.08

Interestingly, pincers **1a** and **1d** form hydrogen-bonded dimers with C_i symmetry (i.e., inversion pairs) in the solid state, with the individual monomers making up each dimer exhibiting near (**1a**) or exact (**1d**) C_2 symmetry (**Figure 3.8a**). These two structures are therefore achiral. Collectively, and considering the symmetry of the monomeric pincer ligands, only one of the five structures crystallized here (**1d**) displays crystallographic C_2 symmetry.

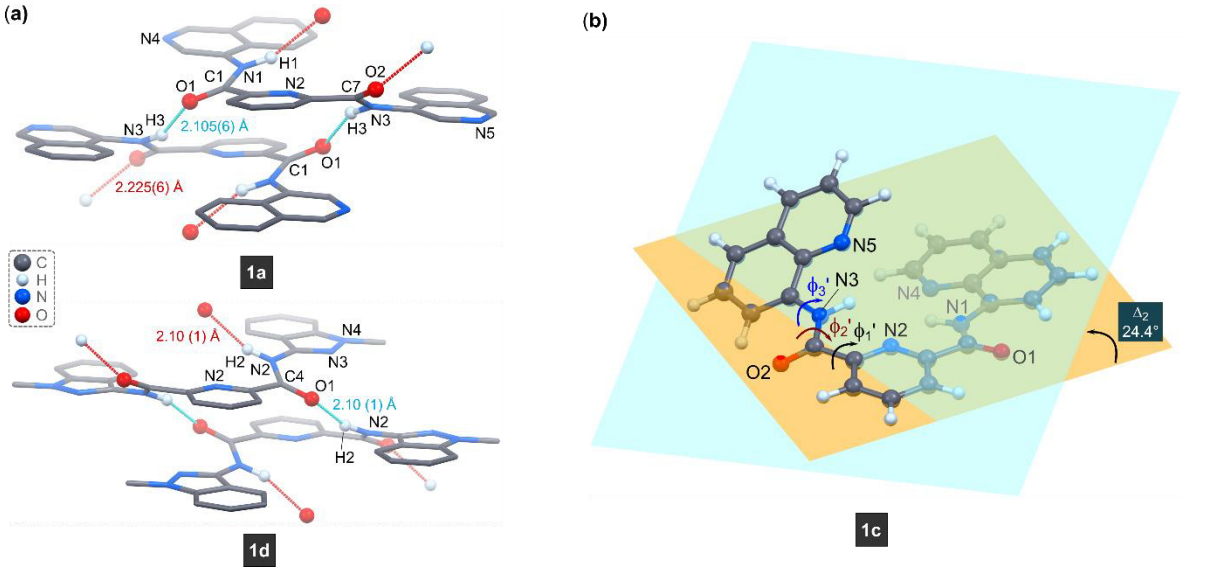


Figure 3.8. a) (**a**) View of the *C*i symmetry hydrogen-bonded dimers formed by monomers of **1a** (top; symmetry codes *x*,*y*,*z* and 1-*x*,1-*y*,1-*z*) and **1d** (bottom, exact C_2 point group symmetry; symmetry codes *x*,*y*,*z* and 1-*x*,*y*,1/2-*z*). The linear chain of dimers (**1a**) or evenly spaced monomers (**1d**), where assembly is about centres of inversion in the lattice, favours crystallisation in non-Sohncke space groups. Non-polar hydrogen atoms are omitted for clarity; atoms involved in hydrogen bonding are rendered as spheres (arbitrary radii). (**b**) Illustration highlighting the nonplanarity of pincer 1**c** and the dihedral angle (Δ_2, 24.4°) between the planes passing through the central pyridine ring and the canted quinoline ring appended to the amide group containing carbonyl oxygen O2. Torsion angles defining the orientation of the second quinoline ring substituent ($\phi1'$–$\phi3'$) are defined; the equivalent torsion angles for the first quinoline ring (right side) are $\phi1$–$\phi3$ (i.e., unprimed).

The key questions are (i) how common are crystalline C_i symmetry dimers formed by bis(arylcarboxamide)pyridine pincers in the literature and (ii) how many of these comprise monomers with exact C_2 symmetry?

Inspection of the 250 structures available in the CSD for this class of compounds indicates that only 13 (or 5%) of the compounds comprise C_2 symmetry monomers within hydrogen-bonded or p-stacked inversion pairs (C_i symmetry dimers). Only one compound, *N*,*N*'-bis(2-((4-oxopent-2-en-2-yl)amino)phenyl)pyridine-2,6-dicarboxamide; CSD code POHNOQ)[65] crystallises in the space group *P*2/c (akin to **1d**); the remaining 12 compounds crystallize in the related space group *C*2/c. Salient examples with similar structures to **1d** include *N*,*N*'-bis(4-bromophenyl)pyridine-2,6-dicarboxamide (CSD code MEWNEJ),[66] *N*,*N*'-bis(4-methylphenyl)pyridine-2,6-dicarboxamide (CSD code RABZUQ),[67] and more elaborate helical C_2 symmetry derivatives such as *N*,*N*'-bis(2-{[(anthracen-9-yl)methylidene]amino}phenyl)pyridine-2,6-dicarboxamide (CSD code WOMTOK).[68] The remaining structures in the series (**1b**, **1e**) have reduced molecular symmetry (C_1) due to conformational distortions engendered by nonbonded crystal packing interactions and/or hydrogen-bonding interactions. In the case of **1b**, hydrogen-bonding to the solvent methanol molecules significantly distorts the conformation from ideal (expected) C_2 symmetry (Figure 3.7). For the above reasons, **1a**, **1b**, **1d**, and **1e**, all crystallise in non-Sohncke space groups (the are flexible and belong to Group B (**iv**) in **Scheme 3.3)**, despite their inherent propensity to adopt C_2 molecular symmetry in the gas phase (DFT simulations, *vide infra*).

Clearly, the key conformational signature of structures **1a**–**1e** is that none is planar; the substituent arms of the pincers are all canted relative to the mean plane of the pyridine core (**Figure 3.8b, Table 3.8**). For **1b**, the nonplanarity is particularly marked with the 10-atom mean plane of the quinoline ring containing N4 canted by 40.6° relative to the 8-atom mean plane of the central pyridine ring and the two carbonyl carbon atoms of the amide substituents. The distortion reflects the formation of a C–H×××N hydrogen bond between the quinoline ring's nitrogen atom (N4) and the *para*-C–H group of the neighboring pincer's central pyridine ring (**Figure 3.8)**). Nonbonded crystal packing interactions, which include hydrogen bonding to solvent methanol molecules, clearly perturb the conformation of **1b**, which would otherwise be flat and have exact C_{2v} symmetry (its ideal gas-phase geometry).

Table 3.8. Selected geometric and conformational data for the low temperature X-ray structures of **1a–1e**. Standard uncertainties (where relevant) for the least significant digit are given in parentheses.

parameter	**1a**	**1b**	**1c**	**1d**	**1e**
C=O ave (Å)	1.227(1)	1.223(4)	1.223(3)	1.2282(7)	1.219(4), 1.228(1)[c]
(CO)–N ave (Å)	1.359(4)	1.356(3)	1.349(1)	1.3516(8)	1.356(5)
Δ_1 (°)[a]	10.6	40.6	9.0	1.6	37.9
Δ_2 (°)[a]	5.6	8.6	24.4	1.6	12.4
ϕ_1 (°)[b]	156.63(3)	169.32(5)	174.75(5)	154.67(6)	−166.29(9)
ϕ_1' (°)[b]	155.95(3)	177.14(5)	167.56(5)	154.67(6)	−169.98(9)
ϕ_2 (°)[b]	−175.34(3)	−171.33(5)	173.83(5)	178.50(5)	−179.8(1)
ϕ_2' (°)[b]	−175.89(3)	179.78(4)	178.69(6)	178.50(5)	172.9(1)
ϕ_3 (°)[b]	−159.67(3)	154.32(5)	−177.65(6)	−154.54(6)	−156.3(1)
ϕ_3' (°)[b]	−155.44(3)	175.55(5)	164.34(6)	−154.54(6)	174.7(1)

[a] Δ_1 and Δ_2 are dihedral angles between the mean plane of the central pyridine ring and the mean plane of the pincer aryl group appended to the amide groups containing O1 and O2, respectively (see Figure 5b). [b] The three torsion angles spanning the amide groups containing carbonyl oxygen atoms O1 and O2 are labelled ϕ_1–ϕ_3 and ϕ_1'–ϕ_3', respectively (Figure 5b), and are measured by default as their obtuse angles. The torsion angles ϕ_3 and ϕ_3', for example, gauge the tilts of the aryl substituents ("arms") relative to the pyridine ring core of the pincer. [c] Mean C–O bond distance for the two non-amide carbonyl groups.

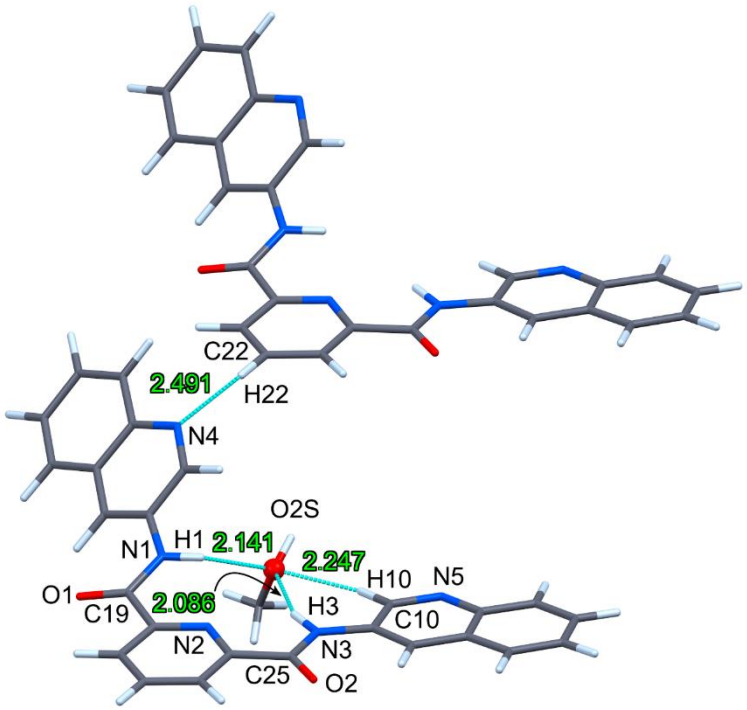


Figure 3.9. View of a pair of neighboring molecules in the crystal lattice of **1b.** The non-classical hydrogen bond C22–H22···N4 (2.491(7) Å) tips the quinoline ring out of the mean plane encompassing the central pyridine ring of the pincer, with the dihedral angle C19–N1–C2–C1 measuring 162.87(5)°. The dihedral angle for the second quinoline group (C25–N3–C11–C10, 176.31(5)°) is almost coplanar with the amide group and central pyridine ring.

For **1a** and **1d**, the nonplanarity observed in the crystalline solid state reflects (i) the conformational adjustment made by each monomer to establish a C_i symmetry dimer (inversion pair) and (ii) canting of the resultant closely juxtaposed isoquinoline or indazole rings to avert a significant intramolecular steric clash (**Table 3.8**). For **1c**, the intramolecular steric repulsion between what would amount to being substantially overlapped quinoline rings in a planar conformation is acute, such that only a nonplanar conformer is feasible. However, from **Figure 3.8** and **Table 3.8**, the two quinoline rings are not canted equally relative to the plane of the central pyridine ring of the pincer, thereby obviating exact C_2 point group symmetry for the molecule. The conformational perturbation evident for **1c** mainly reflects sandwiching of the N4 quinoline ring between a pair of neighboring molecules by C–H----π hydrogen bond formation (**Figure 3.11**).

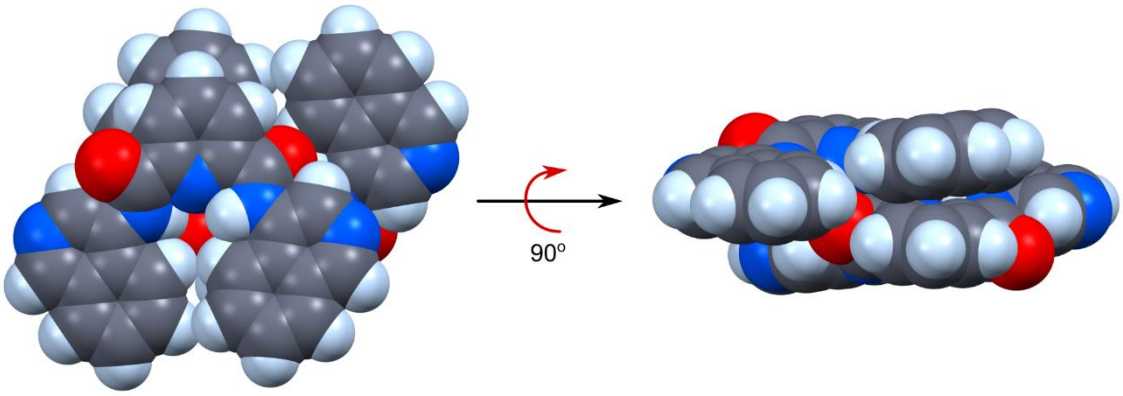


Figure 3.10. Space filling views of the hydrogen-bonded C_i symmetry dimer of structure **1a.** The diagram at the left is a view from above the dimer perpendicular to the plane of the pincer's central pyridine ring, while the diagram at the right is the same view rotated counterclockwise through 90° to highlight the out-of-plane arrangement of the two isoquinoline rings. The conformation of each monomer in the crystalline solid state is markedly different from the lowest-energy conformer in the gas phase (DFT simulation), which highlights the impact of crystal packing and dimer formation on the observed conformation.

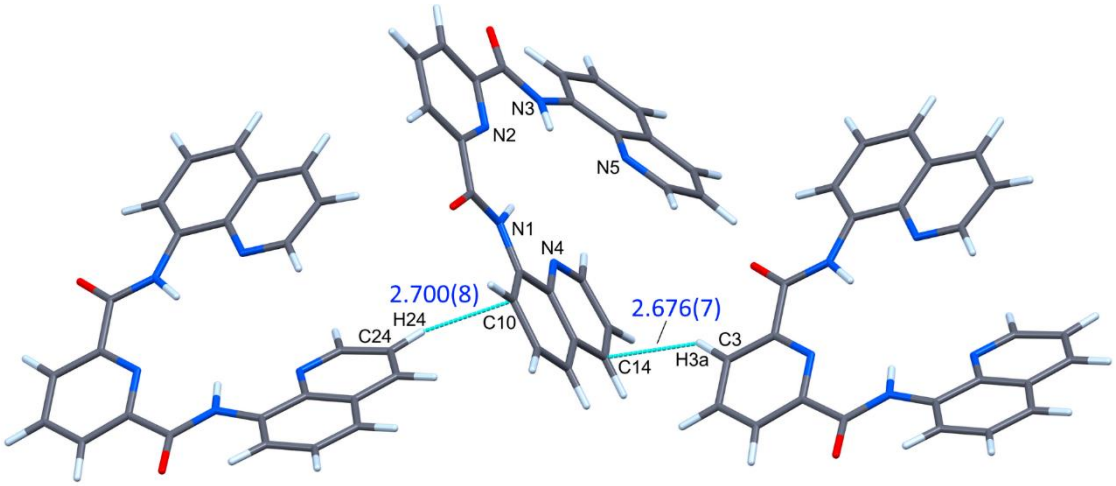


Figure 3.11. View depicting the short nonbonded interactions (blue stippled bonds) between the lower quinoline ring of **1c** and neighboring molecule heteroaromatic rings (contact distances are given in Å). The highlighted contacts constitute C–H···π type hydrogen bonding interactions which planarise the amide group (N1) and quinoline substituent by neatly sandwiching the substituent group. The quinoline ring appended to the second amide nitrogen atom (N5) lacks short contacts involving its aryl ring carbon atoms and thus has a more canted dihedral angle relative to the plane of the central pyridine ring of the pincer.

As summarised in **Table 3.8** the structures of **1a**–**1e** are all similar in terms of the geometry of their amide groups with the average C=O and (CO)–N bond distances falling tightly in the ranges 1.22–1.23 Å and 1.35–1.36 Å, respectively, which are typical for metal-free amides.[69] This observation is consistent with negligible perturbation of the electron delocalisation over the amide groups, irrespective of the nature of the appended aryl rings or the conformational distortion induced by crystal packing. The latter effect on the amide groups can be seen in the parameter Φ_2 (or Φ_2'), which deviates by ~9° at most from the ideal torsion angle of 180° in the case of **1b**. From **Figure 3.12**, the three torsion angles for **1a**–**1e** listed in **Table 3.8**, all fall within two standard deviations of the mean (180°) in each case and

display the same pattern of variance with Φ_1 and Φ_3 evidently more flexible and prone to out-of-plane distortions than the central torsion angle of the amide group itself (Φ_2). In the case of structures such as **1c**, and as noted above, intramolecular steric strain (repulsion between quinoline rings) is the main driving force for the observed nonplanar conformation especially since **1c** exhibits few other short nonbonded contacts in the crystal lattice.

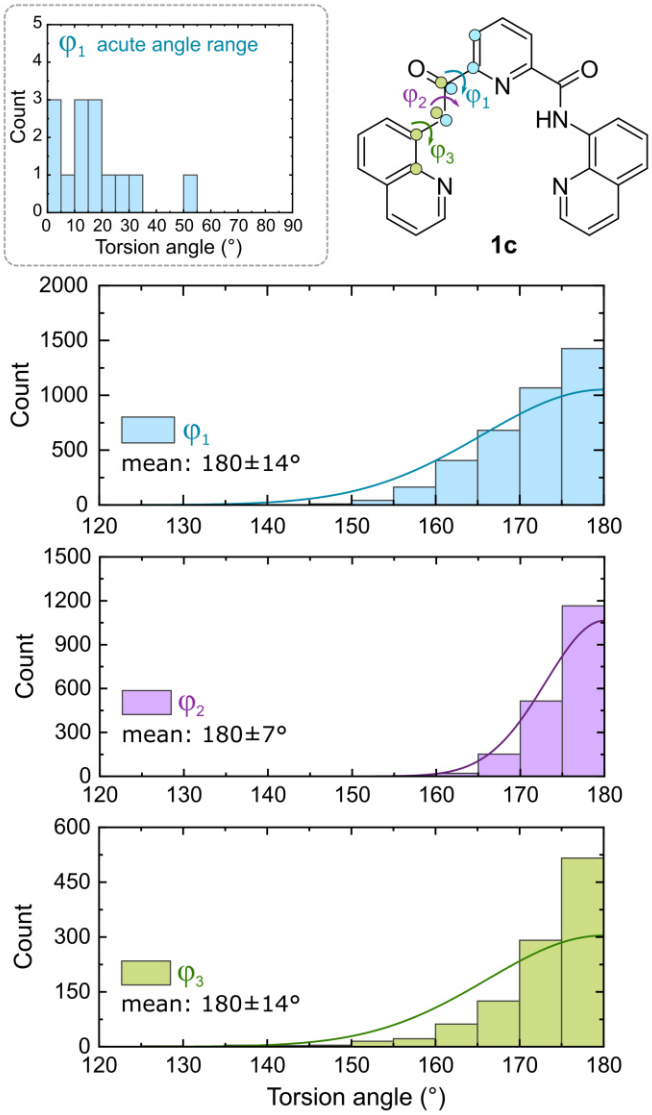


Figure 3.12. Histograms displaying the distribution of the torsion angles ϕ_1–ϕ_3 from an analysis of all available X-ray structures with the same functional group components as **1c** in the CSD. For ϕ_2 and ϕ_3 there are < 6 structures in each case with the torsion angle < 90° in contrast to ϕ_1 which, though still rare (0.37% of 3815 structures), has slightly more conformers with inwardly flipped amide C=O groups.

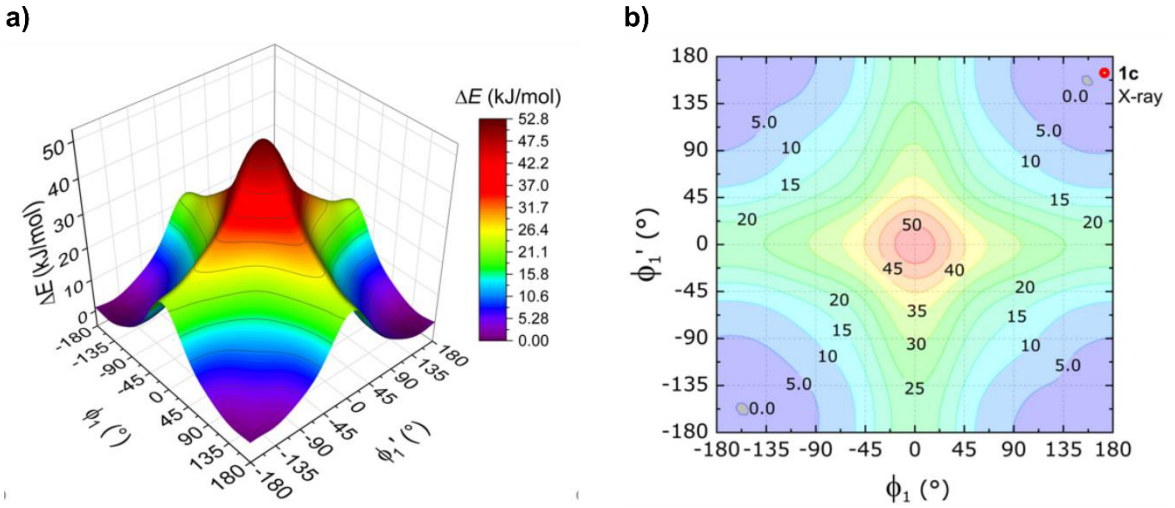


Figure 3.13. a) Potential energy surface (3D) for 1c calculated by rotations of ϕ_1 and ϕ_1' (see **Figure 3.7** and **Figure 3.12**) in the gas phase using the semi-empirical method PM6. The surface has 2-fold symmetry. **b)** The lowest energy barrier to rotation of ϕ_1 (23.11 kJ/mol) occurs at ϕ_1; $\phi_1' = 0°$; $\pm180°$ (contour map). The pathway involves the flipping of one amide C=O group while the other substituent maintains coplanarity with the central pyridine ring. The location of the X-ray structure of **1c** is indicated and the global minimum occurs at ϕ_1; $\phi_1' = 160°$; 160° (mirrored at −160°; −160°).

The fundamental question is what happens to the conformation of each compound upon dissolution and solvation? Dissociation of any oligomers or dimers and the formation of a statistical ensemble of lowest-energy conformers dependent on the temperature and physical properties of the solvent would be expected. And only the most rigid conformers (those "locked in" by high steric energy barriers to inversion such as **1c**) might retain solution conformations like those observed in their crystal structures. Conformational studies on these compounds were do to attempt to delineate the solution behavior of **1a**–**1f** to shed further light on key aspects of the conformational dynamics of this class of pincers.

3.3 Conformational analysis

3.3.1 X-ray crystallography and PM6 simulations

Single crystal X-ray data provides key atomic-resolution insights on the stereochemistry and conformation of each pincer in the crystalline phase. Our structural study reveals that the ostensibly planar pincers in fact have notably different conformations and that lattice packing effects may confer chirality on a pincer with appropriately sized and shaped substituents.[40,41,70] This is supported by our analysis of the spread in the torsion angles of this class of pincers in the CSD (**Figure 3.12**) which reveals that distortions up to 30° from planarity are experimentally observed.

As mentioned earlier, **1c** crystallised in a chiral space group, indicating chirality in the pincer compound. Upon further analysis, it was concluded that all compounds exhibit axial chirality due to the presence of a crystallographic 2-fold screw axis or molecular C_2 axis passing through the molecules and should thus exist as atropisomers (**Figure 3.7**). The atropisomer enantiomer which crystallises in the case of **1c** exhibited left-handed helicity and can be assigned as the M (minus) stereoisomer. The M-helicity assignment was unambiguously confirmed by the negative CD bands[71] appearing in the CD spectra of solid **1c** (**Figure 3.15)**.

The conformational energy landscape of **1c** was calculated by semi-empirical quantum mechanics (gas phase, **Figure 3.13**) and provides the appropriate 2-D and 3-D energy mapping to reveal that the X-ray structure is very close to the global minimum (a mildly nonplanar structure with $\phi_1 = \phi_1' \cong 180° - 30° = 150°$), despite being potentially subject to crystal packing effects. Interestingly, the calculated minimum energy conformation is not perfectly flat for **1c**. Steric repulsion between the quinoline rings is clearly relieved by the compound adopting a nonplanar conformation with its quinoline rings tipped out-of-plane. The energy perturbation required to tip the quinoline rings out-of-plane is, furthermore, surprisingly small. Specifically, only 5.0 kJ/mol is required to drive the torsion angle ϕ_1 for the quinoline ring from 180° to the perpendicular orientation at 90° relative to the central pyridine ring. This suggests (within the limitations of the computational method) that this class of pincer compounds is conformationally considerably more pliant than might be expected at first glance.

Although all the crystallised pincers may populate two main atropisomer conformers, **1c** was the only pincer that crystallised in a chiral Sohncke space group. Compound **1c** thus fits criterion (iii) in **Scheme 3.3**, and the remaining pincers fit criterion (iv). These pincers have flexible arms, which enables them to change their conformations through internal degrees of freedom. The barrier governing enantiomerisation determines whether the conformers can interconvert, and therefore directs the crystallisation of the pincers into chiral (enantiomorphic) or nonchiral (centrosymmetric) Sohncke space groups. It is likely that **1c** becomes locked in one conformer because the distance between its two arms is small, culminating in a substantial barrier of enantiomerisation. The remaining pincers crystallised as racemates as their barriers of enantiomerisation are presumably and by comparison, relatively low.

Racemisation and isomerisation of the present group of pincer compounds is seemingly required to achieve efficient close packing in the crystalline solid state. The principles governing efficient close packing in crystals[72–74] evidently play a key role in determining the Sohncke space group into which compounds **1a–1e** crystallise. All the current pincer compounds (except **1c**) racemise during crystallization. However, as shown by our analysis of the bulk solids (*vide infra*), racemization is not quantitative and an enantiomeric excess of the P-type atropisomer (right-handed helicity) results in measurable negative intensity CD spectra to a lesser or greater degree (**Figure 3.14**).

In addition to the "*endo*" 2-fold screw axis, and unlike the other pincers, the structure of **1e** has a further two "*exo*" screw axes involving each of its substituent arms because of the flexibility of the benzophenone groups. Compound **1e** thus has a total of three 2-fold screw (helical) axes, as depicted for the two most-easily visualized axes in **Figure 3.14**. Despite having several 2-fold screw axes, the overall conformation of **1e** is determined by its *endo* 2-fold screw axis (i.e., its primary helical axis), which is a counterclockwise screw (right-handed helicity), thereby assigning the compound's stereoisomer as a P-type enantiomer. Although the flexible pincer arms of **1e** fit into scenario (iv) of **Scheme 3.3**, their exact conformation is influenced by packing interactions with neighbouring molecules, rendering them inflexible in the crystalline solid state and locked in one conformation.

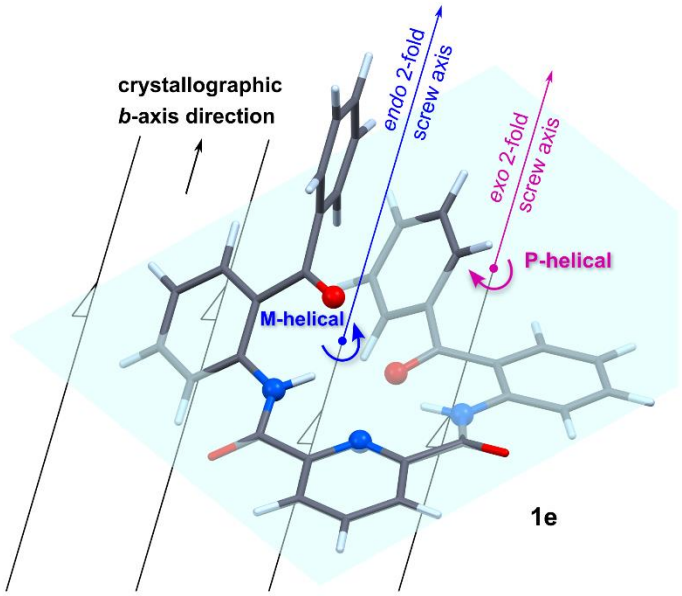


Figure 3.14. Illustration of the different helicity found at two 2-fold screw axes for crystalline **1e.** The central (intramolecular or "*endo*") axis reflects a P-helical conformation (right-handed helicity). Left-handed helicity, i.e., an M-helical conformation, involves the 2-fold screw axis located "*exo"* to the pincer cavity.

3.3.2 Circular Dichroism (CD) Spectroscopy

It was expected that the compounds **1a-1f** are planar (flat), but X-ray crystallographic data proved otherwise. These compounds exhibit chirality (atropisomerism) as previously stated in **Section 3.3.1**. In this study, CD spectroscopy was used to investigate the chirality of the carboxamide pincer molecules (**1a-1f**), for both solid samples and in solution.

Chiral molecules have the ability to absorb circularly polarised light of a certain wavelength traversing through an isotropic medium, which reduces the intensity of the light emerging from the medium. Depending on their chirality, chiral molecules absorb Right Circularly Polarised Light (R-CPL) and Left Circularly polarised light (L-CPL). Circular dichroism spectroscopy is the difference in absorption of right and left circularly polarised light by chiral chromophores (chiral molecules containing light absorbing groups).[53,75]

According to the light they absorb, the CD for chiral molecules can be either positive (L-CPL is absorbed to a greater extent as compared to R-CPL) or negative (RCP is absorbed to a greater extent as compared to LCP light). In compounds which exhibit atropisomerism or helicity, M or left-handed isomers yield positive CD, and P or right-handed isomers yield negative CD.[76,77] Some compounds have both.[78–80]

As explained earlier, molecules with a C_2-symmetry, but without a stereogenic centre can exhibit axial chirality if there is a restriction of rotation about the axial axis,[18] which is the case with the synthesised pincer ligands in this study. This means that these compounds absorb circularly polarised light, making CD spectroscopy an ideal technique to measure the polarity or chirality of the compounds **1a-1f**.

From the crystallographic data in **Section 3.2.5**, only **1c** crystallized in a chiral Sohnke space group as an enantiomerically pure conformer, although individual molecules for all compounds possessed a

rotational axis, conferring the molecules with chirality, (helicity). As explained earlier, to aid in close packing the molecules would rotate between their atropisomers, contingent on the energy of the isomerisation barrier.

The main questions to be answered with these conformational studies were, (i) Do the solvents used affect the chirality of **1a-1f**, and (ii) Do the molecules exist as a racemate in nature, and if not, which one is dominant and to what degree?

Solid and Liquid CD was measured for all compounds to investigate the dissolution of the compounds in a solvent that alters the ratio of the two atropisomers in the compound. The FDCD, FDLD and HT data (for solids) and CD, DC and absorbance data (in solution), were measured for each sample in triplicate on a Jasco J1500, with PM-539 and PML-534 detectors, between 200-600 nm, at a scan speed of 100 nm/min, data pitch 0.2 nm, and a bandwidth of 1.00 nm at 25˚C. The CD spectra for **1a-1f** are shown in **Figure 3.15.**

Experimental solid-state and solution CD spectroscopic studies of **1a**–**1f** (Figure 3.15) show that all pincers studied exhibited chirality as evidenced by their negative intensity CD spectral peaks. The CD data confirm the presence of an excess population of the M-helicity atropisomer in each sample. For **1c**, this obviously correlates with its X-ray structure and culminates in a strong bulk solid state CD spectrum (**Figure 3.15a**). For the remaining compounds, even if racemization has occurred, a slight excess of the M-helicity atropisomer can account for the CD spectra of the bulk solid. The present solid-state CD spectroscopic analysis shows that the M-type atropisomer is the natural state for the pincers and that the CD signals are not spurious. The negative intensity CD spectra were, furthermore, corroborated by TD-DFT simulations in different solvents (**Figure 3.16b**) and using a single point calculation on the X-ray structure of **1c.**

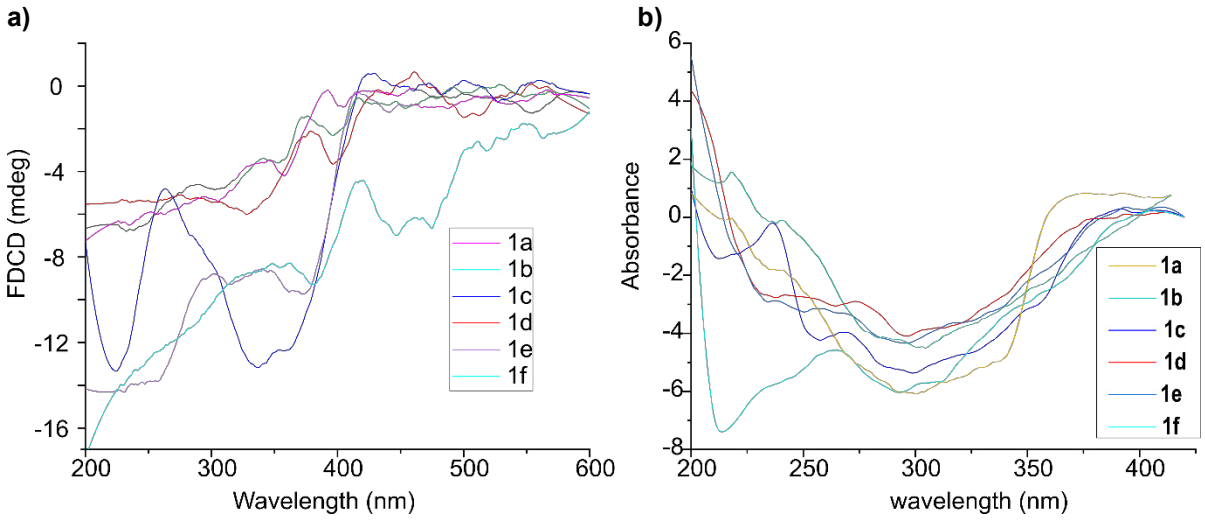


Figure 3.15. CD spectroscopy spectra for **(a)** compounds **1a-1f** in powder form (crystals of **1e** were crushed into a powder, and the spectra was the same with the powder) **(b)** in solution, (**1a-1b** and **1f** dissolved in 2-methoxyethanol, **1c** dissolved in Chloroform, **1e** dissolved in THF). Resultant spectra were cleaned up using the Savitzky–Golay filter in Origin 2019b by 250 pts in **(a)** and 50 pts in **(b).**

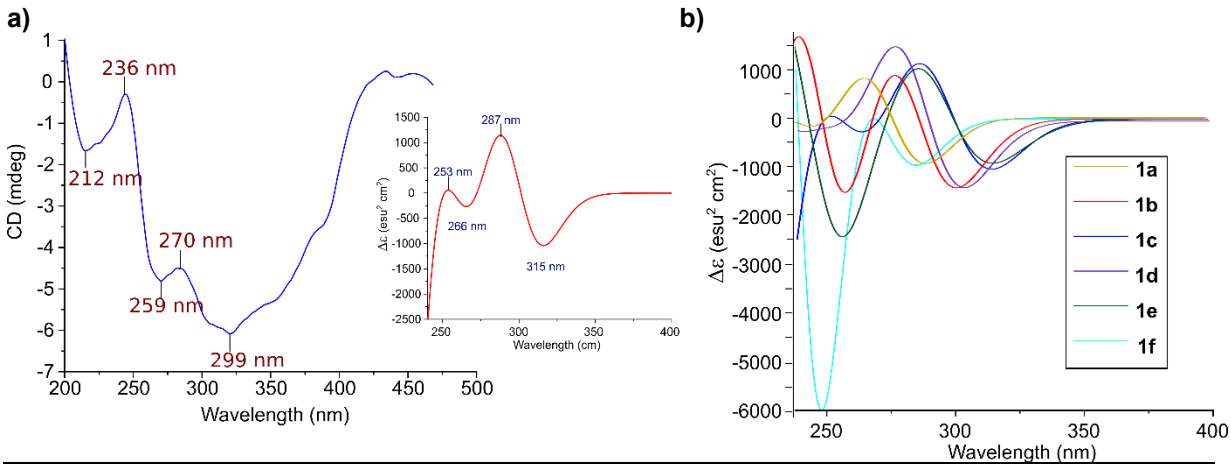


Figure 3.16. a) Experimental and DFT-calculated (insert) CD spectra of C_2 symmetry **1c** in chloroform**. (b)**The CD for the DFT-calculated spectrum is plotted with full width at half maximum intensity (FWHM) of 3000 cm^{-1}.

The electronic structures of the ligands **1a**–**1f** were measuredsed to better understand the electronic structure of the compounds and their CD spectra. The UV-vis absorption spectra of the ligands can be found in the supplementary information (**Section S1.3, Figures S19-S23**). The predicted absorption maxima and the major contributors to each transition are given in **Section S1.3**, **Table S1** in the supplementary information. **Figure 3.16** showcases the experimental and predicted UV-vis spectra of **1c**, as well as the orbitals and transitions responsible for the major peaks.

Two absorption bands at 310 nm (ε = 7.4 × 10^4 M^{-1} cm^{-1}) and 326 nm (ε = 8.6 × 10^4 M^{-1} cm^{-1}) were observed in chloroform, which correlates with data found in the literature.[70] Only two peaks (one clear peak and a slight shoulder) were detected when the spectra were recorded in chloroform, as these were the only peaks within the instrument's spectral range. The transitions in chloroform were assigned according to the TD-DFT calculations at the CAM-B3LYP/def2-tzvp level of theory. The DFT-calculated electronic spectrum of **1c** in chloroform is shown in the inset of **Figure 3.16a**; the broad band centred at 300 nm matches the experimental band well (to within about 25 nm).

Although our experimental CD data showed that the ligands **1a**–**1f** generally exist in nature and in solution as an excess population of one chiral atropisomer (the M-helicity enantiomer), our DFT simulations on **1c** predictably indicated that the two enantiomers have the same energy, confirming that the two stereoisomers are equally stable and that racemization (if feasible via a suitable internal reaction coordinate pathway and unrestricted by the molecule's environment) might be observed.

The purpose of this study was to establish if ligands **1a-f** existed as racemates under physiological conditions, and if not, which atropisomer was predominant. Due to their difference in structures, there were different degrees of inhibition of rotation around the axial axis and hence **1c** molecules crystallised in chiral space groups while the rest crystallised in achiral space groups. This phenomenon was mainly attributed to close packing in crystal structures. Liquid and solid CD proved that these compounds predominantly exist in one atropisomer. Because they have a certain level of freedom of rotation, some molecules could rotate to enable close fitting in the crystal cell. From the results of this study, it was

concluded that these compounds only exist as racemates in their crystal form, under the right conditions, but not in nature.

3.3.3 NMR

3.3.3.1 Temperature variable NMR

Due to the poor solubility of the synthesised compounds, **1d** was selected for variable temperature NMR analysis as a representative member of the compound group **1a**–**1f**. Pincer **1d** (5.2 mg) was dissolved in DMF-d_7. NMR spectra were recorded at 10 K intervals from 223–363 K to gather spectroscopic evidence for dynamic conformational changes in the system. In the case of compound **1d**, the existence of atropisomers separated by a relatively large energy barrier can, in principle, enable full or partial chiral resolution of the enantiomers, with the compound becoming largely trapped in one conformer by virtue of intermolecular interactions or another imposed extraneous physical constraint. From **Figure 3.17**, it is evident that as the temperature increases from 323 to 343 K, changes in the signal multiplicities for the aromatic protons of **1d** occur along with noticeable line broadening. While the spectral behaviour is not fully commensurate with a typical slow-to-fast exchange equilibrium process for amide rotamers wherein a properly coalesced signal or set of signals is seen between the exchange limits, the data for **1d** at 333 K (broadened, partly coalesced signals) are not fully inconsistent with such a scenario either. Evidently, the temperature-increase within the upper bound of the range studied here allows **1d** to cross one or more barriers, one of which might be the barrier for interconversion between its two symmetry-distinct atropisomers.

To transition between the two atropisomers, molecules of **1d** must pass through a planar geometry where Δ_2 (mentioned in **Figure 3.8 (b)** for the related derivative **1c**) is exactly 0°). This rotamer would clearly allow for close interaction between the aromatic protons on the two indazole rings of the pincer arms, thereby perturbing the effective local magnetic field for the aromatic protons. Analysis of the likely transition state for compound **1c** from the PES of **Figure 3.13** suggests that one of the two torsion angles (say ϕ_1) will pass through an angle of 0° while the other stays fixed at 180°. If pincer **1d** behaves similarly and has a similar PES to **1c**, then the transition state structure would favour perturbation of the aromatic proton resonances (notably, the multiplicities and linewidths of the indazole ring protons). The gas phase barrier calculated for **1c** is ~22 kJ/mol. However, a more thorough *ab initio* calculation of the PES for **1d** with inclusion of the solvent would be needed to properly account for the dynamic NMR for this system, a study beyond the scope of the present report.

Regarding the amide protons of **1d**, **Figure 3.17** indicates that the NH signal broadens (due to enhanced exchange) and exhibits an upfield shift (due to loss of deshielding by an H-bond acceptor). This is consistent with dissociation of H-bonded DMF solvent from **1d** as a function of increasing temperature. The amide NH chemical shift thus correlates linearly (R^2 = 0.996) with temperature in the region studied (**Figure 3.17 (b)**).

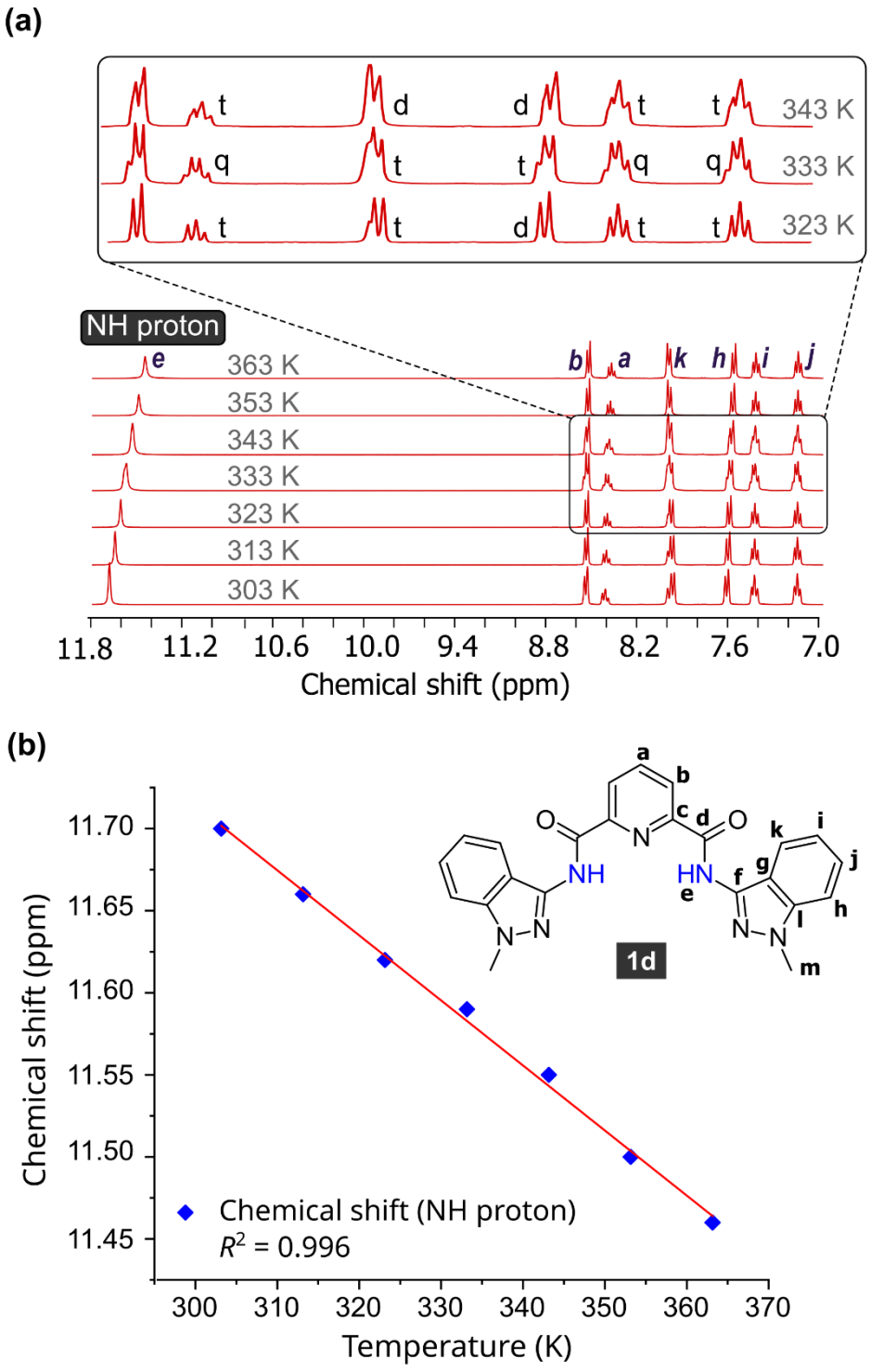


Figure 3.17. a) Illustration of the temperature-dependent changes in the ^{1}H NMR spectrum for **1d** between 303 K and 363 K in deuterated DMF. The inset figure showcases the changes in signal multiplicity (d = doublet, t = triplet and q = quartet) seen for the aromatic protons of compound **1d**. **(b)** Plot of the amide proton chemical shift as a function of temperature.

3.3.3.2 Variable concentration NMR study

To evaluate how hydrogen bonding is affected by an increase in concentration, the ^{1}H NMR spectrum of **1d** was analysed at different concentrations (3.5 – 157 nM) in DMSO-d_6. Self-association by hydrogen bonding with increasing [**1d**] shifts the singlet NH signal downfield with no detectible change in signal

multiplicity. The NMR data clearly reflect formation of H-bonded dimers and oligomers akin to the extended X-ray structure of **1d** shown in **Figure 3.8**. Specifically, the pyridine and indazole protons do not show discernible chemical shift changes with increasing [**1d**] because their magnetic environment(s) remain relatively unchanged. This observation reflects the rather open arrangement (as opposed to a ring-stacked structure) for the H-bonded species seen in the X-ray structure of the compound, and such an arrangement is apparently also favoured in solution. From **Figure 3.18 (b)**, the nonlinear concentration dependence of the NH proton resonance, while subtle, follows a simple polynomial relationship that is commensurate with weak dimer or oligomer formation.[81,82] The relevant solution equilibrium is depicted by **Equation 3.2** below.[81,82]

$$2\,A \rightleftharpoons A_2$$ **Equation 3.2**

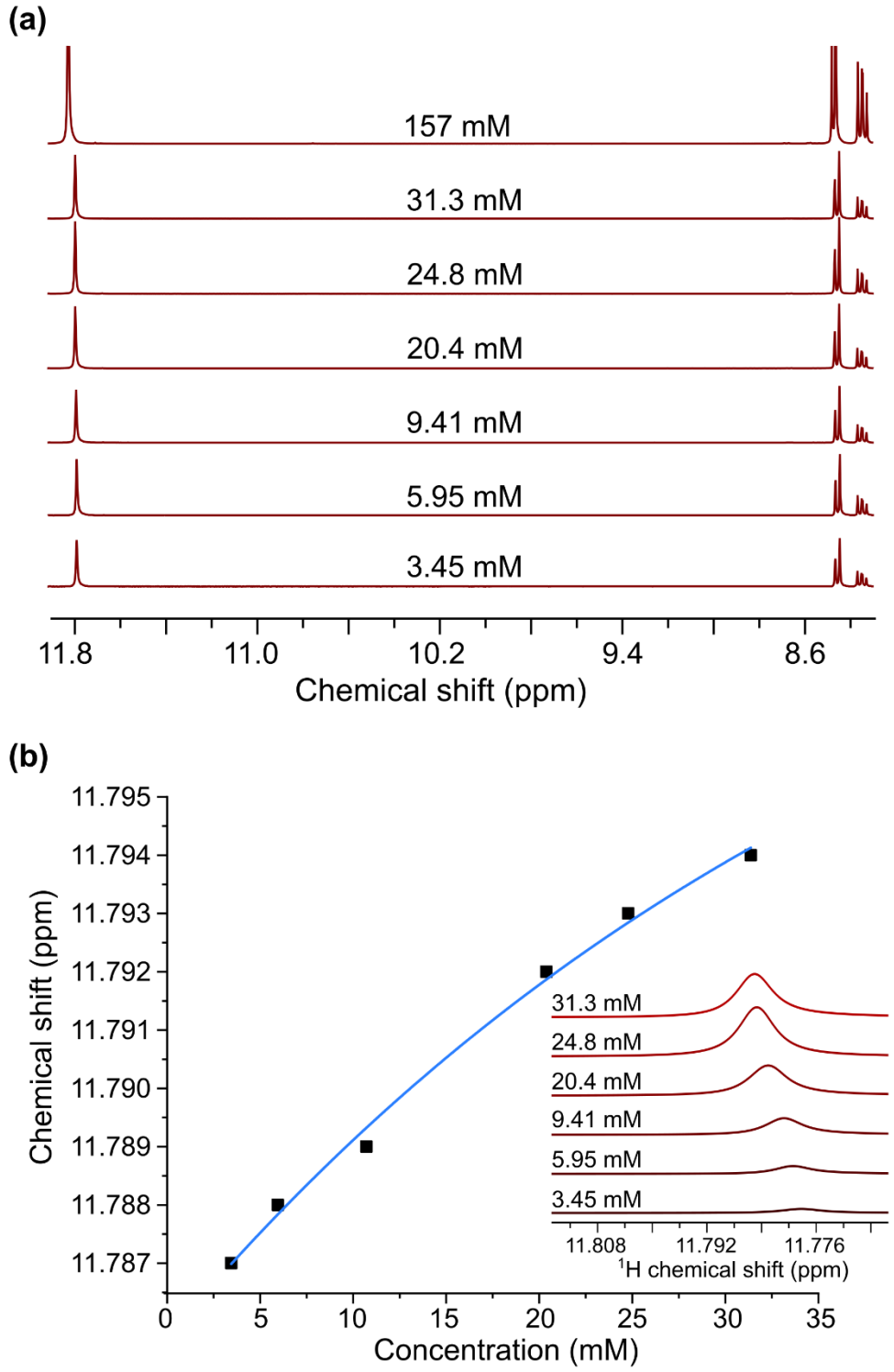


Figure 3.18. (a) Selected NMR scans of the amide proton for **1d** as a function of total concentration in DMSO at 25°C. **(b)**) Simple polynomial fit of the concentration dependence of the amide proton chemical shift. From the nonlinearity of the graph, **1d** likely undergoes weak dimerization in DMSO in accord with the equilibrium depicted in **Equation 3.2**.

3.4 Summary and conclusion

In addition to the described characterisation, HRMS was also used and the spectra for all compounds are illustrated in the supplementary information (**Section S1.4, Figures S26-S31**). The compounds in this study were fully characterised, and the data was fully corroborated with calculated data.

A group of related tridentate bis(carboxamide) pincer ligands was investigated. All are C_2-symmetric chiral compounds, and all have the potential to populate a specific enantiomer under certain conditions (e.g., limited atropisomerism). Of the five compounds crystallographically characterized here, only the bis(isoquinoline) derivative **1c** crystallised in a chiral Sohncke space group. The steric bulk and intramolecular juxtaposition of the peripheral isoquinoline rings in this system evidently lock in a single, chiral atropisomer in the crystalline solid state. The intrinsic chirality, coupled with the observed stability and flexibility of this group of C_2-symmetric ligands suggests they might find utility, upon coordination with suitable metal ions, as catalysts suitable for chiral induction in asymmetric synthesis.

3.5 References

1. Razuwika R, Munro OQ. Synthesis and characterization of C2-symmetric bis(carboxamide) pincer ligands. *New J Chem*. 2024;48(10):4229-4244. doi:10.1039/D3NJ05502G
2. Moulton CJ, Shaw BL. Transition metal–carbon bonds. Part XLII. Complexes of nickel, palladium, platinum, rhodium and iridium with the tridentate ligand 2, 6-bis [(di-t-butylphosphino) methyl] phenyl. *J Chem Soc Dalton Trans*. 1976;(11):1020-1024.
3. A. Danopoulos A, D. Tulloch AA, Winston S, Eastham G, B. Hursthouse M. Chelating and 'pincer' dicarbene complexes of palladium; synthesis and structural studies. *Dalton Trans*. 2003;0(5):1009-1015. doi:10.1039/B209739G
4. Lawrence MA, Green KA, Nelson PN, Lorraine SC. Pincer ligands—Tunable, versatile and applicable. *Polyhedron*. 2018;143:11-27.
5. Peris E, Crabtree RH. Key factors in pincer ligand design. *Chem Soc Rev*. 2018;47(6):1959-1968.
6. Hiratani K, Taguchi K. 2,6-Bis[N-(8-quinolyl)carbamoyl]pyridine as a Highly Selective Extractant for Cu(II). *Bull Chem Soc Jpn*. 1990;63(11):3331-3333. doi:10.1246/bcsj.63.3331
7. Babcock WC, Baker RW, Lachapelle ED, Smith KL. Coupled transport membranes II: The mechanism of uranium transport with a tertiary amine. *J Membr Sci*. 1980;7(1):71-87. doi:10.1016/S0376-7388(00)83186-5
8. Costero AM, José Bañuls M, José Aurell M, Ward MD, Argent S. Biphenyl macrolactams in anion complexation. Selective naked-eye fluoride recognition. *Tetrahedron*. 2004;60(42):9471-9478. doi:10.1016/j.tet.2004.07.088
9. Dorazco-González A, Höpfl H, Medrano F, Yatsimirsky AK. Recognition of anions and neutral guests by dicationic pyridine-2, 6-dicarboxamide receptors. *J Org Chem*. 2010;75(7):2259-2273.
10. Yamnitz CR, Negin S, Carasel IA, Winter RK, Gokel GW. Dianilides of dipicolinic acid function as synthetic chloride channels. *Chem Commun*. 2010;46(16):2838-2840.
11. Roy M, Berezhnaia V, Villa M, et al. Stereoselective Syntheses, Structures, and Properties of Extremely Distorted Chiral Nanographenes Embedding Hextuple Helicenes. *Angew Chem Int Ed*. 2020;59(8):3264-3271. doi:10.1002/anie.201913200
12. Jeletic MS, Lower CE, Ghiviriga I, Veige AS. Chemical Exchange Saturation Transfer (CEST) as a Tool to Measure Ligand Flexibility of Chelating Chiral Di-N-heterocyclic Carbene Complexes. *Organometallics*. 2011;30(21):6034-6043. doi:10.1021/om200913c
13. Choi K, Hamilton AD. Macrocyclic anion receptors based on directed hydrogen bonding interactions. *Coord Chem Rev*. 2003;240(1-2):101-110. doi:10.1016/S0010-8545(02)00305-3
14. Filippini G, Gavezzotti A. A quantitative analysis of the relative importance of symmetry operators in organic molecular crystals. *Acta Crystallogr B*. 1992;48(2):230-234.
15. Miyashita a_A, Yasuda A, Takaya H, et al. Synthesis of 2, 2'-bis (diphenylphosphino)-1, 1'-binaphthyl (BINAP), an atropisomeric chiral bis (triaryl) phosphine, and its use in the rhodium (I)-catalyzed asymmetric hydrogenation of. alpha.-(acylamino) acrylic acids. *J Am Chem Soc*. 1980;102(27):7932-7934.
16. Grimme S, Peyerimhoff SD. Theoretical study of the structures and racemization barriers of [n] helicenes (n= 3–6, 8). *Chem Phys*. 1996;204(2-3):411-417.
17. Schaack C, Arrico L, Sidler E, Górecki M, Di Bari L, Diederich F. Helicene Monomers and Dimers: Chiral Chromophores Featuring Strong Circularly Polarized Luminescence. *Chem – Eur J*. 2019;25(34):8003-8007. doi:https://doi.org/10.1002/chem.201901248
18. LaPlante SR, Edwards PJ, Fader LD, Jakalian A, Hucke O. Revealing Atropisomer Axial Chirality in Drug Discovery. *ChemMedChem*. 2011;6(3):505-513. doi:10.1002/cmdc.201000485

19. Clapham KM, Rennison T, Jones G, et al. Potent enantioselective inhibition of DNA-dependent protein kinase (DNA-PK) by atropisomeric chromenone derivatives. *Org Biomol Chem*. 2012;10(33):6747. doi:10.1039/c2ob26035b
20. "Atropisomeric" Drugs: Basic Concept and Example of Application to Drug Development. Accessed March 14, 2023. https://www.scirp.org/journal/paperinformation.aspx?paperid=97661
21. Wang X, Howell CP, Chen F, Yin J, Jiang Y. Gossypol--a polyphenolic compound from cotton plant. *Adv Food Nutr Res*. 2009;58:215-263. doi:10.1016/S1043-4526(09)58006-0
22. Privileged Chiral Ligands and Catalysts | Wiley. Wiley.com. Accessed June 21, 2021. https://www.wiley.com/en-us/Privileged+Chiral+Ligands+and+Catalysts-p-9783527327041
23. Lavoine N, Bras J, Saito T, Isogai A. Optimization of preparation of thermally stable cellulose nanofibrils via heat-induced conversion of ionic bonds to amide bonds. *J Polym Sci Part Polym Chem*. 2017;55(10):1750-1756. doi:10.1002/pola.28541
24. Lavoine N, Bras J, Saito T, Isogai A. Improvement of the Thermal Stability of TEMPO-Oxidized Cellulose Nanofibrils by Heat-Induced Conversion of Ionic Bonds to Amide Bonds. *Macromol Rapid Commun*. 2016;37(13):1033-1039. doi:10.1002/marc.201600186
25. Kumar P, Kaur S, Gupta R, Bowman-James K. Pincers Based on Dicarboxamide and Dithiocarboxamide Functional Groups. In: *Pincer Compounds*. Elsevier; 2018:295-325. doi:10.1016/B978-0-12-812931-9.00014-1
26. Marlin DS, Olmstead MM, Mascharak PK. Extended structures controlled by intramolecular and intermolecular hydrogen bonding: a case study with pyridine-2,6-dicarboxamide, 1,3-benzenedicarboxamide and N,N H-dimethyl-2,6-pyridinedicarboxamide. *J Mol Struct*. Published online 2000:13.
27. Kang SO, Johnson TS, Day VW, Bowman-James K. Pyridine-2,6-dicarboxamide pincer-based macrocycle: a versatile ligand for oxoanions, oxometallates, and transition metals. *Supramol Chem*. 2018;30(4):305-314. doi:10.1080/10610278.2017.1361534
28. Peris E, Crabtree RH. Recent homogeneous catalytic applications of chelate and pincer N-heterocyclic carbenes. *Coord Chem Rev*. 2004;248(21):2239-2246. doi:10.1016/j.ccr.2004.04.014
29. Liu W, Oliver AG, Smith BD. Macrocyclic Receptor for Precious Gold, Platinum, or Palladium Coordination Complexes. *J Am Chem Soc*. 2018;140(22):6810-6813. doi:10.1021/jacs.8b04155
30. Wang B, Howard IG, Pope JW, Conte ED, Deng Y. Bis(imino)pyridine iron complexes for catalytic carbene transfer reactions. *Chem Sci*. 2019;10(34):7958-7963. doi:10.1039/C9SC02189B
31. Wang H, Liu J, Deng Y, et al. Pincer thioamide and pincer thioimide palladium complexes catalyze highly efficient Negishi coupling of primary and secondary alkyl zinc reagents at room temperature. *Chem Weinh Bergstr Ger*. 2009;15(6):1499-1507. doi:10.1002/chem.200801860
32. Akaiwa M, Kanbara T, Fukumoto H, Yamamoto T. Luminescent palladium complexes containing thioamide-based SCS pincer ligands. *J Organomet Chem*. 2005;690(18):4192-4196. doi:10.1016/j.jorganchem.2005.06.026
33. Brooks J, Babayan Y, Lamansky S, et al. Synthesis and characterization of phosphorescent cyclometalated platinum complexes. *Inorg Chem*. 2002;41(12):3055-3066. doi:10.1021/ic0255508
34. Neve F, Crispini A, Di Pietro C, Campagna S. Light-emitting cyclopalladated complexes of 6-phenyl-2,2′-bipyridines with Hydrogen-bonding functionality. *Organometallics*. 2002;21(17):3511-3518. doi:10.1021/om020204j
35. Kanbara T, Okada K, Yamamoto T, Ogawa H, Inoue T. Preparation of platinum complexes containing a thioamide-based SCS pincer ligand and their light emitting properties. *J Organomet Chem*. 2004;689(10):1860-1864. doi:10.1016/j.jorganchem.2004.03.003
36. Heyduk E, Dummit B, Chang YH, Heyduk T. Molecular Pincers: Antibody-Based Homogeneous Protein Sensors. *Anal Chem*. 2008;80(13):5152-5159. doi:10.1021/ac8004154
37. Tian L, Wang RE, Chang YH. Molecular PINCERs® for biomarker analysis and their potential application in hepatitis C diagnosis. *Antivir Ther*. 2012;17(7 Pt B):1437-1442. doi:10.3851/IMP2469
38. Albrecht M, van Koten G. Platinum Group Organometallics Based on "Pincer" Complexes: Sensors, Switches, and Catalysts In memory of Prof. Dr. Luigi M. Venanzi and his pioneering work in organometallic chemistry, particularly in PCP pincer chemistry. *Angew Chem Int Ed Engl*. 2001;40(20):3750-3781.
39. Bertrand B, Williams MRM, Bochmann M. Gold(III) Complexes for Antitumor Applications: An Overview. *Chem – Eur J*. 2018;24(46):11840-11851. doi:10.1002/chem.201800981
40. Bates GW, Gale PA, Light ME. Isophthalamides and 2,6-dicarboxamidopyridines with pendant indole groups: a 'twisted' binding mode for selective fluoride recognition. *Chem Commun*. 2007;(21):2121-2123. doi:10.1039/B703905K
41. Yu Q, Baroni TE, Liable-Sands L, Rheingold AL, Borovik AS. Synthesis and structure of chiral 2,6-bis[(2-carbamoylphenyl)carbamoyl]pyridine ligands. *Tetrahedron Lett*. 1998;39(38):6831-6834. doi:10.1016/S0040-4039(98)01486-5
42. Rajiv Gandhi M, Yamada M, Haga K, Shibayama A. Synthesis of pincer-type extractants for selective extraction of palladium from PGMs: An improved liquid-liquid extraction approach to current refining processes. *Sci Rep*. 2017;7(1):8709. doi:10.1038/s41598-017-09053-z
43. Rajiv Gandhi M, Yamada M, Kondo Y, Shibayama A, Hamada F. Rapid and selective extraction of Pd(ii) ions using the SCS type pincer ligand 1,3-bis(dimethylthiocarbamoyloxy)benzene, and its Pd(ii) extraction mechanism. *RSC Adv*. 2016;6(2):1243-1252. doi:10.1039/C5RA23146A
44. Ouellette RJ, Rawn JD. 22 - Carboxylic Acid Derivatives. In: Ouellette RJ, Rawn JD, eds. *Organic Chemistry (Second Edition)*. Academic Press; 2018:665-710. doi:10.1016/B978-0-12-812838-1.50022-0

45. Roos G, Roos C. Chapter 7 - Functional Classes II, Reactions. In: Roos G, Roos C, eds. *Organic Chemistry Concepts*. Academic Press; 2015:103-149. doi:10.1016/B978-0-12-801699-2.00007-9
46. Clayden J, Greeves N, Warren S. *Organic Chemistry*. OUP Oxford; 2012.
47. RP D. Acid-Base VI. Using pKa to Predict the Course of a Reaction – Part 2. RetroSynthetiX. Published February 2, 2017. Accessed July 31, 2023. https://retrosynthetix.com/2017/02/02/acid-base-vi/
48. Yamazaki N, Higashi F. Studies on Reactions of the N-Phosphonium Salts of Pyridines. I. A New Method for the Activation of Carboxylic Acids via the N-Phosphonium Salts by Means of the Oxidation of Tri- and Di-esters of Phosphorous Acid in the Presence of Tertiary Amines. *Bull Chem Soc Jpn*. 1973;46(4):1235-1238. doi:10.1246/bcsj.46.1235
49. Yamazaki N, Matsumoto M, Higashi F. Studies on reactions of the N-phosphonium salts of pyridines. XIV. Wholly aromatic polyamides by the direct polycondensation reaction by using phosphites in the presence of metal salts. *J Polym Sci Polym Chem Ed*. 1975;13(6):1373-1380. doi:10.1002/pol.1975.170130609
50. Yang CP, Hsiao SH. Preparation of poly(amide-imide)s by means of triphenyl phosphite, 1. Aliphatic-aromatic poly(amide-imide)s based on trimellitimide. *Makromol Chem*. 1989;190(9):2119-2131. doi:10.1002/macp.1989.021900912
51. Barnes DJ, Chapman RL, Vagg RS, Watton EC. Synthesis of novel bis(amides) by means of triphenyl phosphite intermediates. *J Chem Eng Data*. 1978;23(4):349-350. doi:10.1021/je60079a006
52. Thompson JM. *Infrared Spectroscopy*. CRC Press; 2018.
53. Robinson JW. *Practical Handbook of Spectroscopy*. CRC Press; 1991.
54. Saluja H, Mehanna A, Panicucci R, Atef E. Hydrogen Bonding: Between Strengthening the Crystal Packing and Improving Solubility of Three Haloperidol Derivatives. *Molecules*. 2016;21(6):719. doi:10.3390/molecules21060719
55. Mihalovits M. Temperature and pressure effects on the hydrogen-bonding Hansen solubility parameter: Cases of n-alkanols (C1-C5). *J Mol Liq*. 2022;363:119910. doi:10.1016/j.molliq.2022.119910
56. Antosiewicz JM, Shugar D. UV–Vis spectroscopy of tyrosine side-groups in studies of protein structure. Part 1: basic principles and properties of tyrosine chromophore. *Biophys Rev*. 2016;8(2):151-161. doi:10.1007/s12551-016-0198-6
57. Pidcock E. Achiral molecules in non-centrosymmetric space groups. *Chem Commun*. 2005;(27):3457. doi:10.1039/b505236j
58. Kleemiss F, V. Dolomanov O, Bodensteiner M, et al. Accurate crystal structures and chemical properties from NoSpherA2. *Chem Sci*. 2021;12(5):1675-1692. doi:10.1039/D0SC05526C
59. Dolomanov OV, Bourhis LJ, Gildea RJ, Howard J a. K, Puschmann H. OLEX2: a complete structure solution, refinement and analysis program. *J Appl Crystallogr*. 2009;42(2):339-341. doi:10.1107/S0021889808042726
60. Furness JW, Kaplan AD, Ning J, Perdew JP, Sun J. Accurate and Numerically Efficient r2SCAN Meta-Generalized Gradient Approximation. *J Phys Chem Lett*. 2020;11(19):8208-8215. doi:10.1021/acs.jpclett.0c02405
61. Dunning TH Jr. Gaussian basis sets for use in correlated molecular calculations. I. The atoms boron through neon and hydrogen. *J Chem Phys*. 1989;90(2):1007-1023. doi:10.1063/1.456153
62. Yang QY, Zhou ZY, Qi JY. N,N′-Bis(2-methoxy-phenyl)-pyridine-2,6-dicarbox-amide. *Acta Crystallogr Sect E Struct Rep Online*. 2001;57(12):o1161-o1162. doi:10.1107/S1600536801018694
63. Groom CR, Bruno IJ, Lightfoot MP, Ward SC. The Cambridge Structural Database. *Acta Crystallogr Sect B Struct Sci Cryst Eng Mater*. 2016;72(2):171-179. doi:10.1107/S2052520616003954
64. Meghdadi S, Nalchigar S, Khavasi HR. N,N′-Bis(8-quinol-yl)pyridine-2,6-dicarboxamide. *Acta Crystallogr Sect E Struct Rep Online*. 2008;64(2):o431-o431. doi:10.1107/S1600536807055031
65. Dai MB, Zhang QL, Zhu XC, Zhang Y, Zhu B. Synthesis and crystal structure of Schiff base Ligand and dinuclear Cu (II) complex. *Chin J Inorg Chem*. 2008;24:1381-1386.
66. Waris G, Siddiqi HM, Flörke U, Hussain R, Butt MS. N,N′-Bis(4-bromo-phen-yl)pyridine-2,6-dicarboxamide. *Acta Crystallogr Sect E Struct Rep Online*. 2013;69(3):o416-o416. doi:10.1107/S1600536813002705
67. Qi JY, Yang QY, Lam KH, Zhou ZY, Chan ASC. N,N′-Bis(4-methyl-phenyl)-pyridine-2,6-dicarbox-amide. *Acta Crystallogr Sect E Struct Rep Online*. 2003;59(4):o415-o416. doi:10.1107/S1600536803004604
68. Kumar R, Aggarwal H, Bhowal R, Chopra D, Srivastava A. An Electron-Rich Helical Host for the Exclusive Removal of a Planar Electron-Deficient Organic Compound. *Chem – Eur J*. 2019;25(45):10756-10762. doi:https://doi.org/10.1002/chem.201902418
69. Clement O, Rapko BM, Hay BP. Structural aspects of metal–amide complexes. *Coord Chem Rev*. 1998;170(1):203-243. doi:10.1016/S0010-8545(98)00066-6
70. Hiratani K, Taguchi K. 2,6-Bis[N-(8-quinolyl)carbamoyl]pyridine as a Highly Selective Extractant for Cu(II). *Bull Chem Soc Jpn*. 1990;63(11):3331-3333. doi:10.1246/bcsj.63.3331
71. Akine S, Sairenji S, Taniguchi T, Nabeshima T. Stepwise Helicity Inversions by Multisequential Metal Exchange. *J Am Chem Soc*. 2013;135(35):12948-12951. doi:10.1021/ja405979v
72. Kitaigorodskii AI. The principle of close packing and the condition of thermodynamic stability of organic crystals. *Acta Crystallogr*. 1965;18(4):585-590. doi:10.1107/S0365110X65001391
73. Bernal J, Knight K, Cherry I. Growth of crystals from random close packing. *Nature*. 1964;202(4935):852-854.
74. Goodenough JB. A Theory of the Deviation from Close Packing in Hexagonal Metal Crystals. *Phys Rev*. 1953;89(1):282-294. doi:10.1103/PhysRev.89.282
75. Lightner DA, Gurst JE. *Organic Conformational Analysis and Stereochemistry from Circular Dichroism Spectroscopy*. John Wiley & Sons; 2000.

76. Gold V, ed. *The IUPAC Compendium of Chemical Terminology: The Gold Book*. 4th ed. International Union of Pure and Applied Chemistry (IUPAC); 2019. doi:10.1351/goldbook
77. Ernst KH. Molecular chirality at surfaces: Molecular chirality at surfaces. *Phys Status Solidi B*. 2012;249(11):2057-2088. doi:10.1002/pssb.201248188
78. Katoono R, Sakamoto K, Suzuki T. Dual dynamic chirality generated in the assembly of three achiral rods through the three-fold twisting of a macrocycle. *Chem Commun*. 2019;55(38):5503-5506. doi:10.1039/C9CC02226K
79. Kinney ZJ, Hartley CS. Twisted Macrocycles with Folded ortho-Phenylene Subunits. *J Am Chem Soc*. 2017;139(13):4821-4827. doi:10.1021/jacs.7b00149
80. Hel-Or Y, Peleg S, Avnir D. Two-dimensional rotational dynamic chirality and a chirality scale. *Langmuir*. 1990;6(11):1691-1695. doi:10.1021/la00101a012
81. Chen JS, Shirts RB. Iterative determination of the NMR monomer shift and dimerization constant in a self-associating system. *J Phys Chem*. 1985;89(9):1643-1646. doi:10.1021/j100255a018
82. Q. Munro O, D. Strydom S, D. Grimmer C. Complementary hydrogen bonding in a new tridentate Schiff base ligand : X-ray, DFT and solution NMR studies. *New J Chem*. 2004;28(1):34-42. doi:10.1039/B305946D

4. Gold(III) Complexes Synthesis and Characterisation

Pincer-ligated metal complexes were first reported in 1976 by Moulton and Shaw, marking a significant development in,[1,2] material science, and medicinal chemistry.[3] Since gold(III) complexes are relatively scarce due to their high reduction potential, they typically require strong sigma-donor ligands for enhanced stability.[4] Pincer ligands, especially those with monoanionic coordinating atoms or strong σ-donors, have emerged as key stabilisers for gold(III) metal ions.[5,6]

While carboxamide NNN pincer-type complexes have been reported, gold(III) complexes within this category remain relatively rare.[7] Among them, cyclometallated complexes, where the gold ion is bound to one or more carbon atoms, are more prevalent.[2,7,8] Despite advancements in the study of Au(III) complexes, further research is needed, particularly on pincer complexes, considering their stability and reactivity. The limited availability of these molecules in existing libraries underscores the potential for deeper exploration and understanding.

4.1 Gold(III) complexes chemistry

The synthetic methods employed in this study were carefully selected, taking into account various factors, which will be thoroughly discussed in this chapter. Different spectroscopic techniques were utilised to characterise the synthesised compounds, with individual discussions on each method.

The synthesis of the complexes **2d-f** involved a direct reaction between the ligand and a gold(III) salt. Attempts were made to synthesise **2a-c**, resulting in different products, which are not discussed in detail in this study. Before the successful synthesis of **2d**, two other unexpected products were obtained, contributing to a better understanding of these complexes and the various factors affecting the reaction.

Given the nature of the ligands in this study, their reaction with gold(III) metalions were influenced by factors such as type of reactants, catalyst, energy, solubility, and concentration, leading to the formation of kinetic or thermodynamic products.[9–11]

As discussed in **Chapter 1**, gold(III) can be stabilised by strong σ-donor atoms or monoanionic atoms. Gold(III) also has a partial preference for neutral and ionic nitrogen atoms as well as ionic oxygen atoms. During a metalation reaction, the gold(III) metal ion will preferably coordinate with the ligand through these specified atoms. This aspect made it challenging to obtain the desired product in this study, as nitrogen atoms on the pincer arms were more easily accessible than the desired nitrogen atoms.

To achieve the desired product during the metalation of the ligands, the amides had to be deprotonated.[7] Typically, this process would require a mild base, as strong bases could reduce the gold(III), and weak bases might not be sufficiently strong.[7] The choice of base would depend on the structure of the pincer, including the groups within the molecules and their proximity to the proton to be deprotonated. Strong electron-withdrawing groups close to the proton to be deprotonated weaken the N-H bond, making it easily deprotonated with a weak or no base. Conversely, weak electron-withdrawing groups may require strong bases.[12–14]

The conditions for the metalation reaction depend primarily on the nature of the ligand, considering factors such as the ease of deprotonation and the negative charge on the reacting atoms (anionic or neutral nature and electronegativity). In some cases, it is necessary to dechlorinate the gold(III) ion by replacing the chloride (Cl^-) with water molecules or other readily replaceable molecules/atoms to enhance its reactivity toward the pincer ligands. For reactions involving gold salts, silver phosphorous hexafluoride is often used to dechlorinate the gold salt to replace the Cl^- with the weakly coordinating hexafluorophosphate anion, especially in dry conditions.[15] Reactions with highly reactive ligands that are not sensitive to water can be performed in water, where the Cl^- ions are easily displaced by water molecules due to the higher concentration of water.

Apart from the nature of the reactants, solubility plays a crucial role in determining the availability of reacting groups and this affected the reactivity of ligands in this study, which lead to side reactions, especially since alternative reactive groups were present. The desired product could be obtained if the reactive groups were on the surface of the molecules and the product was soluble in the reaction solution. In such cases, the product formed dissolved, exposing more of the reactive group, and facilitating the completion of the reaction.

Solvents had a significant impact on the reaction rate by either dissolving reagents, participating as a reagent, or acting as a catalyst that differentially stabilised the ground and transition states. Therefore, selecting the appropriate solvent was essential.

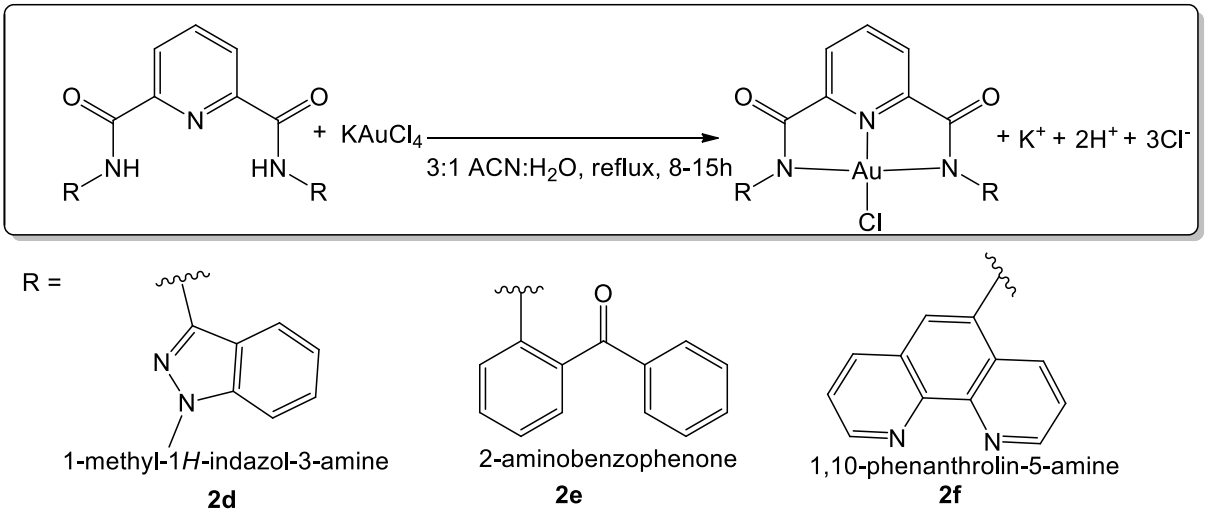
Since only certain solvents could be used, heating increased the soluble of the ligands,[16] and in addition to improving solubility, the heat facilitated the endothermic reaction. The temperature was optimised such that the reagents did not decompose, but could still dissolve.

4.2 Gold(III) complexes synthesis

In this study, the six pincer ligands **1a-1f** were to be used as precursors to the synthesis of gold(III) pincer complexes. Various methods were applied for all complexes, sometimes yielding different products than expected. Despite the diversity in methods, all reactions involved the direct metalation of the pincers in one-pot reactions.

The gold(III) complexes **2d-2f** (**Scheme 4.1**) were synthesised by reacting the appropriate ligands, with the gold salt, potassium tetrachloroaurate ($KAuCl_4$), in a solution of water and acetonitrile in a 1:3 ratio under reflux for 8-15 h. Due to the structure of the pincer ligands, the amide was easily deprotonated with water acting as a weak base. Since the reaction occurred in excess water, the tetrachloroaurate was readily solvated (displacing the four Cl^-s coordinated to gold(III) with H_2O molecules), forming HCl in solution with the protons from the amide. Typically, a red solution was observed, and after cooling down and evaporating the acetonitrile from the solution, a red or orange crystalline powder was filtered off, washed with 10% cold ethanol-water and dried under vacuum. As the resultant products were neutral, there were no counter ions.

The high temperature during reflux was sufficient to dissolve all reagents, and thus solubility did not affect the reaction. Compounds **2d-2f** were the thermodynamic products of this reaction, and they are all stable under high temperatures, air, and light.



Scheme 4.1. General synthetic scheme of the complexes **2d-f** and their structures.

4.3 Complex Characterisation

4.3.1 IR Spectroscopy

In the synthesis of the metal complexes, the deprotonation of the amide N-H occurs as gold(III) exhibits a preference for binding to the ionic amide N, known for its stronger δ-donor properties compared to the neutral amide N. This deprotonation process leads to the disappearance of the NH bands, serving as a definitive indicator of the successful complexation of the ligands with the gold(III) metal. Chelation of the gold(III) ion by the ligands results in a reduction of electron density on the amide N, rendering its lone pair of electrons less readily available. Consequently, electron density on the C=O bond is diminished, causing a shift in the C=O peak in the up-field direction. The vanishing NH bands and the shift in the C=O bands collectively constitute the primary features observed in the spectra of the metal complexes. The alterations in the spectra of **2d**, when compared to **1d**, are visually represented in **Figure 4.1.**

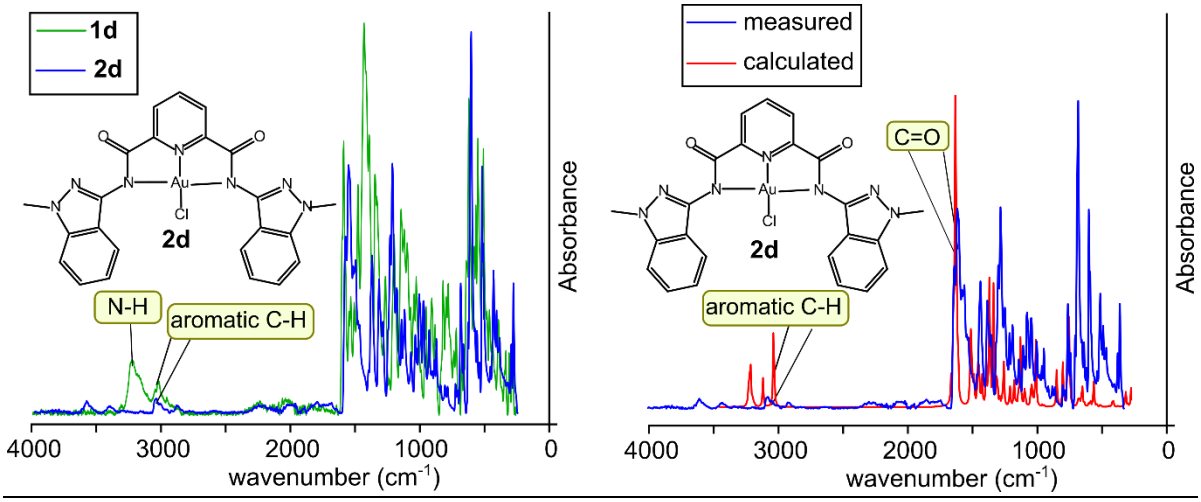


Figure 4.1. An illustration of change in the IR spectra of **1d** upon metalation with gold(III) (left), and the comparison between the experimental and calculated IR spectra of **2d** (right).

The recorded significant bands from both experimental and calculated data for the metal complexes at selected wavenumbers are presented in **Table 4.1. Table 4.2** outlines that all values fall within the anticipated ranges from literature,[17,18] with marginal percentage differences from the calculated data. This concurrence led to the deduction that the complexes **2d**, **2e** and **2f** were successfully synthesised. The observation of the anticipated changes in the bands, coupled with robust corroboration with the calculated data, further supports this conclusion.

Table 4.1. Wavenumbers for significant experimental and calculated IR absorption bands for the synthesised gold(III) complexes **2d-2f.**

	Experimental		Calculated	
	C=O	C-N stretch	C=O stretch	
			symmetric	asymmetric
2d	1677.07	1333.23	1662.43	1669.92
2e	1682.70	1368.86	1677.68	1703.64
2f	1671.78	1390.56	-	-

Table 4.2. The percentage difference between calculated and experimental IR data for **2d**

	C=O stretch
Experimental	1677.07
Calculated	1662.43
% Difference	0.0088

Data obtained from the IR experiments revealed that crucial bands (C=O, 1680-1630 cm^{-1}) were effectively accounted for and fell within the anticipated range. While this method may not be deemed conclusive for compound characterisation, it played a vital role in assigning new bands and discerning the shift or disappearance of original bands, all aligning with expectations (**Figure 4.1**). Confidence in the successful synthesis of the compounds was bolstered by the comprehensive disappearance of NH bands, indicative of complete metalation in the reported metal complexes. Theoretical calculations on these compounds exhibited a strong correlation with the experimental data, with a percentage difference of less than 2%, further elevating our level of confidence.

4.3.2 NMR Spectroscopy

Upon complexation, the deprotonation of amide nitrogens resulted in the disappearance of the singlet peak corresponding to the NH proton (***e***) in the ^{1}H NMR spectrum. Simultaneously, the amide carbonyl C (***d***) exhibited a further downfield shift in the ^{13}C NMR spectrum (**Figure 4.2**, **Table 4.3**).

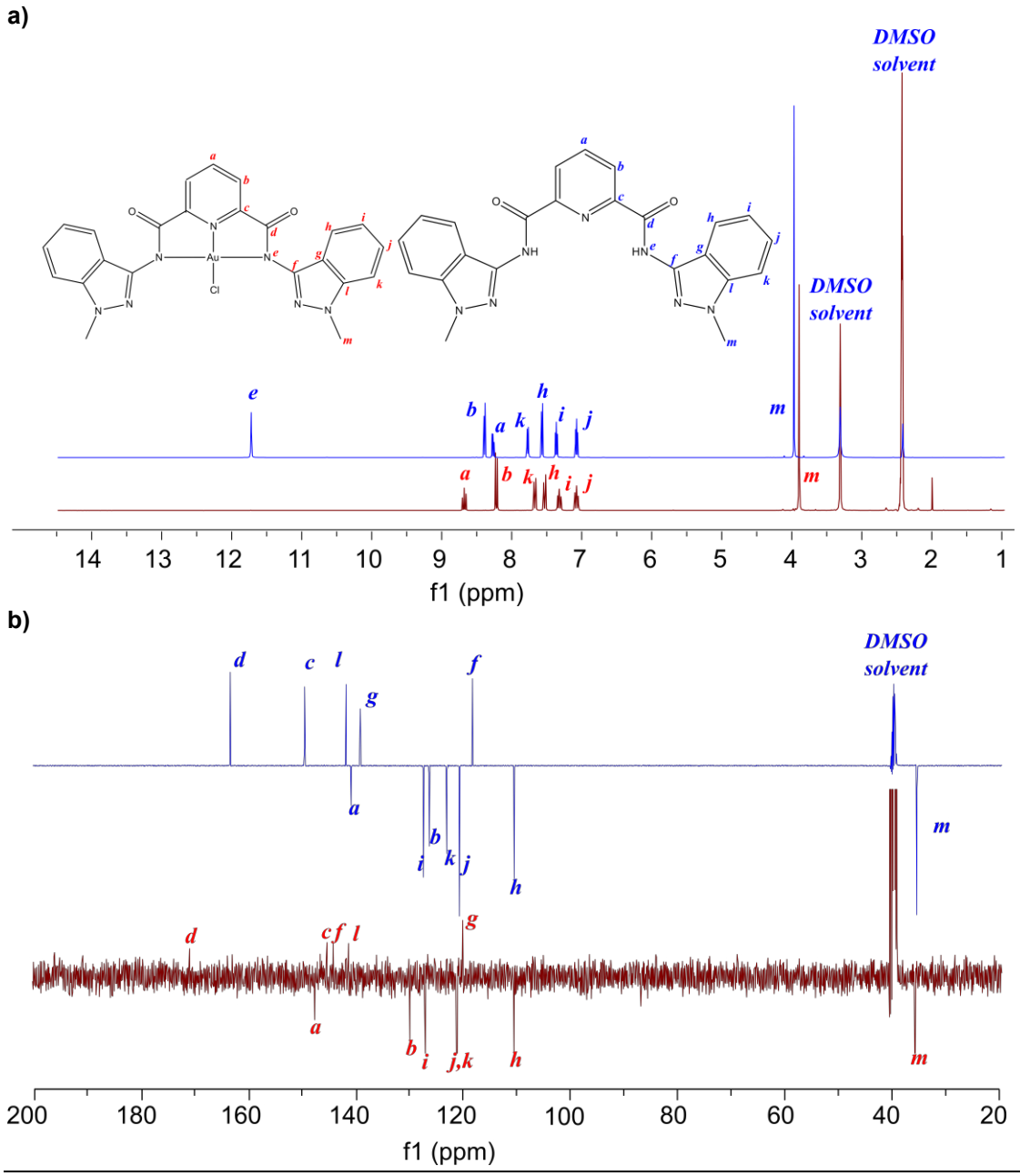


Figure 4.2. An illustration of the changes in the ^{1}H **(a)** and ^{13}C **(b)** NMR spectra in DMSO upon chelation of **1d** with gold(III) to yield **2d.**

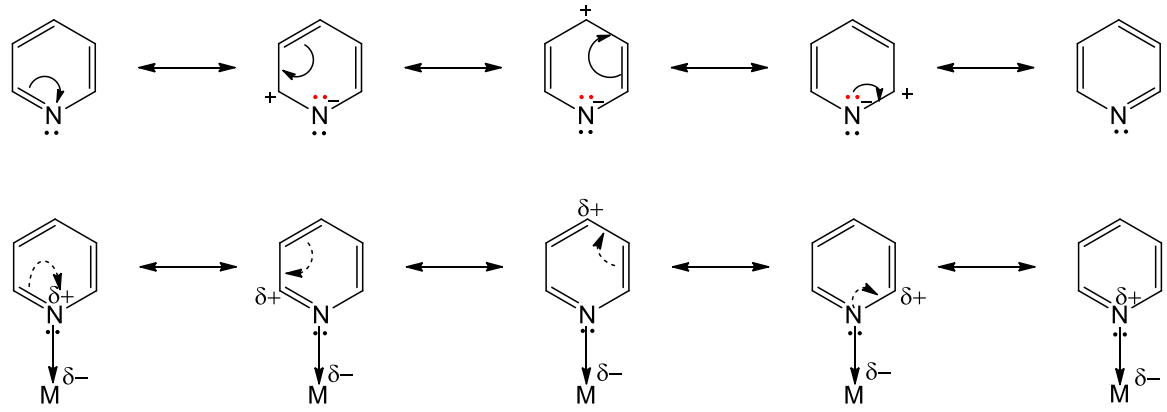
Table 4.3. Chemical shifts in ppm for selected atoms in the synthesised gold(III) complexes **2a-2f.**

	Amide C	Pyridine H (a)	Pyridine H (b)	Pyridine C (a)	Pyridine C (b)	Pyridine C (c)
2d	170.36	8.75	8.29	147.20	129.25	144.93
2e	169.24	8.62	8.30	143.23	127.42	143.66
2f	170.65	8.93	8.52	144.83	128.12	144.91

Similarly, since compounds **2d-2f** share the same backbone motif, the signals for these atoms appear within the same range on the spectrum, approximately 4 ppm of each other. The changes observed after complexation with the metal followed a similar trend (**Table 4.3**). The discussion will focus on the detailed trends observed in **2d**, as the same trends were observed in all the complexes.

The indazole protons ***h, i, j*** and ***k*** were not significantly affected by the complexation of **1d**. This lack of significant impact can be attributed to the indazole ring not actively participating in coordination with the gold metal centre. As these protons are situated on the benzene ring of the indazole, they are positioned sufficiently far away from the metalation site to be significantly influenced by the complexation process. This observation is consistent with the findings in **2e** and **2f**, where there was no significant change observed in the chemical shifts of the atoms on the pincer arms.

On the other hand, the pyridine protons ***a*** and ***b*** underwent notable changes. This can be attributed to the nature of the pyridine ring and its resonance structures (**Scheme 4.2**. During transitions between resonance structures, electrons are withdrawn either from the *ortho*- or *para*-positions, centralising the positive charge on these specific positions. The pyridine nitrogen, functioning as an L-type ligand, binds to the gold metal through dative bonding. This leads to a shift in the electron cloud from the nitrogen towards the metal centre. Consequently, the electron density around the nitrogen is reduced, causing it to draw electrons from the *ortho*-C. In turn, this influences the electron cloud around the *para*-position. The result is a downfield shift of the signal for proton ***a*** upon complexation, indicating reduced electron density on this carbon and proton (deshielding). Simultaneously, during this process, the electron density on the *meta*-position slightly increases, leading to the upfield shift of the signal for proton ***b*** due to increased shielding.[19,20]



Scheme 4.2. An illustration of the resonance in the pyridine molecule before and after metallation.[20]

The ^{13}C NMR spectra provide a more comprehensive insight into the impact of metalation on the electron density of atoms within the synthesised compounds. Carbons ***h***, ***i***, ***j*** and ***k*** are minimally or not affected at all, consistent with their locations on the indazole ring, which does not participate significantly in metal binding.

Notably, signals for carbons ***a*** and ***c*** are more significantly affected than carbon ***b***, despite their positions on the same ring. This differential effect can be attributed to the nature of resonance structures, where electron densities are withdrawn from the *para*- and *meta*-positions, as explained earlier.

Upon complexation, the substitution of hydrogen on the amide nitrogen (proton ***e***) by the cationic Au(III) results in a stronger electron-withdrawing effect due to the highly electron-deficient nature of the gold(III) ion. Consequently, the electron density of nitrogen is reduced. As the lone pair of electrons on nitrogen is delocalised across the amide bond, the electron density on carbon ***d*** is dramatically decreased, leading to its pronounced deshielding and a substantial downfield shift in the carbon signal.

In summary NMR spectroscopy, by reflecting the changes in chemical shifts upon complexation, provides valuable insights into the structures of the synthesised carboxamide ligands. The observed shifts align with the anticipated changes, confirming the successful synthesis of the metal complexes **2d-2f**.

4.3.3 UV-vis Spectroscopy

Upon complexation of the ligands, a metal charge transfer and ligand field transitions occur, leading to the introduction of new bands in the spectra of the compounds. This phenomenon was observed for all complexes **2d-f**, although only **2d** is discussed in detail in this section. The spectra for **2e** and **2f** can be found in the supplementary information (**Section S1.1.3, Figures S19 and S21**).

Due to the occurrence of multiple transitions in the same region, there is a tendency for overlap, making it challenging to distinguish between different types of transitions. However, an additional transition at 439 nm observed in the UV spectrum of **2d** is characteristic of the gold(III) band as reported in the literature, indicating a metal-ligand transition.[4,21] This is illustrated in **Figure 4.3**, where. The extinction coefficients for **2d-2f** are recorded in **Table 4.4**. **Figure 4.3** provides an example of how these data were calculated.

The solution electronic absorption spectra of the metal complexes displayed intense bands at 267 nm, and 296 nm for **2d**, 335 nm for **2e** and 269 nm and 315 nm for **2f**. All these were attributed to intra-ligand ($\pi \rightarrow \pi^*$) charge transfer transitions.[22,23] With reference to the previous spectroscopic studies of Au(III) complexes,[23,24] the high energy transitions gave absorption bands in the region 430-460 nm, which corresponded to the ligand-to-metal charge transfer (LMCT) occurring between the chloride ligand and the gold(III) center.

Table 4.4. Extinction coefficients at λ_{max} for compounds **2d-2f.**

	solvent	Λ_{max} (nm) ε (M^{-1} cm^{-1})	Λ_{max} (nm) ε (M^{-1} cm^{-1})	Λ_{max} (nm) ε (M^{-1} cm^{-1})	Λ_{max} (nm) ε (M^{-1} cm^{-1})
2d	DMSO	267 3.674×10^3	296 8.247×10^3	439 8.169×10^3	
2e	DMSO	335 5.298×10^3	429 7.321×10^3		
2f	DMSO	269 7.5016×10^3	315 1.5699×10^3	455 9.772×10^3	

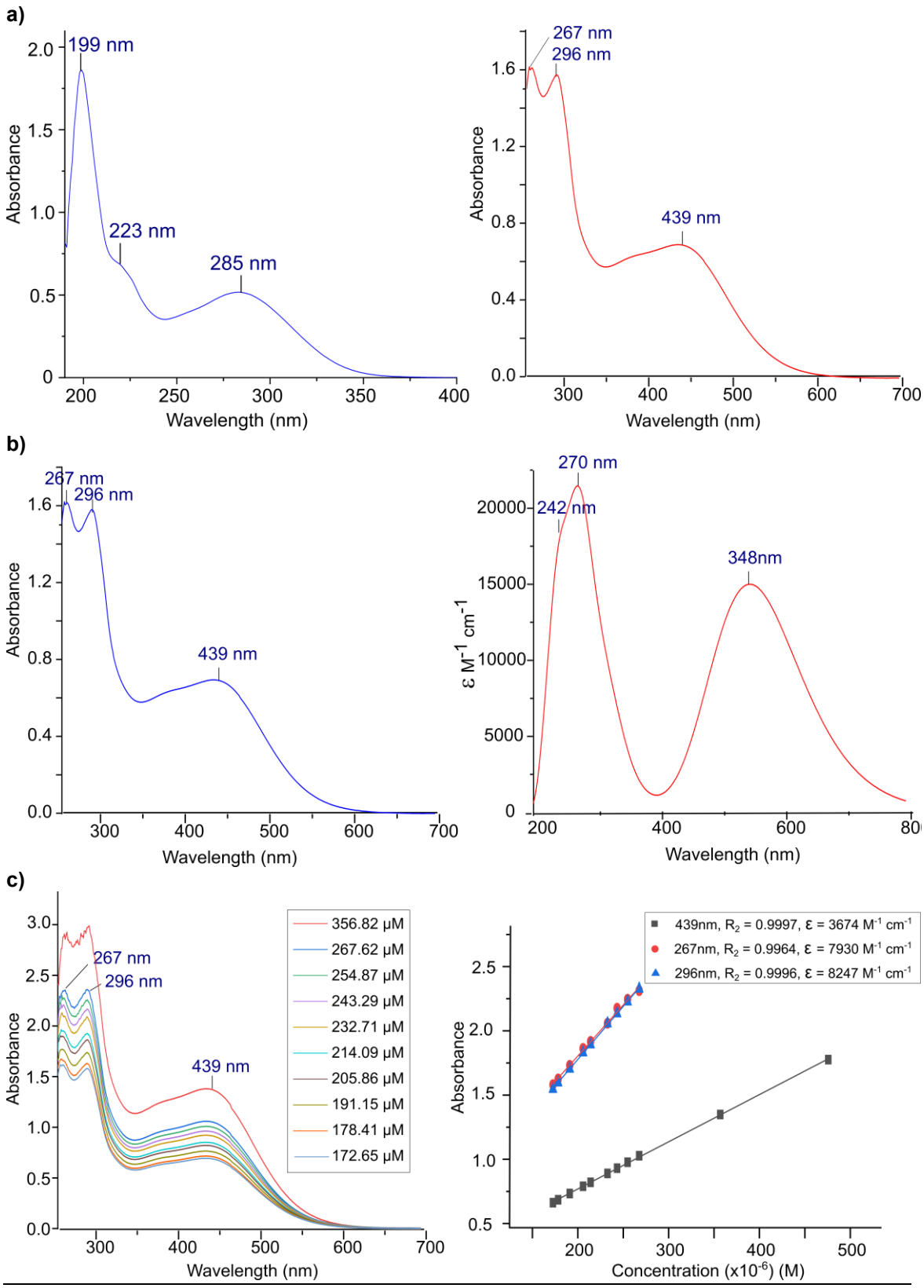


Figure 4.3. **(a)** Comparison between **1d** (left) and **2d** (right), illustrating the shift in the indazol bands, below 350 nm and the introduction of the bands at 439 nm, which is d-d transitions, **(b)** Experimental (left) and DFT-calculated (right) electronic absorption spectra of **2d** in DMSO. The absorption maxima are indicated for the experimental spectrum at 267, 296 and 439 nm. The absorption envelope for the DFT-calculated spectrum is plotted with a bandwidth of 2200 cm^{-1} (full width at half maximum intensity, FWHM). **(c)** Absorption spectra at a concentration range between 172 and 357 µM, to calculate the extinction coefficients at the λ_{max} using the Beer-Lambert's Law.

The molecular orbitals in **Figure 4.3** showcased that there were electron transitions in the d-orbitals of the orbitals at high energy levels. This is due to the availability of the empty d-orbitals in the LUMO. This behaviour is typical of transition metal complexes.[25–28]

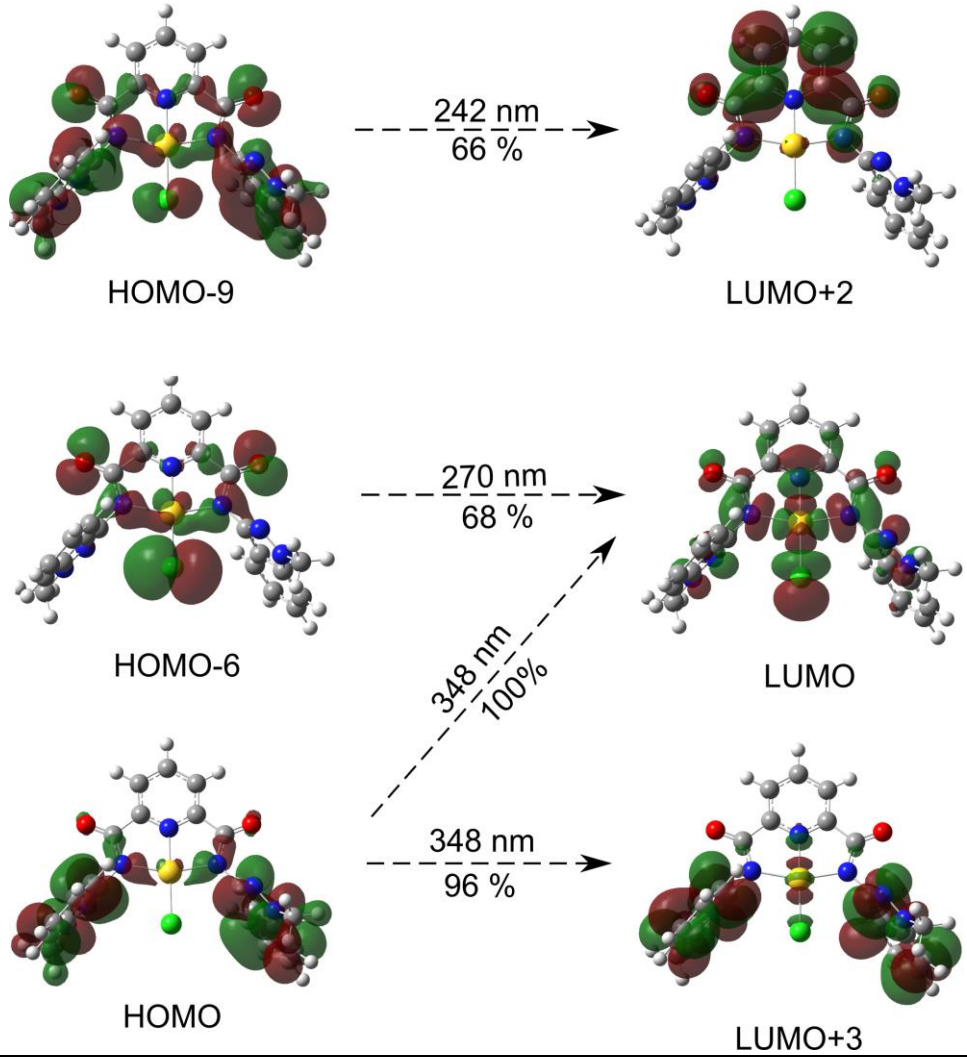


Figure 4.4. Molecular orbitals involved in the three most intense bands in the DFT-calculated electronic spectrum of **1d** in DMSO. The percentage contribution of the electronic transitions to each band are indicated.

The synthesised compounds exhibited electronic transitions that align with the expected transitions reported in the literature, [4,21–23] and these findings were further supported by computed data as discussed in this section. This provides evidence for the successful metallation of the complexes **2d-f**.

4.3.4 Unexpected metal complexes

The unexpected metal complex discussed in this section are illustrated in **Figure 4.5**.

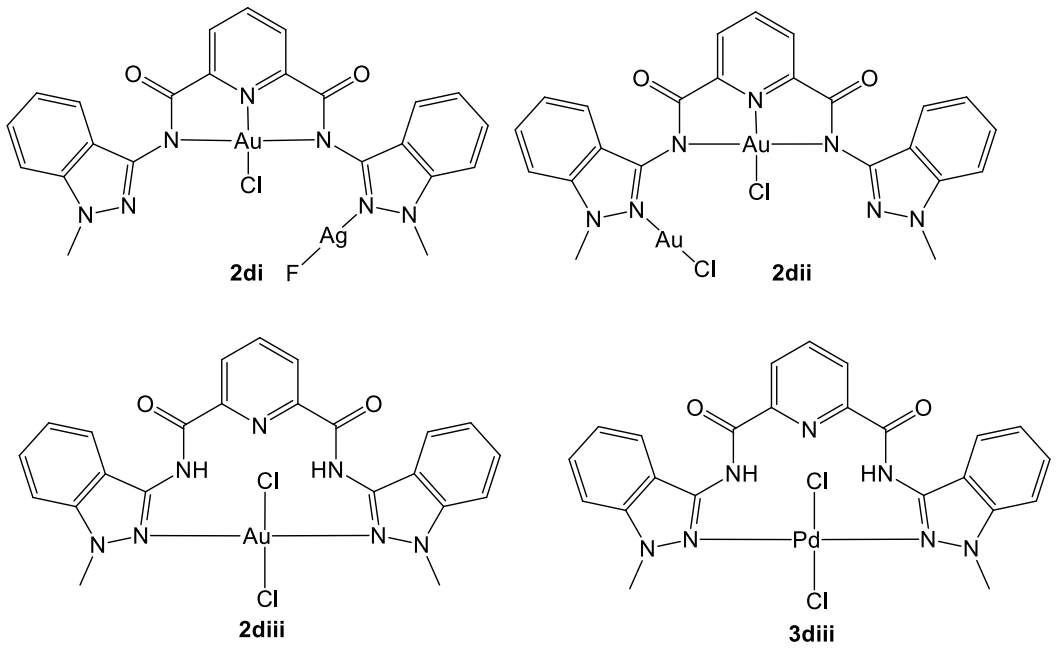


Figure 4.5. 2D Structures of the unexpectedly synthesised pincer complexes according to X-ray crystallography (**2di, 2dii** and **3diii**) and the proposed structure of **2diii.**

The atypical complexes of **1d** (**2di** and **2dii**) consequence of the distinctive behaviour of the indazole groups on the arms of the pincer molecule. The indazole nitrogen (N2) (**Scheme 4.3**) on the ^{1}H-methyl-indazole is a relatively reactive nucleophile, facilitated by the enhanced nucleophilicity of N2 due to the presence of the methyl group on N1.

Compound **2di** was synthesised through a one-pot reaction. Ligand **1d** was dissolved in acetonitrile, and the gold salt $KAuCl_4$, dissolved in acetonitrile was slowly added to the ligand mixture and stirred at room temperature for 5 minutes. Silver hexafluorophosphate ($AgPF_6$) dissolved in water, was added to the mixture, and the reaction was refluxed for 15 hours, yielding a red precipitate upon cooling. The ratio of acetonitrile to water in the resultant solution was 2:1. Subsequent filtration, acetonitrile evaporation, and washing steps resulted in a red crystalline powder.

2dii was also synthesised in a one-pot reaction. Ligand **1d** was dissolved in acetonitrile, and the gold salt dissolved in acetonitrile was slowly added to the ligand mixture and stirred a room temperature for 5 minutes. Sodium tetrafluoroborate ($NaBF_4$), dissolved in water was added to the mixture and the reaction was refluxed for 15 hours, yielding a red precipitate upon cooling. The ratio of acetonitrile to water in the resultant solution was 2:1.

The Ag^+ ion in $AgPF_6$ played a crucial role in dechlorinating the $AuCl_4^-$ anion, forming a white precipitate. The PF_6^- anion then acted as a weak base, deprotonating the amide protons, and forming HPF_6 acid and an anionic ligand. The AgCl precipitate was filtered before the product precipitation to prevent contamination.

$AgPF_6$ was selected for its inert nature, being chemically inert. The PF_6^- anion is considered non-coordinating, interacting weakly with cations due to its poor nucleophilic nature.[29,30] Although generally

considered chemically inert, $AgPF_6$ can undergo decomposition at elevated temperatures (>60°C) to form PF_5 and F^- in water (**Scheme 4.3a**).[26,31–34] Unexpectedly, this decomposition occurred during the reaction, leading to the production of F^- ions.

The Ag metal centre, possessing empty d orbitals, demonstrated reactivity toward z-type ligands (N2). This facilitated the reaction of Ag^+ with the N2 on the indazole rings. The N2 nitrogen, being nucleophilic, formed a dative bond with the electron-deficient Au and Ag metal centres. This nitrogen functioned similarly to the pyridine nitrogen, while N1 behaved akin to the pyrrole nitrogen with its lone pair of electrons being delocalised in the aromatic ring.

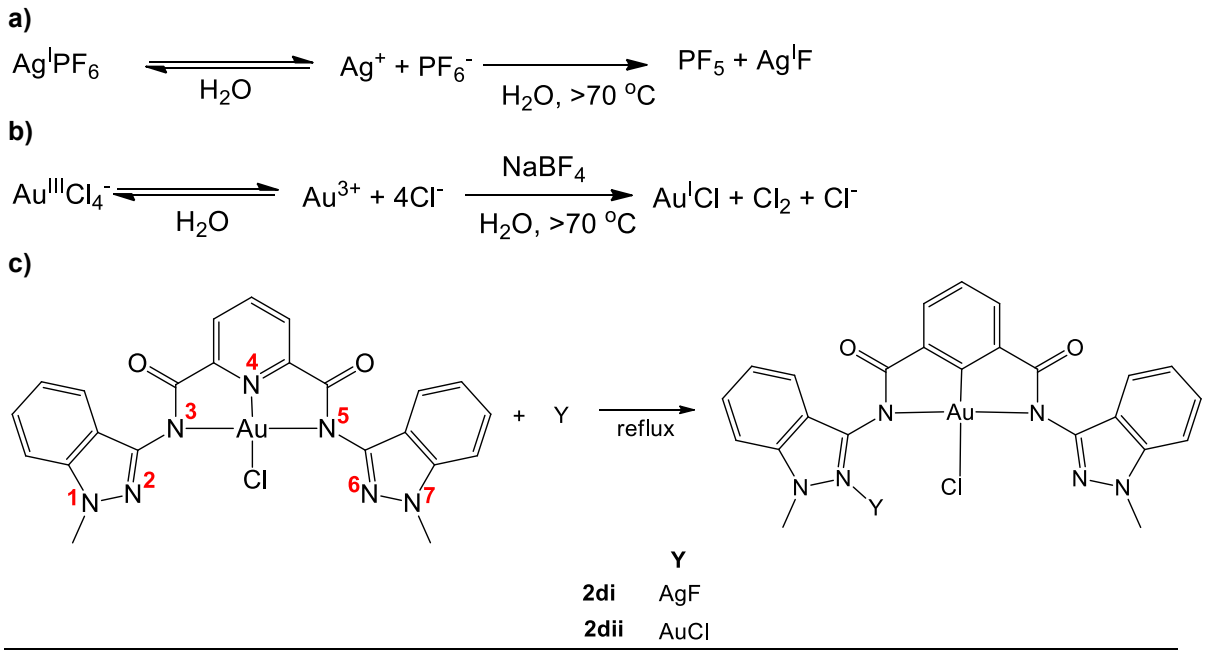
The N2 nitrogen, with its high electron density and nucleophilic nature due to the availability of its lone pair of electrons, formed a dative bond shared with the metal centres. On the other hand, chloride and fluoride ions acted as x-type ligands, providing one of the shared pairs of electrons. Possessing high electronegativities (2.83 and 4.10 Å respectively)[35], chloride and fluoride ions served as strong electron-withdrawing groups, rendering them highly nucleophilic. The electron-deficient Au and Ag metal centres, with their positive charge, exhibited electrophilic reactivity, making them responsive to x-type and z-type ligands.

The resulting AgF reacted with one of the indazole N2 nitrogens, facilitated by the electron-donating nature of the methyl group on N1, enhancing the reactivity of nitrogen N2.

Crystallographic data presented later in this chapter provides information about this product. However, NMR studies revealed that the indazole hydrogen peaks integrated for 2 equivalents each, implying the similarity of both rings on the molecule. Consequently, it was concluded that the presence of AgF was negligible and not detectable through NMR spectroscopy and FTIR.

An adjustment in the synthetic method of **2di** by replacing $AgPF_6$ with $NaBF_4$, aimed to avoid the formation of the AgF, as observed in **2di**. X-ray crystallography data indicated that AgF was replaced by AuCl with 35% occupancy. NMR spectroscopy data showed that similar protons on two arms of the pincer complex were equivalent, suggesting that a negligible amount of **2di** was present. As a result it was concluded that gold(III) (Au^{3+}) was reduced to gold(I) (Au^+), albeit in small amounts and reacted with the preformed **2d**. Similar to **2di**, the quantity of the compound reacting with AuCl was too small to be accounted for by NMR spectroscopy, resulting in spectra identical to that of **2d**.

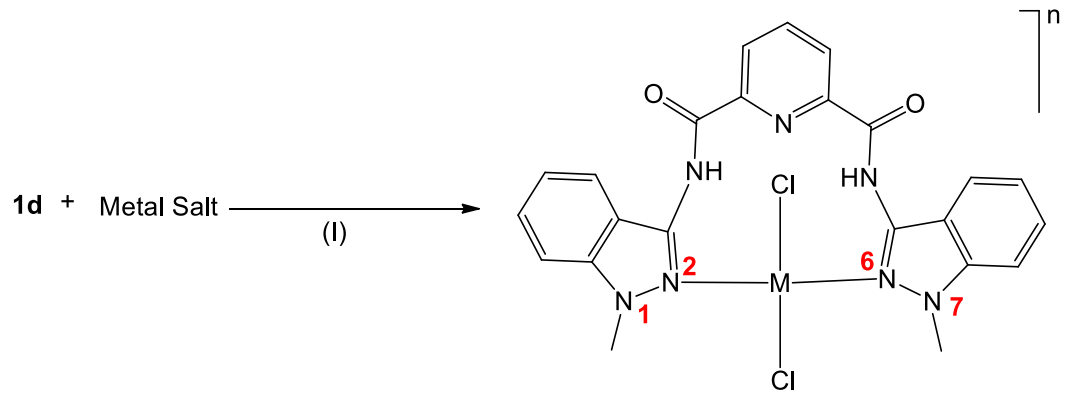
The proposed mechanism for the formation of **2di** and **2dii** is illustrated in **Scheme 4.3**.



Scheme 4.3. The illustration of the proposed mechanism for the formation of the **a)** AgF from $AgPF_6$ and the decomposition of the PF_6[24,25] and **b**) AuCl from $AuCl_4$ from the reduction of Au(III) to Au(I) in the presence of $NaBH_4$, at high temperatures, and **c**) the reaction of AgF and AuCl with the **2d** resulting in **2di** and **2dii** respectively.

To prevent potential side reactions, the method employed for the synthesis of **2d** ensured the absence of excess gold(III), which could potentially be reduced to gold(I). Additionally, no silver ions or any other foreign cations and anions were introduced, mitigating the risk of unintended reduction of gold(III).

If **2d**, **2di**, and **2dii** are considered thermodynamic products, in contrast, **2diii** and **3diii** were identified as kinetic products in the reactions of **1d** with $AuCl_4^-$ and $PdCl_2$, respectively (**Scheme 4.4**). While **3diii** is a palladium(II) complex and may not be directly relevant to this study, its crystal structure provided insights into the reactivity of the carboxamide pincer molecules based on their structure. It was inferred that **2diii** would yield a similar product to **3diii** under similar conditions, as characterisation data (NMR) suggested the presence of NH bonds in the molecules. These reactions were conducted at room temperature, and thus there was not enough energy to compel the metal ions to react with the central pincer pockets, but they instead reacted with the more easily accessible indazol nitrogens N2 and N6 **(Scheme 4.4**).



Scheme 4.4. Illustration of the synthesis of 2diii (MS = $KAuCl_4$; (I) = ACN at 40 °C, 15 h; n=+1) and **3diii** (Metal salt = $PdCl_2$, (I) = THF at room temperature °C, 10 h; n=0)

The indazole rings, particularly at N1 and N7 where a methyl group is attached, are electron-rich, exhibiting an enhanced electron-donating capacity. This increased electron density on N2 and N6, which are equivalent atoms, enhances their nucleophilicity. Consequently, both N2 and N6 actively participate in forming dative bonds with gold(III) and palladium(II) metal centres.

Ultimately, it was also inferred from this information that although under different conditions metalation reactions of **1a-1c** yielded similar products. The complexes were, however, unstable and dissociated in solution and could not be characterised.

4.3.5 X-ray Crystallography

X-ray crystal data were collected for complexes **2d**, **2e**, **2di**, **2dii**, **3d** and **2dT** (**Figure 4.6, Table 4.5**). These complexes were crystallised by slow liquid-to-liquid diffusion method, wherein ethanol (**2dii, 2dT**), methanol (**2e, 3d**), t-butanol (**2dii**), or water (**2d**) was gradually diffused into DMSO by layering the solvents on the DMSO solution of the respective complex. Crystals obtained from these processes exhibited various shades of red.

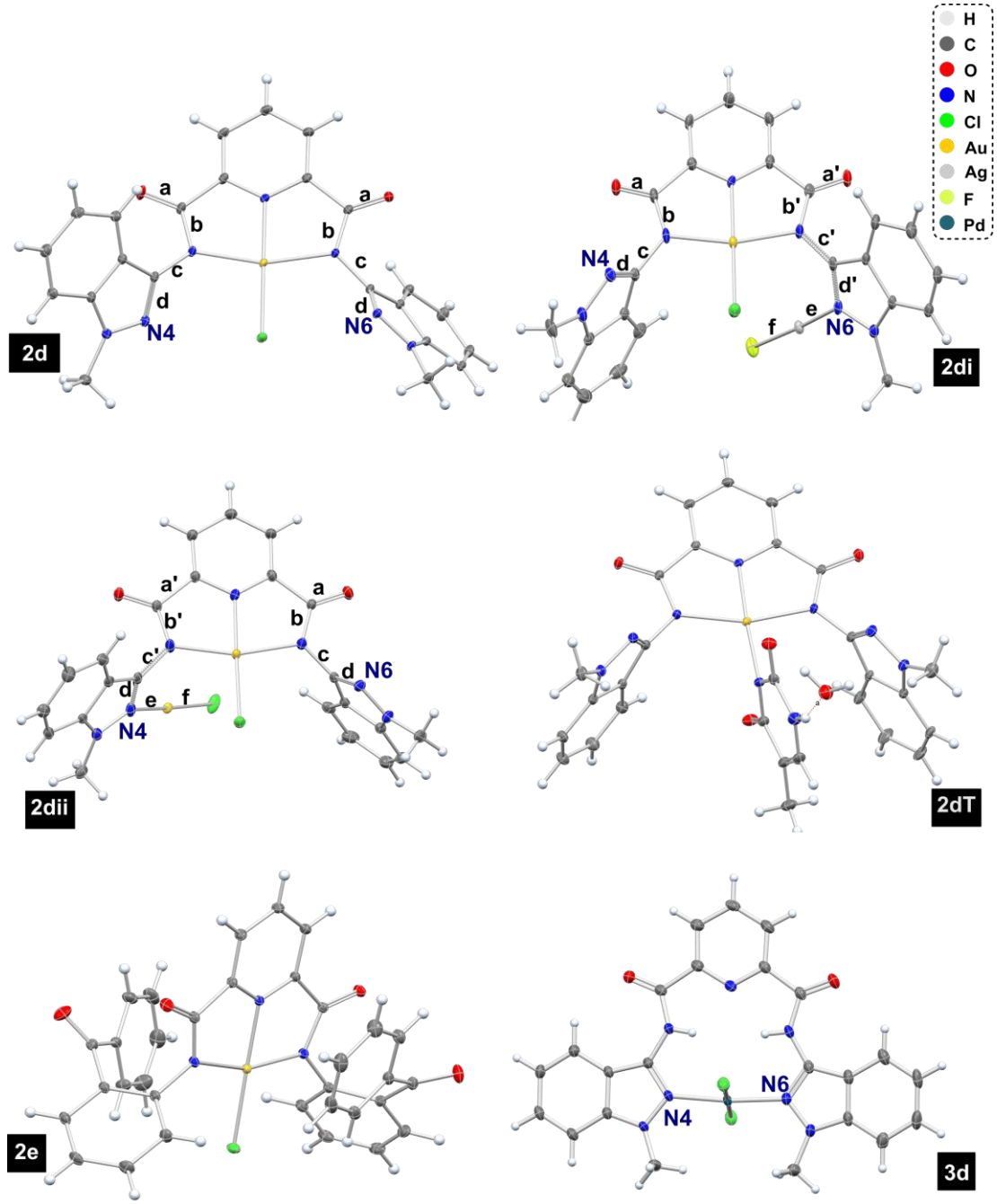


Figure 4.7. Selectively labelled views of the X-ray crystal structures of **2d, 2di, 2dii, 2dT, 2e, 3d.** Thermal ellipsoids are rendered at the 50% probability level and H atoms are drawn as spheres of an arbitrary radius. Space groups: $P\bar{1}$, **2d, 2di, 2dii, 2dT**; $P2_1/n$, **2e, 3d**. Complexes **2d, 2di, 2dii, 2dT, 2e** have C_i symmetry, but **3d** maintains the C_2 symmetry, and none of them crystallise in a Sohncke space group. The indicated bonds and molecules in **2d, 2di, 2dii** and 2dT were used as references when discussing the change in the molecules.

There was no existing crystallography data for all crystallised complexes in the CDS database, which implies that. X-ray crystallography had not been previously employed to study these complexes. Notably, only three carboxamide pincer gold(III) complexes were found in the CDS database, suggesting that this particular class of compounds is not widely explored.[7,36]

Unlike the carboxamide pincer ligands, these complexes lose their chirality upon complexation. The metal ions hold the molecules, which are initially non-planar, in a relatively planar configuration around the metal centre (**Figure 4.6**). While the anchoring site remains planar, the presence of a dihedral bond allows the arms to rotate. As a result, the complexes crystallise with C_i symmetry. The rigidity imposed on the anchoring site reduces the flexibility of the compounds, leading to the loss of atropisomerism.

Table 4.5 Crystal data and structure refinement for the synthesised gold(III) complexes **2d, 2e, 2di, 2di, 2dT** and the palladium(II) complex **3d.**

	2d	**2e**	**2di**	**2dii**	**2dT**	**3d**
Empirical formula	$C_{23}H_{17}AuClN_7O_2$	$C_{33}H_{21}AuClN_3O_4$	$C_{23}H_{17}AgAuClFN_7O_2$	$C_{23}H_{17}Au_{1.35}Cl_{1.35}N_7O_2$	$C_{28}H_{25}AuN_9O_{5.5}$	$C_{23}H_{19}Cl_2N_7O_2Pd$
Formula weight	655.85	755.94	782.72	737.99	772.54	602.75
Temperature/K	153.15	173.15	173.15	153.2	173	152.95
Crystal system	triclinic	monoclinic	triclinic	triclinic	triclinic	monoclinic
Symmetry	C_i	C_i	C_i	C_i	C_i	C_2
Space group	P-1	$P2_1/n$	P-1	P-1	P-1	$P2_1/n$
a/Å	8.8115(3)	13.3998(5)	8.670(3)	8.5381(4)	10.3116(7)	8.4125(4)
b/Å	10.4987(3)	12.9269(5)	11.448(4)	11.3000(5)	11.8798(7)	14.3306(7)
c/Å	12.0821(4)	15.8441(6)	13.101(5)	13.1055(6)	13.2653(8)	18.7046(9)
α/°	82.449(2)	90	105.909(19)	104.735(2)	69.269(2)	90
β/°	74.233(2)	96.1180(10)	97.97(2)	97.970(3)	68.398(2)	95.258(2)
γ/°	81.344(2)	90	97.98(2)	98.032(3)	86.901(2)	90
Volume/Å^3	1058.58(6)	2728.85(18)	1216.9(8)	1190.65(10)	1407.59(15)	2245.47(19)
Z	2	4	2	2	2	4
ρ_{calc}g/cm^3	2.058	1.84	2.136	2.059	1.823	1.783
μ/mm^{-1}	7.114	3.021	6.979	8.542	5.285	1.103
F(000)	632	1472	744	699.9	758	1208
Crystal size/mm^3	0.161 × 0.094 × 0.08	0.332 × 0.223 × 0.21	0.18 × 0.05 × 0.044	0.05 × 0.035 × 0.01	0.18 × 0.15 × 0.12	0.334 × 0.204 × 0.154
Radiation	MoKα (λ = 0.71073)	AgKα (λ = 0.56086)	MoKα (λ = 0.71073)	MoKα (λ = 0.71073)	MoKα (λ = 0.71073)	MoKα (λ = 0.71073)
2Θ range for data collection/°	3.518 to 66.494	4.778 to 61.356	3.29 to 56.89	3.268 to 58.068	5.874 to 61.17	5.632 to 59.296
Index ranges	-13 ≤ h ≤ 13, -16 ≤ k ≤ 16, -18 ≤ l ≤ 18	-24 ≤ h ≤ 24, -23 ≤ k ≤ 23, -28 ≤ l ≤ 28	-11 ≤ h ≤ 11, -15 ≤ k ≤ 15, -17 ≤ l ≤ 17	-11 ≤ h ≤ 11, -15 ≤ k ≤ 15, -17 ≤ l ≤ 17	-14 ≤ h ≤ 14, -16 ≤ k ≤ 16, -18 ≤ l ≤ 18	-11 ≤ h ≤ 11, -19 ≤ k ≤ 19, -26 ≤ l ≤ 25
Reflections collected	59569	323126	33090	32923	86111	43715
Independent reflections	8133 [R_{int} = 0.0387, R_{sigma} = 0.0240]	17190 [R_{int} = 0.0583, R_{sigma} = 0.0190]	6077 [R_{int} = 0.0829, R_{sigma} = 0.0654]	6309 [R_{int} = 0.0476, R_{sigma} = 0.0405]	8626 [R_{int} = 0.0366, R_{sigma} = 0.0188]	6314 [R_{int} = 0.0344, R_{sigma} = 0.0236]
Data/restraints/parameters	8133/0/309	17190/0/379	6077/0/327	6309/0/327	8626/0/394	6314/2/326
Goodness-of-fit on F^2	1.069	1.086	1.112	1.334	1.108	1.069
Final R indexes [I>=2σ (I)]	R_1 = 0.0194, wR_2 = 0.0423	R_1 = 0.0220, wR_2 = 0.0416	R_1 = 0.0532, wR_2 = 0.1244	R_1 = 0.0569, wR_2 = 0.1329	R_1 = 0.0198, wR_2 = 0.0404	R_1 = 0.0292, wR_2 = 0.0639
Final R indexes [all data]	R_1 = 0.0241, wR_2 = 0.0437	R_1 = 0.0322, wR_2 = 0.0449	R_1 = 0.0811, wR_2 = 0.1381	R_1 = 0.0728, wR_2 = 0.1394	R_1 = 0.0259, wR_2 = 0.0433	R_1 = 0.0406, wR_2 = 0.0685
Largest diff. peak/hole / e Å^{-3}	2.51/-1.09	0.80/-1.48	3.55/-2.86	3.98/-3.70	1.94/-1.21	0.52/-0.52

Crystals of **2d** were grown by slow diffusion of water into its DMSO solution. **2d** crystallised in the P-1 space group due to the centre of inversion induced by the indazole arms of the pincer. In comparison to its ligand **1d**, the C=O and (CO)–N bond distances of **2d** decreased from 1.231 Å to 1.219 Å and increased from 1.353 Å to 1.378 Å, respectively, and significantly. One explanation is that the Au(III) ion is more electronegative and bigger than the H^+ ion, and has empty d orbitals, all of which reduce

the electron density on the nitrogen, weakening the π bond, and making it longer. Another explanation could be that the C–N bond elongated to an optimum length to accommodate the metal binding (the amide N and the pyridine N form a five-membered ring with the metal ion centre, and the bonds should be long enough for the compound to be stable). This, in turn, shortens the C=O bond. The complex is planar around the gold metal ion but loses planarity in the indazole arms. This makes the complex **2d** to lose its chirality as well as its symmetry compared to **1d**.

Complexes **2di** and **2dii** are derivatives of **2d**, crystallised by slow diffusion of ethanol and t-butanol, respectively, in the complex-DMSO solution. They both crystallised in the triclinic space group P-1 which only has a centre of inversion, just like **2d**.

Complex **2dii** has two types of Au–Cl bonds (Au(III)–Cl and Au(I)–Cl) and Au–N bonds (Au(III)–N and Au(I)–N). It is not easy to compare Au(I)–N and Au(III)–N bonds as the Au(III)–N bond length is governed by the pincer framework, and the Au(I)–N can be considered as freestanding, with minimal interference.

The bond lengths for Au(III)–N are at an optimal length, such that the metal forms stable five-membered rings with the pincer nitrogens (Au(III)–N_{amide} is 2.037 Å and Au(III)–$N_{pyridine}$ is 1.945 Å). Because of the restriction in the Au(III)–N (1.945 Å), there is a difference of 0.007 Å in comparison to the Au(I)-N ***e*** (1.953 Å). which is an insignificant amount compared to the Au–Cl (2.264 Å for Au(III)–Cl and 2.240 for Au(I)–Cl ***f***), which has a length difference of 0.024 Å. Since there was a negligible difference in the Au–N bond length, it could be deduced that the charge on the metal atoms did not affect their bond lengths significantly. This is in correlation with some studies in the literature.[37]

The Ag–F bond length in **2di** is 2.200 Å, (**Table 4.6,** (bond **f**)), which is 0.217 Å longer than the free Ag–F bond in literature,[38–40] and the Au(I) –Cl bond length in **2dii** is 2.239 Å, (**Table 4.6,** (bond **f**)), which is 0.047 Å shorter than the free Au–Cl bond in literature.[21,37,41] This could be attributed to the difference in electronegativities of the individual halides bound to the metal centres.

Table 4.6. Bond lengths of selected bonds in the analogues of **2d**. The labels are indicated in **Figure 4.6.**

	2di	**2dii**	**2d**
Bond	**Bond length / Å**	**Bond length / Å**	**Average bond length/ Å**
a	1.214	1.225	1.121
a'	1.244	1.226	
b	1.397	1.367	1.372
b'	1.354	1.359	
c	1.410	1.427	1.410
c'	1.392	1.412	
d	1.325	1.313	1.323
d'	1.341	1.326	
e	1.974	1.953	
f	2.200	2.239	
X	**Au^{III}–X bond length (Å)**	**Au^{I}–X bond length (Å)**	
Cl	1.946	1.953	
N	2.265	2.239	

From the structures in **Figure 4.6,** it was noted that the introduction of a metal ion on the indazole nitrogen, N4 or N6 induced changes in bonds indicated in **Figure 4.6**.

According to literature, the difference in electronegativity of atoms participating in a bond affects the bond polarity and bond length.[42,43] Chlorine and fluorine have high electronegativities of 3.50 and 4.00 Å respectively.[35,44] In comparison to Au (2.81) and Ag (2.88),[44] this results in a difference of 0.69 between Au and Cl, and 1.12 between Ag and F. The Ag-F bond is more polar than the Au-Cl bond,and thus the Ag-F bond in **2di** should be shorter than the Au-Cl bond in **2dii**, which is what was observed on bond **f** in **2di** and **2dii**. Apart from the polarity of the bonds, the Ag and F are smaller in diameter as compared to the Au and Cl atoms, making the Ag–F bond shorter than the Au–Cl bond.

The high electronegativities of chlorine and fluorine make their anions strong withdrawing groups, and consequently very nucleophilic. On the other hand, the Au and Ag metal centres are electron deficient (have an overall positive charge), which makes them very electrophilic. This is expected to increase the polarity in the metal–halide bond (bond **f** in **Figure 4.6)**, consequently decreasing its bond length. The nitrogen, however, has a lone pair of electrons, which binds datively to the metal centre, reducing the overall positive charge around the metal centre, and ultimately reducing the polarity of the bond, and increasing the bond length, which is what was observed in complexes **2di** and **2dii**.

The bond Ag-N (bond **e**) in the **2di** bond is longer than the Au–N (bond **e**) bond in **2dii** (1.974 and 1.953 Å respectively). These two bonds are both dative covalent bonding as the N is an L-type ligand (donate a pair of electrons to the metal centre) in this case. Because the Au–Cl bond is longer than the Ag–F bond, the Au is more electron deficient than the Ag, which makes the Au more electrophilic, thus the Au–N bond is shorter than the Ag–N bond.

Previous studies have shown that an electrophilic addition reaction on the pyridine-like nitrogen of the indazole, decreases the bond length of **c**.[45] This was also evident in complexes **2di** and **2dii**, where the bond **c'** is shorter than the bond **c.**

Bonds c' (N bound to a metal centre) are longer than c (free N), and d' is shorter than d because bond lengths decrease with an increase in bond order, (double bond > pseudo double bond > single bond).[46–48] **c'** and **d'** are pseudo double bonds, and compared to the N=C and C–N bonds, which have bond orders of two and one respectively, **c'** has to be longer than **c,** and **d'** shorter than **d**.

2dT was very useful in determining how the thymine base binds to the metal centre. The thymine binds to the metal center in its ionic form, as it is deprotonated. The resultant compound is still neutral. The introduction of this aromatic group changed the orientation of the indazole arms of the complex, and they now face the same side. While all other analogues of **2d** exhibit nearly similar bond lengths for both Au–N_{amide} bonds, **2dT** behaves differently, showing a difference of 0.015Å (**Figure 4.7**).

The bonds around the metal centre in **2dT** shorten in comparison to the ones in **2d**. The most notable change in these bonds is the difference between the Au–$N_{Thymine}$ (2.014 Å) and Au–Cl (2.264 Å) bonds. The bond is reduced by 0.25 Å upon the substitution of Cl^- with thymine. Thymine is bulkier than Cl^-, causing the angle between the two indazole arms in **2dT** to increase to 90° from 65° in **2d (Figure 4.7)**.

Due to less repulsion of the molecule from steric hindrance, thymine has better access to Au than Cl^-, resulting in the Au–$N_{Thymine}$ being stronger and shorter than the Au–Cl bond.

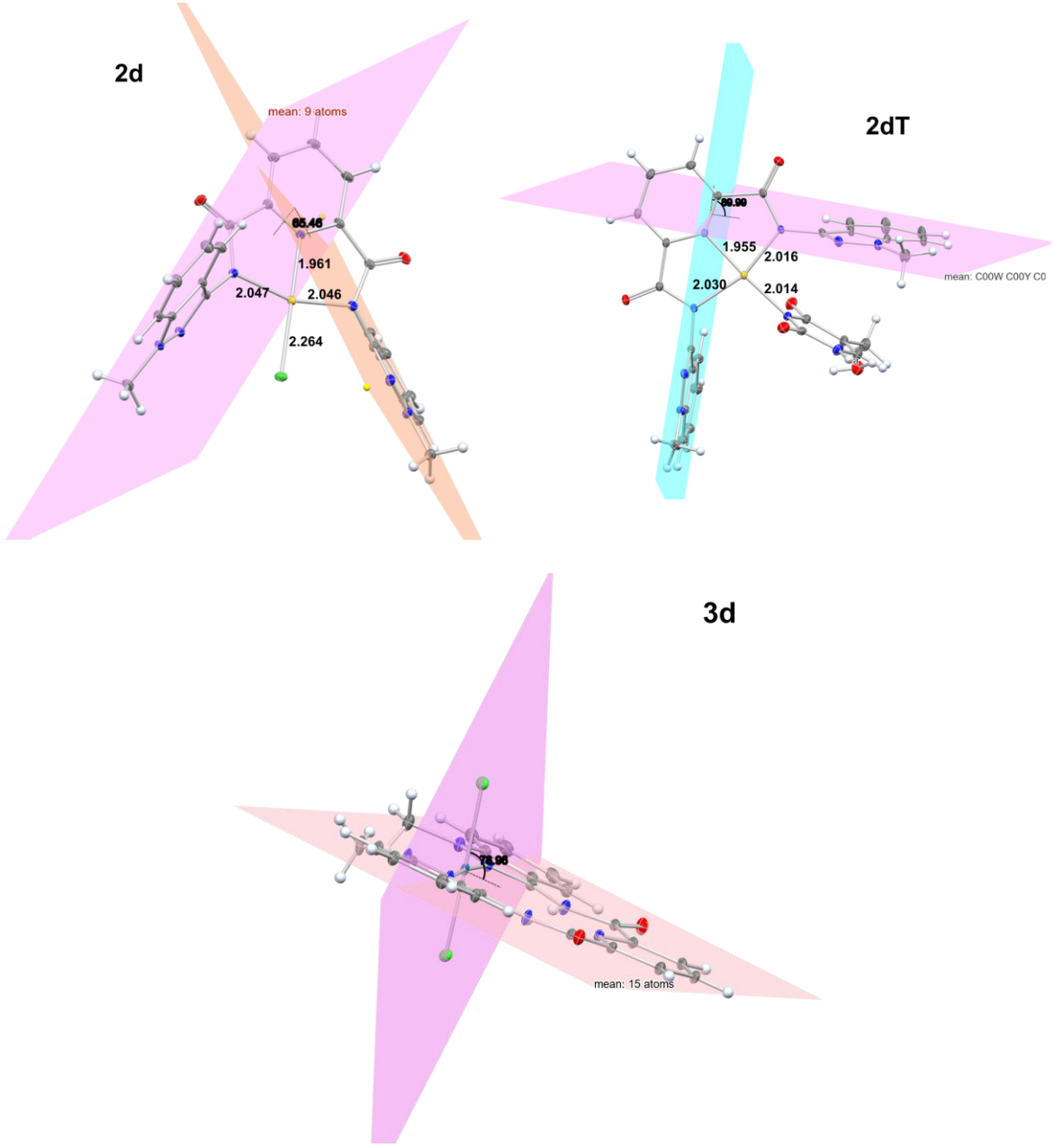


Figure 4.8. Illustration of change in plane angles between (**a)** the two arms of the pincer complexes with the Cl (**2d**) displaced with the Thymine (**2dT**), due to their difference in size. **(b)** the Cl^- ions and the plane of the pincer molecule in **3d.**

Crystals of complex **2e** were grown by slow diffusion of methanol into its solution with DMSO. Complex **2e** crystallised in the $P2_1/n$ space group, which is a chiral space group. There are likely cation-π interactions in the molecule, as for each arm, one phenyl moiety is directly above and below the Au metal ion. In comparison to ligand **1e**, there was a significant decrease in the C=O bond distance and an increase in the (CO)-N bond distances.

Complex **2e** crystallised in methanol at room temperature to form deep red crystals. However, it was not very stable in solution and decomposed fairly quickly, with plenty of free ligands surrounding the crystal structures.

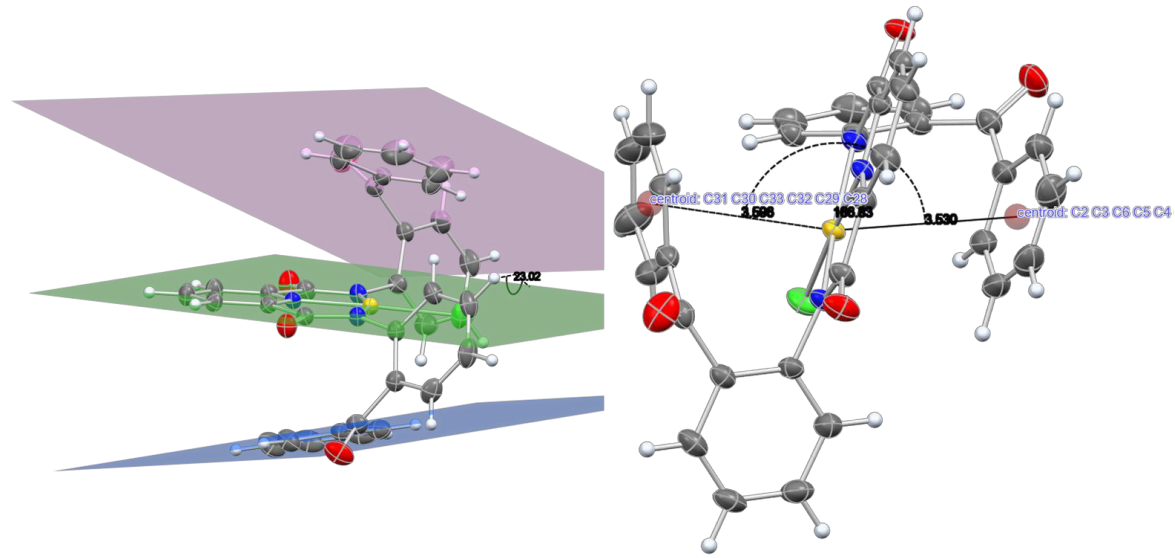


Figure 4.9. X-ray crystallography structures of **1e** show casing **(a)** the cation π interactions in the molecule. The molecule is in three planes, which are 14.20° (pink) and 23.02° (blue) relative to the main plane (green), and 23.19° of each other. **(b)** The distance between the sandwiched gold(III) metal ion centre and the two sandwiching C_6 rings 3.596 Å and 3.530 Å, at an angle of 166.83° of each other.

Hydrogen bonding is well-known for stabilising crystal structures, according to the literature, especially when there is more than one molecule in the structure.[49] Au-Au interactions are on par with hydrogen bonding in stabilising crystal structures, as are Au-π (cation-π) interactions.[50] Due to the high relativistic effect in Au, the distance between the Au ion and the π system is shortened, allowing for stronger interaction between them.[51,52]

Although there has not been much focus on this type of interaction in crystallography, surveys have been conducted in the CSD database to study how often this interaction occurs. From the studies, it was shown that if the gold(III) or gold(I) metal centre is within 4.0 Å of an aryl ring, at an angle of not more than 20° from the centre of the ring, then there is a very high possibility of an Au-π interaction.[50,53]

From the 45 structures that possibly exhibit Au-π interactions in the CSD database, 22 had gold(III) metal centres, and of these, none were intramolecular. However, some exhibited intermolecular Au-π interactions for Au(I) metal centres. **2e** showcased intramolecular Au-π interactions between one gold(III) metal centre and two C_6 rings on each side. From **Figure 4.8**, the average distance between the metal centre and the C_6 rings is 0.563 Å, and the ring centres have an average of 12.49° off from the Au(III) metal centre plane, which is well within the range allowed for in literature. [50,53]

Since the arms for this molecule are flexible on the carbonyl bridges, the arms tend to “coil” around the metal centre and the only possible interaction that could stabilise the crystal structure is the Au-π interaction. This is an inference, as this interaction does not show on the 3D crystal structure, but a form of interaction has to hold the structure together.

Complex **3diii** is the only complex which has a perfect C_2 symmetry. Palladium reacted with the indazole nitrogens N4 and N6 as indicated in **Figure 4.5**. The conformation around the palladium metal centre is planar, but the whole molecule is not planar, as the chloride ions are almost perpendicular (~80 °) to the pincer ligand. Although we did not have a crystal structure to prove this, as discussed in **Section 4.3.4**, gold(III) probably reacted in the same way when there was poor solubility and at low temperatures, and it is the kinetic product of this reaction.

4.4 Conclusion

The structure elucidation in this chapter was crucial in the determination of the conformation of the compounds. The conformational structure of the gold(III) complexes is essential in predicting the binding of the complex to DNA as a base binder, groove binder or intercalator. From these studies, these metal complexes have the potential to bind to DNA by base binding, groove binding or intercalating to DNA. Due to the stability of **2d**, was selected for biochemical and biological studies. This is discussed in detail in the next chapter. **2dT** was also pivotal in determining the binding of **2d** to DNA bases.

4.5 References

1 P. Jerome, P. N. Sathishkumar, N. S. P. Bhuvanesh and R. Karvembu, *Journal of Organometallic Chemistry*, 2017, **845**, 115–124.
2 K. T. Neumann, A. S. Donslund, T. L. Andersen, D. U. Nielsen and T. Skrydstrup, *Chemistry – A European Journal*, 2018, **24**, 14946–14949.
3 S. G. Churusova, D. V. Aleksanyan, E. Y. Rybalkina, O. Y. Susova, V. V. Brunova, R. R. Aysin, Y. V. Nelyubina, A. S. Peregudov, E. I. Gutsul, Z. S. Klemenkova and V. A. Kozlov, *Inorganic Chemistry*, 2017, **56**, 9834–9850.
4 B. Bertrand, M. R. M. Williams and M. Bochmann, *Chemistry – A European Journal*, 2018, **24**, 11840–11851.
5 L. Messori and G. Marcon, *Metal ions in biological systems*, 2004, **42**, 385–424.
6 M. Albrecht and G. van Koten, *Angewandte Chemie (International ed. in English)*, 2001, **40**, 3750–3781.
7 M. W. Johnson, A. G. DiPasquale, R. G. Bergman and F. D. Toste, *Organometallics*, 2014, **33**, 4169–4172.
8 S. L. Jain, P. Bhattacharyya, H. L. Milton, A. M. Z. Slawin, J. A. Crayston and J. D. Woollins, *Dalton Trans.*, 2004, 862.
9 A. K. Cheetham, G. Kieslich and H. H.-M. Yeung, *Acc Chem Res*, 2018, **51**, 659–667.
10 K.-C. Lin, *J. Chem. Educ.*, 1988, **65**, 857.
11 S. Gu, R. J. Nielsen, K. H. Taylor, G. C. Fortman, J. Chen, D. A. Dickie, W. A. I. Goddard and T. B. Gunnoe, *Organometallics*, 2020, **39**, 1917–1933.
12 S. Kumari, A. V. Carmona, A. K. Tiwari and P. C. Trippier, *J Med Chem*, 2020, **63**, 12290–12358.
13 J. K. Mukhopadhyaya, S. Sklenák and Z. Rappoport, *J. Am. Chem. Soc.*, 2000, **122**, 1325–1336.
14 J. Ashenhurst, 3 Factors That Stabilize Carbocations, https://www.masterorganicchemistry.com/2011/03/11/3-factors-that-stabilize-carbocations/, (accessed August 1, 2023).
15 PubChem, Silver hexafluorophosphate, https://pubchem.ncbi.nlm.nih.gov/compound/168464, (accessed May 31, 2024).
16 M. Mihalovits, *Journal of Molecular Liquids*, 2022, **363**, 119910.
17 J. M. Thompson, *Infrared Spectroscopy*, CRC Press, 2018.
18 J. W. Robinson, *Practical Handbook of Spectroscopy*, CRC Press, 1991.
19 J. Clayden, N. Greeves and S. Warren, *Organic Chemistry*, OUP Oxford, 2012.
20 N. Yamazaki and F. Higashi, *BCSJ*, 1973, **46**, 1235–1238.
21 M. Hargittai, A. Schulz, B. Réffy and M. Kolonits, *J. Am. Chem. Soc.*, 2001, **123**, 1449–1458.
22 A. Casini, M. A. Cinellu, G. Minghetti, C. Gabbiani, M. Coronnello, E. Mini and L. Messori, *J. Med. Chem.*, 2006, **49**, 5524–5531.
23 F. Abbate, P. Orioli, B. Bruni, G. Marcon and L. Messori, *Inorganica Chimica Acta*, 2000, **311**, 1–5.
24 M. Zahran, H. Agwa, A. Osman, S. Hammad, B. El-Aarag, N. Ismail, T. Salem and A. Gamal-Eldeen, *Eur. J. Chem.*, 2017, **8**, 391–399.
25 S. Radisavljević and B. Petrović, *Front Chem*, 2020, **8**, 379.
26 P. L. Taberna, P. Simon and J. F. Fauvarque, *J. Electrochem. Soc.*, 2003, **150**, A292.
27 N. Arsenijević, V. Volarevic, M. Milovanovic and Ž. D. Bugarčić, in *Encyclopedia of Metalloproteins*, eds. R. H. Kretsinger, V. N. Uversky and E. A. Permyakov, Springer, New York, NY, 2013, pp. 922–927.
28 T. Owen, *Fundamentals of UV-visible spectroscopy*, Agilent Technologies, 2000.

29 S. Constant and J. Lacour, in *New Aspects in Phosphorus Chemistry V: -/-*, ed. J.-P. Majoral, Springer, Berlin, Heidelberg, 2005, pp. 1–41.
30 J. A. Davies, Synthetic coordination chemistry World Scientific Pub. Co., Singapore 1996.
31 S. Wiemers-Meyer, M. Winter and S. Nowak, *Phys. Chem. Chem. Phys.*, 2016, **18**, 26595–26601.
32 Y. Okamoto, *J. Electrochem. Soc.*, 2013, **160**, A404.
33 C. L. Campion, W. Li and B. L. Lucht, *J. Electrochem. Soc.*, 2005, **152**, A2327.
34 C. L. Campion, W. Li, W. B. Euler, B. L. Lucht, B. Ravdel, J. F. DiCarlo, R. Gitzendanner and K. M. Abraham, *Electrochem. Solid-State Lett.*, 2004, **7**, A194.
35 Cotton-Wilkinson – Advanced Inorganic Chemistry Sixth Edition - Uechemia, https://uechemia.com/cotton-wilkinson-advanced-inorganic-chemistry-sixth-edition/, (accessed June 24, 2022).
36 S. Engbers, E. A. Trifonova, K. M. Hess, F. de Vries and J. E. M. N. Klein, *European Journal of Inorganic Chemistry*, 2021, **2021**, 3561–3564.
37 D. B. Dell'Amico, F. Calderazzo, F. Marchetti, S. Merlino and G. Perego, *J. Chem. Soc., Chem. Commun.*, 1977, 31–32.
38 N. R. Walker, L. M. Reynard and M. C. L. Gerry, *Journal of Molecular Structure*, 2002, **612**, 109–116.
39 J. Hoeft, F. J. Lovas, E. Tiemann and T. Törring, *Zeitschrift fur Naturforschung - Section A Journal of Physical Sciences*, 1970, **25**, 35–39.
40 L. Wu, S.-Y. Tang and S. Zhou, *ACS Omega*, 2021, **6**, 34904–34911.
41 S.-Y. Chang, A. Uehara, S. G. Booth, K. Ignatyev, J. F. W. Mosselmans, R. A. W. Dryfe and S. L. M. Schroeder, *RSC Advances*, 2015, **5**, 6912–6918.
42 P. F. Lang and B. C. Smith, *Dalton Transactions*, 2014, **43**, 8016–8025.
43 R. T. Sanderson, *J. Am. Chem. Soc.*, 1983, **105**, 2259–2261.
44 C. Tantardini and A. R. Oganov, *Nat Commun*, 2021, **12**, 2087.
45 J. Elguero, 137.
46 W. Gordy, *J. Chem. Phys.*, 1947, **15**, 305–310.
47 J. P. Paolini, *Journal of Computational Chemistry*, 1990, **11**, 1160–1163.
48 C. Q. Sun, B. K. Tay, X. T. Zeng, S. Li, T. P. Chen, J. Zhou, H. L. Bai and E. Y. Jiang, *J. Phys.: Condens. Matter*, 2002, **14**, 7781–7795.
49 E. R. T. Tiekink and J. Zukerman-Schpector, *CrystEngComm*, 2009, **11**, 2701–2711.
50 B. R. Sreekanth, P. Vishweshwar and K. Vyas, *Chem. Commun.*, 2007, 2375.
51 K. M. Wedderburn, S. Bililign, M. Levy and R. J. Gdanitz, *Chemical Physics*, 2006, **326**, 600–604.
52 M. Filatov and D. Cremer, *Chemical Physics Letters*, 2003, **370**, 647–653.
53 E. R. T. Tiekink and J. Zukerman-Schpector, *CrystEngComm*, 2009, **11**, 1176–1186.

5. Biochemistry and Cellular Biology

As outlined in **Chapter 1**, DNA stands out as a primary molecular target in cancer therapy due to its central role in cellular functions. [1] Disrupting DNA functions can lead to the impairment of cancerous cellular activities, making it a potent target for cancer treatment. [1–3] Ultimately, binding drugs to DNA and influencing its secondary and tertiary structures is crucial for halting uncontrolled cell replication. This is achieved through mechanisms such as base binding/displacement, intercalation, or groove binding.

Considering that drug administration occurs externally to cells, the drug must be transported to the target cells. This requires interactions with specific proteins, such as Human Serum Albumin (HSA). Additionally, the drug should have the capability to traverse cellular barriers like the phospholipid bilayer and nuclear membranes. Solubility in both aqueous and non-polar mediums is vital for efficient drug uptake into cells and, consequently, its efficacy.

Studies have indicated that covalently binding a metal complex to HSA can enhance its tumour-inhibiting properties, potentially leading to improved accumulation in tumours with reduced side effects.[4–6] This underscores the significance of HSA as an effective transport protein for drugs.

A crucial consideration is comparing the affinity of drugs to DNA against HSA (or transport proteins) to ensure that the compound is efficiently transferred from the transport protein to the target DNA. In other words, the compound must exhibit a higher affinity for the ensuing carrier compound compared to the subsequent carrier for easier transportation to the final target.

The compound **2d** was synthesised to target cellular DNA or other components essential for cell replication, ultimately inducing apoptosis. The DNA binding studies were conducted to assess the mode and extent of binding to DNA and its components. Due to its structure, **2d** has the ability to interact with DNA through, intercalation (given its flat structure around the metal centre with a distorted square planar configuration), minor groove binding and base binding (facilitated by its labile Cl, which can easily be substituted with DNA bases). The interaction of **2d** with HSA, a transport protein was also studied to evaluate its binding parameters, pharmacodynamics and pharmacokinetics. Its cytotoxicity *in vitro* was assessed against cancer cell lines MCF-7 (a breast cancer cell line) and HT-29 (a human colorectal adenocarcinoma cell line).

In this part of the study, various experimental techniques were employed to investigate the stability of **2d** to reduction, the species active in biological media and its effects on ct-DNA, HSA, and cells, all aimed at predicting the extent of its toxicity to cancer cells in the human body.

5.1 Instrumentation and Methods

All experiments were done at the University of the Witwatersrand. Stability studies, pK_a determination and DNA binding studies were carried out in the School of Chemistry, and cytotoxicity assays were conducted in the School of Molecular and Cell Biology with the assistance of Ruth Aronson.

Spectra for all experiments were acquired using an AnalytikJena Specord 210/plus, double-beam UV/Vis spectrophotometer equipped with single-cell holders. Alternatively, spectra were recorded on a Perkin Lambda 365 Spectrometer featuring multiple cell holders. The spectrophotometers employed a double-beam configuration, where each beam ran parallel to the other, with one beam measuring the sample and the other serving as the reference (blank) solution. A 1 cm path length was maintained for all samples. To ensure precision and reliability, data were collected in triplicate.

The pK_a values were determined through pH spectrophotometric titration of **2d**. This experiment was conducted at a temperature of 310.15 K in a multicomponent buffer, maintaining a constant ionic strength. The buffer consisted of 10 mM each of potassium dihydrogen phosphate, MES, MOPS, TRIS, and CHES buffers, along with 1.0 M KCl, and 5% DMSO. pH measurements were carried out using an OHAUS STARTER 5000 Bench pH Meter. Before initiating the titration, the pH was adjusted to approximately 2 using concentrated HCl. NaOH was then incrementally added to the **2d**-buffer solution while simultaneously measuring its absorbance across the spectral range of 200 - 900 nm. Absorption values at wavelengths displaying significant shifts in the spectra were utilised to construct the titration curves.

Reduced L-Glutathione (GSH) binding experiments were conducted in a 0.10 M TRIS-HCl buffer containing 10% DMSO, maintained at 37 °C and pH 7.4. To identify the appropriate wavelength for monitoring kinetic measurements, the absorption spectral changes between 200-700 nm were recorded, and the kinetic measurements were specifically performed at 354 nm. The observed spectral changes were attributed to the binding of GSH to **2d**, and the spectra were corrected for dilution effects. All reactions were continuously monitored for a minimum duration of 6000 seconds at 15, 20, 25 and 30 °C.

Electrophoretic mobility shift assays (EMSA) were conducted using hand-cast 1.25% agarose gels dissolved in 1x TAE buffer (Sigma-Aldrich, 10x, diluted with Type 1 ultrapure water, containing 40 mM Tris-acetate and 1 mM EDTA, pH 8.3) within a Mini-Sub-Cell GT® Agarose Gel Electrophoresis System (Bio-Rad). The gels underwent staining with an Ethidium Bromide solution (0.5 mg/L in Type 1 ultrapure water) for 30 minutes, followed by a 20-minute wash in Type 1 ultrapure water. The visualisation was performed using a G: Box Chemi XRQ gel doc system (Syngene) with mid-wave transillumination and a UV filter (GeneSys 1.4.6.0). The agarose gels were prepared by dissolving agarose (1.2 v/w, 0.437 g) in 37 ml boiling TAE buffer (40 mM Tris-Acetate, 1 mM EDTA, pH 7.4). After cooling to 60°C, the solution was poured onto a well-balanced mould, the comb was inserted, and the mixture was allowed to cool down and solidify for at least 30 minutes. Various sample solutions, including different concentrations of **2d**, control Ethidium Bromide (**EB**) and Hoechst stain (**HS**), and a blank, were prepared in a solution of TEA buffer, 5% v/v DMSO, and water. The samples underwent a 30-minute incubation with ct-DNA at 37 °C before being loaded into wells on the agarose gel, fully immersed in TEA buffer.

UV-vis absorption titration experiments were carried out in 0.10 M TRIS-HCl buffer (10% DMSO for solubilising **2d**) under physiological conditions (37 °C, pH 7.4). The DMSO concentration was

maintained at 10%, which is the maximum acceptable concentration for DNA binding tests and biological studies with minimal interference.[7,8] Deionised water was used for preparing buffers and solutions. The buffer temperature was kept below 37 °C, and reactions were conducted at 37 °C and pH 7.4. TRIZMA base from Sigma-Aldrich was used, and calf thymus DNA (ct-DNA) in its soluble sodium form, along with DMSO solvent, was sourced from Sigma. Absorbance measurements of all solutions were performed on a double-beam UV-vis spectrometer using a 1 cm quartz UV-vis cuvette in the range of 200-700 nm. The ct-DNA salt was dissolved in premade TRIS-HCL buffer, and the DNA stock solution's final concentration (2.15 mM) was determined using the Beer-Lambert law from absorbance measurements at 260 nm. The absorptivity constant of ct-DNA (13200 bp M^{-1})[9,10] was employed for this calculation. The **2d** stock solution was prepared in DMSO, with the DMSO concentration maintained at 10%. Complex-DNA solutions were created by adding and mixing aliquots (1-30 µL) of concentrated ct-DNA standard solutions to a fixed concentration of **2d** solution (117 µM - 99 µM). This process resulted in increments of DNA solution ranging from 0.11 nM to 2.63 µM, achieving a total concentration of 37 µM. Precipitation of DNA occurred at concentrations above this level, rendering the results invalid. The highest [ct-DNA]:[**2d**] ratio before precipitation was approximately 2:3. During the experiments, **2d** was added only to the measurement cell (cuvette), while ct-DNA was added to both the reference and measurement cuvettes. Absorption spectra were recorded after each increment in the 200-700 nm spectral region following a 10-minute incubation period at 37 °C.

The viscosity of a DNA solution was determined in the presence of varying amounts of complex **2d**. Flow time was measured using a digital stopwatch, with each sample measured six times to calculate the average flow time. The data is presented in **Figure 5.8(a)** as $(\eta-\eta_0/\eta_0)^{1/3}$ against r, where η_0 and η represent the viscosity of DNA alone and in the presence of complex DNA in the buffered solution, respectively, and r is the ratio of the concentrations of **2d** to ct-DNA ([2d]/[ct-DNA]). Viscosity values were measured using an Anton Paar Lovis 2000 M Microviscometer, employing a Lovis Low Volume Filling set made of 1.62 PCTFE.

The melting temperatures of DNA were measured in the presence of increasing concentrations of complex **2d** (0 – 25 µM) using a Perkin Lambda 365 Spectrometer. The measurements were taken at 5 °C intervals from 20–60 °C and 2 °C intervals between 60–95 °C.

The HSA-binding study of **2d** involved UV-vis absorption titration experiments conducted under conditions similar to DNA titration experiments, with the additional inclusion of multiple temperatures. HSA, sourced from Sigma, was dissolved in premade TRIS-HCL buffer to achieve a final concentration of the HSA stock solution (1.6 mM). The **2d** stock solution, prepared in DMSO, maintained a DMSO concentration of ~10%. Using the AnalytikJena Specord 210/plus UV-vis spectrometer, absorbance measurements were taken between 200-700 nm. For the preparation of complex-HSA solutions, aliquots (1-20 µL) of concentrated ct-DNA standard solutions were added and mixed with a relatively fixed concentration of **2d** solution (156 µM – 151 µM) to achieve incremental concentrations of HSA, totalling 50 µM. Beyond this concentration, HSA precipitation occurred, rendering the results invalid. The highest achievable ratio of [HSA]:[**2d**] before precipitation was approximately 1:3. In the experimental setup, **2d** was exclusively added to the measurement cell (cuvette), while HSA was added

to both the reference and measurement cuvettes. Absorption spectra were recorded in the 200-700 nm spectral region following a 10-minute incubation period at 37 °C, 25 °C, and 15°C.

For cytotoxicity experiments, cells were seeded in 96-well plates with media. Test compounds, including **2d**, cisplatin, and topotecan hydrochloride, were diluted in DMEM (Dulbecco's Modified Eagle Medium), and solutions at different concentrations were added to the wells.

MTT [3-(4,5-Dimethylthiazol-2-yl)-2,5-Diphenyltetrazolium Bromide] assays were conducted on these cells following 24, 48, or 72 hours of incubation. Sterile MTT in PBS was added to the cell culture, and after a 2-hour incubation, a solution of 10% SDS in 10 mM HCl was added to dissolve the resulting formazan. Incubation continued for an additional 16 hours. The optical density (absorbance) of each well at 570 nm was measured using a microtiter plate reader (Multiskan GO Microplate Reader) with Thermo Fisher Scientific SkanIt™ software. The percentage cell inhibition/viability was determined using Excel, and graphs were generated with OriginPro 2023b software.[11] These assays were performed in biological duplicates and technical triplicates. All experiments were conducted in biological triplicates in each 96-well plate. The cell viability of HT-29 and MCF-7 cell lines in the presence of **2d** was measured at 24, 48, and 72 hours after treatments with **2d**, cisplatin, and topotecan hydrochloride, separately, at low (0.1, 0.2, 0.5, 1, and 5 µM) and high (5, 10, 20, 50, and 100 µM) concentration ranges.

For the APOPercentage assay, following a 24, 48, or 72-hour incubation period, APOPercentage™ Dye was added to each well, and the samples were incubated for 30 minutes. Cells were then washed with PBS until the resulting PBS was clear. Images of the wells were captured using a microtiter plate reader (Multiskan GO Microplate Reader). The apoptosis assays were performed once in technical triplicates on each plate.

5.2 *p*K_a determination

The identification of distinct chemical species at various pH levels is a crucial aspect of understanding the behaviour of a compound in solution. In the context of **2d**, the number of species often corresponds to the number of *p*K_a values, where each *p*K_a represents a point of transition between two species, which indicative of an equilibrium shift.

The primary goal of this study was to discern the specific species of **2d** at physiological pH, particularly at pH 7.4.[12,13] **Figure 5.1a** provides insights into the presence of five different species in a solution of **2d** at different pH values. This observation led to the formulation of an equation to describe the speciation of **2d**, emphasising its behaviour at pH 7.4.

The study's focus on physiological pH (pH 7.4) is particularly relevant as it aligns with the conditions encountered in biological systems. The derived equation contributes to the comprehension of the speciation behaviour of **2d** under these physiological conditions, offering valuable insights for further interpretation of experimental data.

The resulting equation (**Equation 5.1**) reflects the equilibria of different species of **2d**. It is a mathematical representation that accounts for the transitions between these species, capturing the

dynamic nature of the system under different pH conditions. This equation allows for a quantitative understanding of how the concentration of each species changes with variations in pH.

$$[\mathbf{2d}H_2]^{2+} \rightleftharpoons [\mathbf{2d}H]^{+} \rightleftharpoons [\mathbf{2d}] \rightleftharpoons [\mathbf{2d}H_2O]^{+} \rightleftharpoons [\mathbf{2d}OH], \quad \textbf{Equation 5.1}$$

where the equilibrium constants for the forward reactions are K_1, K_2, K_3 and K_4 from left to right.

Equation 5.2 delineates the relationship between the molar concentrations of different species $[\mathbf{2d}H_2]^{2+}$, $[\mathbf{2d}H]^{+}$, [**2d**], $[\mathbf{2d}H_2O]^{+}$ and [**2d**OH] and their respective contributions A_A, A_B, A_C, A_D and A_E, to the total absorbance (A_T) in a solution at various pH levels. The fractional contributions of each species to the total absorbance are therefore represented by the terms A_A, A_B, A_C, A_D and A_E.

The equation is expressed as follows:

$$\mathbf{A_T = A{\times}A_A + B{\times}A_B + C{\times}\ A_C + D{\times}A_D + E{\times}A_E} \quad \textbf{Equation 5.2}$$

In this equation:

- A_T is the total absorbance of the solution,
- A, B, C, D, and E are the molar concentrations of $[\mathbf{2d}H_2]^{2+}$, $[\mathbf{2d}H]^{+}$, [**2d**], $[\mathbf{2d}H_2O]^{+}$ and [**2d**OH] respectively.
- A_A, A_B, A_C, A_D and A_E represent the fractional contributions of each species to the total absorbance.

This equation provides a means to correlate the concentrations of different species in the solution with the overall absorbance, allowing for a quantitative understanding of the distribution of species at various pH levels. The coefficients (A_A, A_B, A_C, A_D, A_E) are influenced by the equilibrium constants (k_1, k_2, k_3, k_4) and the pH-dependent terms in the numerator and denominator of **Equation 5.3** (full derivation is in **Section S7.2** of the supplementary information). The complexity of these relationships underscores the dynamic nature of the speciation of **2d** in response to changes in pH.

$$\mathbf{A_T = (A_A{\times}10^{-4pH} + K_1A_B{\times}10^{-3pH} + K_1K_2\ A_C{\times}10^{-2pH} + K_1K_2K_3\ A_D{\times}10^{-pH} + K_1K_2K_3K_4A_E)/(\ 10^{-4pH} + K_1{\times}10^{-3pH} + K_1K_2{\times}10^{-2pH} + K_1K_2K_3{\times}10^{-pH} + K_1K_2K_3K_4)} \quad \textbf{Equation 5.3}$$

The pH speciation titration curves presented in **Figure 5.1 b-d** revealed four distinct transition points over the pH range of 2–13. These transition points correspond to five ionisation states of compound **2d** within this pH range. The calculated *p*K_a values associated with each ionisation state are 3.2, 5.8, 11.0, and 12.3. These values were determined using **Equation 5.3** and calculated in OriginPro 2023b.[11]

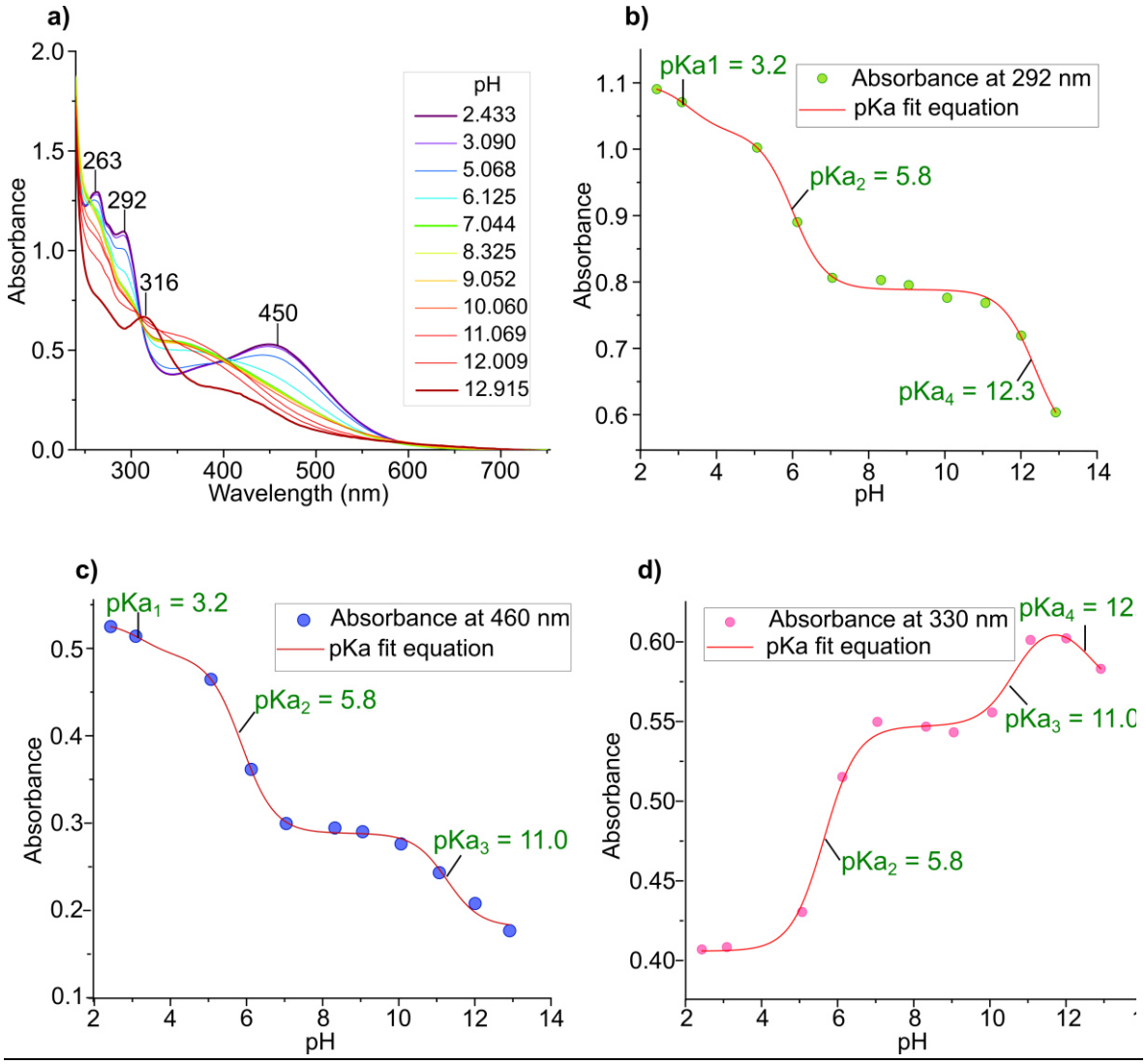


Figure 5.1. UV-Visible spectra for a) **2d** (1.52×10^{-4} M) at pH range of 1–13, T = 37 ◦C, and **b), c), d)** plots of absorbance vs. pH at 292 460 and 330 nm respectively.

DFT (Density Functional Theory) calculations were employed to predict the most likely species formed at different pH values, and a proposed scheme is illustrated in **Figure 5.2b,** derived from computational studies on various possible states of **2d**. The species exhibiting calculated electronic spectra closest to the experimental UV spectra at specific pH values were then selected for comparison. The computational insight complements the experimental data, providing a more comprehensive understanding of the molecular behaviour of **2d** under different pH conditions.

At acidic pH's, the indazole rings undergo protonation, with one of the protons forming a hydrogen bond with water molecules, which further interacts with the Cl on the metal centre. The resulting species carries an overall charge of +2. As the pH increases to 3.2, the free indazole becomes deprotonated, altering the molecule's charge to +1. At pH 5.8, the water molecule undergoes deprotonation, yielding a neutral compound. At pH 11.0, an ion exchange occurs between Cl^- and OH^-, resulting in a neutral molecule. Finally, at pH 12.3, the remaining indazole is deprotonated, restoring the complex to a neutral state.

Based on the collected data, it can be inferred that under physiological conditions, **2d** predominantly exists as species ***3*** in **Figure 5.2b**. However, it could be argued that the neutral water molecule forms hydrogen bonds with the indazole nitrogen, potentially eliminating charge separation between O and N.

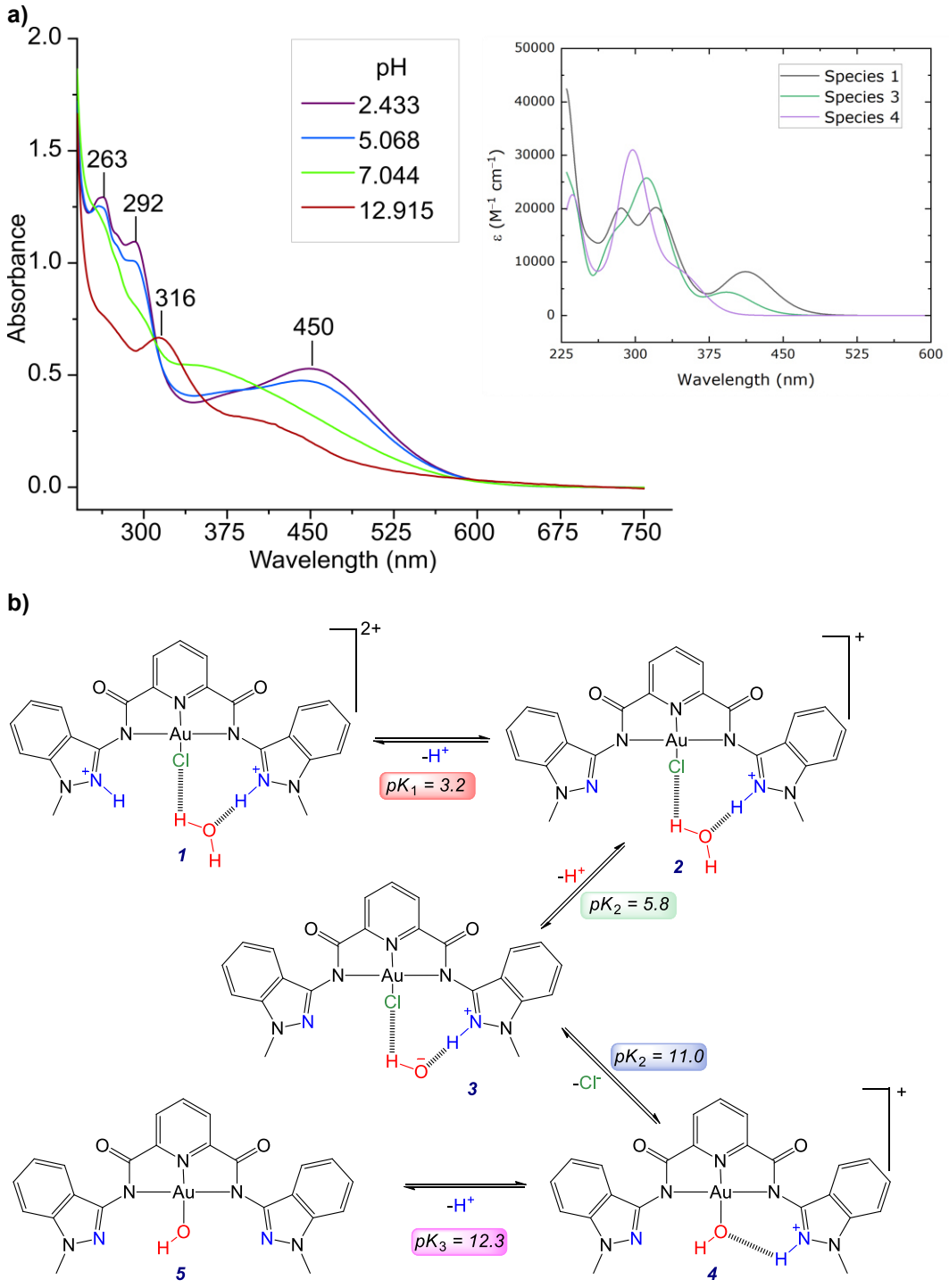


Figure 5.2. Illustration of **a)** Limiting spectra for reproduction and species assignment by TD-DFT Simulations and the insert is the spectrum calculated for all the species at different pHs. **b)** is the proposed speciation mechanism of **2d** with the increase in pH as per calculated data.

5.3 GSH binding studies (stability studies)

Glutathione (GSH) serves a crucial role as the major component of the intracellular antioxidant system.[14] One of its main functions is the detoxification of heavy metal complexes within cells. With GSH concentrations ranging between 1 and 20 mM in cells, it is imperative to assess the stability of **2d** in the presence of the intracellular reductant GSH. In this study, the kinetics of the reaction between GSH and **2d** were investigated.[15,16]

The kinetics measurements were conducted under pseudo-first-order conditions ([**2d**]:[GSH] ≥ 10) with **2d** used in excess due to its precipitation in excess GSH. While this condition may not precisely replicate physiological conditions within cells, it allowed for the delineation of how **2d** binds to GHS without being reduced.

Time-dependent UV-vis absorbance spectra for the reaction of **2d** with GSH revealed that the Au(III) metal ion is not reduced (i.e., from Au(III) to Au(I)/Au(0)), as confirmed by the lack of colour change in the solution (maintaining its red hue rather than turning purple). However, there was an introduction of a new band, indicating a change likely due to the binding of GSH to **2d**. The resultant spectra for all reactions exhibited distinctive differences from that of the starting chlorinated complex **2d**, and isosbestic points were observed. These observations collectively suggested an interaction between **2d** and GSH, leading to the proposal of chemical **Equation 5.4**.

2d + GSH ⇌ 2d-GSH + Cl^- **Equation 5.4**

Representative spectra indicating the change in absorbance over time are presented in **Figure 5.3a**. Pseudo-first-order rate constants (k_{obs}) were determined for each concentration ratio (10, 20, 40, 80, 160) at various temperatures (15, 20, 25, 30 °C). The analysis involved fitting the kinetic data with a single-exponential fit, as described by **Equation 5. 5**, where A_o, A_t and A_∞ represent the absorbances of the solution initially, at time t, and at the end of the reaction, respectively.

$$\boldsymbol{A_t = A_o + (A_o - A_\infty)e^{(-k_{obs}\cdot t)}}$$ **Equation 5.5[17]**

$$\boldsymbol{k_{obs} = k_2\,[2d]}$$ **Equation 5.6[17]**

The second-order reaction constant (k_2), illustrated in **Figure 5.3b**, was calculated at each temperature using **Equation 5.7**. The resulting k_2 values were used for the Arrhenius plot (**Figure 5.3c** and the Erying plot (**Figure 5.3d**) following **Equations 5.8** and **5.11,** respectively. These plots were used to determine the activation parameters, including activation energy (E_a), the enthalpy change of activation ($\Delta H^‡$), the entropy change of activation ($\Delta S^‡$) and the Gibbs free energy of activation ($\Delta G^‡$). The detailed data analysis results are presented in **Tables 5.1** and **5.2**.

$$\boldsymbol{k_2 = Ae^{-\frac{E_a}{RT}}}$$ **Equation 5.7[17,18]**

$$lnk_2 = lnA + \left(\frac{-E_a}{RT}\right)\cdot\frac{1}{T}$$ **Equation 5.8[18]**

$$\boldsymbol{k_2 = k_b\frac{T}{h}\cdot e^{-\Delta G/RT} = k_b\frac{T}{h}\cdot e^{-(\Delta H - T\Delta S)/RT}}$$ **Equation 5.9**

where

- k_b is the Boltzmann constant (1.381 ×10^{-23} J K^{-1}),
- h is Planck's constant (6.626 x10^{-34} s),
- R is the gas constant (8.315 J mol^{-1} K^{-1}).

$$ln k_2 = ln\frac{k_b}{h} + lnT - \frac{\Delta G^{\ddagger}}{RT} = ln\frac{k_b}{h} + lnT - \frac{\Delta H^{\ddagger}}{RT} + \frac{\Delta S^{\ddagger}}{R}$$ **Equation 5.10**[18]

such that

$$ln\frac{k_2}{T} = 23.76 + \frac{\Delta S^{\ddagger}}{R} - \frac{\Delta H^{\ddagger}}{R} \cdot \frac{1}{T}$$ **Equation 5.11**[18]

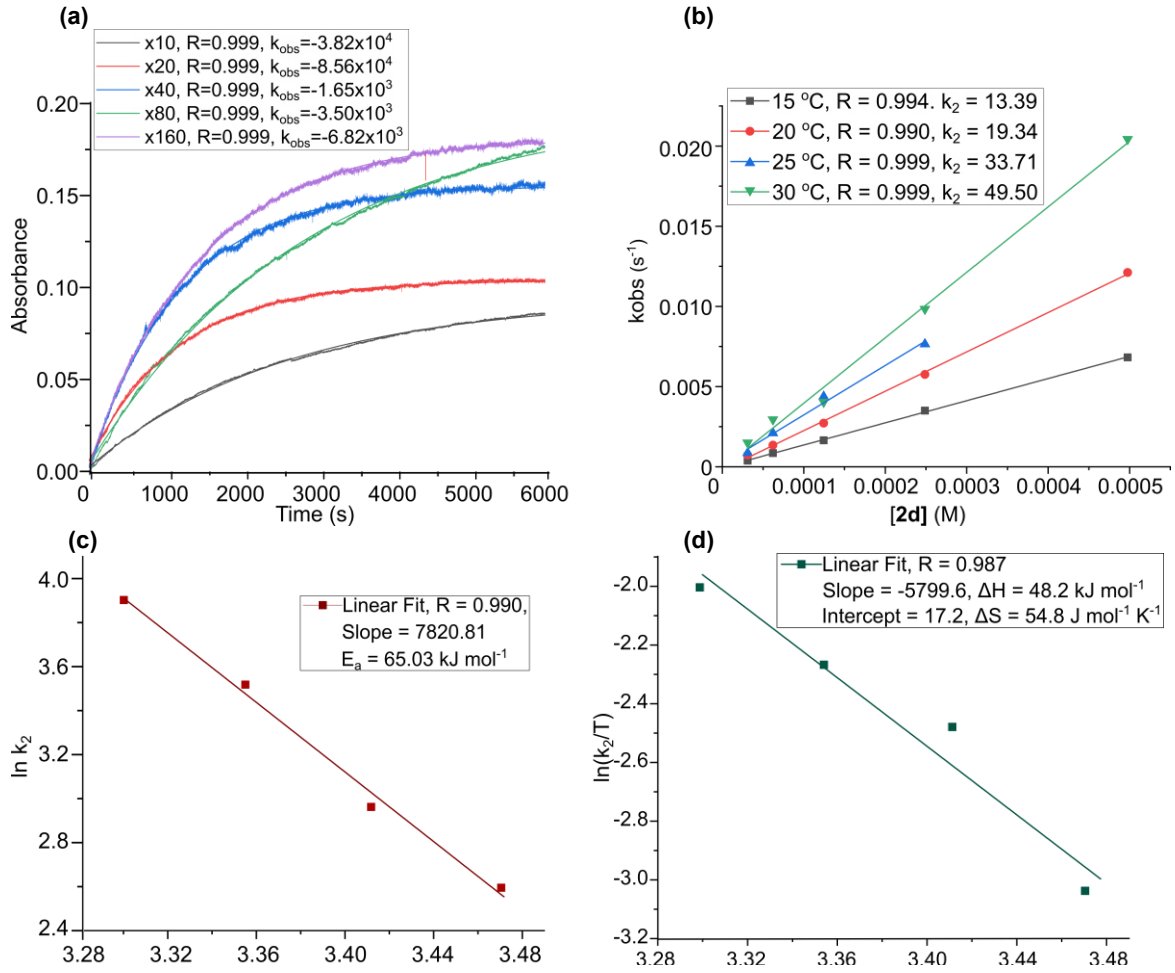


Figure 5.4. Time dependence of the binding of GSH to **2d** with ratios of [**2d**]:[GSH] between 10 and 160. **a)** shows first-order exponential fits of the kinetics at 15 °C as plots of absorbance against time, **b)** plots of k_{obs} against [**2d**], **c**) is the Arrhenius plot and **d)** is the Erying plot for the reaction of **2d** with GSH.

Table 5.1. The k_{obs} for the reaction of **2d** with GSH at different temperatures and concentration ratios

[**2d**] x10^{-5} (M)	Ratio, [**2d**]:[GSH]	k_{obs} x10^{-4}			
		288.15 K	293.15 K	298.15 K	303.15 K
3.11	10	3.11	5.50	7.55	15.00
6.22	20	8.05	12.90	18.70	29.40
12.44	40	16.50	28.80	43.80	50.50
24.88	80	33.55	45.53	151.00	123.00
49.76	160	66.67			326.20

Table 5.2. k_2, $\Delta G^{\ddagger}$, E_a, $\Delta H^{\ddagger}$ and $\Delta S^{\ddagger}$ for the reaction of **2d** with GSH at diffierent temperatures

Temperature (K)	k_2 (M^{-1} s^{-1})	$\Delta G^{\ddagger}$ x10^4 (kJ mol^{-1})	E_a	$\Delta H^{\ddagger}$	$\Delta S^{\ddagger}$
288.15	13.39	4.649	65.03 kJ mol^{-1}	48.22 kJ mol^{-1}	-54.75 J mol^{-1} K^{-1}
293.15	19.34	4.643			
298.15	33.71	4.640			
303.15	49.51	4.637			

The thermodynamic analysis presented in **Table 5.2** suggests that the formation of the transition state is endothermic, as evidenced by the $\Delta H^{\ddagger}$. With an increase in temperature, there is a corresponding reduction in $\Delta G^{\ddagger}$ for the reaction, suggesting that the stability of the transition state improves at elevated temperatures.[18] This implies that the stability of the transition state increases with higher temperatures. Furthermore, The negative $\Delta S^{\ddagger}$ value implies an associative mechanism in the formation of the transition state, albeit one that is highly unstable.[19]

Based on this thermodynamic data, the proposed mechanism suggests that GSH binds to **2d** without demetalation of **2d**. The isosbestic points in the spectra further support this proposal, suggesting that Cl^- is replaced by GSH, signifying covalent bond formation during the reaction.[20,21] It was however impossible to determine if GSH binds to **2d** through one of the amines or the thiolate anion.

In conclusion, complex **2d** appears to be stable in the presence of the reducing agent GSH. Furthermore, given that GSH is a crucial component of the antioxidant system in cells, there is a high probability that complex **2d** will not be reduced *in vitro*. The only potential concern is the competition for binding to **2d** between the target DNA and GSH.

5.4 DNA binding studies

The binding affinity of complex **2d** to ct-DNA was comprehensively investigated using multiple techniques, including EMSA, viscometry, DNA melting studies, and UV–vis spectroscopic titrations. The integration of these methods aimed to ensure the reliability of the observed results and provide a comprehensive understanding of the interaction between **2d** and DNA.

5.4.1 EMSA

The alterations in the tertiary and secondary structure of ct-DNA were evaluated through electrophoretic mobility shift assays (EMSA) as a function of concentration. **Figure 5.4** illustrates the results of the EMSA conducted on **2d**.

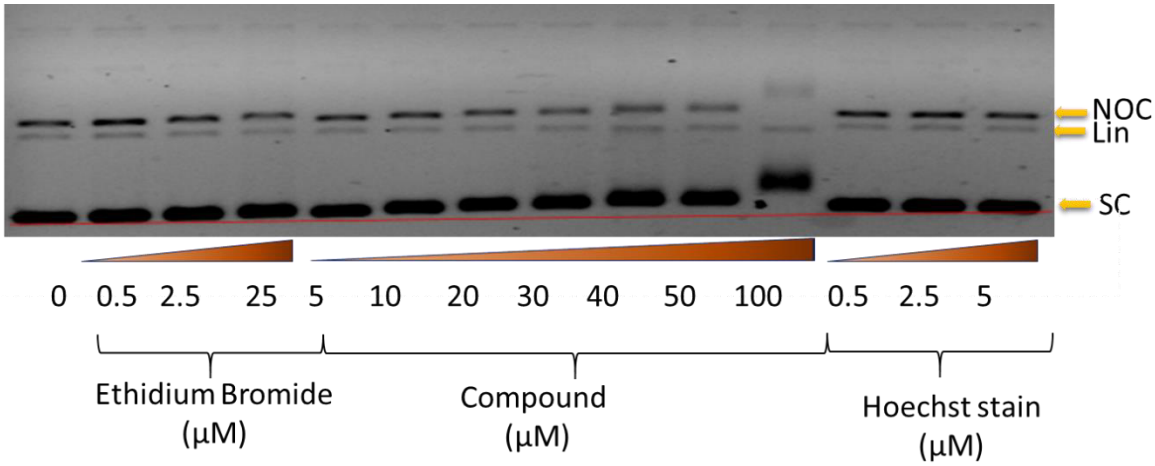


Figure 5.5. EMSA agarose gel for **2d** with calf thymus DNA (2.5 ng/well, 1x TAE buffer, 5% v/v DMSO). The DNA peaks formed are for supercoiled (SC), nicked-open circular (NOC), and linear (Lin). Lane 1 is the control lanes containing ct-DNA only. Lanes 2-14 has increasing concentrations of ethidium bromide (EB, 2–4), 2d (5–11), and Hoechst 33258 (HS, 12–14), and they compare the behaviour of a DNA intercalator, EB, the gold(III) complex, and a DNA minor groove binder, HS respectively. Experiments were done in triplicates and a representative assay is shown.

The reference lane exclusively contained native DNA, representing the mobility of untreated ct-DNA. Ethidium bromide (**EB**) served as the intercalator control, while Hoechst 33258 (**HS**) was employed as a control for a minor groove binder. The well-defined binding modes of both **EB** and **HS** to ct-DNA made them suitable controls, with their migration in the EMSA gel helping to assess the binding mode of **2d** to ct-DNA.[22–25]

In the EMSA gel, linear ct-DNA is unaffected by the binding of either the intercalator or the minor groove binder. The binding of **EB** tends to reduce the mobility of supercoiled DNA and nicked-open circular ct-DNA on the agarose gel.[22] This reduction in mobility occurs because intercalation partially unwinds the supercoiled ct-DNA, increasing steric bulkiness in the nicked-open circular ct-DNA. there is enhanced unwinding of the ct-DNA, leading to a further reduction in the mobility of supercoiled (SC) and nicked-open circular (NOC) ct-DNA (due to increased hydrodynamic drag).[22] On the other hand, the minor groove binder **HS** results in an increase in the mobility of DNA molecules along the gel, as the DNA molecules become more compactly packed.[24] Although the change is not as pronounced as the **EB**, an increase in **HS** concentration enhances the supercoiling in the supercoiled ct-DNA, causing the DNA sample to exhibit increased mobility across the agarose gel. From **Figure 5.4**, **EB** leads to reduced mobility in the DNA, with concentration being directly proportional to this reduced mobility shift, while the opposite is observed for **HS**.

Complex **2d** exhibited an exaggerated reduction in the mobility shift of the SC and NOC ct-DNA. This suggests a robust interaction between **2d** and ct-DNA, likely involving intercalation and/or base binding. If **2d** binds to the ct-DNA bases, it increases the bulkiness of the ct-DNA (resulting in kinking), leading to higher dynamic drag and reduced mobility on the gel. The observable reduction in ct-DNA mobility is evident even at low concentrations, starting from 10 μM, making **2d** a highly promising DNA base-binder. To strengthen the findings from the EMSA results, additional experiments were undertaken.

5.4.2 UV-vis titration experiments (ct-DNA, nucleobases, nucleosides and nucleotides titrations)

The EMSA results postulate that **2d** binds to and/or intercalates ct-DNA. UV-vis absorption titration studies of **2d** with ct-DNA were conducted to measure the binding affinity of **2d** to DNA and investigate possible binding modes of the complex. Additionally, **2d** was titrated with nucleobases, nucleosides and nucleotides to explore its base-binding properties to DNA and determine the extent of its interaction.

Due to interference from DMSO, data below 250 nm could not be utilised, preventing the observation of the behaviour of the aromatic rings on the compounds upon the addition of DNA. Nonetheless, hypochromicity was observed at 342 nm upon the addition of DNA to the solution, and absorbance at this wavelength was used to construct the Hill plot in **Figure 5.5**. While no visible isosbestic points were noted at high DNA concentrations (>90 nM), they were observed below 90 nM of DNA (insert in **Figure 5.5**).

Analysis of the changes in the spectra for the titration of the **2d** with ct-DNA was done at 342 nm. The absorbance values at this wavelength were corrected for dilution, before fitting the data to the modified Hill-Langmuir model.[26,27] The fit was accomplished using a sigmoidal function OriginPro2019.[28] The resulting fit quantified the affinity of **2d** to DNA with binding constants K_{a1} = 1.48 x10^9 M^{-1} and K_{a2} = 6.59 x10^5, achieving an R_2 value of 0.997, which indicated a relatively good fit (**Figure 5.5**, **Table 5.3)**.

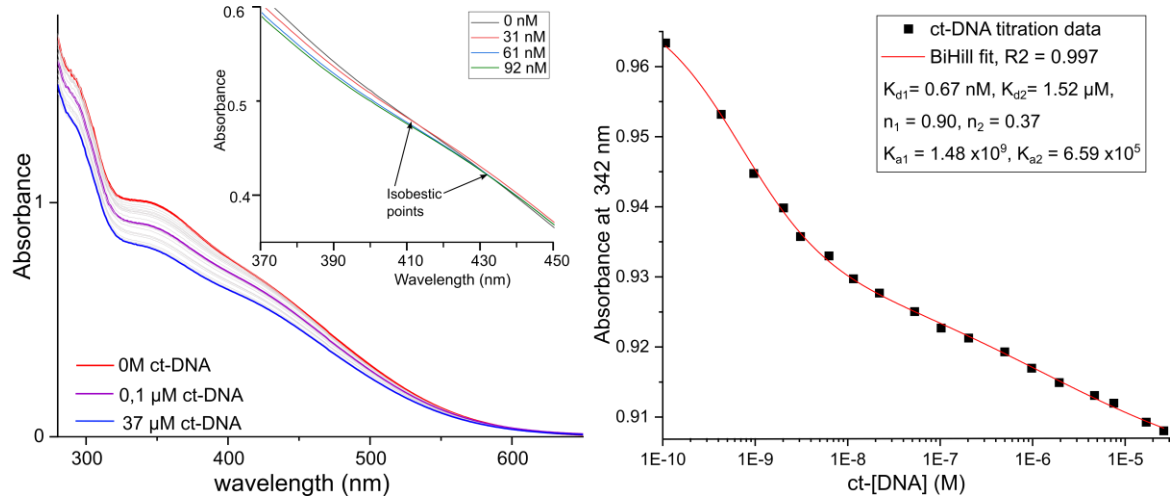


Figure 5.6. A representative of the triplicates for the UV-vis absorption spectra of 117 µM **2d** in 0.10 M TRIS-HCl buffer 10% DMSO (red spectrum) after sequential additions of ct-DNA 0.1 µM (purple spectrum) and final concentration (37 µM ct-DNA) before precipitation (blue spectrum). The insert shows the isobestic points at low concentrations of DNA. The graph on the right is an illustration of the Uv-vis titration spectra at 342 nm with a change in concentration of the ratio of **2d**:ct-DNA

Table 5.3: The binding parameters of **2d** to ct-DNA and its components with ct-DNA

		Binding constant (K_a)		
DNA	**K_{a1}**	1.48 x10^9		
	K_{a2}	6.59 x10^5		
		Base / M^{-1}	**Nucleoside / M^{-1}**	**Nucleotide / M^{-1}**
Adenine		1.20957 x10^4	1.74939 x10^3	3.71597 x10^3
Thymine		1.82812 x10^3	2.18775 x10^3	-
Cytosine		2.19796 x10^3	1.73579 x10^3	3.59202 x10^3
Guanine		-	1.64876 x10^3	1.25690 x10^3

The resulting spectral profile of the interaction between **2d** and ct-DNA exhibited similarities to that of a cationic Ru(II) polypyridine complex (with an order of binding constant of 10^6)[29] and an anionic DNA-binding probe (order of binding constant of 10^2, the low value was ascribed to the negative charge).[30] This observation is characterised by a significant drop in absorbance between 300-400 nm. Notably, this hypochromicity aligns with the behaviour of most NNN-type gold pincer complexes in the literature, albeit with binding constants falling in the range of 10^3 – 10^5 M^{-1}. [31–36]

DNA binding constants serve as predictive indicators of the binding mode of the test molecule to DNA. Typically, base binders exhibit the highest binding constants, as they form covalent bonds with DNA, and their interaction is usually irreversible. This stands in contrast to other types of DNA binding, which primarily rely on electrostatic, hydrophobic interactions, and π stacking (intercalation and groove bonding).

Most intercalators in literature have binding constants between 10^3 - 10^6 M^{-1}, examples of which include **EB** (2.5 × 10^6 – 8.2 × 10^4 M^{-1})[37] psoralen (9.75 × 10^3 M^{-1}),[38] and acrilidine (1.74 × 10^4 - 1.0 × 10^6 M^{-1}).[39] Groove binders however generally have higher affinities with binding constants between 10^5 and 10^8 M^{-1}.[24,25] It is difficult to distinguish base binders based on the binding constant, but some base-binding gold(III) pincer complexes have been reported to have binding constants of 4.5 × 10^5 and 5.4 × 10^5 M^{-1}. Although these ranges often overlap, they provide insight into the binding mechanism of the binders.

In this study, the interaction of **2d** with ct-DNA resulted in two binding constants, indicating the involvement of two modes of binding. K_{a1} was determined to be 1.48 x10^9 M^{-1}, suggesting that **2d** interacts with DNA through groove binding, as reported in the literature.[24,25] K_{a2} (6.59 x10^5 M^{-1}) suggested the interaction of **2d** with ct-DNA facilitated by intercalation or base binding. This value falls within the range observed for many base binders and intercalators in the literature.[31–33,35,37–39] Both forms of interaction are plausible due to the partially planar geometry of the metal complex **2d** and its tridentate nature, including a labile Cl^- ion, allowing for intercalation and base binding, respectively. However, EMSA studies suggested that base binding is involved in the interaction of **2d** with ct-DNA, prompting further investigation into this aspect.

To explore the potential base-binding (alkylating) properties of **2d**, UV-vis absorption titration experiments of **2d** with DNA were conducted with DNA bases, sugars, and phosphorylated sugars. The obtained information aimed to elucidate whether steric bulk around individual bases on DNA (ribose and phosphate groups) influences the binding of the base pairs to the gold complex, to what extent, and which atoms participate in the alkylation of DNA by **2d**.

The same procedure used for DNA titrations was used for all DNA components with variations in concentration as indicated in **Figure 5.6. Figure 5.6** illustrates the binding of **2d** to the DNA components, thymine and thymidine (thymine, guanine and cytosine components are illustrated in the **Section S4, Figures S42-S45** of the Supplementary information). The binding constants for all DNA components are also tabulated in **Table 5.3**.

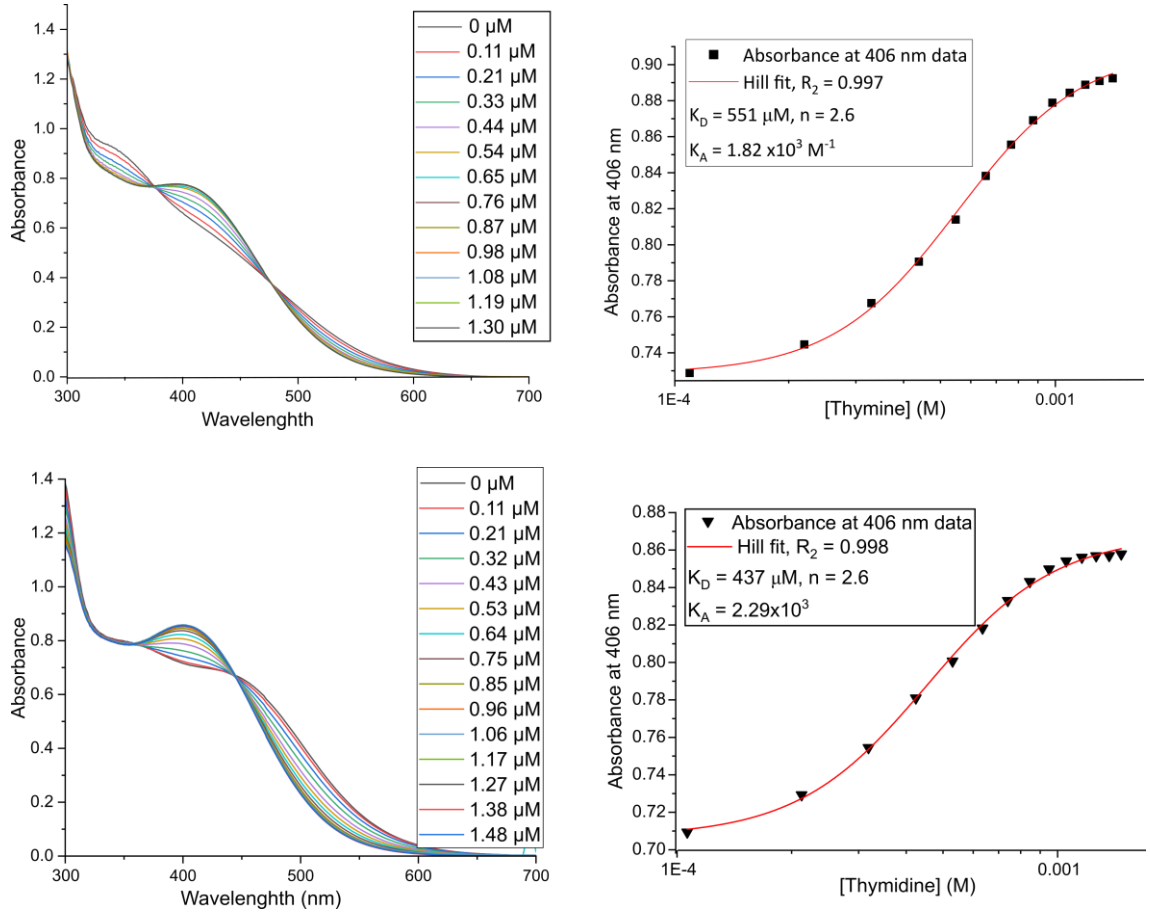


Figure 5.7. A representative of the triplicates for the UV-vis absorption spectra of 117 µM **2d** in 0.10 M TRIS-HCl buffer 10% DMSO after sequential additions of DNA components and final concentration before precipitation. The graphs on the right are an illustration of the Uv-vis titration spectra at specified wavelengths with a change in ratio of **2d** to the DNA components.

Analysis of the data was also done using the same protocol for the DNA studies between 400-450 nm, at a wavelength with the highest hypochromicity. Unlike in DNA titrations, there were distinct isosbestic points for all bases, nucleosides and nucleotides, which indicated a permanent interaction (covalent bonding) between **2d** and the DNA components.

A crystal structure of thymine bound to **2d** (**2dT**) was obtained (**Figure 5.7b**), providing insights into the interaction of the complex with DNA. In the DNA strand, N1 in the pyrimidines and N9 in purines (**Figure 5.7a**) play pivotal roles in nucleoside formation. It was inferred that although these nitrogens are free in the bases, they remain unreactive to the complex **2d.** This scenario is advantageous, as the nitrogens are not involved in base binding, thereby enhancing the affinity of the base binder to DNA, as no bond breaking is required (the nitrogens are easily accessible).

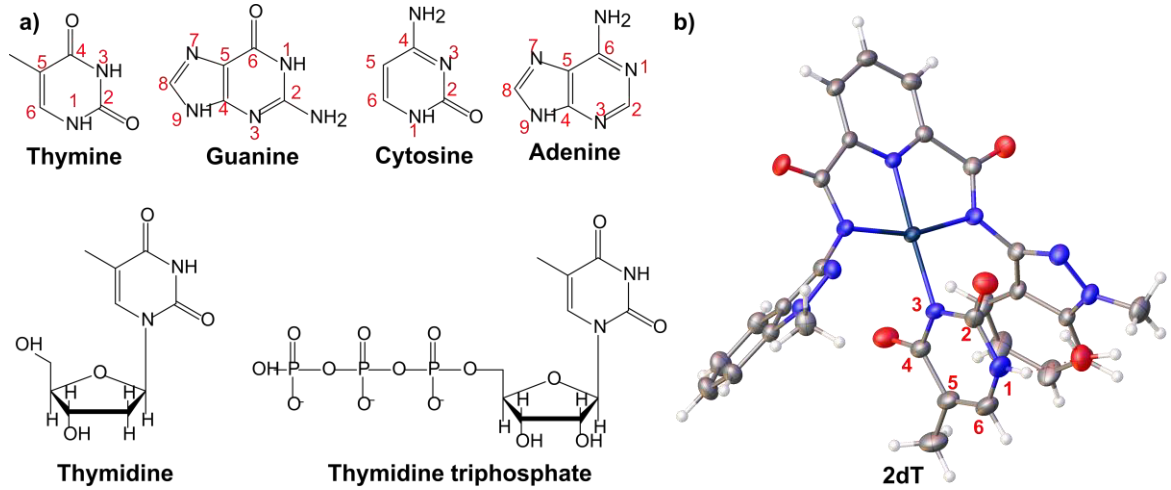


Figure 5.8. a) is an illustration of the structures of DNA components, purine bases guanine (G) and adenine (A) and the pyrimidines, cytosine (C) and thymine (T), examples of a nucleosides, thymidine and the nucleotide thymidine triphosphate. The bases binds to the ribose molecule through N1 for pyrimidines and N9 for the purines. **b)** is the crystal structure of a thymine molecule covalently **bound** to **2d** through N3 by displacing the Cl^- ion.

Base binders exhibit a higher affinity to N3 than N1 in thymine due to the highly polarised N3-H bond in the thymine molecule, resulting from the presence of two adjacent acetyl groups. This polarisation makes N3 easily deprotonated, rendering it more reactive than N1.[40] Studies have indicated that cisplatin, an alkylating agent, preferably binds to the N7 guanine residue,[41] rather than the N9, supporting the theory that N1 in pyrimidines and N9 in purines are not actively involved in base binding. Therefore, it is speculated that **2d**, as a base binding agent, will also preferentially bind to N1 in pyrimidines and N9 in purines.[42]

It is noteworthy that N7 on purines is not engaged in hydrogen bonding between the bases or the bond between the sugar and the base. Consequently, it is more accessible, potentially explaining why cisplatin exhibits a preference for binding to the guanine molecule.[43] Conversely, N3 is involved in hydrogen bonding, making it less accessible for binding with the metal complexes. It was therefore deduced that the DNA components bind to **2d** using the same donor atom, whether it is a nucleobase, nucleoside, nucleotide or DNA strand.

Increasing the size of the molecules from bases to nucleotides did not have a consistent effect on the binding to the metal complex with A, C, G and T components (**Table 5.3**).

Although it could have been argued that the smaller size of the DNA components improves their binding to **2d** as compared to the DNA structure, size did not make much of a difference between bases, nucleotides and nucleosides, which have different sizes. The fact that N9 participates in the binding with **2d** showed that the bulk of the DNA, (the ribose sugar and the phosphates), was not interfering in the binding process, with no steric bulk. Rather electronic effects are responsible for the reactivities of these components.

Adenine components exhibited a relatively higher binding affinity to **2d**, compared to Guanine, Cytosine and Thymine, but this was not consistent with the nucleotide and nucleosides such that no trend could be established. All four bases are most likely to bind to **2d** on N1 for the purines and N9 for the pyrimidines.

Binding constants for the bases, nucleotides and nucleosides were relatively high, (1.2×10^5–1.3×10^4), implying that alkylation could be one of the binding methods of **2d** to DNA. It could have been the only mode of binding, but the binding constants of the bases are very low compared to the binding constant of **2d** to DNA. It was therefore deduced that other modes of binding were contributing to the astounding binding constant of **2d** to DNA, together with base binding.

2d demonstrated two different binding modes to DNA with very high affinity to ct-DNA, and these modes were proposed to be groove binding and base-binding. It was however concluded that alkylation is involved in the interaction of **2d** to ct-DNA because of its ability to bind to the DNA components, which only allows for covalent interactions. This information is in correlation to the data from EMSA studies, where it was concluded that base-binging was involved in the interaction of **2d** with ct-DNA Consequently, to get a conclusive theory on the mode of binding more experiments had to be conducted.

5.4.3 Viscometry and melts

Viscometry is a method used frequently for the determination of the binding mode for DNA, between intercalation and groove binding and alkylation. This hydrodynamic measurement is one of the most essential tests to determine the binding model in solution, as it is sensitive to the length of the DNA in solution. DNA elongation without any kinks and bends increases its viscosity, and on the other hand, shortening of the same DNA with kinks and bends reduces its viscosity. As a result, the intercalation of compounds into the DNA strands increases its length as the bases are pushed apart to accommodate the intercalator, and groove binders do not change the length of the DNA or might cause bends, resulting in a slight reduction of or no change in viscosity of the DNA.[44–46] Typically, alkylation of the DNA can result in kinks and bends on the DNA molecule resulting in retarded viscosity.[47]

DNA thermal melt analysis is also crucial in differentiating between the different binding modes of compounds to DNA. DNA strands are annealed together by weak interactive forces, (H-bonding, pi-stacking etc.) and these are dependent on temperature. As temperature increases, the two strands separate into two, and the melting temperature is the temperature at which half of the DNA is denatured. Intercalation of compounds in between the DNA base pairs increases its length and stabilises the DNA such that the melting point of DNA increases.[33,48,49] Groove binding decreases its melting point as it

distorts the binding on the base pairs in the DNA grooves, by weakening their interactions.[33,48,49] Alkylators disrupt the interaction between base pairs, causing local denaturing, and this reduces the melting point of the DNA.[50–52] This is only true for monofunctional alkylation (only one binding site on the complex), as bifunctional alkylation (interstrand linking) increases the energy needed to denature the DNA, thus raising its melting temperature.

The viscometry and DNA thermal melt analysis (**Figure 5.8**) suggest that **2d** has two modes of binding to DNA. Both the viscosity and melting temperatures of DNA decrease at low concentrations of **2d** (<8μM), which is an indication of monofunctional alkylation (as only **2d** one labile Cl), and increase at higher concentration (>8μM), an indicator of intercalation.

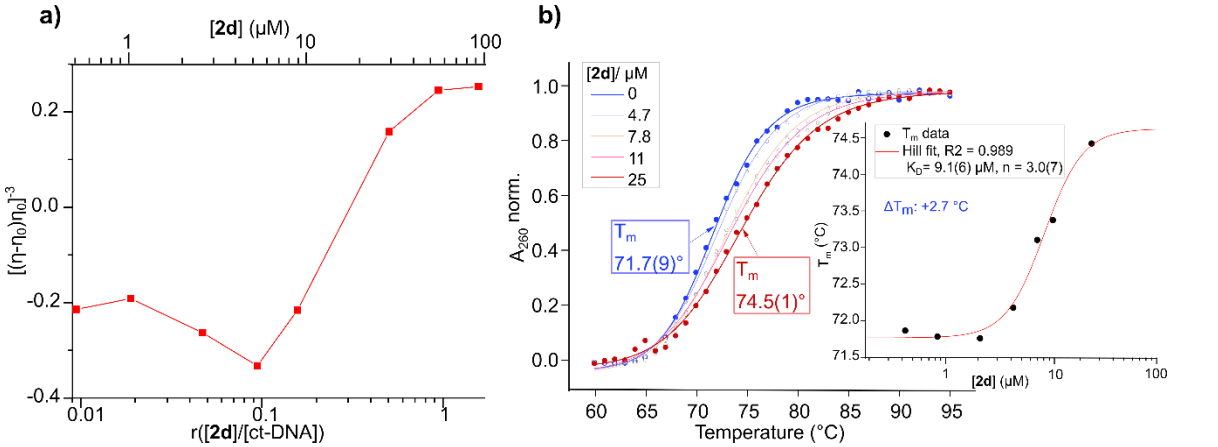


Figure 5.9. a) A plot of the change in relative viscosity of ct-DNA solution with the increase in the ratio of **2d** to ct-DNA at 37°C in 1x TAE buffer, 5% v/v DMSO at pH 7.4. **b)** The melt curves for ct-DNA with different concentrations of **2d** to calculate T_m from the Boltzmann sigmoidal fit. The insert is the change in T_m with the change in [**2d**], fitted on a hill sigmoidal function, and ΔT_m is +2.7 °C.

The results from viscometry and DNA thermal melt analysis are in correlation with gel electrophoresis and DNA titration studies, where the trend shifted at high concentrations of **2d**. From these DNA binding studies, it was concluded that **2d** binds to ct-DNA through groove binding and base binding. The ability of **2d** to bind to DNA meant that it could potentially inhibit cell growth and/or proliferation. This ability makes it a potential anticancer agent.

5.5 HSA binding studies

Human serum albumin (HSA) is a multifaceted carrier of exogenous and endogenous compounds in the human body.[53] These include therapeutic drugs used to treat multiple diseases, thereby improving their pharmacokinetic and pharmacodynamic properties.[53,54] The distribution and bioavailability of drugs are often improved by interactions with HSA, contingent on the particular pharmacokinetic characteristics of the drug molecules.[6] HSA is also widely distributed and, as such, influences many aspects of the pharmacodynamic behaviour of different therapeutics, such as the drug half-life in the bloodstream, drug efficacy regulation, drug toxicity reduction, and improved drug targeting specificity.[55–58]

Due to its poor solubility in an aqueous medium, it was envisaged that a transport mechanism for **2d** to cells would be essential in biological conditions to prevent its precipitation before reaching cellular DNA, thereby improving its pharmacokinetic behaviour. The binding of **2d** to HSA was envisioned to confer several advantages, including protection of the metal complex from reduction, improved solubility in aqueous media, and facilitation of access through plasma membranes.[5,6,59]

To allow for the successful transportation of **2d** to DNA, the metal complex must exhibit a relatively higher affinity for DNA compared to that of HSA, ensuring the complex is released onto DNA upon encountering it. Therefore, understanding the binding of **2d** to HSA becomes imperative. This involves elucidating the thermodynamics, mode of binding, and, significantly, the affinity of **2d** to HSA in comparison to that of DNA.

5.5.1 Thermodynamics of 2d binding to HSA

Absorbance values at 336 nm were corrected for dilution prior to data fitting using the modified Hill-Langmuir model.[26,27] The fitting process involved employing a sigmoidal function within OriginPro2019.[28] The resulting fit allowed for the quantification of the binding affinity of **2d** to HSA, expressed as a binding constant (K_a). The obtained K_a values were 1.57 x10^4 M^{-1}, 1.16 x10^5 M^{-1} and 9.28 x10^4 M^{-1} at 37 °C, 25 °C and 15°C, respectively (**Figure 5.9a** and **b**, **Table 5.4)**.

The binding constant (K_a) was derived from the dissociation constant obtained from the Hill plot, as per **Equation 5.14**, elucidated below. This is according to the proposed equation of **2d** binding to HSA (**Equation 5.12**)

$$\mathbf{2d} + \mathbf{HSA} \rightleftharpoons \mathbf{2d\text{-}HSA} \qquad \textbf{Equation 5.12}$$

at equilibrium,

$$\boldsymbol{k_{on}}[\boldsymbol{2d}][\boldsymbol{HSA}] = \boldsymbol{k_{o_{ff}}}[\boldsymbol{2d - HSA}] \qquad \textbf{Equation 5.13}$$

where k_{on} and k_{off} are rate constants for the forward (association) and reverse (dissociation) reactions. Following this equation, the equilibrium binding constant constant (K_a), and its inverse K_d, (equilibrium dissociation constant) are given by

$$\frac{k_{on}}{k_{0ff}} = \frac{[\boldsymbol{2d}\text{-}HSA]}{[\boldsymbol{2d}][HSA]} = K_a = \frac{1}{K_d} \qquad \textbf{Equation 5.14}^{60}$$

A low K_a indicates weak binding (low affinity), suggesting a fast dissociation rate relative to the association rate. Conversely, a high K_a indicates strong binding (high affinity), as the ligand is more likely to remain bound to the target molecule.

The thermodynamics governing the interaction between **2d** and HSA was extracted from the Van 't Hoff plot (**Figure 5.9c**). The change in enthalpy (17.7 kJ mol^{-1}) and entropy (157 J K^{-1} mol^{-1}) were calculated according to **Equations 5.17** and **5.18** respectively. The Gibbs free energy for the association of **2d** and HSA at each temperature was calculated according to the Gibbs–Helmholtz equation (**Equation 5.15**). The data is recorded in **Table 5.4**.

Gibbs–Helmholtz equation

$$\Delta G^0 = \Delta H - T\Delta S = -RT \ln K_a$$ **Equation 5.15**[60]

Van't Hoff's equation

$$\ln K_a = \frac{\Delta H}{R} \cdot \frac{1}{T} - \frac{\Delta S}{R}$$ **Equation 5.16**[60]

$$slope = \frac{\Delta H}{R}$$ **Equation 5.17**[60]

and,

$$y\text{-}intercept = \frac{\Delta S}{R}$$ **Equation 5.18**[60]

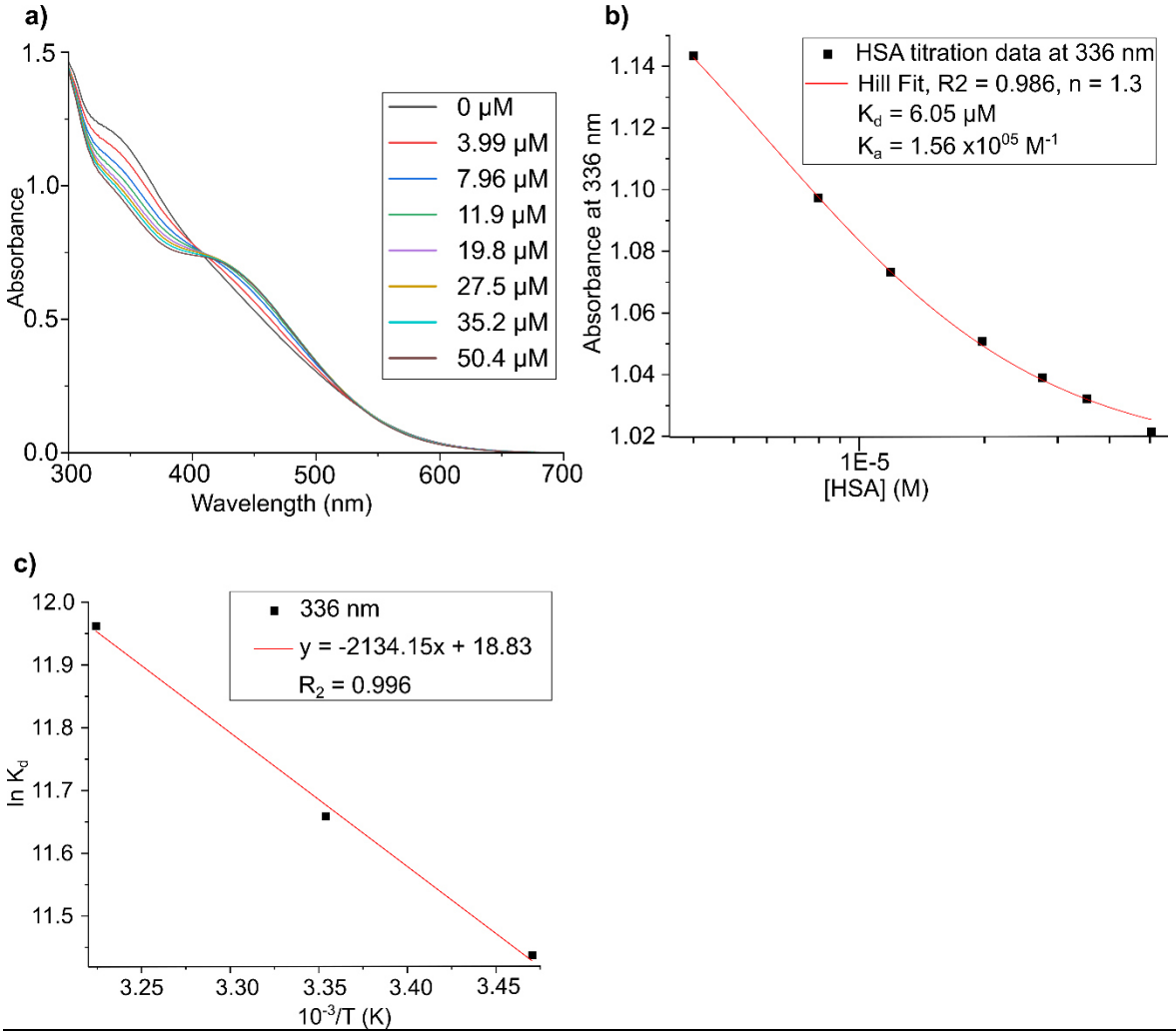


Figure 5.10. a) A representation of the triplicates for the UV-vis absorption spectra of 150 µM **2d** in 0.10 M TRIS-HCl buffer 10% DMSO after sequential additions of HSA from (0 µM to 50.4 µM) before precipitation at 37 °C **b**) An illustration of the Uv-vis titration spectra at 336 nm with a change in concentration of the ratio of 2d:HSA at 37 °C and **c)** the Van't-Hoff plot to determine the thermodynamic parameters for the binding of **2d** to HSA.

Table 5.4. Thermodynamic parameters for the binding of **2d** to HSA

T / K	K_a x 10^4 / M^{-1}	n	ΔG / kJ mol−1	ΔH / kJ mol^{-1}	ΔS / JK^{-1} mol^{-1}
288.15	9.28	1.8	-27.4	17.7	157
298.15	11.6	1.6	-28.9		
310.15	15.7	1.3	-30.8		

The positive values for both ΔH (enthalpy) and ΔS (entropy) suggest that hydrophobic interactions play a dominant role in the binding between **2d** and HSA. Despite both ΔH and ΔS being positive, the larger

magnitude of ΔH compared to a smaller value of TΔS results in a negative ΔG (Gibbs free energy), indicating that the binding of **2d** to HSA is a spontaneous process. Thus, the binding of **2d** to HSA is primarily entropy driven.

The positive ΔH implies that the reaction is endothermic, absorbing heat from the surroundings. Additionally, the positive ΔS signifies the displacement of ordered water molecules, contributing to the increased entropy of the system during the binding process. This behaviour is commonly observed in the interaction of HSA with metal complexes, such as platinum and gold.[53,59,61,62]

According to this study, the binding constant for the interaction of **2d** with HSA at 310 K is 15.7 x 10^4 M^{-1}. In comparison to the binding constant of **2d** to ct-DNA under similar conditions, this value is significantly lower (difference of 10^5). This suggests that the compound **2d** can be transferred from HSA to DNA in cells, indicating that **2d** can be transported through the HSA-mediated pathway since it has a moderate binding affinity to HSA.

5.5.2 Site displacement assays

HSA possesses multiple drug-binding sites, creating the possibility that compounds may preferentially bind to one or more sites on the HSA molecule.[57] Studies indicate that blocking a primary site may lead to either the compound displacing the blocker or the compound binding to alternative sites on the protein. Conducting a site displacement assay can offer insights into the primary drug binding site.

In this study, competitive blocking assays were conducted using fluorescence spectroscopy to elucidate the preferred binding site(s) for **2d**. The two main drug-binding sites of HSA were selectively and sequentially blocked using site-specific probes, warfarin, and dansyl glycine, aiming to delineate the binding specificity of **2d** on HSA. It is noteworthy that, according to the literature, warfarin and dansyl glycine bind exclusively to subdomain IIA and subdomain IIIA, respectively.[55,57]

Complex **2d** (0-27.5 μM) was titrated into a solution of native HSA and solutions of HSA pre-equilibrated with either warfarin or dansyl glycine. The fluorescence emission spectra for HSA-warfarin and HSA-dansyl glycine are illustrated in **Figure 5.10a** and **b**, respectively.

According to **Figure 5.10c** the maximum fluorescence emission of HSA-warfarin is 387 nm, which is a blue shift of 8 nm from the free warfarin peak at 395 nm. The fluorescence of this solution decreased monotonically with the increase in the concentration of **2d**. This was accompanied by a red shift of 5 nm (towards the warfarin peak). This suggests that **2d** binds to subdomain IIA of HSA, as the warfarin was being displaced from the HSA.

According to **Figure 5.10d**, the peak fluorescence emission of HSA-dansyl glycine is 479 nm, which is a blue shift of 11 nm from the free dansyl glycine peak at 490 nm. The fluorescence of this solution also decreased progressively with the increase in the concentration of **2d**. This was accompanied by a slight red shift of 3 nm (towards the dansyl glycine peak). This suggests that **2d** binds to subdomain IIIA of HSA, as the dansyl glycine was being displaced from the HSA.

This was also corroborated by the displacement assays **Figure 5.10e** of both the warfarin and the dansyl glycine, as more than 70 % of both compounds are displaced with **2d**. The values of n from

Figure 5.10f showed that at least one mole of **2d** binds to each of the subdomains IIA and IIIA of HSA. The value is slightly higher for subdomains IIA (1.3) in comparison to that of subdomains IIIA (1.1). This implies that **2d** has a slightly higher affinity for subdomains IIA.

$$log\,\frac{I_0 - I}{I} = \log K_a + n\log[\mathbf{2d}] \qquad \textbf{Equation 5.19}$$

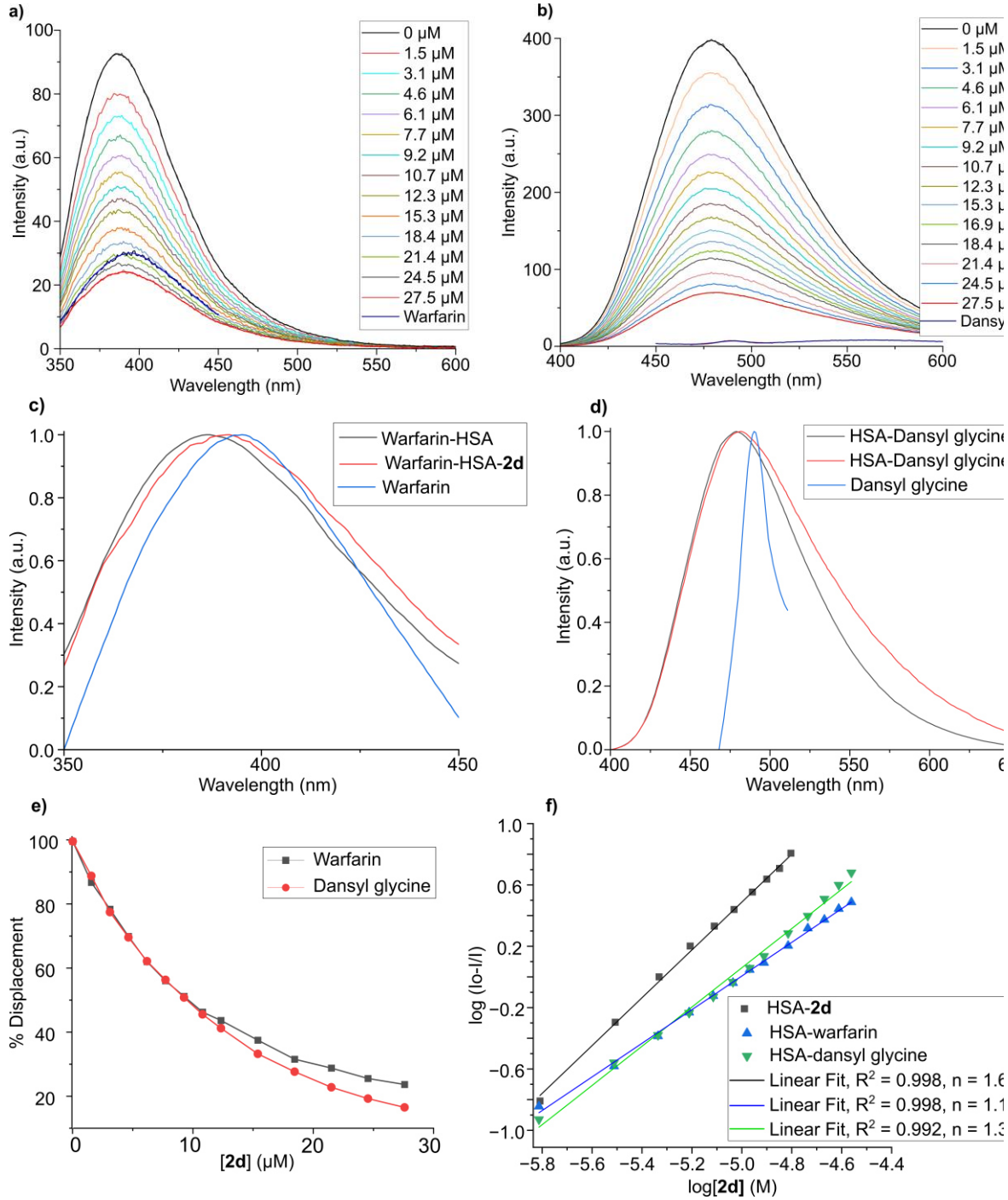


Figure 5.11. The emission spectra of **a)** HSA-warfarin and **b)** HSA-dansyl glycine as a function of concentration, **c)** Normalised fluorescence emission spectrum of HSA-warfarin, HSA-warfarin-**2d** and warfarin and **d)** Normalised fluorescence emission spectrum of HSA-dansyl glycine, HSA-dansyl glycine-**2d** and dansyl glycine **e)**The % displacement of warfarin and dansyl glycine with an increace in [**2d**]. **f)** A double log plot of the fluorescence quenching to measure the reaction stoichiometry n, according to the **Equation 19.** The sample solutions were excited at 320 and 420 nm respectively for warfarin (5 µM) and dansyl glycine (5 µM) to determine the binding site of **2d** on HSA (5 µM HSA in 50 mM potassium phosphate buffer at pH 7.4 at 37 °C).

This study sought to ascertain the binding constant of **2d** to ct-DNA and compare it to that of HSA, elucidating the specific binding sites on the HSA molecule. The findings indicate that overall, **2d** predominantly binds to HSA at subdomains IIA and IIIA, (Sudlow's site I and II) with a possibility of binding to other sites. Consequently, it was concluded that HSA holds the potential to serve as a

transporter for **2d** in biological systems. The study further proposed that the transfer of **2d** to cellular DNA is likely, given the substantial difference in their binding constants, which vary by an order of 4 ($x10^4$), signifying significant binding affinity.

5.6 Cellular Biology

To test the effect of **2d** on the viability in cancer cell lines, Growth inhibition, (MTT [3-(4,5-Dimethylthiazol-2-yl)-2,5-Diphenyltetrazolium Bromide]) assays and apoptosis assays (APOPercentage assays), were performed on two cell lines, HT-29 and MCF-7, which represented hormone-responsive breast cancer and colorectal cancer, respectively. Plumbagin was used as an internal control which also helped in assessing the technical reliability of the assays.

5.6.1 MTT assays

An MTT colorimetric assay assesses the effect of a drug on the cytotoxicity of cells, by measuring changes in cell viability.[63,64] MTT (3-(4,5-Dimethylthiazol-2-yl)-2,5-diphenyltetrazolium bromide) is a tetrazolium salt that helps detect reductive metabolism in cells. The yellow tetrazolium salt is cleaved by the mitochondrial enzyme reductase to form purple formazan crystals (**Figure 5.11**), and the colour change is the indicator for metabolic activities in the cell, thus an indicator of cell viability.[64] The production of purple formazan crystals is directly proportional to the metabolic activity of cells and therefore, cell viability.

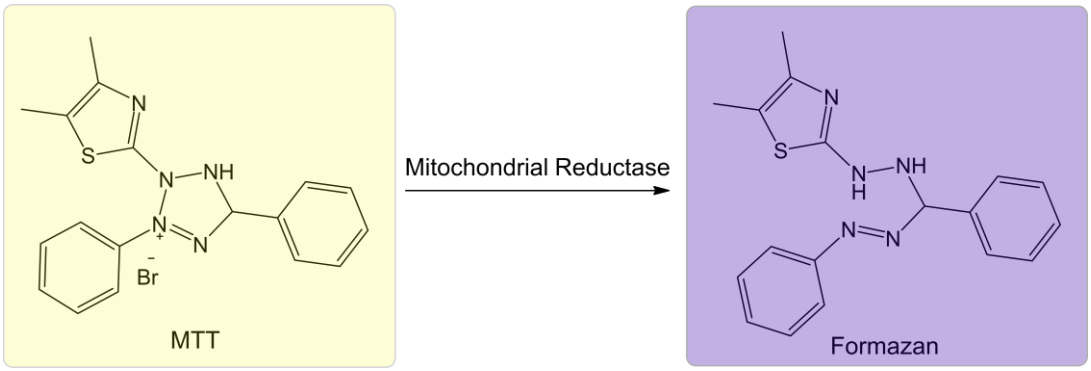


Figure 5.12. An illustration of the conversion of MTT to formazan in the cells by mitochondrial reductases.

The MTT assay was used to evaluate the cytotoxicity of **2d** in an *in vitro* model of human colorectal adenocarcinoma, HT-29 and human breast adenocarcinoma MCF-7, and the results are illustrated in **Figure 5.12**. In the HT-29 cell line, **2d** did not show a significant reduction in cell viability after 48 hours of treatment in both the low (0-5 μM) and high (5-100 μM) concentration ranges (IC_{50} >100 μM) compared to the negative control set to 100% cell viability, using a One-Way ANOVA ($p>0.05$; n=2).

After 48 h at high concentrations, the data showed significant variability upon treatment of the MCF-7 cell line with **2d** (One-Way ANOVA $p<0.05$; n=2), with an IC_{50} = 9 μM. This value is comparable to that of cisplatin which has been recorded in literature to be within the range of 0.5 – 40 μM.[65–67] This shows that **2d** has comparable cytotoxicity against the MCF-7 cancer cell line to cisplatin *in vitro*, and could potentially be effective in breast cancer treatment. More tests however have to be done *in vivo* to have a clear understanding of its cytotoxicity.

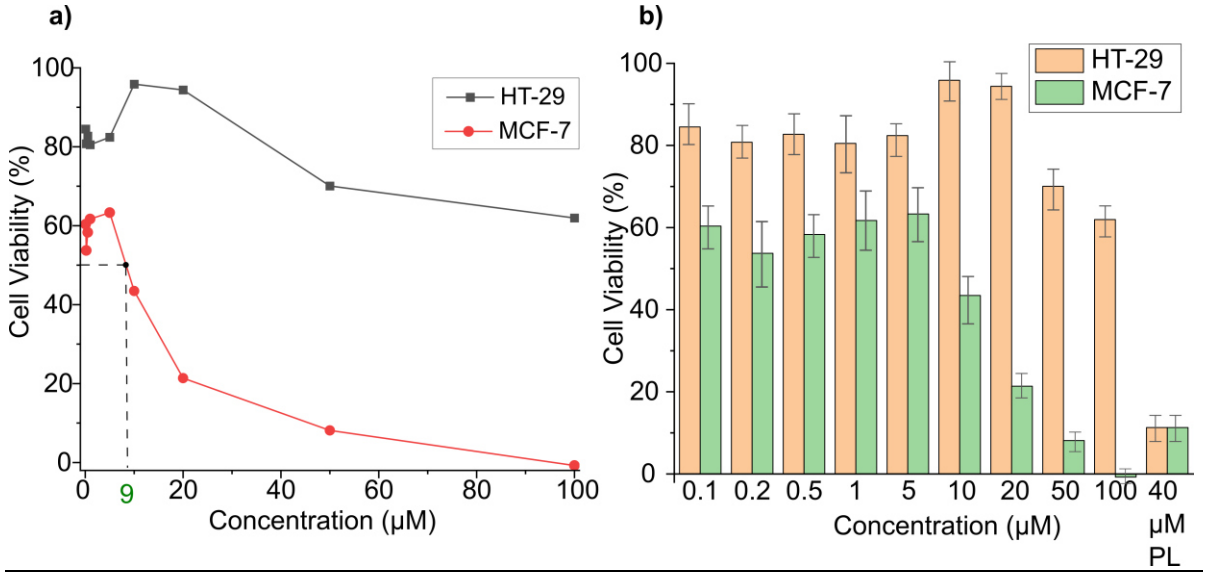


Figure 5.13. Growth inhibition of the HT-29 and MCF-7 cell lines with different doses of **2d** (0, 0.2, 0.5, 1, 5, 10, 20, 50, and 100 μM) after 48 h. IC_{50} values for the HT-29 and MCF-7 cell lines were calculated to be, >100 and 9 μM respectively.

The positive control, 40 μM plumbagin, killed cells in both cell lines with cell viability ranging between 0 to 25% between all data sets.[68] This confirms the success of the MTT assay.

5.6.2 APOPercentage assay

All cellular events associated with apoptosis, (cell surface exposure of phosphatidylserine (PS), including caspase activation and DNA fragmentation), can be assessed and quantified by an apoptosis assay.[69,70]

APOPercentage assay was performed to detect cells directly undergoing apoptosis (cell death). The red APOPercentage dye is selectively taken up into apoptotic cells. Subsequently, cytotoxicity can be measured by spectrophotometry or imaging.

The APOPercentage assay was used as a qualitative evaluation of the apoptosis-inducing properties of **2d**. The micrographs in **Figure 5.13** show the APOPercentage dye uptake after 48 hours of treatment in the HT-29 cell line. At a concentration of 100 μM, **2d** did not greatly increase dye uptake after 48 hours, compared to the negative control. In comparison, both 5 μM topotecan hydrochloride and 100 μM cisplatin seemed to increase APOPercentage dye uptake, indicating an increase in the number of apoptotic cells as a result of these treatments after 48 hours. After 72 hours, 100 μM of **2d** seemed to increase the number of apoptotic cells compared to the positive control, the margin was relatively large.

Despite strongly binding to DNA *in vitro* **2d** is only mildly cytotoxic to HT-29 cells. This suggests that the compound in its present form is unable to target key biochemical pathways/macromolecules in live cells (in vivo). Several factors could lead to this result, the main one being that **2d** may have difficulty being taken up by the cancer cells investigated. The cell imaging work with the APOPercentage assay shows that a better response occurs after 72 h of incubation with **2d**. This could also be due to the slow uptake of **2d** by the cells, among many other reasons.

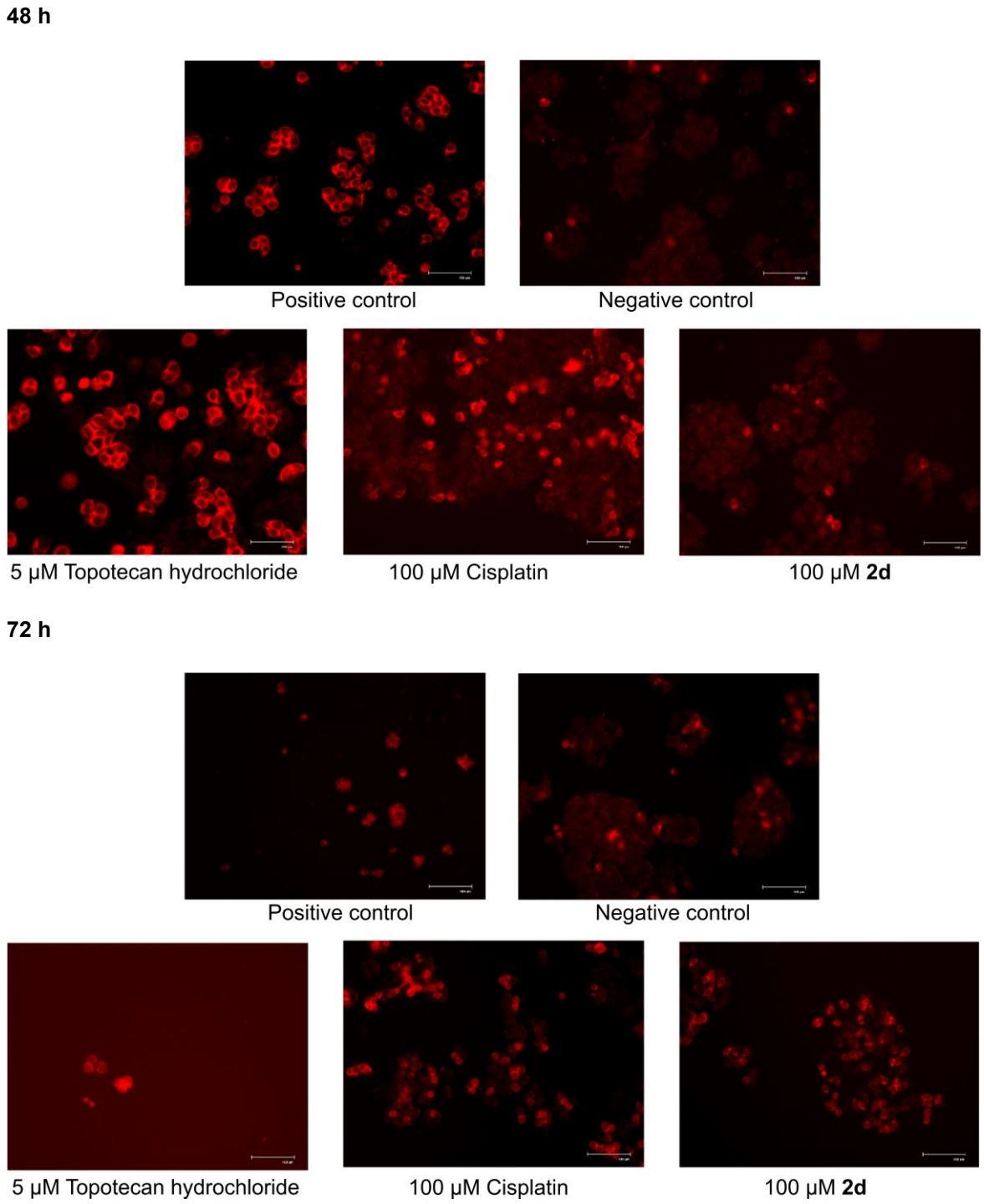


Figure 5.14. An illustration of apoptosis seen in HT-29 cells treated with test compounds after 48 and 72 hours.

5.7 Conclusion

All the studies in this chapter were to understand the biochemical behaviour of the gold(III) carboxamide pincer complex **2d** with different biological components to have an idea of what to expect in cells and the biological environment. **2d** has the potential to inhibit cell replication by binding to DNA as a groove

binder and base binder. The compound binds to reduced GSH without demetallation or reduction of gold(III), thus exhibiting its stability in biological conditions.

The main concern arising from the discoveries in this study is that **2d** has low solubility in aqueous conditions, as it could only dissolve in at least 10% v/v of DMSO. This poses a potential challenge as this is not the constitution of the body, and DMSO is toxic to the body. One other concern is that although **2d** has a high affinity to DNA, it also has a slight affinity for GSH. This is a cause for concern as this would influence the detoxification of the cells by GSH. This also means that there will be a slight two-way competition to bind the **2d** complex in the body, which would reduce its efficacy, as our target is DNA. Despite the reasons stated earlier, **2d** exhibited cytotoxicity towards breast cancer cells, which is comparable to that of cisplatin *in vitro*. It however exhibited poor cytotoxicity to human colorectal adenocarcinoma. This potentially makes it a good anticancer drug against breast cancer.

5.8 References

1 K. Collins, T. Jacks and N. P. Pavletich, *Proceedings of the National Academy of Sciences*, 1997, **94**, 2776–2778.
2 B. Alberts, A. Johnson, J. Lewis, M. Raff, K. Roberts and P. Walter, in *Molecular Biology of the Cell. 4th edition*, Garland Science, 2002.
3 G. M. Cooper and R. E. Hausman, *The cell: a molecular approach*, ASM Press ; Sinauer Associates, Washington, D.C. : Sunderland, Mass, 4th ed., 2007.
4 M. Hanif, S. Moon, M. P. Sullivan, S. Movassaghi, M. Kubanik, D. C. Goldstone, T. Söhnel, S. M. F. Jamieson and C. G. Hartinger, *J Inorg Biochem*, 2016, **165**, 100–107.
5 R. Graeser, N. Esser, H. Unger, I. Fichtner, A. Zhu, C. Unger and F. Kratz, *Invest New Drugs*, 2010, **28**, 14–19.
6 W. H. Ang, E. Daldini, L. Juillerat-Jeanneret and P. J. Dyson, *Inorg Chem*, 2007, **46**, 9048–9050.
7 M. Moskot, J. Jakóbkiewicz-Banecka, A. Kloska, E. Piotrowska, M. Narajczyk and M. Gabig-Cimińska, *Int J Mol Sci*, 2019, **20**, 304.
8 L. de Abreu Costa, M. Henrique Fernandes Ottoni, M. dos Santos, A. Meireles, V. Gomes de Almeida, W. de Fátima Pereira, B. Alves de Avelar-Freitas and G. Eustáquio Alvim Brito-Melo, *Molecules*, 2017, **22**, 1789.
9 H.-M. Lee, D. S.-H. Chan, F. Yang, H.-Y. Lam, S.-C. Yan, C.-M. Che, D.-L. Ma and C.-H. Leung, *Chem. Commun.*, 2010, **46**, 4680.
10 G. Felsenfeld and S. Z. Hirschman, *Journal of Molecular Biology*, 1965, **13**, 407–427.
11 OriginPro 2023b (version 2023b) OriginLab Corporation, Northampton, MA, USA.
12 T. M, Buffers for the physiological pH range, https://pubmed.ncbi.nlm.nih.gov/15801182/, (accessed May 23, 2021).
13 Munessar. Sankar and R. G. Bates, *Anal. Chem.*, 1978, **50**, 1922–1924.
14 J. P. Richie, S. Nichenametla, W. Neidig, A. Calcagnotto, J. S. Haley, T. D. Schell and J. E. Muscat, *Eur J Nutr*, 2015, **54**, 251–263.
15 Reduced Glutathione | Pure | Doctors and Patients Access, https://www.pureencapsulationspro.com/reduced-glutathione.html, (accessed June 27, 2023).
16 A. Krezel and W. Bal, *Acta Biochim Pol*, 1999, **46**, 567–580.
17 D. Jaganyi, F. Tiba, O. Q. Munro, B. Petrović and Ž. D. Bugarčić, *Dalton Trans.*, 2006, 2943–2949.
18 C. Tantardini and A. R. Oganov, *Nat Commun*, 2021, **12**, 2087.
19 L. Arnaut, in *Chemical Kinetics (Second Edition)*, ed. L. Arnaut, Elsevier, 2021, pp. 409–439.
20 R. G. Mayer and R. S. Drago, *Inorg. Chem.*, 1976, **15**, 2010–2011.
21 S. Hemdan, A. Mansour and F. Ali, 2019, **62**, 1–21.
22 J. Sigmon and L. L. Larcom, *ELECTROPHORESIS*, 1996, **17**, 1524–1527.
23 D. Řeha, M. Kabeláč, F. Ryjáček, J. Šponer, J. E. Šponer, M. Elstner, S. Suhai and P. Hobza, *J. Am. Chem. Soc.*, 2002, **124**, 3366–3376.
24 P. E. Pjura, K. Grzeskowiak and R. E. Dickerson, *Journal of Molecular Biology*, 1987, **197**, 257–271.
25 B. H. Geierstanger and D. E. Wemmer, *Annual Review of Biophysics and Biomolecular Structure*, 1995, **24**, 463–493.

26 S. Goutelle, M. Maurin, F. Rougier, X. Barbaut, L. Bourguignon, M. Ducher and P. Maire, *Fundam Clin Pharmacol*, 2008, **22**, 633–648.
27 R. Gesztelyi, J. Zsuga, A. Kemeny-Beke, B. Varga, B. Juhasz and A. Tosaki, *Arch. Hist. Exact Sci.*, 2012, **66**, 427–438.
28 OriginPro 2019b (version 2019b) OriginLab Corporation, Northampton, MA, USA.
29 B. C. Poulsen, S. Estalayo-Adrián, S. Blasco, S. A. Bright, J. M. Kelly, D. C. Williams and T. Gunnlaugsson, *Dalton Trans.*, 2016, **45**, 18208–18220.
30 S. Ghosh, P. Kundu, B. K. Paul and N. Chattopadhyay, *RSC Adv.*, 2014, **4**, 63549–63558.
31 Pincer Compounds - 1st Edition, https://www.elsevier.com/books/pincer-compounds/morales-morales/978-0-12-812931-9, (accessed May 25, 2023).
32 J. J. Yan, A. L.-F. Chow, C.-H. Leung, R. W.-Y. Sun, D.-L. Ma and C.-M. Che, *Chem. Commun.*, 2010, **46**, 3893–3895.
33 D. van der Westhuizen, C. A. Slabber, M. A. Fernandes, D. F. Joubert, G. Kleinhans, C. J. van der Westhuizen, A. Stander, O. Q. Munro and D. I. Bezuidenhout, *Chemistry – A European Journal*, 2021, **27**, 8295–8307.
34 B. Bertrand, M. R. M. Williams and M. Bochmann, *Chemistry – A European Journal*, 2018, **24**, 11840–11851.
35 S. Radisavljević and B. Petrović, *Front Chem*, 2020, **8**, 379.
36 S. Radisavljević, I. Bratsos, A. Scheurer, J. Korzekwa, R. Masnikosa, A. Tot, N. Gligorijević, S. Radulović and A. R. Simović, *Dalton Trans.*, 2018, **47**, 13696–13712.
37 J.-B. Lepecq and C. Paoletti, *Journal of Molecular Biology*, 1967, **27**, 87–106.
38 X. Zhou, G. Zhang and L. Wang, *International Journal of Biological Macromolecules*, 2014, **67**, 228–237.
39 S. M. V. De Almeida, E. A. Lafayette, L. P. B. G. Da Silva, C. A. da C. Amorim, T. B. De Oliveira, A. L. T. G. Ruiz, J. E. De Carvalho, R. O. De Moura, E. I. C. Beltrão, M. D. C. A. De Lima and L. B. de C. Júnior, *International Journal of Molecular Sciences*, 2015, **16**, 13023–13042.
40 S. Perreault, F. Arjmand, J. Chandrasekhar, J. Hao, K. S. Keegan, D. Koditek, E.-I. Lepist, C. K. Matson, M. E. McGrath, L. Patel, K. Sedillo, J. Therrien, N. A. Till, A. Tomkinson, J. Treiberg, Y. Zherebina and G. Phillips, *ACS Med. Chem. Lett.*, 2020, **11**, 1236–1243.
41 A. Gelasco and S. J. Lippard, in *Metallopharmaceuticals I: DNA Interactions*, eds. M. J. Clarke and P. J. Sadler, Springer, Berlin, Heidelberg, 1999, pp. 1–43.
42 W. Zeng, Y. Zhang, W. Zheng, Q. Luo, J. Han, J. Liu, Y. Zhao, F. Jia, K. Wu and F. Wang, *Molecules*, 2019, **24**, 1852.
43 S. Ghosh, *Bioorganic Chemistry*, 2019, **88**, 102925.
44 M. Sirajuddin, V. McKee, M. Tariq and S. Ali, *Eur J Med Chem*, 2018, **143**, 1903–1918.
45 M. Sirajuddin, S. Ali and A. Badshah, *Journal of Photochemistry and Photobiology B: Biology*, 2013, **124**, 1–19.
46 M. Sirajuddin, A. Haider and S. Ali, *Int. J. Adv. Res*, 2014, **1**, 510–530.
47 M. Wanunu and Y. Tor, *Methods for Studying Nucleic Acid/Drug Interactions*, CRC Press, 2011.
48 M. T. Bjorndal and D. K. Fygenson, *Biopolymers*, 2002, **65**, 40–44.
49 H. Loskotová and V. Brabec, *European Journal of Biochemistry*, 1999, **266**, 392–402.
50 D. Y. Lando, E. N. Galyuk, C.-L. Chang and C.-K. Hu, *Journal of Inorganic Biochemistry*, 2012, **117**, 164–170.
51 D. Y. Lando, C.-L. Chang, A. S. Fridman, I. E. Grigoryan, E. N. Galyuk, Y.-W. Hsueh and C.-K. Hu, *Journal of Inorganic Biochemistry*, 2014, **137**, 85–93.
52 A. S. Fridman, V. Brabec, S. G. Haroutiunian, R. M. Wartell and D. Y. Lando, *Journal of Biomolecular Structure and Dynamics*, 2003, **20**, 533–545.
53 S. Sookai and O. Q. Munro, *Dalton Transactions*, 2023, **52**, 14774–14789.
54 E. Danelius, R. G. Ohm, Ahsanullah, M. Mulumba, H. Ong, S. Chemtob, M. Erdelyi and W. D. Lubell, *J. Med. Chem.*, 2019, **62**, 11071–11079.
55 P. Lee and X. Wu, *Curr Pharm Des*, 2015, **21**, 1862–1865.
56 M. Fasano, S. Curry, E. Terreno, M. Galliano, G. Fanali, P. Narciso, S. Notari and P. Ascenzi, *IUBMB Life*, 2005, **57**, 787–796.
57 F. Yang, Y. Zhang and H. Liang, *Int J Mol Sci*, 2014, **15**, 3580–3595.
58 D. Sleep, J. Cameron and L. R. Evans, *Biochimica et Biophysica Acta (BBA) - General Subjects*, 2013, **1830**, 5526–5534.
59 R. Yousefi, A. Taheri-Kafrani, S. M. Nabavizadeh, Z. Pouryasin, M. B. Shahsavani, K. Khoshaman and M. Rashidi, *Mol Biol Res Commun*, 2015, **4**, 167–179.
60 X. Du, Y. Li, Y.-L. Xia, S.-M. Ai, J. Liang, P. Sang, X.-L. Ji and S.-Q. Liu, *Int J Mol Sci*, 2016, **17**, 144.
61 B. A. Babgi, J. Alsayari, H. M. Alenezi, M. H. Abdellatif, N. E. Eltayeb, A.-H. M. Emwas, M. Jaremko and M. A. Hussien, *Pharmaceutics*, 2021, **13**, 461.
62 A. Mukhija and N. Kishore, *Journal of Molecular Liquids*, 2019, **283**, 558–572.

63 M. V. Berridge, P. M. Herst and A. S. Tan, in *Biotechnology Annual Review*, Elsevier, 2005, vol. 11, pp. 127–152.
64 M. Ghasemi, T. Turnbull, S. Sebastian and I. Kempson, *Int J Mol Sci*, 2021, **22**, 12827.
65 T. Kashkoulinejad-Kouhi, S. Safarian, B. Arnaiz and L. Saa, *Oncol Rep*, 2021, **45**, 665–679.
66 J. Suberu, I. Romero-Canelón, N. Sulluvan, A. Lapkin and G. Barker, *ChemMedChem*, , DOI:10.1002/cmdc.201402285.
67 J. Zou, L. Zhu, X. Jiang, Y. Wang, Y. Wang, X. Wang and B. Chen, *Oncotarget*, 2018, **9**, 11268–11278.
68 S. Sagar, L. Esau, B. Moosa, N. M. Khashab, V. B. Bajic and M. Kaur, *Anticancer Agents Med Chem*, 2014, **14**, 170–180.
69 M. Oancea, S. Mazumder, M. E. Crosby and A. Almasan, *Methods Mol Med*, 2006, **129**, 279–290.
70 O. Kepp, L. Galluzzi, M. Lipinski, J. Yuan and G. Kroemer, *Nat Rev Drug Discov*, 2011, **10**, 221–237.

6. Summary and conclusion

6.1. Summary of the study

The primary objective of this study was to investigate the potential anticancer properties of gold(III) carboxamide pincer complexes, inspired by NNN-type pincer ligands. Six pincer ligands **1a-f** were successfully synthesised and characterised. Although attempts were made to synthesise all six proposed complexes, only **2d-f** were successfully synthesised and characterised. The synthetic efforts provided valuable insights into the behaviour of these compounds, revealing their sensitivity to solubility and temperature adjustments.

During the attempts, unexpected complexes (**2di and 2dii**) were formed but could not be isolated for further studies. Nevertheless, these unexpected complexes offered insights into the reactivity of the indazole rings, suggesting potential avenues for future investigations. Additionally, a palladium(II) metal complex was isolated, contributing to the understanding of the behaviour of pincer complexes and gold metal.

It was concluded that the failure to synthesise complexes **2a-c** was attributed to the accessibility of the quinolone nitrogens, which readily reacted with the gold metal. The observed demetallation in solution was likely due to the elongated N–Au–N distance, preventing the stabilisation of the complex. This finding highlights the importance of the spatial arrangement of these nitrogens in the synthesis of such complexes.

The investigation of the biochemistry of complex **2d** included studies with DNA, HSA, and GSH. The binding studies with GSH revealed that the complex is stable to reduction and metalation, binding to GSH with a relatively low binding constant of 33.71 $M^{-1}s^{-1}$. This suggests that the complex interacts with GSH through a stable process, emphasising its stability in the presence of this reducing agent.

The notable difference in the binding constants between DNA (1.48 $x10^9$ and 6.59 $x10^5$ M^{-1}) and HSA (15.7 x 10^4 M^{-1}) indicates that **2d** can be easily transferred from DNA to HSA. This finding implies a potential mode of transport for **2d** in a biological setting, indicating that it is likely transported to cells through the HSA-mediated pathway. This insight into the interaction of **2d** with biological molecules is crucial for understanding its behaviour in a biological context.

6.2. Study evaluation

This study highlights the crucial role of synthetic feasibility in drug design, showcasing how the use of strong σ-donors, specifically nitrogen-based pincers, effectively stabilises gold(III) under physiological conditions. The versatile pincer framework allows for modifications on the arms, introducing diverse properties to the compounds. The project aimed to explore the potential of a group of gold(III) pincer complexes in DNA binding and cytotoxicity.

The ability of compound **2d** to target ct-DNA structures, essential during DNA replication, was demonstrated in DNA binding studies, suggesting potential cytotoxicity in cancer cells by inhibiting cell

replication. Despite being less-than-ideal for synthesis, **2d** exhibited significant cytotoxicity against MCF-7 cancer cells, with moderate effects on HT-29 cancer cells, along with clear interactions with DNA. This class of gold(III) pincer complexes emerges as a promising anticancer agent.

Unlike many documented gold(III) complexes, where the metal complex's effects are attributed to specific ligands, **2d**'s anticancer properties likely involve the entire complex, with the labile Cl^- being exchangeable. The observation of two modes of binding to DNA supports this hypothesis. Additionally, HSA binding studies indicate that **2d** can be transported to cells by the HSA-mediated pathway.

In conclusion, the comprehensive investigation of **2d** in this study, covering stability, DNA and HSA binding, underscores the potential of gold(III) carboxamide pincer complexes as effective anticancer drugs. Their ability to impede uncontrolled cell replication in cancer cells, facilitated by transport by the HSA-mediated pathway, presents a promising avenue for further research in anticancer therapeutics.

6.3. Future work

A more comprehensive *ab initio* calculation of the Potential Energy Surface (PES) for the ligands in this study, while incorporating solvent effects is deemed necessary to accurately interpret the dynamic NMR observations. Modifications to the ligands for metal complexes **2a-2c** should be considered to prevent the metal ion's reactivity with the quinolone nitrogens. An alternative proposal involves reacting the ligands/complexes with CH_3I to protect the nitrogens and enhance the compounds' solubility.

While this study established that **2d** can be easily transferred from DNA to HSA due to the difference in binding constants, further investigations are warranted to determine the extent of this exchange. A diffusion cell system, employing Amicon size-exclusion membrane filters to separate DNA and HSA-**2d** solutions, can be utilised to measure the metal complex's uptake by DNA from HSA.

Additionally, to validate the promising cytotoxicity findings of the Au(III) chelates against cancer, further research in a mouse model is imperative. This approach will provide valuable insights into the effectiveness of Au(III) chelates in a living model, facilitating a more comprehensive understanding of their potential therapeutic applications.